PHOTOINDUCED ELECTRON AND ENERGY DYNAMICS IN ARCHITECTURALLY DESIGNED MOLECULAR ASSEMBLIES CONTAINING C_{60}-FULLERENE

LI WANG

001311

CENTRE FOR NFLD. STUDIES
[illegible] 8 1978
MEMORIAL UNIVERSITY
OF NEWFOUNDLAND

Photoinduced Electron and Energy Dynamics in Architecturally Designed Molecular Assemblies Containing C_{60}-Fullerene

by

© Li Wang

A Thesis Submitted in Partial Fulfillment of the

Requirements for the Degree of

Doctor of Philosophy

August 20, 2009

Department of Chemistry

Memorial University

St. John's, Newfoundland

Canada

Abstract

The studies presented in this thesis describes the excited state dynamics of electron and energy transfer in one- and two-dimensional π-conjugated molecular constructs with fullerenes as electron accepting chromophores.

This thesis first starts with the energetics and dynamical processes in the excited state of π-conjugated OPV/OPE oligomers following photon capture. Systematic analysis and characterization of the excited states formed after excitation includes the detailed quantitative understanding of the structural, electronic and vibronic parameters of π-conjugated OPV/OPE oligomers, as well as the substituent and orientation effects that dictate radiative, non-radiative relaxation pathways and the reaction dynamics of these transient excited states.

With the detailed understanding of the excited state properties of π-conjugated OPV/OPE bridges, the photo-induced electron and energy transfer in the π-bridged C_{60} systems $[A\text{-}(\pi\text{-}B)_{C/L}\text{-}A]$ was undertaken. A major portion of the research centered on diphenylamino derivatized molecular assemblies. The excited states of molecular assemblies containing phenylamino moieties are known to be complex and many facets of dynamics are still controversial. Systematic investigations of the donor substituent effect on the excited state dynamics and the photo-induced electron and energy transfer in the donor substituted (π-B)-bridged C_{60} systems $(A\text{-}[\pi\text{-}(D)B_C]_n\text{-}A)$ were scrutinized. Ultimately, this research should teach us how to engineer molecules in the potential opto-photonic device applications, *i.e.* photosynthetic devices that convert photonic energy into chemical energy.

With the increased understanding of the ground and excited state properties of π-conjugated OPV/OPE oligomers with donor substituents, the last chapter is to assess the performance of two-dimensional H-shaped OPV/OPE chromophores with electron donor and acceptors as potential sensors for specific analytes.

Acknowledgement

Four-years of Ph. D. study and research are approaching the end. It is time to express my sincere gratitude to the people who make my Ph. D. work successful and my life enjoyable.

Thanks must go first to my supervisor, Prof. Chet Jablonski, for offering me an opportunity to work in his lab as a master student, and then subsequently be recruited as a Ph. D. student. Throughout the past six years, I have benefited greatly from independent thinking and planning; at the same time, I was stimulated to propose my experiments, and generate the considerable funding required to undertake the experiment and reasonable schedule. These past years had a profoundly positive impact on my personal and professional development.

Great thanks must go to Dr. David Thompson and Dr. Yuming Zhao, my co-supervisors, for their creative ideas, continuous encouragement and patient guidance in my hunt for new insights and understanding behind the phenomena of my studies. I also thank Dr. David Thompson for diligent proofreading this entire thesis, and making numerous comments and suggestions.

Special thanks also go to Dr. Raymond Poirier for being an integral part of my supervisory committee. With your contribution, effort and constructive suggestions, this thesis presents my Ph. D. work in a much nicer way.

I am grateful for the financial support from Graduate Studies, Chemistry Department and many people associated to Chemistry Department, Memorial University, for their help and support.

Thanks to Thompson's and Zhao's group members. Much collaboration and discussion goes on between two groups, and I have benefited a lot from everyone's help and camaraderie. Ningzhang, Guang and Ilias provided many samples with great quality. Brent taught me many new words and offered a sharp wit. Thanks to Rachel (Xuemei), sharing the happiness and hardness together with me during the most difficult time that I have experienced. Thanks for your support, for your helpful suggestions and for sharing this experience with me. All of you are talented, and will no doubt go extremely far. Keep up the good work.

Finally, to my family, THANKS, these six letters can never fully express my love and appreciation for all of you. Thank you for standing by me, for sharing the joy and the sweat, for picking me up in the toughest times and reassuring my doubts. Thank you for every sacrifice you made for me, for your unconditional love and generous giving of all things that one could ever need.

Li Wang

December 2008

Contents

Chapter1: Supramolecular Assemblies for Artificial Photosynthetic Systems, Electron Transfer and Electronic Energy Transfer............................1

1.1 Introduction for Solar Energy Conversion 3

1.2 Architecture of PSI and PSII 8

1.3 Electron Transfer Theory...10

  1.3.1 Conceptual Background 10

  1.3.2 Electron Transfer Theory 12

    1.3.2.1 The Evolution of Electron Transfer Theory..............................12

    1.3.2.2 The Classical Marcus ET Theory 14

    1.3.2.3 Quantum Mechanical Corrections: Vibronic Theory 19

    1.3.2.4 Radiative Processes 23

  1.3.3 Mechanism of Electron Transfer in Solution...................................27

    1.3.3.1 Outer-sphere and Inner-Sphere Mechanism..............................27

    1.3.3.2 Bridged Mediated Electron Transfer......................................29

1.4 Energy Transfer 32

  1.4.1 Radiative Energy Transfer: Trivial Mechanism 32

  1.4.2 Nonradiative Energy Transfer: Förster Mechanism and Dexter Mechanism 32

1.5 Super-molecular Assemblies for Artificial Photosynthetic Systems 40

  1.5.1 Artificial Reaction Center 42

1.5.2 More Complex Systems: Coupled Electron Transfers 51

1.5.3 Artificial Antenna-Reaction Centre Complex 53

1.6 Defining the Problem and Organization of Thesis 57

1.7 References 58

Chapter 2: Experimental and Experimental Methodology...........................65

2.1 Conceptual Background 67

2.1.1 Formation of Excited State 67

2.1.2 Excited State Decay 68

2.1.3 Bimolecular Photophysical Processes 70

2.2 Materials and Solvents 71

2.3 Ground State Measurements and Gaussian Deconvolution 72

2.3.1 Introduction 72

2.3.2 Optical System of Spectroscopy and Data Acquisition 73

2.3.3 Gaussian Deconvolution 74

2.4 Excited State Measurements 75

2.4.1 Introduction 75

2.4.2 Optical System of Fluorometer and Data Acquisition 76

2.4.3 Data Analysis: Emission Spectral Fitting 77

2.5 The Time-Resolved Fluorescence 82

2.5.1 Introduction 82

2.5.2 Experimental Set-up and Data Acquisition 83

2.5.3 Time-Resolved Data Analysis 84

2.6 Transient Absorption Spectroscopy 89

2.6.1 Introduction 89

2.6.2 Theoretical background 90

2.6.3 Experimental Set-up and Data Acquisition 94

2.6.4 Kinetic Data Analysis 97

2.7 Global Kinetic Analysis 99

2.7.1 Introduction 99

2.7.2 Theory of nonlinear least-squares fitting of Multivariate Absorption Data 100

2.7.3 Error Estimates and Correlation Coefficients 105

2.8 References 107

Chapter 3: Radiative and Non-radiative Processes of OPV/OPE Chromophores..109

3.1 Introduction 111

3.1.1 Conducting Polymers 111

3.1.2 Bonding in π-Conjugated Polymers 112

3.1.3 Conformation and Structural Dynamics 118

3.1.4 Matrix Effect 120

3.2 Results 125

3.2.1 Overview 125

3.2.2 Ground State Conformation and FMO Calculations 126

3.2.3 Absorption and Band Assignments 127

3.2.3.1 Absorption Spectral Deconvolution 128

3.2.3.2 TD-DFT Band Assignments of Multi-electron States 130

3.2.4 Excited States: Chromophoric Bridges 131

3.2.4.1 Photochemistry 131

3.2.4.2 Radiative Decay: Electronic Structure 133

3.2.4.3 Emission Spectral Fitting 135

3.3 Discussions..139

3.3.1 OPE/OPV as Chromophores: Substituent Effect 139

3.3.2 Electronic Coupling Between Donor and Acceptor via the Bridge 146

3.3.3 Low Frequency Torsional Modes, Evidence for Quadratic Coupling 150

3.3.4 Non-Radiative Decay and Energy Gap Law 153

3.4 Conclusions 155

3.5 References 156

Chapter 4: Electron Transfer *vs.* Energy Transfer in Bisfullerene Terminated OPE/OPV Oligomers...160

4.1 Introduction 163

4.1.1 The Electron Transfer Mechanism in Donor-Bridge-Acceptor Systems...163

4.1.2 Exponential Distance Dependence of Bridge-Mediated Electron Transfer...165

4.1.3 Solvent Mediated Superexchange in Donor-Bridge-Acceptor Molecule...168

4.1.4 Effect of the Donor-Bridge Energy Gap on the ET Mechanism.............172

4.1.5 Effect of Torsional Motion on ET Rates 175

4.1.6 Effect of Donor- Acceptor Orientation on ET Rates 176

4.1.7 Covalently Linked System Containing Fullerene (C_{60}) 177

4.1.8 π-Conjugated Oligomers or Derivatives as Bridges 179

4.2 Results 182

4.2.1 Structure of OPV/OPE Oligomers and Bisfullerene Terminated Assemblies 182

4.2.2 Radiative Processes of DEB and DEB-C_{60} 183

4.2.3 Radiative Processes of SC-$(C_{60})_2$ and LC-$(C_{60})_2$............................187

4.2.4 Transient Absorption of SC-$(C_{60})_2$ and LC-$(C_{60})_2$...........................190

4.2.5 Radiative Processes of SL-$(C_{60})_2$ and LL-$(C_{60})_2$............................194

4.2.6 Transient Absorption of SL-$(C_{60})_2$ and LL-$(C_{60})_2$............................197

4.2.7 Global Kinetic Analysis...201

4.3 Discussions...213

4.3.1 The Effect of Varying Donor-Acceptor Distance 213

4.3.2 Back Electron Transfer or Charge Recombination..........................218

4.3.3 Orientation Effect 221

4.4 Conclusions...225

4.5 References..226

Chapter 5: Radiative, Non-radiative Processes of OPV/OPE Chromophore with Donor Substituents and Derivative Bisfullerene Terminated Oligomers

5.1 Introduction 233

5.1.1 Twist Intramolecular Charge Transfer (TICT) 234

5.1.2 Planarization of the Molecule (PICT) 236

5.1.3 Wagged Intramolecular Charge Transfer (WICT) 238

5.1.4 Rehybridization of the Acceptor (RICT) 240

5.1.5 Excited-State Structural Relaxation in Donor Acceptor Substituted Stilbenes 240

5.2 Results: Radiative Processes 246

5.2.1 Structure of OPE/OPV Oligomers with Donor Substituents 246

5.2.2 Absorption and Emission of OPE/OPV Oligomers with Donor Groups...247

5.2.3 Transient Absorption of OPE/OPV Oligomers with Donor Groups.........254

5.2.4 Absorption and Emission of Derivative Bisfullerene Terminated Oligomers 256

5.2.5 Transient Absorption of Derivative Bisfullerene Terminated Oligomers...260

5.3 Discussions..263

5.3.1. Substituent Effect 263

5.3.2. The Effect of Varying Donor-Acceptor Distance and the Interplay with the Energy-gap Dependence 269

5.3.3. The Distance and Energy-gap Dependence of Energy Transfer 273

5.3.4. Back Electron Transfer or Charge Recombination 274

5.4 Conclusions..277

5.5 References 278

Chapter 6: H-Shaped OPE/OPV Oligomers: A New Member of 2D Conjugated Fluorophore as Chemosensor..282

Part A Background..284

6.1 Introduction 284

6.1.1 Principles of Fluorescent Chemosensor 284

6.1.2 Different Design Principles for Fluorescent Sensor 291

6.1.3 Conjugated Polymer Based Fluorescent Sensor 294

Part B Results and Discussion..297

6.2 Spectroscopic, Electronic Structure of D-OPE-D and Adducts 297

6.2.1 Spectroscopic Properties of 1,4-bis(phenylethynyl)benzene (BPEB) 297

6.2.2 Spectroscopic Properties of 4,4`-dimethylamine-1,4-bis(phenylethynyl)-benzene 298

6.2.3 Spectroscopic Properties of D-OPE-D Adducts 301

6.3 Spectroscopic, Electronic Structure of H-mers and H-mer Adducts 308

6.3.1 Spectroscopic Properties of Donor and/or Acceptor Substituted H-mers...308

6.3.2 Spectroscopic Properties of SH-4D Adducts 313

6.3.3 Spectroscopic Properties of 2D-SH-2A Adducts 320

6.4 Substituent Affect on H-mers' Ground and Excited States Chemistry..............323

6.5 Conjugation Length Affect on H-mers' Ground and Excited States Chemistry 328

6.6 Conclusions...335

6.7 References 336

Chapter 7: Summary and Important Issues to be Addressed..........................340

Appendix I: Supplemental materials

Appendix II: Synthetic Schemes

List of Figures:

Figure 1-1. A conventional single p-n junction inorganic PV cell............................4

Figure 1-2. (A) Examples of organic semiconductors used in organic solar cells and (B) illustration of the photoinduced charge transfer with a sketch of the energy level..........7

Figure 1-3. Schematic representation of photosystem I and II................................9

Figure 1-4. (A) Two-state PES for thermal ET ($\Delta G^o < 0$). (B) Two-state PES for optical ET ($\Delta G^o > 0$). (C) three-state PES for photoinduced ET processes..........................11

Figure 1-5. Libby's model for electron transfer theory.......................................13

Figure 1-6. Visulization of the inner and the outer (solvent reorientation) changes accompanying ET reaction and plot of potential energy surfaces of the reactants and products as a function of nuclear configuration for ET.......................................14

Figure 1-7. Plot of free energy *vs.* the reaction coordinate of reactants and products for four different value of ΔG^o, and plot of $\Delta G^{\neq}$ *vs.* ΔG^o..18

Figure 1-8. (A) Intramolecular electron transfer rate constants as a function of ΔG° in frozen solution. (B) The difference between the plot of k_{ET} *vs.* $-\Delta G^o$ for the classical (solid) and that for semi-classical (dotted) Marcus equation.................................19

Figure 1-9. Schematic energy-coordinate (E-Q) diagram illustrating electron transfer in the inverted region (A) by a vibrational channel below the intersection region and vibrational wave function overlap between the initial and final vibrational levels and (B) by classical barrier crossing..21

Figure 1-10. Definition of spectral fitting parameters.......................................27

Figure 1-11. Superexchange and hopping hechanisms for photoinduced charge separation between an excited acceptor and ground-state donor……………………………………30

Figure 1-12. Schematic description of Förster energy transfer by dipole-dipole interaction (top) and geometrical configuration of dipole-dipole interaction between donor and acceptor molecules (bottom)……………………………………………………………36

Figure 1-13. Schematic description of exchange energy transfer by electronic overlap….38

Figure 1-14. Illustration of the essential elements for artificial photosynthesis assembly...41

Figure 1-15. Schematic diagram of energy-level for a dyad……………………………43

Figure 1-16. Schematic representation of charge separation in a triad and energy level…45

Figure 1-17. Structure of photosynthetic model of triads………………………………46

Figure 1-18. Porphyrin-fullerene linked systems…………………………………………49

Figure 1-19. Tetrads, pentads, hexads containing porphyrin-fullerene…………………50

Figure 1-20. In photosynthetic oxygen generation, photons move PS II through five successive oxidation states……………………………………………………………………52

Figure 1-21. Structure of multinuclear ruthenium and manganese complexes…………53

Figure 1-22. Coupled light harvesting and charge separation assemblies………………54

Figure 1-23. Polystyrene derivatized antenna-chromophore-electron transfer assembly…56

Figure 2-1: Jablonski diagram……………………………………………………………...68

Figure 2-2: Optical system of spectrophotometer…………………………………………73

Figure 2-3: Optical system for fluorometer………………………………………………..77

Figure 2-4. Block diagram of an N_2/dye laser-based stroboscopic system……………..83

Figure 2-5. Experimental laser profile decay (dotted functions) and the best numerical fit in a typical time-domain experiment……………………………………………………85

Figure 2-6. Left: The relative timing of the laser, flash lamp pulses and the transient absorption signal. Right: the output from the flash lamp (rear window) as detected at the photomultiplier (PMT). Inset is an expansion of the signal showing the decrease in light detected at the PMT due to short-lived species produced by the laser pulse................92

Figure 2-7. Diagram of the energy levels of a chromophore (left) and corresponding transient absorption (right)...94

Figure 2-8. Schematical representation of nanosecond transient absorption system......96

Figure 3-1: (A) Band gap excitation illustrating the formation of exciton, (B) Schematic presentation of a single-layer EL device 112

Figure 3-2. (A) Band diagrams for positive and negative solitons with associated electronic transitions. (B) Schematic picture of a negative bipolaron in PPP and band diagram for a negative bipolaron (left); Schematic picture of a polaron in PPP and band diagram of an electron polaron (right)...115

Figure 3-3. The main electronic configurations contributing to the ground state S_0 and the lowest singlet excited states S_1 and S_2..116

Figure 3-4. INDO/SCI simulated linear absorption spectrum of the OPV oligomer.....119

Figure 3-5. Molecular orbital energy diagram for photoinduced (left) electron (e^-) transfer and; (right) hole (h^+) transfer between semiconducting polymers and C_{60}................122

Figure 3-6. Energy levels of molecular orbitals for the isolated chain (left), and a cofacial dimer in the case of strong interaction (right)..124

Figure 3-7. FMO plots and energies for linear and cruciform OPE/OPV oligomers **SL** (left) and **SC** (right) calculated at the HF/6-311G (d) level. Note that the pendent alkyloxy groups were replaced by OH groups to save the computational time........................127

Figure 3-8. Absorption spectra of **SL**, **SC** and **SH** in $CHCl_3$ at 298 (±2) K..............128

Figure 3-9. Gaussian deconvolution of OPE/OPV oligomers **SL** and **SC**................130

Figure 3-10. Photoinduced isomerization of **SC** in N_2 saturated $CHCl_3$ solution at 298 (± 3 K) using broadband white light excitation..133

Figure 3-11. Emission spectra of **SL**, **SC** and **SH** in $CHCl_3$ at 298 (±2) K. The emission spectra have been arbitrarily scaled to illustrate the most important differences..........134

Figure 3-12. The result from the emission spectral fitting analysis for **SL** by eq 3-8. The observed emission spectrum for **SL** in $CHCl_3$ solution at 298±3K is shown in black....137

Figure 3-13. Absorption (black) and emission (red) spectra for DEB in N_2 saturated $CHCl_3$ solution at 298 (± 3) K...139

Figure 3-14. Structure of 1,4-bis(phenylethynyl)benzene (BPEB) and oligo(*p*-phenylene-ethynylenes) (OPEs).. 140

Figure 3-15. Energy diagram and structure of DSB and OPVs............................141

Figure 3-16. MO diagram for substituted DSB by application of perturbation...........144

Figure 3-17. Dependence of optical energy (E_{abs} and E_{em}) for DSB on Hammet $\sigma(p)$. Data from ref [28]..145

Figure 3-18. Absorption spectra of **SC** (o) and **LC** (●) obtained in $CHCl_3$ at 298±2 K...147

Figure 3-19. The shape of spectral envelope of **SC** (top), and **SL** (bottom) along with several underlying $\Phi_0 \rightarrow \Phi_v$ optical excitations..149

Figure 3-20. Representation of the quadratic coupling in three-dimension...............150

Figure 3-21. Vibrational transitions in absorption and emission within the harmonic

Condon approximation. (A) coupling in a double-bond stretching mode, (B) coupling in a ring-torsional mode, (C) coupling in both modes, adapted from ref 59..................151

Figure 3-22. The exciton model for OPEs (top) and RO substituted OPEs (bottom). The short arrows are the transition dipole moments of the monomeric units and the long arrows are the transition dipole moment of the oligomers, adapted from ref 55..........152

Figure 3-23. Plot of the electron-electron repulsion *vs.* torsional angles in stilbene.....154

Figure 4-1. Parabolic curves for ET of donor-C_{60} and donor-quinone systems........... 178

Figure 4-2. The transient absorption difference spectrum of DEB (•) obtained immediately following pulsed laser excitation at 355 nm (5 ns fwhm) in N_2 saturated $CHCl_3$ solution at 298 (± 3) K..183

Figure 4-3. Schematic energy level diagram illustrating the energetics of the singlet and triplet states...185

Figure 4-4. Absorption (●) and emission (o) spectra of C_{60}-DEB acquired in N_2 saturated $CHCl_3$ at 298 (± 3) K in comparison with the absorption (blue dot line) and emission (green dot line) acquired under the same condition...185

Figure 4-5. Visible spectrum (blue dot line) and emission (red dot line) spectra of DEB-C_{60} respectively in N_2 saturated $CHCl_3$ solution at 298 (± 3) K......................187

Figure 4-6. (Left) The absorption and emission spectra of SC-$(C_{60})_2$ (Abs ●, Em○) in comparison with that of SC (dot line). (Right) LC-$(C_{60})_2$ (Abs ★, Em ☆) in comparison with that of LC (dot line) measured in $CHCl_3$ at 298±3K...................................188

Figure 4-7. Nanosecond transient absorption spectrum of SC-$(C_{60})_2$ (green •) obtained immediately following 355 nm pulsed excitation in N_2 saturated $CHCl_3$ solution at 298

(± 3) K. The absorption (blue dot line) and emission (red dot line) are for comparison...191

Figure 4-8. Nanosecond transient absorption spectrum of LC-$(C_{60})_2$ (green ●) obtained immediately following 355 nm pulsed excitation in N_2 saturated $CHCl_3$ solution at 298 (± 3) K. The absorption (blue dot line) and emission (red dot line) are for comparison...193

Figure 4-9. The absorption and emission spectra of SL-$(C_{60})_2$ (Abs ●, Em○) in comparison with that of SL (dot line), and LL-$(C_{60})_2$ (Abs ●, Em○) in comparison with that of LL (dot line) measured in $CHCl_3$ at 298±3K...194

Figure 4-10. The transient absorption difference spectrum of SL (green ●) obtained in N_2 saturated $CHCl_3$ solution at 298 (± 3) K immediately following 355 nm pulsed excitation. The absorption (blue dot line) and emission (red dot line) are for comparison...........197

Figure 4-11. The transient absorption difference spectrum of SL-$(C_{60})_2$ (green ●) obtained in N_2 saturated $CHCl_3$ solution at 298 (± 3) K immediately following 355 nm pulsed excitation. The absorption (blue dot line) and emission (red dot line) are for comparison...198

Figure 4-12. The transient absorption difference spectrum of LL (green ●) obtained in N_2 saturated $CHCl_3$ solution at 298 (± 3) K immediately following 355 nm pulsed excitation. The absorption (blue dot line) and emission (red dot line) are for comparison.........200

Figure 4-13. The transient absorption difference spectrum of LL-$(C_{60})_2$ (green ●) obtained in N_2 saturated $CHCl_3$ solution at 298 (± 3) K immediately following 355 nm pulsed excitation. The absorption (blue dot line) and emission (red dot line) are for comparison...200

Figure 4-14. The transient absorption difference spectral changes of SC-$(C_{60})_2$ with time in N_2 saturated $CHCl_3$ solution at 298(± 3) after 355 nm laser excitation..................203

Figure 4-15. Singular value decomposition of the spectral-kinetic data matrix **Y** in Figure

4-14 for the first eight temporal eigenvectors from U x S.....................................204

Figure 4-16. Schematic energy level diagram showing excitation, EnT, ISC, CS, and CR in SC-$(C_{60})_2$ system..205

Figure 4-17. Representative decay traces shows the goodness of global fitting for the defined kinetics model as in Figure 4-11 for SC-$(C_{60})_2$.....................................207

Figure 4-18. Predicted transient absorption spectra for four colored species and the concentration profiles obtained from global fit for SC-$(C_{60})_2$..............................208

Figure 4-19. The transient absorption difference spectral changes of LC-$(C_{60})_2$ with time in N_2 saturated $CHCl_3$ solution at 298±3K after 355 nm laser excitation..................208

Figure 4-20. Singular value decomposition of the spectral-kinetic data matrix Y in Figure 4-19. (top) The first five spectral eigenvectors V and (bottom) the first five temporal eigenvectors from U x S..209

Figure 4-21. Schematic energy level diagram showing excitation, energy transfer, intersystem crossing in LC-$(C_{60})_2$ system...210

Figure 4-22. Predicted transient absorption spectra for three colored species and the concentration profiles obtained from global fit for LC-$(C_{60})_2$..............................211

Figure 4-23. Schematic energy level diagram showing excitation, EnT, ISC, CS, and CR in SL-$(C_{60})_2$ system..212

Figure 4-24. Intersystem crossing by coupling a change in spin angular momentum with a change in orbital angular momentum on converting a $^1(n\pi)^*$ state to a $^3(\pi\pi)^*$ state...222

Figure 4-25. Orientation effect on intersystem crossing to convert a $^1(n\pi)^*$ state to a $^3(\pi\pi)^*$ state for SC *vs.* SL...223

Figure 5-1. Structure of substituted DMABN and adiabatic reaction pathway for TICT...235

Figure 5-2. Structure and potential energy surfaces for the ground state S_0 and the excited states S_1, S_2, LE, and ICT for planarized FPP4C and flexible PP4C........................238

Figure 5-3. Schematic representation of WICT in comparison with TICT, PICT and RICT...239

Figure 5-4. Structure of *N,N*-dialkyl substituted *trans*-4-aminostilbenes....................241

Figure 5-5. Photodynamic scheme proposed for *N*-aryl substituted *trans*-4-amino-stilbenes. States ${}^1t^*$, ${}^3t^*$, ${}^1p^*$, ${}^3p^*$, PICT, and TICT refer to the singlet and triplet excited states of the *trans* isomer and those of the C-C twisted perpendicular states and the planar and twisted intramolecular charge transfer states, respectively 243

Figure 5-6. Simplified potential energy surface for the lowest electronic states of *trans*-aminostilbenes. The dash arrows show the *trans*→*cis* photoisomerization pathway along the S_1 state..244

Figure 5-7. The absorption and emission spectra of DSC (Abs ●, Em○) in comparison with that of SC (solid line), and DLC (Abs ▲, Em△) in comparison with that of LC (solid line) measured in N_2 saturated $CHCl_3$ at 298(± 3) K...248

Figure 5-8. Emission spectral fitting for DSC (left) and DLC (right) measured in $CHCl_3$ at 298(± 3) K...253

Figure 5-9. Transient absorption spectrum of DSC in comparison with Abs (green dot line) and Em (red dot line) in N_2 saturated $CHCl_3$ at 298±3 K.............................255

Figure 5-10. Transient absorption spectrum of DLC in comparison with Abs (green dot line) and Em (red dot line) in N_2 saturated $CHCl_3$ at 298±3 K.............................255

Figure 5-11. The absorption and emission spectra of DSC-$(C_{60})_2$ (Abs ●, Em ○) in comparison with that of DSC (solid line), and DLC-$(C_{60})_2$ (Abs ★, Em ☆) in comparison with that of DLC (solid line) measured in N_2 saturated $CHCl_3$ at 298 ± 3K................256

Figure 5-12. Emission spectral fitting for DSC-(C60)2 (left) and DLC-$(C_{60})_2$ (right) in $CHCl_3$ at 298 ± 3K...259

Figure 5-13. Transient absorption of DSC-$(C_{60})_2$ (●) in comparison with Abs (green dot line) and Em (red dot line) and TA of LC-$(C_{60})_2$ (☆) in N_2 saturated $CHCl_3$ at 298±3K.....261

Figure 5-14. Transient absorption of DLC-$(C_{60})_2$ (●) in comparison with Abs (green dot line) and Em (red dot line) and TA of SC-$(C_{60})_2$ (☆) in N_2 saturated $CHCl_3$ at 298±3 K...261

Figure 5-15. FMOs for cruciform calculated with HF/6-311G(d) and donor substituted one calculated with B3LYP 6-31G//6-31G(d. p) using Spartan............................264

Figure 5-16. Solvent dependence of absorption and emission for donor substituted cruciform at 298±3K..264

Figure 5-17. Optimized geometries for the ground and excited states of *trans*-4-(*N,N*-diphenylamino)stilbene...265

Figure 5-18. Emission band shape analysis by Gaussian deconvolution for DSC and DLC...266

Figure 5-19. MO diagram and optical transitions from the ground state..................268

Figure 5-20. Schematic energy level diagram showing excitation, EnT, ISC, CS, and CR in SC-$(C_{60})_2$ system...270

Figure 6-1. The essential structure of a fluorescent sensor.................................285

Figure 6-2. PET processes before interacting with analytes, A (off) and after interacting with analytes for fluorescence "turn-on" sensors, B (on)....................................285

Figure 6-3. PET process with the participation of an empty orbital from the analyte for the fluorescence "turn-off" sensor...286

Figure 6-4. EET process for Dexter energy transfer between the excited fluorophore and the analyte bound to receptor followed by analyte return to the ground state by non-radiative decay...287

Figure 6-5. Photoinduced intramolecular charge transfer (ICT) by interacting with donor group (A) or acceptor group (B)...289

Figure 6-6. On-off excimer formation process of calix[4]crown-5-bispyrenyl system...290

Figure 6-7. Fluorescent sensors based on the displacement approach.....................293

Figure 6-8. Chemodosimeter approach: in the first example, the anion reacts with the chemodosimeter and remains covalently attached, and in the second example, the cation catalyzes a chemical reaction.. 294

Figure 6-9. Calculated HOMO and LUMO orbitals (B3LYP/6-31+g (d, p)) of BPEP.....297

Figure 6-10. Absorption and Emission of 4,4`-dimethyamine-1,4-bis(phenylethynyl) benzene...298

Figure 6-11. The influence of the donor and acceptor substitution in D-π-A systems on the energy of the electronic excitation...299

Figure 6-12. (A) Absorption and (B) emission spectral change of D-OPE-D upon addition of TFA in $CHCl_3$...302

Figure 6-13. Spectral change of D-OPE-D upon addition of TFA plotted by wavelength (top), and the spectra for the extract colorful species (bottom)............................305

Figure 6-14. Absorption and emission change of D-OPE-D titration with $Cu(OTf)_2$....307

Figure 6-15. Spectral changes of D-OPE-D *vs*. the concentration of $Cu(OTf)_2$ at different wavelengths...307

Figure 6-16. Absorption and Emission of 2D-SH-2A (▲), SH-4D (■) and SH-4A (dash line) in comparison with SH (solid line)...310

Figure 6-17. Optimized structures and FMOs of SH, SH-4A, 2D-SH-2A, and SH-4D...311

Figure 6-18. Absorption and emission spectral change of SH-4D upon protonation (top) and complexion (bottom) with AgOTf in $CHCl_3$...314

Figure 6-19. Optimized structures and FMOs of SH-4D and SH-4D + $4H^+$..............315

Figure 6-20. (A) Absorption and (B) emission Spectral changes of SH-4D *vs*. the concentration of AgOTf at different wavelengths..316

Figure 6-21. Spectral change of SH-4D by complexation with $Cu(OTf)_2$ (top), Spectra of the extracted colorful reacting species from global analysis (bottom)......................319

Figure 6-22. Absorption and emission change of 2D-SH-2A upon protonation (top) and complexion with AgOTf (bottom) in $CHCl_3$..321

Figure 6-23. Optimized structures and FMOs of 2D-SH-2A and 2D-SH-2A + $2H^+$.....322

Figure 6-24. (A) Absorption and (B) emission spectral changes of 2D-SH-2A *vs*. the concentration of AgOTf at different wavelengths..323

Figure 6-25. Illustration of the offsetting conjugation effect and ICT effect. (A) overall bathochromic effect, (B) overall hypsochromic behavior, (C) hypsochromic convergence after passing through a minimum of $E_{DA}(n)$...324

Figure 6-26. FMOs plot for H-mer and donor substituted H-mer calculated with

HF/6-311G (d) 327

Figure 6-27. Solvent dependence of absorption and emission for donor substituted H-mer at 298±3K..328

Figure 6-28. Absorption and emission spectra of substituted LH in comparison with substituted SH, measured in $CHCl_3$ at 298±3K...330

Figure 6-29. Solvent effect on optical properties of LH-2D (2, 3).........................333

Figure 6-30. Absorption and emission spectral changes with AgOTf titration in $CHCl_3$ at 298±3K..334

List of Tables:

Table 3-1. Correspondence between a variety of molecular and solid state terms……..113

Table 3-2. Absorption spectral data for OPV/OPE oligomers and model samples in CHCl3……………………………………………………………………………………128

Table 3-3. UV-Vis spectral assignments for co-oligomers **SL** and **SC** based on TD B3LYP/6-31G (d) calculations……………………………………………………………131

Table 3-4. Absorption and emission data for OPV/OPE oligomers in $CHCl_3$ at 298±3K.134

Table 3-5. The spectral fitting parameters for OPV/OPE oligomers…………………..138

Table 4-1. Comparative absorption and emission spectral data for SC-$(C_{60})_2$, SC and LC-$(C_{60})_2$, LC measured in $CHCl_3$ at 298 ± 3 K…………………………………………...190

Table 4-2. Comparative absorption and emission spectral data for SL-$(C_{60})_2$, SL and LL-$(C_{60})_2$, LL measured in $CHCl_3$ at 298±3 K…………………………………………196

Table 5-1. Absorption and emission data of DSC and DLC and comparative data for SC and LC in N_2 saturated $CHCl_3$ at 298±3 K……………………………………………...248

Table 5-2. Emission spectral fitting parameters for the spectra of DSC and DLC measured in $CHCl_3$ at 298±3K…………………………………………………………253

Table 5-3. The absorption and emission data of DSC-$(C_{60})_2$ and DLC-$(C_{60})_2$ in comparison with those of DSC and DLC measured in $CHCl_3$ at 298±3 K……………..258

Table 5-4. Emission spectral fitting parameters of DSC-$(C_{60})_2$ and DLC-$(C_{60})_2$ in $CHCl_3$ at 298±3K…………………………………………………………………………259

Table 5-5. Fluorescence quenching of $\phi(\pi\text{-}B)/\phi$, rate constants for energy Transfer (k_{EnT}), indirect charge separation (k_{CS}), charge recombination (k_{CR})[a], the energy and the redox potential of donor...271

Table 5-6. Rate constants for forward and back electron transfer, driving forces, reorganization energies and electronic coupling constants for SC/LC-(C_{60})$_2$ and DSC/DLC-(C_{60})$_2$ systems...275

Table 6-1. Binding constants (log K_1) of D-OPE-D titration with TFA, AgOTf and Cu(OTf)$_2$ in $CHCl_3$...305

Table 6-2. Photophysical data for 2D-SH-2A, SH-4D and SH-4A in comparison with unfunctionalized SH, measured in $CHCl_3$ at 298±3K...309

Table 6-3. Binding constants of SH-4D with proton and metal cations in the ground and excited states...318

Table 6-4. Binding constants (log K_1) of 2D-SH-2A with proton and metal cations in the ground and excited states...323

Table 6-4. Photophysical data for donor and/or acceptor substituted LH measured in $CHCl_3$ at 298±3K...329

Table 6-5. Emission spectral fitting data for donor and/or acceptor substituted LH...322

List of Schemes:

Scheme 3-1. Structure of hydrogen terminated OPV/OPE co-oligomers..................125

Scheme 3-2. Photoinduced isomerization of DSB with broadband white light excitation.132

Scheme 4-1. The structure of OPV/OPE oligomers and bisfullerene terminated OPV/OPE oligomers..182

Scheme 5-1. Structures of donor substituted OPE/OPV oligomers and bisfullerene terminated derivatives...247

Scheme 6-1. The structure of 2D-SH-2A, SH-4D and SH-4A..............................308

Scheme 6-2. Illustration of the electric field effect through intervening medium.........317

Scheme 6-3. VB model for D-OPV-A systems and MO model for D-OPE-A systems...325

Scheme 6-4. Structure of donor and/or acceptor substituted long H-mers..................329

List of Abbreviations

PV	Photovoltaic
IPCE	Incident photon to electricity conversion
PEC	Photoelectron-chemical
PPV	Poly(*p*-phenylenevinylene)
PAT	Poly(alkylthiophene)
OEC	Oxygen evolving center
ET	Electron transfer
EnT	Energy transfer
TCNE	Tetracyanoethylene
FC	Franck-Condon
MS-EPT	Multiple-site coupled electron proton transfer
MET	Multi-electron transfer
HOMO	Highest occupied molecular orbital
LUMO	Lowest unoccupied molecular □orbital
OPE	Oligo(*p*-phenylenethynylene)
OPV	Oligo(*p*-phenylenevinylene)
PMT	Photomultiplier tube
DGG	Digital delay gate generator
LED	Light-emitting diode
IRF	Instrument response function
ΔOD	Absorption change
SE	Stimulated emission
Nd:YAG	Neodymium-doped yttrium aluminum garnet
SVD	Singular Value Decomposition
SC	Short cruciform
LC	Light cruciform
SL	Short linear

LL	Long linear
SH	Short H-mer
LH	Long H-mer
EL	Electro-luminescent
ITO	Indium-tin-oxide
PPP	poly(*p*-phenylene)
CI	Configuration interaction
π-B	hydrogen terminated OPV/OPE co-oligomers
FMO	Frontier molecular orbital
TD-DFT	Time-dependent density functional theory
DEB	1,4-Bis- decyloxy-2-dec-1-ynyl-5-ethynyl-benzene
BPEB	1, 4-bis(phenylethynylene)benzene
DSB	1, 4-distyrylbenzene
SC- $(C_{60})_2$	$C_{60}\text{-}(\pi\text{-B})_{SC}\text{-}C_{60}$
LC- $(C_{60})_2$	$C_{60}\text{-}(\pi\text{-B})_{LC}\text{-}C_{60}$
SL- $(C_{60})_2$	$C_{60}\text{-}(\pi\text{-B})_{SL}\text{-}C_{60}$
LL- $(C_{60})_2$	$C_{60}\text{-}(\pi\text{-B})_{LL}\text{-}C_{60}$
CS	Charge separation
CR	Charge recombination
π-(D)B_C	Donor substituted (π-B)-bridged
DSC- $(C_{60})_2$	$C_{60}\text{-}(\pi\text{-B})_{DSC}\text{-}C_{60}$
DLC- $(C_{60})_2$	$C_{60}\text{-}(\pi\text{-B})_{DLC}\text{-}C_{60}$
TICT	Twisted intramolecular charge transfer
PICT	Planar intramolecular charge transfer
WICT	Wagged intramolecular charge transfer
RICT	Rehybridized intramolecular charge transfer
DMABN	4-(*N*,*N*-dimethylamino)-benzonitrile

DSC	Donor substituted short cruciform
DLC	Donor substituted long cruciform
D-OPE-D	4,4`-dimethylamine-1,4- bis(phenylethynyl)benzene
IP	Ionization energy
EA	Electron affinity
ICT	Intramolecular charge transfer
$\Delta\bar{\nu}_{1/2}$	The full width at half height of absorption/emission peak
ε	In UV-Vis spectroscopy, the molar extinction coefficient
τ	In transient absorption spectroscopy, the lifetime of transient species
λ_o	Solvent reorganization energy
λ_t	Total reorganization energy
λ_i	Vibrational reorganization energy
λ_{max}	In UV-Vis spectroscopy, the wavelength at which maximum absorption or emission occurs.
ϵ_o	The optical dielectric constants of the solvent
ϵ_s	The static dielectric constants of the solvent
ϕ_{f}	The quantum yield of fluorescence
f_{osc}	Oscillator strength
S_m	The electron-vibrational coupling constant or Huang-Rhys factor
$\hbar\omega$	Quantum spacing
TFA	Trifluoroacetic acid
AgOTf	Silver (I) trifluoroacetate
$Cu(OTf)_2$	Copper (II) trifluoroacetate
$Mg(OTf)_2$	Magnenium (II) trifluoroacetate
$Zn(OTf)_2$	Zinc (II) trifluoroacetate
$Ba(OTf)_2$	Barium (II) trifluoroacetate

Chapter 1

Supramolecular Assemblies for Artificial Photosynthetic Systems, Electron Transfer and Electronic Energy Transfer

Overview

The goal of this chapter is to build the conceptual network required to understand the excited state behavior. The theories and mechanisms for electron transfer and energy transfer will be introduced. The selected chromophore-quencher complexes will be introduced and the design principle behind these examples will be discussed in light of the theory of electron/energy transfer.

1.1 Introduction for Solar Energy Conversion..........3

1.2 Architecture of PSI and PSII..........8

1.3 Electron Transfer..........10

1.3.1 Conceptual Background..........10

1.3.2 Electron Transfer Theory..........12

1.3.2.1 The Evolution of Electron Transfer Theory..........12

1.3.2.2 The Classical Marcus ET Theory..........14

1.3.2.3 Quantum Mechanical Corrections: Vibronic Theory..........19

1.3.2.4 Radiative Processes..........23

1.3.3 Mechanism of Electron Transfer in Solution..........27

1.3.3.1 Outer-sphere and Inner-Sphere Mechanism..........27

1.3.3.2 Bridged Mediated Electron Transfer..........29

1.4 Energy Transfer..........32

1.4.1 Radiative Energy Transfer: Trivial Mechanism..........32

1.4.2 Nonradiative Energy Transfer: Förster Mechanism and Dexter Mechanism..........32

1.5 Super-molecular Assemblies for Artificial Photosynthetic Systems..........40

1.5.1 Artificial Reaction Center..........42

1.5.2 More Complex Systems: Coupled Electron Transfers..........51

1.5.3 Artificial Antenna-Reaction Centre Complex..........53

1.6 Defining the Problem and the Organization of Thesis..........57

1.7 References..........58

1. 1 Introduction for Solar Energy Conversion

Sunlight provides by far the largest of all carbon-neutral energy sources. The amount of solar energy that reaches the earth in the course of one hour is 4.3×10^{20} J, equivalent to about the entire world's annual energy consumption. Ironically, given the magnitude of this energy resource, the energy derived from the combustion of fossil fuels remains the largest source of energy in industrialized nations, ~85% from oil, gas and coal.[1] The development of solar energy devices that convert sunlight to other forms of energy is slowly evolving. For example, solar energy conversion systems do exist and are classified by their primary products: solar thermal systems, solar electricity, and solar fuels.

Solar Thermal Systems. Solar thermal systems use solar radiation as a source of heat; it can be categorized into low-temperature solar thermal systems and high-temperature solar thermal systems. This heat can be used for climate control in building-heating and cooling, concentrated for solar thermal power plants,[2] and used to induce reactions to make chemical fuels in the concentrated mode. With focused solar radiation, photovoltaic (PV) devices can function at a much higher efficiency.

Solar Electricity. The photovoltaic (PV) effect was discovered by Edmund Becquerel in 1839, when he observed that photocurrents were produced by illumination of a silver chloride electrode immersed in an electrolytic solution and connected to a counter metal electrode.[3] However, approximately 110 years later, solar cells based on a single silicon crystal were developed at Bell Lab. These solid-state devices relied on the excitation of the p-n junction in single silicon crystal. The efficiency of these cells is

5-6% for incident photon to electricity conversion (IPCE).[4] In spite of the high cost of manufacture of solid-state solar cells, this silicon-based PV device still dominates the commercial market.

A schematic diagram illustrating the mechanism of a solid-state PV cell is shown in Figure 1-1. PV cells generally consist of a light absorber that can be either inorganic semi-conductors, organic molecular structures, or a combination of both. By definition, a bulk semiconductor possesses band structure with the valence band lying lower in energy than the next higher energy band, which is known as the conduction band. A band gap exists between the top edge of the valence band and the lower edge of the conduction band that are unoccupied in the ground state. A photon of light will be absorbed if the energy of photon is greater than the band gap. Upon absorption of light, electrons and holes are generated following by band gap excitation to form bound excitons, denoted as [e$^-$, h$^+$]. The bound [e$^-$, h$^+$] dissociates with electrons migrating to the cathode and holes

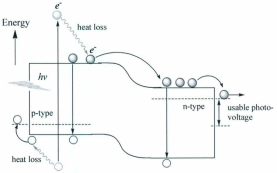

Figure 1-1. A conventional single p-n junction inorganic PV cell.

flowing to the anode, where they are collected and passed through wires connected to the cell to perform electric work. The efficiency of [e^-, h^+] formation, and subsequent dissociation to form mobile charges determines the magnitude of the photocurrent, and the energy difference between the conduction band and Fermi level determines the photo-voltage. PV cells can be broadly classified into three categories: (1) inorganic cells, based on solid-state inorganic semiconductors, *i.e.* GaAs or TiO_2; (2) organic cells, based on conducting polymers, *i.e.* p-type polyphenylvinylidene or polythiophene, n-type fullerene; and (3) photoelectron-chemical (PEC) cells, based on interfaces between semiconductors and molecules. However, the use of silicon in PV devices has to date been limited by the high cost of production and very low photocurrents. In contrast, organic solar cells in which the active layer is made of organic semiconducting polymer will provide a cheaper alternative to conventional inorganic solar cells, because the production costs are expected to decrease in comparison to the current costs in the fabrication of inorganic based PV cells. Furthermore, organic semiconductor thin films can be synthetically manipulated to yield high absorption coefficients exceeding 10^5 $M^{-1}\cdot cm^{-1}$ to collect light for optoelectronic applications.[5] Charge carrier mobilities as high as 10 $cm^2/V\cdot s$ have been achieved and are comparable to amorphous silicon-based devices.[6]

Organic Photovoltaics. Commercial organic photovoltaic devices are in a relatively early stage of development. Since the early "proof of concept experiments" on organic photovoltaic devices comprised of molecular-based systems,[7] the IPCE has increased to a range of 3-5%.[8-11] It should be noted that the efficiency of photosynthesis is

~ 0.5-1%, significantly less than the PV devices described above. The basic principle of operation in an organic PV cell is similar to that of conventional p-n junction cells. Illumination of a mixture of electron-rich (donor) and electron-poor (acceptor) at the p-n junction results in the formation of bound electron-hole pairs [e^-, h^+]. The exciton diffuses to a region where exciton dissociation occurs, [e^-, h^+] $\rightarrow$ e^- + h^+, and charge transport within the organic cell to the respective electrodes. There are a number of parameters that dictate the efficiency of organic based PV devices; such as the formation and dissociation of bound excitons; and enhanced charge mobility as well as the efficiency of charge carriers in reaching the electrodes. These parameters are exactly analogous to those described above for inorganic based PV cells.

Over the past twenty years, most research has focused on developing dye-sensitized,[12] bulk heterojunction,[13] and multiple junction or tandem solar cells that consist of multiple, single junction solar cells joined together or stacked upon each other, with each solar cell absorbing the part of the solar spectrum closest to its band gap.[14,15] most efficient polymer-based bulk heterojunction systems contain poly(*p*-phenylene-vinylene)s (PPVs) or poly(alkylthiophene)s (PATs) blended with soluble C_{60} derivatives (Figure 1-2).[16,17] The efficiencies of such systems (less than 5%, generally 2% or less) are too low to be useful. There are significant challenges to be overcome in order to substantially improve the performance of the polymer based heterojunction assemblies. The development of new molecular assemblies will require a large body of fundamental research directed towards chromophore design where the light absorbing entities possess large absorption cross-section that absorbs throughout the visible spectral region. The ability to synthetically control the HOMO-LUMO band gap, and an understanding of how molecular structure impacts charge transfer mobility in π-conjugated systems.[18-20]

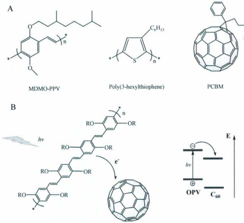

Figure 1-2. (A) Examples of organic semiconductors used in organic solar cells and (B) illustration of the photoinduced charge transfer with a sketch of the energy level.

Solar Fuels. A major limitation of solar photovoltaic cells is the performance of devices dependent on geography and climate. When the solar resource is locally available to the conversion device, or is variable because of day/night alternation, the widespread use of electricity and any other solar energy as a primary power source will require a tightly integrated effective storage and/or global distribution technologies to provide the power to the end-user in accord with demand. Therefore, the direct production of fuels from sunlight is advantageous because it inherently converts solar energy into an economical, convenient form. Currently, there are two solar fuel technologies in use, which are biomass-derived fuels and hydrogen produced by electrolysis. In the second case, electricity is produced principally from fossil fuel sources, which ultimately are derived from biomass as well.

Biomass Derived Fuels. Light-driven photosynthetic processes have enormous capacity for sustainable replacement of fossil fuels by fixing more than 100 Giga-tons of carbon annually, which is roughly equivalent to 100 TW of energy. Biomass derived fuels have been used as an energy source over the entire span of recorded human existence. Biomass based fuels continue to be a functional energy resource being utilized on a significant scale both in developing and developed countries. However, the overall energy efficiency of biomass conversion systems is very low, less than 1% of the incident light energy stored as chemical fuels. Therefore, it is important to increase the efficiencies of many biological pathways leading from photosynthetic light capture.

The understanding of how natural photosynthesis at the molecular level has rapidly evolved due to the publication of highly resolved X-ray crystal structures, which has revealed unprecedented insight into the structure of photosynthetic apparatus. These structures represent a blueprint toward the construction of devices capable of photosynthesis. It is clear that these devices must incorporate molecular-level and/or supramolecular organization of chromophores to collect light energy, separate charge, and use charge transport structures to deliver the oxidizing and reducing equivalents to catalytic sites where water oxidation and carbon dioxide reduction may occur. The key principles will be further elaborated on in Section 1.5.

1.2 Architecture of PSI and PSII

The photosynthetic apparatus in plants and photosynthetic bacteria has evolved over billions of years. As such, there have been numerous mutations, which have been advantageous to the survival of organisms. By understanding this natural process and employing it as a paradigm for artificial constructs, it will be possible to construct artificial photosynthetic systems for sustainable global energy production and efficient energy transformation.

A schematic diagram for PSI and PSII is shown in Figure 1-3. The photosynthetic apparatus has many facets and components involving light harvesting, energy migration to redox sites where catalytic processes occur. Ultimately, the energy derived from the excitation of P-680 yields an excited electron which cascades and delivers energy to plastoquinone, cytochrome b_6f, plastocyanin to the final acceptor ferredoxin in PSI. The ferredoxin is used to reduce NADP$^+$ in a reaction catalyzed by ferredoxin-NADP$^+$ oxidoreductase, providing redox equivalents for the conversion of CO_2 to carbohydrates

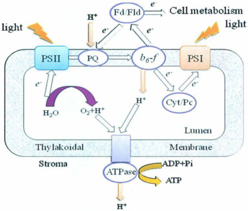
Fd/Fld
e⁻
Cell metabolism
H⁺
light
light
e⁻
e⁻
PSII
PQ
b₆-f
PSI
e⁻
e⁻
e⁻
H⁺
Cyt/Pc
H₂O
O₂+H⁺
Lumen
Thylakoidal
Membrane
Stroma
ATPase
ADP+Pi
ATP
H⁺

Figure 1-3. Schematic representation of photosystem I and II adapted from ref 21.

in the Calvin cycle. Oxygen is evolved from water oxidation in the OEC, and is an essential reagent that drives respiration for all living systems. The whole series of reactions is coupled to trans-membrane proton transfer and the resulting difference in chemical potential across the membrane drives ATP synthesis.

In 1989, Meyer articulated and proposed a module approach for artificial photosynthesis in an Accounts of Chemical Research paper.[22] The design and preparation of an integrated molecule-based assembly that would convert sunlight into useful fuels must involve the light harvesting system, photo-initiated charge separation, redox catalysis and other photo-driven biosynthetic processes. The absorption of light by a chromophore results in the formation of a single electron-hole pair. However, fuel-forming reactions involve the formation of covalent bonds that tend to be a multi-electron process. The photosynthetic apparatus is capable of utilizing single photon/electron transfer to drive multi-electron transfer chemistry in the formation of sugar or other forms of energy.

At this juncture, it is important to understand the basic tenets of electron transfer prior to discussion of molecular assemblies for light conversion to energy.

1.3 Electron Transfer

1.3.1 Conceptual Background

Electron transfer (ET) processes, the movement of an electron from an electron donor (D) to an electron acceptor (A), constitute fundamental processes in chemical reactions, and most importantly in biological systems that are crucial to life, for example photosynthesis. It is convenient in the following discussion to define two limiting systems, two-state and three-state systems respectively. Two-state systems contain a reactant and product potential energy surface as illustrated in Figure 1-4 A and B, possessing different energetic requirement to initiate reactions. In Figure 1-4 A, total free energy change for ET from D to A is thermodynamically favored ($\Delta G^{o} < 0$). The rate constant for this reaction is dictated by molecular parameters such as force constants associated with chemical bonds in D and A, and the nature of solvent which responds to the passage of charge ongoing from the reactants to products during the redox reaction. There exists a complex interplay of intrinsic dynamic processes inherent to the reactants and products, *as well as the thermodynamic* driving force, all of which contribute to activation barrier.

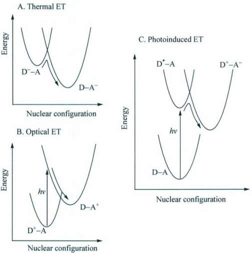
A. Thermal ET
Energy
D^{-}–A
D–A^{-}
Nuclear configuration
B. Optical ET
Energy
$h\nu$
D–A^{+}
D^{+}–A
Nuclear configuration
C. Photoinduced ET
Energy
D^{*}–A
D^{+}–A^{-}
$h\nu$
D–A
Nuclear configuration

Figure 1-4. (A) Two-state PES for thermal ET ($\Delta G^{o} < 0$). (B) Two-state PES for optical ET ($\Delta G^{o} > 0$). (C) Three-state PES for photoinduced ET process.

In Figure 1-4 B, the free energy change ($\Delta G^o > 0$) between D^+-A and $D-A^+$ potential energy surfaces require the input of energy to initiate the reaction to create $D-A^+$. Once formed, the system relaxes from $D-A^+$ to D^+-A and releases energy to the surroundings. It should be noted that there is an activation barrier between D^+-A and $D-A^+$, which is dictated by the same properties as outlined above in case A. For example, dissolving tetracyanoethylene (TCNE) in benzene produces an intense yellow color due to the formation of charge transfer adduct between TCNE and benzene ([TCNE//benzene]). The yellow color arises from the absorption of light by [TCNE//benzene] to form [$TCNE^{-\cdot}$//$benzene^{+\cdot}$]. Thermal relaxation occurs via back ET from [$TCNE^{-\cdot}$//$benzene^{+\cdot}$] to [TCNE//benzene].

The photoinduced ET mechanism shown in Figure 1-4 C constitutes almost all of the investigations outlined in this thesis. The key difference between the optical and the photoinduced ET mechanism is the formation of an excited state species D^*–A, which is produced by absorption of a photon. D^*–A exists transiently because the system will try to dissipate energy to reach the lowest energy configuration. Subsequently D^*–A will undergo ET to form D^+–A^- which is thermodynamically favored. Relaxation of D^+–A^- leading to reformation of the ground state is dictated by the same parameters outlined for thermal ET described above for case A and optical ET for case B.

1.3.2 Electron Transfer Theory

1.3.2.1 The Evolution of Electron Transfer Theory

It was in 1952 that Libby proposed that the rate constant for electron exchange reactions was strongly influenced by the Franck-Condon principle: the more similar the inner coordination shells of the donor and acceptor atom, the less difficult would be the electron transfer.[23] Libby had perceptively introduced the Franck-Condon principle to chemical reactions, but neglected the role of solvent reorganization outside the inner coordination shell. Libby's treatment implicitly assumed that the electronic interaction between reactants undergoing ET was relatively weak. In this case, ET was proposed to occur in a stepwise process with ET occurring first, followed by the solvent response to the change of electron density upon the formation of products as shown in Figure 1-5.

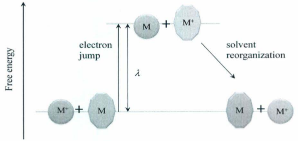

Figure 1-5. Libby's model for electron transfer theory adapted from ref 22.

Unfortunately, this mechanism was flawed as it violated the principle of energy conservation. Marcus recognized the re-orientation of solvent molecules outside the inner coordination shell to satisfy both Franck-Condon and energy conservation conditions for electron transfer occurring in the dark. The mechanism for ET was reformulated using Transition State Theory and from which some of the first theoretical constructs where both the reorganization energies of bonds and solvent was accounted for and the dependence of k on ΔG^o was elucidated.

1.3.2.2 The Classical Marcus ET Theory

Marcus was among the first to appreciate that the activation barrier to electron transfer resulted from the differences in the nuclear configurations of the reactants and products. From 1956 to 1960, Marcus wrote a series of landmark papers where he discussed ET reactions in terms of potential energy surfaces, and derived the analytical expressions from the Transition State Theory that enabled him to calculate the reaction rate constants and treated solvent as a structureless continuum characterized by its bulk dielectric properties (Figure 1-6).[24-26] Based on his earlier work, Marcus proposed that the

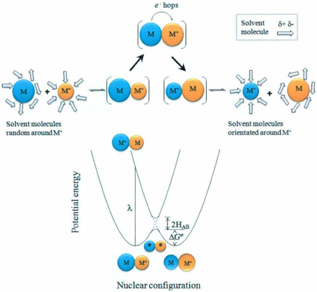
e⁻ hops
M
M⁺
Solvent molecule
δ+ δ-
Solvent molecules random around M⁺
Solvent molecules orientated around M⁺
Potential energy
λ
2H_AB
ΔG≠
*
Nuclear configuration

Figure 1-6. Visualization of the inner and the outer (solvent reorientation) changes accompanying ET reaction and the plot of potential energy of the reactants and products as a function of nuclear configuration for ET.

energy barrier for electron transfer, $\Delta G^{\neq}$, was governed by medium reorganization energy (λ) and the overall free energy change between the reactants and products (ΔG^{o}). The expression of rate constant, k_{ET}, for a bimolecular ET in the classic limit is given by

$$k_{ET} = k_0 \exp\left(\frac{-\Delta G^{\neq}}{k_B T}\right) \qquad (1\text{-}1)$$

where $\Delta G^{\neq}$ is given by

$$\Delta G^{\neq} = \frac{\lambda}{4}\left(1 + \frac{\Delta G^{o}}{\lambda}\right)^2 \qquad (1\text{-}2)$$

The pre-exponential factor k_0 in eq 1-1 is a composite parameter dependent on the nature of the electron transfer reaction. The free energy difference ΔG° for an ET reaction is a function of the overall free energy change for the reaction, and the $\Delta G^{\neq}$ term is the free energy activation for the charge transfer reaction. With respect to the nuclear Franck-Condon factors, it was realized at the early stage that if low frequency modes, *i.e.* M-L stretches (where $\bar{\upsilon} = 400$ cm^{-1}), were the dominant vibrational modes coupled to the ET, the calculated rate constants would underestimate the true rate constant. Medium frequency modes possess high angular frequencies and as such provided a high density of states from which energy dissipation would be increased by coupling to solvent modes. This nuclear coupling can be approximately described in term of the displacement of the intramolecular equilibrium nuclear configuration accompanying ET. In some cases, the barrier to ET is too high ($k_B T \ll \Delta G^{\neq}$) and thermal population is negligible. Therefore, the reaction rate constant will be very small.

Measurement of the self-exchange rate constant indicated that the reaction rate is orders of magnitude higher than which was predicted if ET occurred via a thermal activation. Under these conditions, it was clear that another mechanism for ET had to be considered. Sutin recognized the importance of nuclear tunneling in intramolecular modes.[27] Later, Marcus extended his theoretical treatment to include the effect of intramolecular configuration changes and generalized the concept of potential energy surfaces (PES) to include the entire system consisting of a pair of reactants and products as well as the surrounding solvent. The vibrational reorganization energy (λ_i) was recognized to be a major component of $\Delta G^{\neq}$ as well as the solvent reorganization (λ_o). Therefore, the total reorganization energy is given by

$$\lambda_t = \lambda_o + \lambda_i \qquad (1\text{-}3)$$

where λ_o was calculated by Born eq 1-4.

$$\lambda_o = (\Delta e)^2\left(\frac{1}{2r_1} + \frac{1}{2r_2} - \frac{1}{R}\right)\left(\frac{1}{D_{op}} - \frac{1}{D_s}\right) \qquad (1\text{-}4)$$

where r_1 and r_2 are the ionic radii of the donor and acceptor, R is the center-to-center separation distance of the reactants, D_{op} and D_s are the optical and static dielectric constants of the solvent respectively, and Δe is the charge transferred from the donor to the acceptor. The solvent model using eq 1-4 comes from dielectric continuum theory. In this theory, the solvent is treated as a structureless continuum, whose properties are dictated by D_{op} and D_s.

The expression for the vibrational term λ_i in eq 1-3, is given by

$$\lambda_i = \frac{1}{2}\sum_j f_j\left(Q_j^r - Q_j^p\right)^2 \qquad (1\text{-}5)$$

where Q_j^r and Q_j^p are equilibrium values for the jth normal mode coordination Q and

f_j is a reduced force constant $2k_j^r k_j^p/(k_j^r+k_j^p)$ for the jth inner-sphere vibration, k_j^r being the force constant for the reactants and k_j^p being that for the products.[25]

The original work of Marcus rested on the assumption that the ET process is diabatic and the reaction proceeds on one potential energy surface. The prefactor (k_0) for a unimolecular reaction is $k_0 = \kappa_{el}\, k_B T/h$, where κ_{el} is the electronic transmission coefficient which is unity. The unfortunate terminology adiabatic and nonadiabatic is a historical artifact, which has lead to confusion in the chemical literature. In this work, nonadiabatic reactions are those that occur on more than one PES. In the nonadiabatic limit where the electronic coupling is weak at the intersection of the two potential energy surfaces (Figure 1-6), the general rate constant is derived as

$$k_{ET} = \kappa_{el}\nu_N \exp\left(\frac{-\Delta G^{\neq}}{k_B T}\right) \qquad (1\text{–}6)$$

where κ_{el} is proportional to the electronic coupling matrix element $\mathrm{H}_{\mathrm{AB}}^2$, ranging from zero to unity. In the classic model, ν_N is the frequency of passage across the barrier, the frequency of the vibration that destroys the activated complex configuration.

The ramification of eq 1-6, which relates k_{ET} and ΔG° with λ_t held constant, are profound. The dependence of k_{ET} and ΔG° is illustrated in Figure 1-7. For $-\Delta G^{\circ} < \lambda$, increasing $-\Delta G^{\circ}$ and holding λ_t constant, k_{ET} increases with increasing $-\Delta G^{\circ}$ (Figure 1-7 B). For $-\Delta G^{\circ} = \lambda$, k_{ET} reaches its maximum, $k_{ET} = \kappa_{el}\nu_N$ (Figure 1-7 C), and k_{ET} is independent on $-\Delta G^{\circ}$. An important but counter intuitive prediction of Marcus theory is the existence of the inverted region in which the ET rate constant k_{ET} decreases with increasing driving force $-\Delta G^{\circ} > \lambda$ (Figure 1-7 D). The net effect of k_{ET} *vs.* $-\Delta G^{\circ}$ is

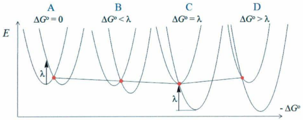

The red dots trace the transition state and ΔG° becomes more negative

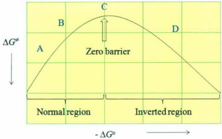

Figure 1-7. Illustrating the influence on the classical barrier to electron transfer of increasing $-\Delta G^{o}$ at fixed reorganization energy, λ, according to eq 1-6 (top), and the plot of $\Delta G^{\neq}$ *vs.* ΔG^{o} (bottom).

illustrated in Figure 1-7. The inverse parabolic dependence predicted by Marcus has been observed. However, several studies have demonstrated the k_{ET} *vs.* $-\Delta G^{o}$ is asymmetric, and this point will be elaborated on in Section 1.3.2.3. Although predicted by Marcus in the early 1960s, the inverted region escaped detection for many years because experimental attempts were based on bimolecular electron transfer. As $-\Delta G^{o}$ increases, the rate limiting step changes and the experimental rate constant (k_{obsd}) becomes diffusion limited (k_{D}), not activation limited. This behavior is known as diffusion masking. Under these conditions, k_{obsd} is given by

$$\frac{1}{k_{obsd}} = \frac{1}{k_{ET}} + \frac{1}{k_D} \qquad (1\text{-}7)$$

in addition, if $k_{ET} >> k_D$, $k_{obsd} = k_D$. The impediment to observe the inverted region was that λ_t for ET was generally too large, precluding the observation of the inverted region. The resulting dilemma was how to get rid of diffusion.

The approaches taken to overcome the diffusion masking problem were adroit, freezing the medium and covalently tethering the donor and acceptor. Miller studied the reaction in rigid media, and provided the first experimental evidence for the inverted region as shown in Figure 1-8 A.[28] However, in the inverted region the rates are higher than expected, suggesting a change in mechanism.

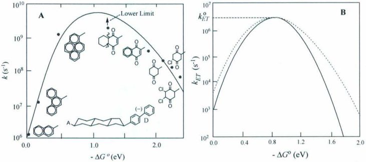

Figure 1-8. (A) Intramolecular electron transfer rate constants as a function of ΔG^o in frozen solution, adapted from ref 28. (B) The difference between the plot of k_{ET} *vs.* $-\Delta G^o$ for the classical (solid) and that for semi-classical (dotted) Marcus equation.

1.3.2.3 Quantum Mechanical Corrections: Vibronic Theory

The original description of the inverted region was based on classical arguments and required thermal activation barrier crossing, analogous to that found when $-\Delta G^o < \lambda_t$.

Quantum mechanical tunneling through the barrier was not considered. However, in the inverted region, electron transfer occurs through a series of vibrational channels rather than by a barrier crossing because of $\Delta G^{\neq} \gg k_BT$ such that the thermal crossing becomes less probable as $-\Delta G^{\circ}$ increases. The evolution of ET occurring via a nonadiabatic surface crossing is conceptually similar to the polaron theory of charge transport in semi-conducting solids.[29-33] Vibrational modes coupled to electron transfer must be treated as quantum mechanical if the quantum spacing ($\hbar\omega \gg k_BT$) between the vibrational levels is large compared to thermal energies, and it is necessary to introduce quantum mechanical corrections.[32,34,35] Using the polaron model, each electronic state is coupled with a number of vibrations, with each vibrational mode treated by using the harmonic oscillator approximation and separation of nuclear and electronic coordinates. Insertion of the vibrational energy levels within the potential curves is shown in Figure 1-9. The transition between the lowest vibrational level ($\nu' = 0$) on the excited state potential energy curve and high vibrational levels on the ground state potential surface is possible and is governed by the magnitude of the overlap of vibrational wavefunctions (Franck-Condon Factor) between the reactant and product potential energy surfaces.

In reality, the number of vibrational modes that exist in molecular donor-acceptor systems is large and the interaction of the vibrational wavefunctions is complex. As such, the vibrational modes are averaged and treated as a one-mode approximation. In cases where a mode-by-mode analysis has been performed, it was found that the one-mode approximation was valid. For a transition between two diabatic states where the electronic wavefunctions are orthogonal, it requires that electron transfer is coupled to vibrational

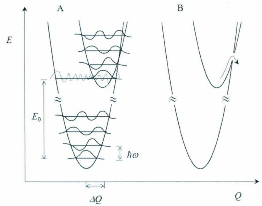

Figure 1-9. Schematic energy-coordinate (E-Q) diagram illustrating the electron transfer in the inverted region (A) by a vibrational channel below the intersection region and vibrational wavefunction overlap between the reactant and product vibrational levels (see the text) and (B) by the classical barrier crossing. Adapted from ref 36.

motion. The Born-Oppenheimer approximation is no longer valid. The transition is facilitated by promoting modes, which mix the excited and ground state electronic wavefunctions and provide electronic coupling between states. When the excited and ground states surfaces are nested and $\hbar\omega \gg k_B T$, the probability for the transition is given by the Fermi Golden rule.[36]

$$k_{ET} = \frac{2\pi}{\hbar}\langle\psi'|\hat{H}|\psi\rangle^2 \delta(E' - E) \qquad (1\text{-}8)$$

where $\hat{H}$ is the operator that induces the transition. E and E' are energies of the initial and final states. ψ and ψ' are total wave functions including the spin part. The Dirac delta function $\delta(E' - E)$ ensures that the transition occurs with energy conservation.

At present, the terminology used by chemists and physicists differ even though the process is the same. The polaron model consists of two electronic states coupled with a large number of vibrational levels, which can be either quantum mechanical or classical. The terminology with respect to charge transport in semi-conductors, *i.e.* polaron, is the coupling of exciton and phonons. The exciton, [e$^-$, h$^+$], is a bound electron and hole pair, and phonon is one quanta of lattice vibration. Exciton is a term used more frequently in excited state electron transfer in chromophore quencher assemblies[37] and photoinduced interfacial electron transfer because it allows an analysis whereby electron and hole can be deduced in the reaction mechanism.[38] If specifying one coupled vibration characterized by frequency ω and equilibrium displacement ΔQ_e, in addition to the classical solvent motions, the intramolecular reorganizational energy for this mode can be defined as

$$\lambda_i = (f/2)\left(\Delta Q_e\right)^2 \qquad \text{(1-9)}$$

This can be related to a dimensionless quantity, the electron vibrational coupling constant or Huang-Rhys factor (*S*), as defined in eq 1-9; μ is the reduced mass.

$$S = \frac{\lambda_i}{\hbar\omega} = \frac{f}{2\hbar\omega}\left(\Delta Q_e\right)^2 = \frac{\mu\omega}{2\hbar}\left(\Delta Q_e\right)^2 \qquad \text{(1-10)}$$

The generalization of eq 1-1 for nonadiabatic ET for one coupled mode with $\hbar\omega \gg k_B T$, then becomes[35]

$$k_{ET} = \frac{2\pi}{\hbar} H_{RP}^2 \left(\frac{1}{4\pi\lambda_o k_B T}\right)^{1/2} \text{(FC)} \qquad \text{(1-11)}$$

$$\text{(FC)} = \sum_{v'} \exp(-S) \frac{S^{v'}}{v'!} \exp\left\{\frac{-(\lambda_o + v'\hbar\omega + \Delta G^o)^2}{4\lambda_o k_B T}\right\} \qquad \text{(1-12)}$$

The change of the vibrational wavefunction overlap with the increase of driving force is attenuated in the inverted region and is the microscopic origin for decreased dependence of the electron transfer rate constant on ΔG° in the inverted region relative to the normal region. There is a clear conceptual connection for electron transfer in the inverted region and nonradiative decay for excited state decay. For nonradiative decay, the electronic coupling matrix elements are eigenvectors associated with two coupled states within the same molecules, and for the inverted electron transfer, the electronic coupling matrix are eigenvectors associated with donor and acceptor in the weak coupling limit. It should be noted that the eigenvectors for the inverted electron transfer also include off diagonal elements. This will be elaborated on in Chapter 3.

1.3.2.4 Radiative Processes

Application of the time-dependent Schrödinger equation and perturbation theory to transition rates between two states (*i.e.* ground and excited states) allow the integral in eq 1-8 to be partitioned between nuclear and electronic parts:

$$W = \frac{2\pi}{\hbar}\langle\psi'_{el}|\hat{H}|\psi_{el}\rangle^2\langle\phi'_{vib}|\phi_{vib}\rangle^2\delta(E'-E) \qquad (1\text{-}13)$$

where W is the transition probability that will occur between two electronic states. ψ'_{el} and ψ_{el} are electronic wavefunctions for the final and initial states. ϕ'_{vib} and ϕ_{vib} are total vibrational wavefunctions for the final and initial states. Application of the Golden rule to single photon emission allows the total spontaneous emission probability, corrected for the presence of a medium, for the transition $\nu \rightarrow \nu'$ to be written as:[39-41]

$$k_r(\bar{v}) = \frac{64\pi^4 f(n)}{3h}\langle\bar{v}^{-3}\rangle^{-1}|\vec{M}|^2\delta(E_{v,v'} - hc\bar{v}) \qquad (1\text{-}14)$$

where the factor $f(n)$ represents correction factors because the emission process takes place in a medium, and in most cases can be expressed by $f(n) = n^3/\varepsilon(E_e/E)^2$; n and ε denote the refractive index and dielectric constant of the medium respectively, and E_e/E, the ratio of the effective electric field E_e to the macroscopic electric field E. The parameter $(E_e/E)^2$ can be approximated by $1/\varepsilon$ and, hence, $a = n^3$. The refractive index factor $f(n)$ is used rather than the more familiar n^3 as described by Strickler and Berg[42] from the density of photon (polaron) states in a medium of refractive index n because it has a somewhat firmer theoretical basis.[43,44] $\vec{M}$ is the transition moment and $E_{v,v'}$ is the energy of the electronic transition between the $v = 0$ to $v' = 0$ vibrational levels. v and v' are the frequencies of the oscillator in the electronic ground and excited states. $\bar{v}$ is the emission energy in units of cm^{-1}, and $\langle \bar{v}^{-3} \rangle^{-1}$ is the inverse of the average value of $\bar{v}^{-3}$ for the emission spectrum. The value of $\langle \bar{v}^{-3} \rangle^{-1}$can be approximated by E_{em}^3, or can be calculated using eq 1-15,[45,46] where I is the emission intensity in units of number of quanta per energy interval per second:

$$\langle \bar{v}^{-3} \rangle^{-1} = \frac{\int I(\bar{v}) d\bar{v}}{\int I(\bar{v}) \bar{v}^{-3} d\bar{v}} \qquad (1\text{-}15)$$

For an electric dipole allowed transition with higher order terms negligible, $\vec{M}$ is given by:

$$\vec{M} = \left\langle \psi'_{el} \middle| e \sum_j \bar{r}_j \middle| \psi_{el} \right\rangle \langle \phi'_{vib} | \phi_{vib} \rangle \qquad (1\text{-}16)$$

$$\vec{\mu} = \left\langle \psi'_{el} \middle| e \sum_j \bar{r}_j \middle| \psi_{el} \right\rangle \qquad (1\text{-}17)$$

The transition intensity is determined by the magnitude of the transition dipole, $\vec{\mu}$, and the sum is over all of the electronic coordinates. ϕ'_{vib} and ϕ_{vib} are the total vibrational wavefunctions, which are the product of the overlaps of the *j* contributing normal modes in eq 1-18 and eq 1-19.

$$\phi_{vib} = \prod_j \chi_{v_j} \qquad (1\text{-}18)$$

$$\phi'_{vib} = \prod_j \chi_{v'_j} \qquad (1\text{-}19)$$

χ_{v_j} and $\chi_{v'_j}$ are wave functions for mode *j* in the initial and final states. v_j and v'_j are the associated vibrational quantum numbers. The integrated emission spectrum is related to $\vec{M}$ by:

$$I_{v,v'} = \int I(\bar{v})d(\bar{v}) = \frac{64\pi^4 f(n)}{3h}\langle\bar{v}^{-3}\rangle^{-1}\left|\vec{M}\right|^2 \qquad (1\text{-}20)$$

Substituting eq 1-16 into eq 1-20 yields

$$I_{v,v'} = \frac{64\pi^4 f(n)}{3h}\langle\bar{v}^{-3}\rangle^{-1}\left|\left\langle\psi'_{el}\middle|e\sum_j \bar{r}_j\middle|\psi_{el}\right\rangle\langle\phi'_{vib}|\phi_{vib}\rangle\right|^2 \qquad (1\text{-}21)$$

If the potential surfaces are harmonic, there is no change in the vibrational frequencies between the ground and excited states ($\hbar\omega_j = \hbar\omega'_j$), and the transition dipole moment is a constant, then

$$I_{v,v'} = \frac{64\pi^4 f(n)|\vec{\mu}|^2}{3h}\langle\bar{v}^{-3}\rangle^{-1}\langle\phi'_{vib}|\phi_{vib}\rangle \qquad (1\text{-}22)$$

where

$$\langle\phi'_{vib}|\phi_{vib}\rangle = \prod_j \left\langle\chi_{v'_j}\middle|\chi_{v_j}\right\rangle \qquad (1\text{-}23)$$

For harmonic oscillators with no frequency change, the form of Franck-Condon factor for the $v \rightarrow v'$ transition is given:[47]

$$\left\langle\chi_{v'_j}\middle|\chi_{v_j}\right\rangle = \exp(-S_j)\, S_j^{\left(v'_j - v_j\right)}\, \frac{v_j!}{v'_j!}\left[L_{v_j}^{\left(v'_j - v_j\right)}(S_j)\right]^2 \qquad (1\text{-}24)$$

$L_{v_j}^{(v_j'-v_j)}(S_j)$ is a Laguerre polynomial:

$$L_{v_j}^{(v_j'-v_j)}(S_j) = \sum_{v=0}^{v_j} \frac{v_j'!\,(-S_j)^v}{(v_j - v)!\,(v_j' - v_j + v)!\,v!} \qquad (1\text{-}25)$$

S_j is the electron-vibrational coupling constant, or Huang-Rhys factor:

$$S_j = \frac{1}{2}\left(\frac{M_j\omega_j}{\hbar}\right)\left(\Delta Q_{e,j}\right)^2 = \lambda_j/\hbar\omega_j \qquad (1\text{-}26)$$

M_j is the reduced mass. $\omega_j = 2\pi\, v_j$ is the angular frequency of the vibration. The physical significance of the vibrational overlap integrals is that they give the extent to which the final and initial states coincide along the normal coordinate. The population in level v_j is given by the Boltzmann distribution function:

$$P(v_j) = \exp[-(v_j\hbar\omega_j/k_B T)]/Z_j = \exp[-(v_j\,\beta_j)]/Z_j \qquad (1\text{-}27)$$

with $\beta_j = \hbar\omega_j/k_B T$ and Z_j the vibrational partition function,

$$Z_j = \sum_{v_j} \exp\left[-\left(v_j + \frac{1}{2}\right)\beta_j\right] \qquad (1\text{-}28)$$

If $\hbar\omega_j \gg k_B T$, only $v_j = 0$ is appreciably populated and

$$\left\langle \chi_{v_j'} \middle| \chi_{v_j} \right\rangle^2 = \exp(-S_j)\,\frac{S_j^{v_j'}}{v_j'!} \qquad (1\text{-}29)$$

The solvent contribution is treated classically, and included in the Gaussian distribution function in the bandwidth. Changes in quantum spacing and densities of levels for the coupled solvent oscillations (librations) are included in $\Delta G°$. For a single coupled vibration or averaged vibration with $\hbar\omega_j \gg k_B T$, the spectral band shape equation for emission can be generalized to include any number of coupled vibrations.

$$I(\bar{\nu}) = \frac{64\pi^4 N_A}{3h^3c^2} \frac{|\vec{\mu}|^2}{(4\pi\lambda_o k_B T)^{1/2}} \sum_{v} (\Delta G^o + v\hbar\omega + \lambda_o)^3 \cdot \exp(-S)\left(\frac{S^v}{v!}\right) \cdot \exp\left[-\frac{\left(h\bar{\nu} - (\Delta G^o - v\hbar\omega + \lambda_o)\right)^2}{4\pi\lambda_o k_B T}\right] \qquad (1\text{-}30)$$

where $I(\bar{\nu})$ is the emitted intensity, ω frequency, and c the speed of light. The definition of spectral fitting parameters is shown in Figure 1-10.

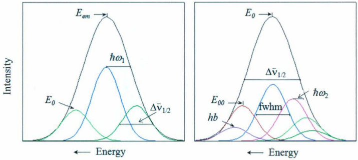

Figure 1-10. Definition of spectral fitting parameters, reproduced from ref 22. (A) The complete spectrum is fit to a series of bands with the spacing $\hbar\omega_1 = 1300\ cm^{-1}$. The band shapes have a half-width of $\Delta\bar{\nu}_{1/2}$, and the maximum of the first peak occurs at E_0. The peak maximum of the complete spectra occurs at E_{em}. (B) The band shapes of the $\hbar\omega_1 = 1300\ cm^{-1}$ progression are generated by summing a series of Gaussians with spacing $\hbar\omega_2 = 300\ cm^{-1}$. These have a full width at half-maximum of fwhm, and the 0-0 transition occurs at E_{00}. Because thermal population in this mode is allowed, "hot bands" (hb) occur at energies higher than E_{00}. All relative peak heights are constrained to Franck-Condon values.

1.3.3 Mechanism of Electron Transfer in Solution

1.3.3.1 Outer-sphere and Inner-Sphere Mechanism

Taube's pioneering studies established the distinction between outer-sphere and inner-sphere electron transfer mechanism. This classification was originally applied to electron transfer between coordination metal complexes, in terms of the changes that the coordination spheres or surrounding ligands of the metal ions experience during electron transfer. In the outer sphere mechanism, an electron transfers from reductant (donor) to oxidant (acceptor) with the coordination sphere of each staying intact. That is one reactant becomes involved in the outer or second coordination sphere of the other reactant when the electron flows from the reductant to oxidant. An inner sphere mechanism is one in which the reactant and oxidant share a ligand in their inner or primary coordination spheres, the electron transfer proceeding via a bridging group between the two redox partners.

The role of the bridge between the donor and acceptor initially was envisioned as a connector, which held the donor and acceptor within close proximity. It is now abundantly evident that the bridge dynamics play a significant and fundamental role in ET from the donor to the acceptor. The recognition of the role for the bridging ligand can be traced back to the "Creutz-Taube ion" for intervalence electron transfer. In the seminal and pioneering work of Gray where the donor and acceptor are bridged by a protein such as myoglobin, the ET over hundreds of angstroms via the electronic pathway provided by the protein required a paradigm shift in the theory of ET. Therefore, the term inner sphere ET became mechanistically ambiguous and the formulation of the theory for ET encompassed both outer and inner sphere ET. The connection required a re-evaluation of electronic coupling and vibronically induced electronic coupling. The bridge dynamics include conformational changes, solvent energetics and the coupling of the bridge to the donor and acceptor. Similarly, outer-sphere electron transfer takes place with very weak

(4–16 kJ/mol) electronic interaction between the reactants in the transition state. The solvent is seen to influence reorganization energetics and the free energy difference between the donor and acceptor in addition to the electronic coupling between the donor and acceptor by providing an electronic pathway for ET. Each pathway is defined in terms of electronic interactions between the reactants in the transition state.[48]

This concept of outer- and inner-sphere electron transfer is also applicable to photoinduced electron transfer. Any molecular unit that links a donor-acceptor pair and transmits the electron is the equivalent of the bridging ligand in an inner-sphere reaction. The terms "inner-sphere" and "bridged" electron transfer have often been treated as synonymous.

1.3.3.2 Bridged Mediated Electron Transfer

Superexchange Mechanism and Hopping Mechanism. Photoinduced electron transfer in which an electron donor and acceptor are separated by a molecular spacer or bridge (D-B-A systems) can occur via either superexchange or hopping mechanisms or some combination of both (Figure 1-11). In the superexchange mechanism, the electron takes a direct route from a donor to an acceptor independent on the length of the bridge, bridges solely serving to mediate donor and acceptor wavefunctions. On the contrary, for the hopping mechanism (sequential charge-transfer), the electron hops from one site to its nearest neighbors, located at the bridge for a short time during its journey from a donor to an acceptor.[49,50] What parameters govern these alternative pathways?

In the case of long range ET, where the donor and acceptor are separated by distance exceeding the sum of their van der Waals radii, electronic coupling (V_{el})

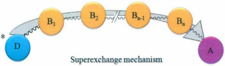

Superexchange mechanism

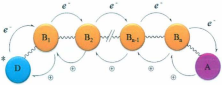

Hopping mechanism

Figure 1-11. Superexchange and hopping mechanisms for photoinduced charge separation between an excited acceptor and ground-state donor.

generally is very small. ET occurs nonadiabatically and the Fermi Golden rule formalism is used to express the ET rate constant k_{ET}, given by[51,52]

$$k_{ET} = \frac{2\pi}{\hbar}|V_{el}|^2 FC \qquad (1\text{-}31)$$

where *FC* is the Franck-Condon weighted density of states, and it consists of the sum over all possible vibrational overlap integrals between the initial vibration level and the final vibration level. In Marcus semi-classical treatment, eq1-6 becomes

$$k_{ET} = \frac{4\pi^2}{h}|V_{el}|^2\left(\frac{1}{4\pi\lambda k_B T}\right)^{1/2} \exp\left[\frac{-(\Delta G^o + \lambda)^2}{4\lambda k_B T}\right] \qquad (1\text{-}32)$$

Thus, from eq 1-32, three important parameters that determine the ET rate constant are V_{el}, λ and ΔG°. V_{el} is the electronic coupling term between donor and acceptor. λ and ΔG° are as defined above.

There is another medium effect on the ET rate constant. The medium will influence

ET dynamics by its effect on the driving force ($-\Delta G^{o}$) and the solvent reorganization terms. The medium also may participate in the ET process by electronic coupling with the donor and acceptor. This effect is manifested by an increase of the electronic coupling term, V_{el}.[52] Such a medium, which may be a saturated hydrocarbon bridge, protein or oligopeptide, or π stacks or even solvent molecules, may facilitate ET by though-bond (TB) coupling.[53-55] In the absence of intervening medium, the electronic coupling between redox pairs depends on the direct through-space (TS) overlap between the orbitals of the donor and acceptor groups that are primarily involved in the electron transfer. Since the hopping (sequential charge-transfer) mechanism is simply several discrete superexchange processes, eq1-32 can be used to calculate the rate constant k_n for the discrete process.

Orbital overlap decays exponentially with the increasing inter-orbital separation, it will be expected that the magnitude of TB electronic coupling should have similar decay characteristics. Therefore, both V_{el} and associated k_{ET} decay exponentially with the increasing inter-chromophore separation, *r*, given by

$$V_{el} \propto \exp(-0.5\,\beta_{el}\,r) \qquad (1\text{-}33)$$

$$k_{ET} \propto \exp(-\beta\,r) \qquad (1\text{-}34)$$

where β_{el} and β are damping factors. β being a phenomenological quantity, incorporating distance dependence contributions, not only from V_{el} but also from Franck-Condon factors such as λ_o. Therefore β is expected to be slightly larger than β_{el}.[56]

In summary, ET occurs via a single-step superexchange mechanism only at short donor-acceptor distances. At longer distances, ET occurs via a multistep hopping mechanism.

1.4 Energy Transfer

1.4.1 Radiative Energy Transfer: Trivial Mechanism

Energy transfer may occur in a radiative mechanism, which is a two-step sequence given below, where D^* is an excited donor, and A is an excitation acceptor.[57,58]

$$\text{Emission: } D^* \longrightarrow D + h\nu \qquad (1\text{-}35)$$

$$\text{Absorption: } h\nu + A \longrightarrow A^* \qquad (1\text{-}36)$$

In the trivial mechanism, a physical encounter between A and D^* is not required and there is no electronic interaction between D^* and A. However, this requires that the excited donor molecule D^* emits a quantum of light which is absorbed by the energy acceptor molecule A, so the photon must be emitted only in an appropriate direction and the medium must be transparent in order to allow transmission. The rate or probability of energy transfer from D^* to produce A^* per unit time will depend on: (1) the quantum yield (ϕ_D) of emission by D^*, (2) the concentration of A molecules in the path of the photons emitted by D^*, (3) the extinction coefficient of A at the wavelength of emission, and (4) the overlap of the emission spectrum of D^* and the absorption spectrum of A. The last factor can be quantified in terms of the spectral overlap integral, J, given by

$$J = \int_0^{\infty} I_D(\bar{\upsilon})\varepsilon_A(\bar{\upsilon})d\bar{\upsilon} \qquad (1\text{-}37)$$

where I_D is the plot of emission of D^* on an energy scale (cm^{-1}). ε_A is the plot of absorption on an energy scale (cm^{-1}). Both are normalized so that the complete overlap will correspond to $J = 1.00$.

1.4.2 Nonradiative Energy Transfer: Förster Mechanism and Dexter Mechanism

Interaction between excited and ground states of two molecular chromophores is a considerably important subject in photophysical processes such as intramolecular electronic energy transfer (intra-EnT) and intramolecular electron transfer (intra-ET) processes. EnT processes occur at distances ranging from 1 Å to more than 50 Å, and on time scales from femto-seconds to milli-seconds. Energy transfer is a special case of nonradiative transfer of electronic excitation from an excited donor molecule D* to an acceptor molecule A. The energy transfer may be an intermolecular process, which can be described in terms of a bimolecular quenching process,

$$\mathrm{D}^* + \mathrm{A} \xrightarrow{k_q} \mathrm{D} + \mathrm{A}^* \qquad (1\text{-}38)$$

where the bimolecular quenching rate constant k_q is related to an intermolecular energy transfer rate constant k_{EnT} by

$$k_{EnT} = k_q[A] \qquad (1\text{-}39)$$

In most cases, k_{EnT} is possibly from two contributions, the long-range Coulombic interaction in terms of dipole-dipole interaction and short-range exchange interaction. The principle for both mechanisms are well understood, and formulated by Förster and Dexter respectively.[33,59-61] Application of time-dependent perturbation theory gives the energy transfer rate constant by the "Golden Rule" in eq 1-40

$$k_{EnT} = \frac{2\pi}{\hbar}\langle\psi'|\hat{H}|\psi\rangle^2 \rho E \qquad (1\text{-}40)$$

where $\hat{H}$ is the matrix element of the perturbation to the Hamiltonian between the initial and final states, and ρE is the density of the states. ψ and ψ' are the corresponding total wavefunctions including the spin part. This result is valid only in the weak coupling limit where the perturbation is small and the transition probability low. The interaction matrix element describing the coupling between initial and final states for nonradiative decay is given by

$$V_{EnT}=\langle \psi' | \hat{V} | \psi \rangle = \langle \psi_{D^*}(1)\psi_A(2) | \hat{V} | \psi_D(1)\psi_{A^*}(2)\rangle + \langle \psi_{D^*}(1)\psi_A(2) | \hat{V} | \psi_D(2)\psi_{A^*}(1)\rangle \quad (1\text{-}41)$$

where $\hat{V}$ is the perturbation part of the total Hamiltonian $\hat{H} = \hat{H}_0 + \hat{V}$, and given by

$$\hat{V} = e^2/\epsilon R_{DA} \quad (1\text{-}42)$$

R_{DA} is the dipole-acceptor separation, and ϵ is the dielectric constant of the medium. The first term in eq 1-41 is the Coulombic interaction and the second term is the exchange interaction, so the coupling matrix can be written as

$$V_{EnT} = V_{EnT}^{d-d} + V_{EnT}^{ex} \quad (1\text{-}43)$$

where

$$V_{EnT}^{d-d} = \langle \psi_{D^*}(1)\psi_A(2) | \hat{V} | \psi_D(1)\psi_{A^*}(2)\rangle \quad (1\text{-}44)$$

$$V_{EnT}^{ex} = \langle \psi_{D^*}(1)\psi_A(2) | \hat{V} | \psi_D(2)\psi_{A^*}(1)\rangle \quad (1\text{-}45)$$

The energy transfer may occur by the Förster mechanism or the Dexter mechanism. In both mechanisms, the electronic wavefunctions include ψ_s' and ψ_s, spin wavefunctions. The operator inducing energy transfer does not include spin, and in the absence of spin-orbit coupling, energy transfer can only occur between states with the same spin multiplicity. For example, $\langle \psi_s' | \psi_s \rangle = 1$ for $S \rightarrow S'$ transfer and $\langle \psi_s' | \psi_s \rangle = 0$ for $S \rightarrow T$ transfer. Spin-orbit coupling mixes the spin character of the states, making spin changes possible but still greatly decreasing the magnitude of V. Within the framework of the Born-Oppenheimer-Condon (BOC) approximation, the integral in eq 1-40 is partitioned between nuclear and electronic parts,

$$k_{EnT} = \frac{2\pi}{\hbar}\langle\psi'_{el}|\hat{H}|\psi_{el}\rangle^2\langle\psi'_{vib}|\psi_{vib}\rangle^2\langle\psi'_{s}|\psi_{s}\rangle^2\delta(E' - E) \qquad (1\text{-}46)$$

This is a general equation applicable to light absorption, emission, electron transfer, and excited-state decay. $\hat{H}$ is different for the different processes. ψ'_{el} and ψ_{el} are electronic wavefunctions for the final and initial states. The associated spin wavefunctions are ψ'_s and ψ_s. It is assumed that the electronic matrix element, $\langle\psi'_{el}|\hat{H}|\psi_{el}\rangle$, is independent on nuclear coordinates. ψ'_{vib} and ψ_{vib} are total vibrational wavefunctions for the final and initial states, and they are the product of all normal modes including collective solvent vibrations,[47,62]

$$\psi_{vib} = \prod_j \chi_{v_j} \qquad (1\text{-}47)$$

$$\psi'_{vib} = \prod_j \chi_{v'_j} \qquad (1\text{-}48)$$

χ_{v_j} and $\chi_{v'_j}$ are wavefunctions for mode j in the initial and final states. v_j and v'_j are the associated vibrational quantum numbers. If only maintaining the dipole-dipole term, the Coulombic integral will be approximated by expanding as

$$V_{EnT} = \frac{1}{\varepsilon R_{DA}^3}\vec{\mu}_D\vec{\mu}_A\left[1 - \frac{3\vec{r}_D\vec{r}_A}{R_{DA}^2}\right]\prod_j\left\langle\chi_{i,v_j}\middle|\chi_{f,v'_j}\right\rangle \qquad (1\text{-}49)$$

μ_D and μ_A are the transition dipole moments of D → D* and A → A* transitions, $\vec{r}_D$ and $\vec{r}_A$ are the dipole moments vectors. By using the Fermi Golden Rule, the energy transfer rate constant can be written as

$$k_{EnT}^{d-d} = \frac{2\pi}{\hbar}\sum_i\sum_f P_i V_{EnT}^2\delta(E_i - E_f) \qquad (1\text{-}50)$$

where P_i denotes the initial distribution, E_i and E_f are the energies of the initial and final states, respectively. Substituting eq1-49 in eq 1-50, the rate constant will become

$$k_{EnT}^{d-d} = \frac{2\pi}{\hbar}\left[\frac{\vec{\mu}_D\vec{\mu}_A}{\varepsilon R_{DA}^3}\Gamma(\theta_D, \theta_A)\right]^2 \times \sum_i \sum_f \left[\prod_j \langle \chi_{i,v_j} | \chi_{f,v'_j} \rangle\right]^2 \delta(E_i - E_f) \qquad \text{(1-51)}$$

$\Gamma(\theta_D, \theta_A)$ is an orientation factor for the two dipoles (Figure 1-12), and expressed as

$$\Gamma = 2\cos\theta_D \cos\theta_A - \sin\theta_D \sin\theta_A \cos(\varphi_D - \varphi_A) \qquad \text{(1-52)}$$

and φ is the angle of rotation about the interdipole axis. For random orientation $\Gamma = 2/3$. Using the expressions for the absorption coefficient of A, the normalized spectral emission distribution of D, the integral representation of the δ function, and carrying the integration over t, the final Förster expression for dipole-dipole induced energy transfer

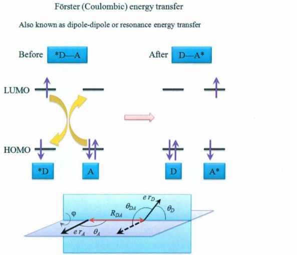
Förster (Coulombic) energy transfer
Also known as dipole-dipole or resonance energy transfer
Before
*D—A
After
D—A*
LUMO
HOMO
*D
A
D
A*
er_D
θ_{DA}
θ_D
φ
R_{DA}
er_A
θ_A

Figure 1-12. Schematic description of Förster energy transfer by dipole-dipole interaction (top) and geometrical configuration of dipole-dipole interaction between donor and acceptor molecules (bottom) adapted from ref 63.

rate constant will be derived as

$$k_{EnT}^{d-d} = \frac{9000 \ln 10 \kappa^2 \phi_D}{128\pi^5 N_A n^4 \tau_D R_{DA}^6} \int \frac{F_D(\bar{v})\varepsilon_A(\bar{v})}{\bar{v}^4} d\bar{v} \qquad (1\text{-}53)$$

The vibrational overlap term,

$$J_{d\text{-}d} = \int \frac{F_D(\bar{v})\varepsilon_A(\bar{v})}{\bar{v}^4} d\bar{v} \qquad (1\text{-}54)$$

The matrix elements and the Franck-Condon factors in eq 1-50 are now expressed in terms of measurable spectroscopic quantities such as the refractive index of the medium, n, the fluorescence quantum yield of the donor, ϕ_D, its fluorescence lifetime τ_D, the normalized donor fluorescence spectrum, $F_D(\bar{v})$, the normalized acceptor's absorption spectrum $\varepsilon_A(\bar{v})$, and the Avogadro number N_A. Often a Förster critical transfer radius R_0 is introduced, defined as

$$R_0^6 = \frac{9000 \ln 10 \kappa^2 \phi_D}{128\pi^5 N_A n^4} \int \frac{F_D(\bar{v})\varepsilon_A(\bar{v})}{\bar{v}^4} d\bar{v} \qquad (1\text{-}55)$$

so that the Förster rate can be written as

$$k_{EnT}^{d-d} = \frac{1}{\tau_D}\left(\frac{R_{DA}^0}{R_{DA}}\right)^6 \qquad (1\text{-}56)$$

In the Förster mechanism, energy transfer is induced by an electrostatic dipole interaction between the electrons in the initial and final states. V_{EnT}^2 varies as $1/R_{DA}^6$ with R_{DA} the internuclear separation distance between donor and acceptor. This mechanism is particularly suitable for describing inter-EnT in solution where conditions for favorable spectroscopic overlap between the emission of D^* and the absorption of A are not met. When these conditions are not fulfilled, a short range exchange interaction, as formulated by Dexter,[64] can facilitate EnT. In the Dexter mechanism, the electron clouds of the reacting species overlap significantly in space. In the range of overlap, physical electron exchange between the donor and acceptor occurs. This situation is shown in Figure 1-13.

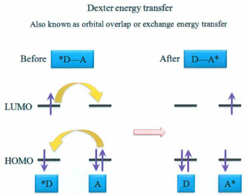
Dexter energy transfer

Also known as orbital overlap or exchange energy transfer

Figure 1-13. Schematic description of exchange energy transfer by electronic overlap.

Dexter's approach followed the general derivation discussed above. In this case, the rate constant for electron-exchange energy transfer depends on the overlap integral and a parameter Z. The exchange matrix element is

$$V_{EnT} = \left\langle \psi_{el}^{D^*}(1)\psi_{el}^{A}(2)\left|\frac{e^2}{r_{DA}}\right|\psi_{el}^{D}(2)\psi_{el}^{A^*}(1)\right\rangle \prod_j \left\langle \chi_{i,v_j} \middle| \chi_{f,v'_j} \right\rangle \qquad (1\text{-}57)$$

Substituting eq 1-57 in eq 1-46 gives the expression for the exchange interaction EnT rate constant, k_{EnT}^{ex},

$$k_{EnT}^{ex} = \frac{2\pi}{\hbar} Z^2 \sum_{v}\sum_{v'} P_v \left| \prod_j \left\langle \chi_{i,v_j} \middle| \chi_{f,v'_j} \right\rangle \right|^2 \delta(E_i - E_f) \qquad (1\text{-}58)$$

where Z is the electronic exchange integral

$$Z = \left\langle \psi_{el}^{D^*}(1)\psi_{el}^{A}(2) \left| \frac{e^2}{r_{DA}} \right| \psi_{el}^{D}(2)\psi_{el}^{A^*}(1) \right\rangle \qquad (1\text{-}59)$$

Z is approximated by assuming hydrogen-like orbitals thus arriving at the final expression for the exchange interaction EnT rate constant as

$$k_{EnT}^{ex} = \frac{2\pi}{\hbar} J_{ex} \exp(-2R/L) \qquad (1\text{-}60)$$

where R is the distance between donor and acceptor, and L is the sum of the van der Waals radii of the donor and acceptor molecules. J_{ex} is the exchange interaction integral of spectral overlap between donor emission and acceptor absorption,

$$J_{ex} = \int_0^\infty F_D\,(\bar{v})\varepsilon_A(\bar{v})d(\bar{v}) \qquad (1\text{-}61)$$

where $F_D(\bar{v})$ is the normalized emission spectrum of the donor and $\varepsilon_A(\bar{v})$ is the normalized absorption spectrum of the acceptor. Therefore, the rate for energy transfer decreases exponentially with increasing distance between donor and acceptor.

In summary, the basic features of Förster and Dexter mechanism as follows:

① The Förster mechanism is a through space based on Coulombic interaction that does not require orbital overlap of donor and acceptor, but it is dependent on the oscillator strengths of $D^* \rightarrow D$ and $A \rightarrow A^*$ radiative transitions. This mechanism can occur over distances up to 100 Å. The Dexter mechanism is independent of the oscillator strengths of $D^* \rightarrow D$ and $A \rightarrow A^*$ radiative transitions, but it requires orbital overlap of donor and acceptor since electrons are exchanged. This is a short-range mechanism, with a distance between donor and acceptor typically shorter than 10 Å.

② The rate of dipole-dipole induced EnT decreases as $1/R^6$ whereas the rate of the electron exchange induced EnT decreases as $\exp(-2R/L)$.

③ The Coulombic mechanism is effective typically for spin allowed processes such as singlet-singlet energy transfer. In addition to allowed transitions, energy transfer according to the Dexter mechanism can occur for spin forbidden processes within the framework of the dipole-dipole mechanism. These include singlet-singlet EnT, triplet-triplet EnT, and triplet-triplet annihilation processes.

④ For energy transfer involving allowed transitions, dipole-dipole interaction cannot be ignored since both mechanisms act in conjunction, not exclusively. This is especially important at small *R* values.

⑤ The exchange mechanism can be effective over larger distances in linked donor-acceptor molecules, if the connecting bridge allows electronic interactions via the orbitals of the bridge (superexchange, in analogy with electron transfer).

1.5 Supramolecular Assemblies for Charge Separation Systems

To understand the structure, composition, and physical principles of photosynthetic energy conversion that has evolved over 2-3 billion years is not only essential to optimizing the natural process for biological solar fuels production but also provides an essential conceptual database and inspiration for the construction of artificial photosynthetic devices to produce solar fuels with higher efficiency. Documented efforts to mimic natural photosynthetic processes have been under way since 1912, when Giacomo Ciamician envisioned artificial photosynthesis to be "the photochemistry of the future".[65] Solar energy has an enormous potential as a clean, abundant and economical energy source, but requires a device, which collects light and converts light energy into useful forms of energy. To construct artificial photosynthetic devices for practical conversion and storage of solar energy, it must incorporate both molecular-level and supra-molecular structural arrays to collect light energy, separate charge, and provide charge transport pathways to deliver the oxidizing and reducing equivalents to catalytic sites capable of redox catalysis, such as water oxidation and carbon dioxide reduction (Figure 1-14).

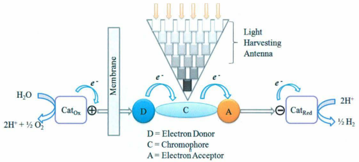

Figure 1-14. Illustration of the essential elements for artificial photosynthesis assembly adapted from ref [36].

This diagram illustrates the essential elements and processes required in an assembly for artificial photosynthesis and the sequence of events that occurs after light is absorbed. The reaction illustrated is the photochemical splitting of water into H_2 and O_2. Light absorption by a single molecule is low, so the light absorption system requires using antenna arrays or multilayer structures for efficient light harvesting. Electronic excitation of chromophore by energy transfer from light absorption system generates spatially separated redox equivalents D^+ and A^-. E^o of the individual fuel-forming half reactions and the overall free-energy change are dictated by the potentials of the $D^{+/0}$ and $A^{0/-}$ couples. For water splitting reaction:

$$2H_2O \rightarrow 2H_2 + O_2 \qquad (1\text{-}62)$$

$$\Delta G^o = +474.7\text{KJ/mol} = 4.92 \text{ eV}$$

This reaction has an overall energy requirement of 4.92 eV per O_2 molecule formed. To drive this reaction with visible light, multiple photons are required. With repetition of the light absorption-electron-transfer sequence, multiple redox equivalents accumulate at Cat_{ox} and Cat_{red} to carry out the half-reactions.

Considerable progress has been made in understanding the molecular mechanisms of photosynthesis.[66-68] X-ray structural characterization and more recent data of complete cofactor arrangement in the 3.0 Å resolution have been invaluable.[69-72] Once the mechanism of natural photosynthesis was at least partially elucidated, several research groups began to mimic this photochemical process for artificial solar energy conversion and storage. In the last 20 years, there have been significant efforts to synthesize and engineer artificial light-harvesting antennae and reaction centers, and a wide variety of donor and acceptor molecules and macromolecular architectures have been produced and characterized.[73,74]

1.5.1 Artificial Reaction Centers

Molecular Dyads: Single Electron Transfer. Photoinduced charge separation or redox splitting in the reaction center is the key process for converting light energy into chemical energy. The dominant strategy has been to utilize the minimum number of components in constructing molecular systems for charge separation. Chromophore-quencher dyads are one example illustrating this strategy. Chromophore-quencher dyads, *i.e.* D-A, are systems where a donor (D) and an acceptor (A) are covalently tethered. The donor acts in dual capacity as a light absorbing pigment and excited state electron donor and A is an electron acceptor. Illumination of this dyad molecule will lead to the sequence of electron-transfer events as shown in Figure 1-15. Generally, all the dyad-type systems suffer from a fast charge recombination to a greater or less extent.

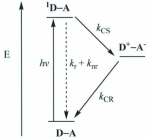

Figure 1-15. Schematic diagram of energy level for a dyad.

So far, it is believed that the rapid charge recombination is overcome by spatially separating the electron acceptors within the protein framework of the photosystem reaction center, thereby supporting efficient charge separation over a long distance.[75-77] The bio-inspired supramolecular systems have been constructed in order to satisfy many requirements. The key step as in natural photosynthesis is a vectorial and multistep ET for long-lived charge separation. The ET products in these systems are stabilized against recombination by their spatial separation in the rigid molecular arrays and the energetics for back electron transfer. Although such multistep electron transfer results in a substantial loss of input energy by each electron transfer step, the physical distance in the resulting separated radical ion pair attenuates the electronic coupling significantly, thereby prolonging the lifetime of the final charge-separated state. It should also be noted for these systems $\Delta G^{o} >> \lambda_t$, and the charge separated state lies in the inverted region where the rate constant for back electron transfer decreases with increasing ΔG^{o} as discussed in Section 1.1.

Molecular Triads: Sequential Multistep Electron Transfer. Early designs for chromophore-quencher triad systems were to use pigments, electron donors and acceptors relative to those found in natural photosynthesis. The sophistication of the triad assemblies is inhibited by the lack of synthetic methodologies, and by necessity of the early C-Q triads reported in the literature were not optimized for long term charge separation, *i.e.* the Ru^{II} based chromophore quencher complex (Figure 1-17 D) reported by Elliott and Meyer has a charge separation lifetime of 130 ns.[78] The appended electron donor and acceptor fragments were attached via configuration flexible alkyl linkages. The reported charge separation was thought to be due to the donor and acceptor coming in closer contact and resulting in charge recombination. Later work from Treadway et al. where the donor and acceptor were *trans* to each other across the Ru^{III} chromophore was synthesized. The charge separation lifetime was 140 ns independent of the conformational isomer. The data clearly show that electron transfer is through bond and configurational flexibility is not an important pathway for charge recombination at least in the polypyridyl systems that were studied.[79] There are two types of sequential electron transfer systems consisting of three components (triads). One is chromophore-acceptor-acceptor ($P\text{-}A_1\text{-}A_2$), and another is donor-chromophore-acceptor (D-P-A), as shown in Figure 1-16.

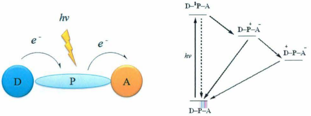
hv
e⁻
e⁻
D
P
A
D–¹P–A
hv
$D{-}\overset{+}{P}{-}\overset{-}{A}$
$\overset{+}{D}{-}P{-}\overset{-}{A}$
D–P–A

Figure 1-16. Schematic representation of charge separation in a triad and energy level.

Sakata and co-workers reported the synthesis and photophysical properties for the first example of the former system, consisting of a porphyrin (P) covalently linked to two quinones (A_1 and A_2) as shown in Figure 1-17 B.[80,81] Excitation of porphyrin-quinone-quinone ($P-A_1-A_2$) triads yields the porphyrin first excited singlet state, and then electron transfer to give a $P^{+\cdot}-A_1^{-\cdot}-A_2$ charge separated state. A second electron transfer from the A_1 to A_2, competing with rapid charge recombination, produces a long-lived $P^{+\cdot}-A_1-A_2^{-\cdot}$ species. The lifetime of the final charge separated state in the triad is at least 3 orders of magnitude longer than that in simple $P-A$ dyad. This implies that the longer distance between $P^{+\cdot}$ and $A_2^{-\cdot}$ is beneficial for extending the lifetime for charge separation state.

The first example for the second type of sequential multistep electron transfer system (*i.e.* carotenoid-porphyrin-quinone ($D-P-A$) was reported by Moore et al. as shown in Figure 1-17 A.[82-85] The final charge separated state ($D^{+\cdot}-P-A^{-\cdot}$) in dichloromethane has a lifetime of about 300 ns, much longer than in simple dyad. The

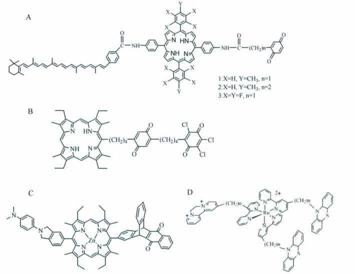

Figure 1-17. Structure of photosynthetic model of triads.

generality of the multistep electron transfer strategy for the generation of long-lived charge separated states in reasonable quantum yield has been amply demonstrated in other systems. For example, Wasielewski et al. have reported supramolecular triads consisting of a porphyrin as chromophore, a quinone acceptor and a dimethylaniline-based donor (Figure 1-17 C).[86] Meyer et al. have reported the preparation of a triad-type system based on the ruthenium trisbipyridyl chromophore using well developed synthetic methodologies (Figure 1-17 D).[78] A number of other successful three-component systems for stabilizing charge separated state have also been reported.[87,88]

To successfully mimic PSII, the intermediates formed must be stable on a time scale that allows electron/hole transfer to occur yielding a redox-separated state. Due to the synthetic complexity and inherent instability of reaction center mimics using quinone as primary electron acceptor, in addition to the low quantum yield of charge separation, it would therefore be desirable to look for alternative systems. In the natural reaction center, forward electron transfer is regulated to be much faster than back electron transfer, resulting in the long-lived final charge-separated state on the order of seconds with an almost 100% quantum yield. The reorganization energy (λ) is one of the important controlling factors in electron transfer. Based on Marcus theory,[89] the nonadiabatic (or weak coupling limit) electron transfer rate constant k_{ET} is expressed by eq 1-63.

$$k_{ET} = \left(\frac{4\pi^3}{h^2 \lambda k_B T}\right)^{1/2} V^2 \exp\left[-\frac{(\Delta G_{ET}^o + \lambda)^2}{4\lambda k_B T}\right] \qquad (1\text{-}63)$$

where V is the electronic coupling, ΔG_{ET}^o is the free energy gap between the equilibrium nuclear configuration of the products and the reactants, λ is the total reorganization energy, h is Planck's constant, and k_{B} is Boltzmann's constant, T is the absolute temperature. As the free energy change becomes more positive, the electron transfer rate will increase (normal region) until it reaches a maximum point where - $\Delta G_{ET}^o = \lambda$ (top region). However, as the free energy change becomes more positive, the electron transfer rate will decrease (inverted region).

In photosynthetic electron transfer, the λ-value is optimized for each electron transfer process. Also, the primary ET processes in photosynthesis are all characterized by small reorganization energies.[90] To achieve small reorganization energies, it is highly desirable for the construction of artificial photosynthetic systems to employ donor-acceptor couples that possess structures to promote electron delocalization, or whose net effect is to lower the vibrational and solvent reorganization energies. The electron deficient fullerene (C_{60}) possesses a small value of λ_t and can store up to six electrons. The small reorganization energy and enhanced electron reservoir properties have made C_{60} one of the most widely used acceptors. In addition, the first reduction potential of C_{60} is similar to that of benzoquinones (E^o = -0.73 V), which are typical electron acceptors in both natural and artificial photosynthetic systems. Therefore, porphyrin-fullerene-linked systems are likely to be suitable for constructing artificial photosynthetic systems. One of the first porphyrin-linked C_{60} systems was reported by Gust and co-workers.[91] Since then, many examples of dyads consisting of fullerenes linked to porphyrins or phthalocyanines have been prepared.[92-97] The forward electron transfer and the charge recombination between porphyrin-quinone dyad and porphyrin-fullerene dyad have been investigated. It was found that the forward electron transfer rate of porphyrin- fullerene system is larger than that of porphyrin-quinone system, whereas the charge-recombination rate is the reverse.[98] The qualitative explanation is proposed that the planar porphyrin and the spherical fullerene's delocalized π-electron systems with their rigid structures and high symmetries and intrinsic small reorganization energies would stabilize the charge separation state. Given the structure and energetics, the charge separated state would not be sensitive to changes of surrounding solvents or environments. The smaller reorganization energies of porphyrin-fullerene systems than that of porphyrin-quinone systems are quite similar to λ_o in the photosynthetic reaction center, where the diminished λ_o is attributed to the environmental effect of the surrounding protein residues.[1,2] Because porphyrin-fullerene systems undergo photoinduced electron transfer in condensed phase media, no protein framework is required. Using porphyrin and C_{60} as modules for photosynthetic applications has been extensively investigated.[99-101] Some examples are shown in Figure 1-18. Example D has also demonstrated that a subtle change

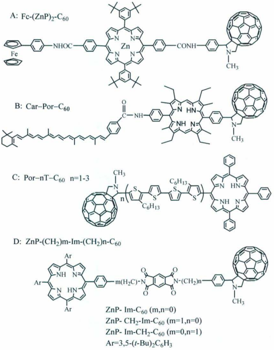
A: Fc-(ZnP)2-C60
Fe
NHOC
Zn
N
CONH
N
CH3
B: Car–Por–C60
O
C–NH
N HN
NH N
N
CH3
C: Por–nT–C60 n=1-3
CH3
N
n
S
C6H13
S
S
C6H13
N HN
NH N
D: ZnP-(CH2)m-Im-(CH2)n-C60
Ar
NH N
N HN
Ar
Ar
m(H2C)-N
O
O
O
O
N-(CH2)n
N
CH3
ZnP- Im-C60 (m,n=0)
ZnP- CH2-Im-C60 (m=1,n=0)
ZnP- Im-CH2-C60 (m=0,n=1)
Ar=3,5-(t-Bu)2C6H3

Figure 1-18. Porphyrin-fullerene linked systems.

---

[1] Conformational changes in proteins are often slower than ET under these conditions. The Born equation is no longer valid.

[2] Note that in proteins, electric fields exist and will alter the mechanism of ET, *i.e.* PSII, and protein helius.

in the number of monomeric linkage between donor and acceptor moieties causes a drastic switch between the sequential and superexchange mediated charge recombination (CR) as well as the modulation of the charge separation (CS) process.[102]

In order to further prolong the lifetime of the final charge separated state, tetrads, pentads, and hexads containing porphyrin and C_{60} have been designed (Figure 1-19).[103-106]

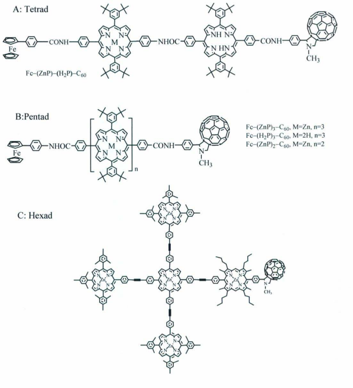
A: Tetrad
Fe
CONH
M
NHOC
NH
HN
CONH
N
CH3
Fc–(ZnP)–(H2P)–C60
B:Pentad
Fe
NHOC
M
n
CONH
N
CH3
Fc–(ZnP)3–C60, M=Zn, n=3
Fc–(H2P)3–C60, M=2H, n=3
Fc–(ZnP)2–C60, M=Zn, n=2
C: Hexad
Zn
N
CH3

Figure 1-19. Tetrads, pentads, hexads containing porphyrin-fullerene.

The lifetime of the resulting charge-separated state (*i.e.* $Fc^{+\cdot}$-ZnP-H_2P-$C_{60}^{\cdot-}$) in frozen benzonitrile is determined as 0.38 s, which is more than one order of magnitude longer than any other intramolecular charge recombination processes of synthetic systems, and is comparable to that observed for the bacterial photosynthetic reaction center.[90]

1.5.2 Coupling Single-Photon Charge Separation with Multielectron Redox Processes

Light harvesting systems and light-induced charge separation in molecular assemblies have been widely investigated for artificial photosynthesis. Significant progress has been made in the fundamental understanding of electron and energy transfer and in stabilizing charge separation by multi-step electron transfer. However, the challenging problem is probably the coupling photoinduced charge separation of a single-electron process with catalytic water splitting and hydrogen production that is a four-electron process; thus, there is a need for structures that facilitate accumulative electron transfer on molecular components. Currently, these simpler analogues of the photosystem reaction center lack the multi-electron process required for water splitting, but it may be possible to include this multi-electron process in the reaction center as a multi-component architecture.

Water oxidation at the Mn_4Ca cluster in the photosynthetic reaction center is a multiple-site coupled electron proton transfer (MS-EPT) reaction in which accumulation of oxidizing equivalents on the Mn_4Ca cluster is coupled to the release of protons.[107,108] Therefore, the increase in oxidation state does not lead to an increase in charge, except probably at the transition from state S_1 to S_2 (Figure 1-20).[109] In this respect, multinuclear ruthenium complexes first prepared by Peterson and extensively studied by Balzani have

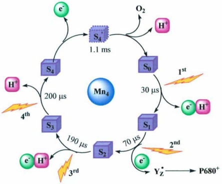

Figure 1-20. In photosynthetic oxygen generation, photons move in PSII through five successive oxidation states.

received the most attention until 1994 when Brewer and coworkers demonstrated that such complexes could store more than one photo-excited electron and therefore potentially participate in multi-electron transfer (MET) reactions.[22,36,110-112] In 2002, Konduri et al. reported that the ruthenium(II) dimers (Figure 1-21 A) undergo up to 2 or 4 sequential photo-reductions when irradiated with visible light in the presence of sacrificial reducing agents, such as TEA or TEOA in MeCN.[112] Manganese clusters covalently linked to a ruthenium trisbipyridyl sensitizer and naphthalenediimide electron acceptor (Figure 1-21B) have proved to be valuable synthetic models to perform multistep electron transfer and may ultimately lead to viable artificial systems for water oxidation.[113-115] In the long term, replacement of the ruthenium core by a more available metal or an organic chromophore will probably be pursued.

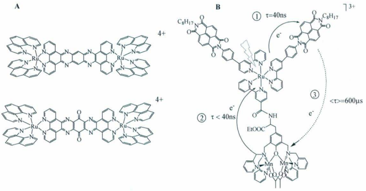

Figure 1-21. Structure of multinuclear ruthenium and manganese complexes.

1.5.3 Coupled Light-Harvesting and Reaction Centre Complex

The conversion of light to chemical energy involves two basic photochemical processes. Light harvesting chromophoric assemblies absorb a large portion of solar spectrum, and then the collected energy is directed to the reaction center via vectorial energy transfer/migration, ultimately sensitizing the special pair and concomitant formation of an exciton. Natural photosynthesis relies on noncovalent interactions for assembling chromophores at specific distances and orientations to regulate energy and electron flow, providing particular photophysical or redox functions. However, most artificial antenna ensembles and reaction centers employ chemically distinct, covalently linked supramolecular scaffold to organize chromophores and redox cofactors for optimizing light-harvesting efficiency and electron or energy transfer rates, which is satisfied by the protein framework in natural photosynthetic systems.[116-118]

Assemblies Based on Sequential Covalent Bond Formation. Some elegant assemblies have been constructed from derivatized porphyrins and organics to couple light-harvesting and charge separation in a single molecule for producing a long-lived charge-separated state for photoexcitation in a wide wavelength range shown in Figure 1-22.[117,119-121] For molecular assembly A, five bis-(phenylethynyl)anthracene (BPEA) antennas surround a central hexaphenylbenzene core bearing a porphyrin-fullerene electron donor-acceptor unit. The BPEA antenna chromophore absorbs intensively in the 430 to 475 nm region, where carotenoid polyenes in natural systems often serve as antenna chromophores and harvest light in this spectral region.[122] Porphyrin-fullerene systems have been shown to efficiently carry out photoinduced electron transfer to yield long-lived charge-separated states.

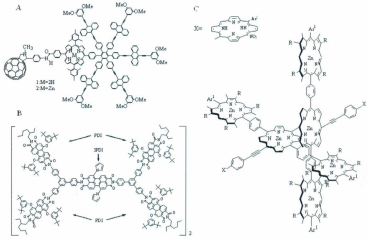

Figure 1-22. Coupled light harvesting and charge separation assemblies.

Assembly B is a cofacially stacked dimer which can efficiently capture energy due to the broad spectral coverage, enhance energy funneling to the core unit (5PDI) which is sensitized, and this results in ultrafast charge separation. This demonstrates that placing two identical core units next to one another to form a special pair structure mimics the primary events occurring in the photosynthetic reaction center, and represents a significant contribution to the design criteria of an artificial reaction center.[121]

In molecular assembly C, three-dimensionally arranged orthogonal geometry, is favorable for the large cross section of the incident light.[123,124] The direct meso-meso connection in the diporphyrin core results in a remarkable enhancement in the intramolecular energy transfer due to optical alignment of the transition dipole of the donor and acceptor, and thus enables an efficient energy transfer from the peripheral porphyrins to the diporphyrin core. The resulting excited state $^1D^*$ (diporphyrin core) donates an electron to the electron acceptor to generate an energetic charge-separated state, which result in a secondary charge-separated state by hole transfer from the diporphyrin core to the peripheral porphyrin monomer.[58]

Derivatization of Preformed Polymers. Incorporating the minimum set of components required for artificial photosynthesis into a preformed polymer is another strategy for assembling artificial photosynthesis. There is a massive background literature for preparing polystyrene samples, which offers considerable synthetic flexibility with regard to linkage chemistry based on known reactions of added functional groups. A derivatized polystyrene assembly with an appended $[Ru(bpy)_3]^{2+}$-typed unit has been used to mimic the antenna-chromophore-electron transfer sequence of photosynthesis (Figure

1-23).[125] Following MLCT excitation by visible laser flash photolysis, the polymer-bound PTZ$^{\cdot+}$–MV$^{\cdot+}$ redox-separated (RS) state was formed with a significant contribution from excitation at antenna sites not adjacent to RC followed by migration and sensitization. In the overall reaction, the 2.13 eV of excited state energy collected in the antenna fragment is transferred to a reaction center where it is converted into a 1.15eV of stored redox energy. The overall efficiency is 12–18% depending on irradiation, and the lifetime of the charge-separated state that is 160 ns. At high intensity of irradiation, multi-photon excitation and excited state annihilation compete with sensitized electron transfer. Also, an additional long-lived transient with low efficiency (0.5%) was observed and attributed to polymers in which PTZ$^{\cdot+}$ and MV$^{\cdot+}$ were formed on spatially separated RC sites. This suggests that photochemically generated redox equivalents can be created and stored on the polymers for extended periods.[126]

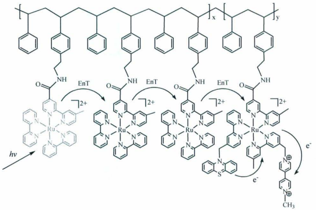

Figure 1-13. Polystyrene derivatized antenna-chromophore-electron transfer assembly.

1.6 Defining the Problem and the Organization of Thesis

1. Understand the role of electronic and vibronic processes that govern excited state decay in π-conjugated OPV/OPE assemblies.
2. Determine how the orientation of the main OPV chromophore (linear *vs.* cruciform) influences electronic coupling between the OPV electron donor and C_{60} acceptor.
3. The orientation effect on intersystem crossing of π-conjugated OPV/OPE chromophores.
4. Application of Franck-Condon line shape analysis to extract vibrational and solvent reorganization energetics.
5. Understand the role of solvent in the photoinduced energy and electron transfer process in OPV/OPE oligomers. Is dielectric continuum theory sufficient to model the kinetics *i.e.* using dipole in a sphere or dipole in ellipsoidal solvent cavities.
6. Examine the competition between energy transfer and electron transfer.

1.7 References

(1) *Report of the Basic Energy science Workshop on Solar Energy Utilization* **April 18-21, 2005**.

(2) Winter, C. J.; Sizmann, R. L.(Eds.), L. L. V.-H. *Solar Power Plants*; Springer-Verlag, 1991.

(3) Becquerel, E. *Comptes Rendus* **1839**, *9*, 561-567.

(4) Chapin, D. M.; Fuller, C. S.; Pearson, G. L. *J. App. Phys.* **1954**, *25*, 676-677.

(5) Hoppe, H.; Sariciftci, N. S.; Meissner, D. *Mol. Cryst. Liq. Cryst.* **2002**, *385*,113-119.

(6) Hoppe, H.; Sariciftci, N. S. *J. Mater. Chem.* **2006**, *16*, 45-61.

(7) Tang, C. W. *Appl. Phys. Lett.* **1986**, *48*, 183-185.

(8) Yu, G.; Gao, J.; Hummelen, J. C.; Wudl, F.; Heeger, A. J. *Science* **1995**, *270*, 1789-1791.

(9) Brabec, C. J. *Sol. Energy Mater. Sol. Cells* **2004**, *83*, 273-292.

(10) Wienk, M. M. *Angew. Chem. Int. Ed. Engl.* **2003**, *42*, 3371-3375.

(11) Peumans, P.; Forrest, S. R. *Appl. Phys. Lett.* **2001**, *79*, 126-128.

(12) Grätzel, M. *Inorg. Chem.* **2005**, *44*, 6841-6851.

(13) Thompson, B. C.; Fréchet, J. M. J. *Angew. Chem. Int. Ed. Engl.* **2008**, *47*, 58-77.

(14) Kim, J. Y.; Lee, K.; Coates, N. E.; Moses, D.; Nguyen, T.-Q.; Dante, M.; Heeger, A. J. *Science* **2007**, *317*, 222-225.

(15) Dharmadasa, I. M. *Sol. Energy Mater. and Sol. Cells* **2005**, *85*, 293-300.

(16) Nguyen, L. H.; Erb, H. H. T.; Günes, S.; Gobsch, G.; Sariciftci, N. S. *Adv. Funct. Mater.* **2007**, *17*, 1071-1078.

(17) Gunes, S.; Neugebauer, H.; Sariciftci, N. S. *Chem. Rev.* **2007**, *107*, 1324-1338.

(18) Singh, T. B.; Sariciftci, N. S. *Annu. Rev. Mater. Res.* **2006**, *36*, 199-230.

(19) Koeppe, R.; Bossart, O.; Calzaferri, G.; Sariciftci, N. S. *Sol. Energy Mater. and Sol. Cells* **2007**, *91*, 986-995.

(20) Kamat, P. V. *J. Phys. Chem. C* **2007**, *111*, 2834-2860.

(21) Hervás, M.; Navarro, J. A.; Rosa, M. A. D. l. *Acc. Chem. Res.* **2003**, *36*, 798-805.

(22) Meyer, T. J. *Acc. Chem. Res.* **1989**, *22*, 163-170.

(23) Libby, W. F. *J. Phys. Chem.* **1952**, *56*, 863-868.

(24) Marcus, R. A. *Annu. Rev. Phys. Chem.* **1964**, *15*, 155-196.

(25) Marcus, R. A. *Reviews of Modern Physics* **1993**, *65*, 599-610.

(26) Marcus, R. A. *J. Electroanal.Chem.* **1997**, *438*, 251-259.

(27) Sutin, N. *Annu. Rev. Phys. Chem.* **1966**, *17*, 119-172.

(28) Miller, J. R.; Calcaterra, L. T.; Closs, G. L. *J. Am. Chem. Soc.* **1984**, *106*, 3047-3049.

(29) Hopfield, J. J. *Proc. Natl. Acad. Sci. USA* **1974**, *71*, 3640-3644.

(30) Kubo, R.; Toyozawa, Y. *Prog. Theor. Phys.* **1955**, *13*, 160-182.

(31) Holstein, T. *Annals of Physics* **1959**, *8*, 343-389.

(32) Beswick, J. A.; Jortner, J. *Chem. Phys. Lett.* **1979**, *65*, 240-245.

(33) Kestner, N. R.; Logan, J.; Jortner, J. *J. Phys. Chem.* **1974**, *78*, 2148-2166.

(34) Bixon, M.Jortner, J. *J. Phys. Chem.* **1991**, *95*, 1941-1944.

(35) Jortner, J. *J. Chem. Phys.* **1976**, *64*, 4860-4867.

(36) Alstrum-Acevedo, J. H.; Brennaman, M. K.; Meyer, T. J. *Inorg. Chem.* **2005**, *44*, 6802-6827.

(37) Henderson, P. T.; Jones, D.; Hampikian, G.; Kan, Y.; Schuster, G. B. *Proc. Natl. Acad. Sci. USA* **1999**, *96*, 8353-8358.

(38) Lu, H. P.Xie, X. S. *J. Phys. Chem. B* **1997**, *101*, 2753-2757.

(39) Gould, I. R.; Young, R. H.; Mueller, L. J.; Albrecht, A. C.; Farid, S. *J. Am. Chem. Soc.* **1994**, *116*, 8188-8199.

(40) Yersin, H.; Otto, H.; Zink, J. I.;Gliemann, G. *J. Am. Chem. Soc.* **1980**, *102*, 951-955.

(41) Matyushov, D. V.; Ladanyi, B. M. *J. Phys. Chem. A* **1998**, *102*, 5027-5039.

(42) Strickler, S. J.; Berg, R. A. *J. .Chem. Phys.* **1962**, *37*, 814-822.

(43) Hirayama, S.Phillips, D. *J. Photochem.* **1980**, *12*, 139-145.

(44) Knoester, J.; Mukamel, S. *Phys. Rev. A* **1989**, *40*, 7065-7080.

(45) Strickler, S. J.; Berg, R. A. *J. Chem. Phys.* **1962**, *37*, 814-822.

(46) Kober, E. M.; Caspar, J. V.; Lumpkin, R. S.; Meyer, T. J. *J. Phys. Chem.* **1986**, *90*, 3722-3734.

(47) Chen, P.; Meyer, T. J. *Chem. Rev.* **1998**, *98*, 1439-1478.

(48) Braslavsky, S. E. *Divisin of Organic and Biomolecular Chemistry Glossary of terms used in photochemistry, 3rd Edition*, 2006.

(49) Lewis, F. D.; Zhu, H.; Daublain, P.; Fiebig, T.; Raytchev, M.; Wang, Q.; Shafirovich, V. *J. Am. Chem. Soc.* **2006**, *128*, 791-800.

(50) Sim, E. *J. Phys. Chem. B* **2005**, *109*, 11829-11835.

(51) Barbara, P. F.; Meyer, T. J.; Ratner, M. A. *J. Phys. Chem.* **1996**, *100*, 13148-13168.

(52) Rips, I.; Jortner, J. *J. Chem. Phys.* **1987**, *87*, 2090-2104.

(53) Paddon-Row, M. N. *Electron transfer in Chemistry*; 1 ed.; WILEY-VCH, 2001; Vol. 3.

(54) Paddon-Row, M. N. *Acc. Chem. Res.* **1982**, *15*, 245-251.

(55) Hoffmann, R. *Acc. Chem. Res.* **1971**, *4*, 1-9.

(56) Paddon-Row, M. N.; Jordan, K. D. *Modern Models of Bonding and delocalization*; VCH Publisher, New York, 1988; Vol. 6.

(57) Lakowicz, J. R. *Principles of Fluorescence Spectroscopy*; Plenum Press: New York, 1983.

(58) Turro, N. J. *Modern Molecular Photochemistry*; University Science Books: Mill Valley, CA., 1991.

(59) Jortner, J.; Ben-Reuven, A. *Chem. Phys. Lett.* **1976**, *41*, 401-406.

(60) Ulstrup, J.; Jortner, J. *J. Chem. Phys.* **1975**, *63*, 4358-4368.

(61) Dexter, D. L. *J. Chem. Phys.* **1953**, *21*, 836-850.

(62) Bixon, M.; Jortner, J.; Cortes, J.; Heitele, H.; Michel-Beyerle, M. E. *J. Phys. Chem.* **1994**, *98*, 7289-7299.

(63) Speiser, S. *Chem. Rev.* **1996**, *96*, 1953-1976.

(64) Dexter, D. L. *J. Chem. Phys.* **1953**, *21*, 836-850.

(65) Ciamician, G. *Science* **1912**, *36*, 385-394.

(66) Gust, D.; Moore, T. A.; Moore, A. L.; Krasnovsky, A. A.; Liddell, P. A.; Nicodem, D.; DeGraziano, J. M.; Kerrigan, P.; Makings, L. R.; Pessiki, P. J. *J. Am. Chem. Soc.* **1993**, *115*, 5684-5691.

(67) Steinberg-Yfrach, G.; Liddell, P. A.; Huang, S.-c.; Moore, A. L.; Gust, D.; Moore, T. A. *Nature* **1997**, *385*, 239-241.

(68) Wasielewski, M. R.; Liddell, P. A.; Barrett, D.; Moore, T. A.; Gust, D. *Nature* **1986**, *322*, 570-572.

(69) Zouni, A.; Witt, H.-T.; Kern, J.; Fromme, P.; Krau, N.; Saenger, W.; Orth, P. *Nature* **2001**, 739-743.

(70) Ferreira, K. N.; Iverson, T. M.; Maghlaoui, K.; Barber, J.; Iwata, S. *Science* **2004**, *303*, 1831-1838.

(71) Kamiya, N.Shen, J. R. *Proc. Natl Acad. Sci. USA* **2003**, *100*, 98-103.

(72) Loll, B.; Kern, J.; Saenger, W.; Zouni, A.; Biesiadka, J. **2005**, *438*, 1040-1044.

(73) Szacilowski, K.; Macyk, W.; Drzewiecka-Matuszek, A.; Brindell, M.; Stochel, G. *Chem. Rev.* **2005**, *105*, 2647-2694.

(74) Gust, D.; Moore, T. A.; Moore, A. *Acc. Chem. Res.* **2001**, *34*, 40-48.

(75) Feher, G.; Allen, J. P.; Okamura, M. Y.; Rees, D. C. *Nature* **1989**, *339*, 111-116.

(76) Huber, R. *Angew. Chem., Int. Ed. Engl.* **1989**, *28*, 848-869.

(77) Johnson, S. G.; Small, G. J.; Johnson, D. G.; Svec, W. A.; Wasielewski, M. R. *J. Phys. Chem.* **1989**, *93*, 5437-5444.

(78) Danielson, E.; Elliott, M.; Merkert, J. W.; Meyer, T. J. *J. Am. Chem. Soc.* **1987**, *109*, 2519-2520.

(79) Treadway, J. A.; Chen, P.; Rutherford, T. J.; Keene, F. R.; Meyer, T. J. *J. Phys. Chem. A* **1997**, *101*, 6824-6826.

(80) Migita, M.; Okada, T.; Mataga, N.; Nishitani, S.; Kurata, N.; Sakata, Y.; Misumi, S. *Chem. Phys. Lett.* **1981**, *84*, 263.

(81) Nishitani, S.; Kurata, N.; Sakata, Y.; Misum, S.; Karen, A.; Okada, T.; Mataga, N. *J. Am. Chem. Soc.* **1983**, *105*, 7771-7772.

(82) Gust, D.; Moore, T. A.; Moore, A. L.; Makings, L. R.; Seely, G. R.; Ma, X.; Trier, T. T.; Gao, F. *J. Am. Chem. Soc.* **1988**, *110*, 7567-7569.

(83) Gust, D.; Mathis, P.; Moore, A. L.; Liddell, P. A.; Nemeth, G. A.; Lehman, W. R.; Moore, T. A.; Bensasson, R. V.; Land, E. J.; Chachaty, C. *Photochem. Photobiol.* **1982**, *36*, 641-645.

(84) Gust, D.; Moore, T. A.; Makings, L. R.; Liddell, P. A.; Nemeth, G. A.; Moore, A. L. *J. Am. Chem. Soc.* **1986**, *108*, 8028-8031.

(85) Gust, D.; Moore, T. A.; Liddell, P. A.; Nemeth, G. A.; Makings, L. R.; Moore, A. L.; Barrett, D.; Pessiki, P. J.; Bensasson, R. V. *J. Am. Chem. Soc.* **1987**, *109*, 846-856.

(86) Wasielewski, M. R.; Niemczyk, M. P.; Svec, W. A.; Pewitt, E. B. *J. Am. Chem. Soc.* **1985**, *107*, 5662-5563.

(87) Gust, D.; Moore, T. A.; Moore, A. L.; Gao, F.; Luttrull, D.; DeGraziano, J. M.; Ma, X. C.; Makings, L. R.; Lee, S. J. *J. Am. Chem. Soc.* **1991**, *113*, 3638-3649.

(88) Wasielewski, M. R. *Chem. Rev.* **1992**, *92*, 435-461.

(89) Marcus, R. A.; Sutin, N. *Biochimica et Biophysica Acta (BBA) - Reviews on Bioenergetics* **1985**, *811*, 265-322.

(90) Deisenhofer, J.; Norris, J. R. *The Photosynthetic reaction center*; San Diego, CA ; Toronto : Academic Press, 1993.

(91) Liddell, P. A.; Sumida, J. P.; N., M. A.; Noss, L.; Seely, G. R.; Clark, K. N.; Moore, A. L.; Moore, T. A.; Gust, D. *Photochem. Photobiol.* **1994**, *60*, 537-541.

(92) Kuciauskas, D.; Lin, S.; Seely, G. R.; Moore, A. L.; Moore, T. A.; Gust, D.; Drovetskaya, T.; Reed, C. A.; Boyd, P. D. W. *J. Phys. Chem.* **1996**, *100*, 15926-15932.

(93) Imahori, H.; Hagiwara, K.; Aoki, M.; Akiyama, T.; Taniguchi, S.; Okada, T.; Shirakawa, M.; Sakata, Y. *J. Am. Chem. Soc.* **1996**, *118*, 11771-11782.

(94) Imahori, H.; Hagiwara, K.; Akiyama, T.; Taniguchi, S.; Okada, T.; Sakata, Y. *Chem. Lett.* **1995**, *24*, 265-266.

(95) Williams, R. M.; Zwier, J. M.; Verhoeven, J. W. *J. Am. Chem. Soc.* **1995**, *117*, 4093-4099.

(96) Williams, R. M.; Koeberg, M.; Lawson, J. M.; An, Y.-Z.; Rubin, Y.; Paddon-Row, M. N.; Verhoeven, J. W. *J. Org. Chem.* **1996**, *61*, 5055-5062.

(97) Maggini, M.; Dono, A.; Scorrano, G.; Prato, M. *J. Chem. Soc., Chem. Commun.* **1995**, 843-845.

(98) Imahori, H.; Hagiwara, K.; Aoki, M.; Akiyama, T.; Taniguchi, S.; Okada, T.; Shirakawa, M.; Sakata, Y. *Chem. Phys. Lett.* **1996**, *263*, 545-550.

(99) Imahori, H.; Tamaki, K.; Araki, Y.; Sekiguchi, Y.; Ito, O.; Sakata, Y.; Fukuzumi, S. *J. Am. Chem. Soc.* **2002**, *124*, 5165-5174.

(100) Ikemoto, J.; Takimiya, K.; Aso, Y.; Otsubo, T.; Fujitsuka, M.; Ito, O. *Org. Lett.* **2002**, *4*, 309-311.

(101) Liddell, P. A.; Kuciauskas, D.; Sumida, J. P.; Nash, B.; Nguyen, D.; Moore, A. L.; Moore, T. A.; Gust, D. *J. Am. Chem. Soc.* **1997**, *119*, 1400-1405.

(102) Imahori, H.; Tamaki, K.; Araki, Y.; Hasobe, T.; Ito, O.; Shimomura, A.; Kundu, S.; Okada, T.; Sakata, Y.; Fukuzumi, S. *J. Phys. Chem. A* **2002**, *106*, 2803-2814.

(103) Imahori, H.; Tamaki, K.; Araki, Y.; Sekiguchi, Y.; Ito, O.; Sakata, Y.; Fukuzumi, S. *J. Am. Chem. Soc.* **2002**, *124*, 5165-5174.

(104) Imahori, H.; Guldi, D. M.; Tamaki, K.; Yoshida, Y.; Luo, C.; Sakata, Y.; Fukuzumi, S. *J. Am. Chem. Soc.* **2001**, *123*, 6617-6628.

(105) Kuciauskas, D.; Liddell, P. A.; Lin, S.; Johnson, T. E.; Weghorn, S. J.; Lindsey, J. S.; Moore, A. L.; Moore, T. A.; Gust, D. *J. Am. Chem. Soc.* **1999**, *121*, 8604-8614.

(106) Imahori, H.; Kashiwagi,Y.; Yukiyasu. S.; Sato, T.; Araki, Y.; Ito, O.; Yamada, H.; Fukuzumi, H.; *Chem. Eur. J.* **2004**, *10*, 3184-3196.

(107) Meyer, T. J.; Huynh, M. H. V.; Thorp, H. H. *Angew. Chem. Int. Ed.* **2007**, *46*, 5284-5304.

(108) Irebo, T.; Reece, S. Y.; Sjodin, M.; Nocera, D. G.; Hammarstrom, L. *J. Am. Chem. Soc.* **2007**, *129*, 15462-15464.

(109) Haumann, M.; Liebisch, P.; Muller, C.; Barra, M.; Grabolle, M.; Dau, H. *Science* **2005**, *310*, 1019-1021.

(110) Wouters, K.; de Tacconi, N.; Konduri, R.; Lezna, R.; MacDonnell, F. *Photosynthesis Research* **2006**, *87*, 41-55.

(111) Molnar, S. M.; Nallas, G.; Bridgewater, J. S.; Brewer, K. J. *J. Am. Chem. Soc.* **1994**, *116*, 5206-5210.

(112) Konduri, R.; Ye, H.; MacDonnell, F. M.; Serroni, S.; Campagna, S.; Rajeshwar, K. *Angew. Chem. Int. Ed.* **2002**, *41*, 3185-3187.

(113) Hammarstrom, L.; Sun, L.; Åkermark, B.Styring, S. *Spectrochimica Acta Part A: Mol. and Biomol. Spectroscopy* **2001**, *57*, 2145-2160.

(114) Borgstrom, M.; Shaikh, N.; Johansson, O.; Anderlund, M. F.; Styring, S.; Akermark, B.; Magnuson, A.; Hammarstrom, L. *J. Am. Chem. Soc.* **2005**, *127*, 17504-17515.

(115) Hammarström, L. *Current Opinion in Chemical Biology* **2003**, *7*, 666-673.

(116) Soto, E.; MacDonald, J. C.; Cooper, C. G. F.; McGimpsey, W. G. *J. Am. Chem. Soc.* **2003**, *125*, 2838-2839.

(117) Rybtchinski, B.; Sinks, L. E.; Wasielewski, M. R. *J. Am. Chem. Soc.* **2004**, *126*, 12268-12269.

(118) Alstrum-Acevedo, J. H.; Brennaman, M. K.; Meyer, T. J. *Inorg. Chem.* **2005**, *44*, 6802-6827.

(119) Nakano, A. O.; Yamazaki, A.; Nishimura, Y.; Akimoto, S.; Yamazaki, I.; Itaya, A.; Murakami, M.; Miyasaka, H. *Chem. Eur. J.* **2001**, *7*, 3134-3151.

(120) Kodis, G.; Terazono, Y.; Liddell, P. A.; Andreasson, J.; Garg, V.; Hambourger, M.; Moore, T. A.; Moore, A. L.; Gust, D. *J. Am. Chem. Soc.* **2006**, *128*, 1818-1827.

(121) Wasielewski, M. R. *J. Org. Chem.* **2006**, *71*, 5051-5066.

(122) Goodwin, T. W. In *Biochemistry of the Carotenoids*; Chapman & Hall: New York, 1980.

(123) Nakano, A.; Nishimura, Y.; Yamazaki, I.; Osuka, A. *Chem. Eur. J.* **2000**, *6*, 3254-3271.

(124) Nakano, A.; Yamazaki, I.; Yamazaki, T.; Nishimura, Y. *Angew. Chem. Int. Ed.* **1998**, *37*, 3023-3027.

(125) Huynh, M. H. V.; Dattelbauma, D. M.; Meyer, T. J. *Coord. Chem. Rev.* **2005**, *249*, 457- 483.

(126) Sykora, M.; Maxwell, K. A.; DeSimone, J. M.; Meyer, T. J. *Proc. Natl. Acad. Sci. USA* **2000**, *97*, 7687-7691.

Chapter 2

Experiment and Experimental Methodology

2.1 Conceptual Background........67

- 2.1.1 Formation of Excited State........67
- 2.1.2 Excited State Decay........68
- 2.1.3 Bimolecular Photophysical Processes........70

2.2 Materials and Solvents........71

2.3 Ground State Measurements and Gaussian Deconvolution........72

- 2.3.1 Introduction........72
- 2.3.2 Optical System of Spectroscopy and Data Acquisition........73
- 2.3.3 Gaussian Deconvolution........74

2.4 Excited State Measurements........75

- 2.4.1 Introduction........75
- 2.4.2 Optical System of Fluorometer and Data Acquisition........76
- 2.4.3 Data Analysis: Emission Spectral Fitting........77

2.5 The Time-Resolved Fluorescence........82

- 2.5.1 Introduction........82
- 2.5.2 Experimental Set-up and Data Acquisition........84
- 2.5.3 Time-Resolved Data Analysis........84

2.6 Transient Absorption Spectroscopy......89

2.6.1 Introduction......89

2.6.2 Theoretical background......90

2.6.3 Experimental Set-up and Data Acquisition......94

2.6.4 Kinetic Data Analysis......97

2.7 Global Kinetic Analysis......99

2.7.1 Introduction......99

2.7.2 Theory of nonlinear least-squares fitting of Multivariate Absorption Data......100

2.7.3 Error Estimates and Correlation Coefficients......105

2.8 References......107

2.1 Conceptual Background

2.1.1 Formation of Excited State

The transfer of an electron from a donor orbital to an acceptor orbital may be initiated by absorption of photon with suitable energy v, eq 2-1. The sensitizer *S* captures a photon creating an excited state S^*.

$$S_0 + hv \longrightarrow S^* \qquad (2\text{-}1)$$

whose physical and chemical properties are distinct from the ground state due to the increased content of the excited state. The processes that deactivate the excited state and the theoretical understanding of these dynamics are properties of the molecular assemblies, which were introduced and discussed in Chapter 1. This chapter is focused on the experimental techniques, methodologies and the IUPAC terminology that describe the fate of the molecular excited state once formed. The discussion will be framed using the general form of chromophore substrate (*S*).

A molecule only absorbs light to bring about a single electronic transition, and the energy of the light must match the energy difference between the ground state and the excited state. This is termed as Stark-Einstein law. The transition from one state to another is governed by an operator and must obey certain symmetry restrictions. Excitation leads to the formation of a Franck-Condon excited state which possesses the nuclear and solvent coordinates of the ground state, but the electronic structure of the excited state because electron motion is ultrafast (10^{-15} s) when compared to nuclear motion ($10^{-12\pm1}$ s) and solvent liberation ($10^{-11\pm1}$ s). The intensity of electronic transitions depends on the square of the transition moment, which is related to the overlap of vibrational wavefunctions of ground and excited states, within the confines of the Franck-Condon approximation. A Jablonski diagram or state energy diagram for a generic chromophore substrate (*S*) is shown in Figure 2-1. The Jablonski diagram illustrates the energetic difference between the singlet and triplet states respectively. The stabilization energy between the singlet and triplet states is driven by the need to minimize the electron-electron repulsion and energy required to spin pair electrons in the excited state.

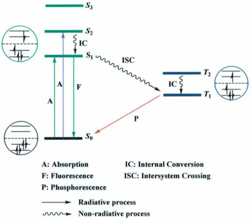
S_3
S_2
IC
S_1
ISC
T_2
IC
T_1
A
A
F
P
S_0
A: Absorption
IC: Internal Conversion
F: Fluorescence
ISC: Intersystem Crossing
P: Phosphorescence
Radiative process
Non-radiative process

Figure 2-1. Jablonski diagram.

2.1.2 Excited State Decay

Irrespective of the nature of the specific system, S^* and S are different species. S^* is more energetic and has the possibility to exhibit a greatly different pattern of reactivity because of its unique electronic configuration. With very few exceptions, all photo- chemistry and photophysics are initiated from the lowest excited states, S_1 and T_1.

Conversion of S_1 to S_0 with emission of a photon is termed as fluorescence. The possible pathways for excited state decay are given by:

$$S_1 \xrightarrow{k_r} S_0 + h\nu \qquad (2\text{-}2)$$

$$S_1 \xrightarrow{k_{nr}} S_0 + heat \qquad (2\text{-}3)$$

$$S_1 \xrightarrow{k_{rx}} product \qquad (2\text{-}4)$$

The fluorescence quantum yield gives the efficiency of the fluorescence process, given by:

$$\phi_F = \frac{k_r}{k_r + \sum k_{nr} + k_{rx}} \qquad (2\text{-}5)$$

and the lifetime for fluorescence refers to the average time the molecule stays in its excited state before emitting a photon.

Non-radiative decays include collisions with surrounding media, internal conversion, and intersystem crossing in which a molecule in a specific spin state and vibronic state has a transition to a new vibronic state in a different spin state with lower energy due to the spin-orbit coupling. Following the intersystem crossing process, non-radiative vibrational relaxation continues to leave the molecule trapped in its lowest excited triplet state before a weak radiative transition returns it to the ground state singlet. The radiative transitions between two states of different spin multiplicity, defined as phosphorescence, *i.e.* $T_1 \rightarrow S_0$, is generally delayed relative to the exciting radiation, about 10^{-5}-10 s.

The quantum yield for intersystem crossing is given by:

$$\phi_{isc} = \frac{k_{isc}}{k_{isc} + \sum k_i} \qquad (2\text{-}6)$$

where ϕ_{isc} is quantum yield for intersystem crossing and k_i is the sum of all other processes which deactivate the excited state.

The phosphorescence quantum yield ϕ_{ph} is defined as:

$$\phi_{ph} = \phi_{isc}\frac{k_r}{k_r + k_{nr} + \sum k_i^{o'}} \qquad (2\text{-}7)$$

where k_{nr} is the rate constant for non-radiative decay, and $\sum k_i^{o'}$ is the sum of the rate constants which deactivate the triplet excited state. The emission spectrum may or may not be observed depending on the magnitude of ϕ_{isc}, k_r, k_{nr} and $\sum k_i$.

2.1.3 Bimolecular Photophysical Processes

Several processes can happen when a molecule in an excited state encounters another molecule in its ground state. These bimolecular photophysical processes provide further insight into the nature of the excited states.

Quenching: the most common outcome for a collision between an excited state molecule and another chromophoric or reactive molecule is *quenching*, which is the collision-induced radiationless relaxation of an excited state to its ground state. The treatment of these quenching processes is referred to as a *Stern-Volmer analysis*, expressed as:

$$S^* \xrightarrow{k_1} S \qquad (2\text{-}8)$$

The lifetime of S^* without Q is $\tau_1 = 1/k_1$

$$Q + S^* \xrightarrow{k_Q} S \qquad (2\text{-}9)$$

The lifetime of S^* with Q is τ_2

$$1/\tau_2 = k_1 + k_2[Q] = 1/\tau_1 + k_2[Q] \qquad (2\text{-}10)$$

Energy Transfer: Another outcome for the interaction of an excited state, S^*, with a molecule in its ground state, A, is energy transfer from S^* to A.

$$S^* + A \longrightarrow S + A^* \qquad (2\text{-}11)$$

Three different mechanisms are possible for this bimolecular photophysical process, as discussed in Chapter 1.

Photoinduced Electron Transfer: Another common process that can lead to quenching of fluorescence is photoinduced electron transfer. Because an excited state has an electron in its anti-bonding orbital, it is considered to be a good donor and easier to oxidize than its ground state. In addition, because there is a vacancy in the lower energy orbital from which the excited electron was removed, it is easier to reduce and thus a better acceptor than its ground state. Therefore, the excited state has both a lower oxidation and a lower reduction potential, and it can undergo electron transfers, accepting electrons from ground states that have a high HOMO and donating electron to ground states that have a lower LUMO.

2.2 Materials and Solvents

All compounds were available from other work. The detailed procedures have been reported or will be reported in subsequent manuscripts.[1,2] The purity of R-(π-B)$_n$-[OPV]$_{C/L}$-(π-B)$_n$-R (R=H, C_{60}) and their OPE/OPV oligomer precursors have been assessed by HPLC. All solvents used in spectroscopic measurements were reagent grade, and were used as supplied except where specified. Samples were prepared by the following method. The solvent absorption spectrum was obtained versus air to identify any absorbing impurities. The next step was to take the emission spectrum of the solvent using the same excitation wavelengths that will be used to obtain the emission spectrum of the sample. This allows detection of emitting impurities in the solvent. With these requisite experiments complete, any observed photo-luminescence is intrinsic to the sample that is added to the solvent. A further check of sample integrity was a comparison of the overlaid excitation spectrum and the absorption spectrum, which requires absorbance to be less than 0.2. All sample solutions were purged by using N_2 (99.9%) for 15-20 minutes to removing O_2 prior to making measurement. For $Ru(bpy)_3^{2+}$, a 10 min sparge was sufficient to remove O_2 as deduced from the lifetime and luminescence, which did not change after a 10 min purge.

2.3 Ground State Measurements and Gaussian Deconvolution

2.3.1 Introduction

After absorption of ultraviolet and/or visible radiation, electrons in molecular orbitals are promoted from the lowest energy ground state configuration and are redistributed in a higher energy excited state electronic configuration. In addition, the atoms can rotate and vibrate with respect to each other. These vibrations and rotations also have discrete energy levels, which can be considered as being packed on top of each electronic level. Therefore, the shape of an absorption band, its intensity, and the spectral width are the result of strong or weak coupling of electronic transitions with the vibrational subsystem of the medium. Possible electronic transitions are $\sigma \rightarrow \sigma^*$, $\pi \rightarrow \pi^*$, $n \rightarrow \pi^*$, $n \rightarrow \sigma^*$ and charge transfer absorption. Absorbance is defined as:

$$A = -\log\frac{I}{I_0} \qquad (2\text{-}12)$$

where I is the intensity of light at a specified wavelength λ that has passed through a sample (transmitted light intensity) and I_0 is the intensity of the light before it enters the sample or incident light intensity. The Beer's law states that absorbance is proportional to both the path length and concentration of the absorbing species, expressed as:

$$A = \varepsilon c l \qquad (2\text{-}13)$$

where ε is molar absorptivity which is a measurement of how strongly a chemical species absorbs light at a given wavelength, l the distance the light travels through the material, and c the concentration c of absorbing species in the material.

2.3.2 Optical System of Spectroscopy and General Protocol for Data Acquisition

Absorption spectra reported in this thesis were recorded in $CHCl_3$ or toluene solutions by using a 1.0 cm quartz cuvette supplied by Starna and an Agilent 8543 Diode Array spectrophotometer. Its optical system is shown in Figure 2-2. Spectra were analyzed by using ChemStation software provided by Agilent.

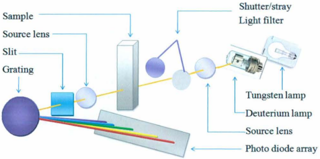
Sample
Source lens
Slit
Grating
Shutter/stray
Light filter
Tungsten lamp
Deuterium lamp
Source lens
Photo diode array

Figure 2-2. Optical system of spectrophotometer.

The light source is a combination of a deuterium-discharge lamp for the ultraviolet (UV) wavelength range and a low noise tungsten lamp for the visible and short wave near-infrared (SWNIR) wavelength range. The deuterium-discharge lamp emits light from the 190 nm to approximately 800 nm wavelengths, and the tungsten lamp emits light over the 370 nm to 1100 nm range. The light from both lamps is received and collimated in the source lens, and then passes through the sample to the spectrograph lens and slit. The shutter is electromechanically actuated and only allows light to pass through the sample for measurements. In the spectrograph, light is dispersed onto the diode array by a holographic grating. The sampling interval of the diode array is about 0.9 nm with a wavelength range from 190 nm to 1100 nm. This allows simultaneous access to all wavelength information. The rate at which spectra can be acquired is fundamentally increased.

2.3.3 Gaussian Deconvolution

Electronic absorption spectra are known to constitute a sum of overlapping bands. An absorption spectrum $A = f(\bar{\nu})$ may be expanded in its individual components on the assumption that, when this spectrum is represented in the form $A = f(\bar{\nu})$, where $\bar{\nu}$ is the wavenumber, the spectral bands become symmetric with respect to $\bar{\nu}_{\max}$ and can be expressed as a sum of Gaussians:[3]

$$\bar{A} = y_0 + \sum_{j=1}^{n} \alpha_j \frac{A_{jmax}}{w_j \cdot \sqrt{\frac{\pi}{2}}} exp\left[-\frac{2\left(\bar{\nu} - b_j\right)^2}{w_j^2}\right] \qquad (2\text{-}14)$$

where $\bar{A}$ is the overall absorbance value determined experimentally, α_j is the fraction of the jth component, A_{jmax} is the maximum value of absorbance for an individual band, The center b_j represents the "mean", $w = 2\sigma$, approximately 0.849 the width of the peak at half height (fwhm), and $\bar{\nu} = 1/\lambda$ is the wavenumber, cm^{-1}.

An individual Gaussian band will be of the form:[3]

$$\bar{A} = y_0 + \frac{A_{1max}}{w \cdot \sqrt{\frac{\pi}{2}}} exp\left[-\frac{2(\bar{\nu} - b_1)^2}{w_1^2}\right] \qquad (2\text{-}15)$$

As a first step to perform the fitting, we have to determine the local maxima, which will be the maxima of the individual Gaussian curves. Those ν values of local maxima will be chosen by the first and second derivative of the absorption spectrum where the first derivative is zero and the second one is negative.[4] This means that at this place the magnitude of absorption curve at $\nu - 1$ and $\nu + 1$ is smaller than that of ν. After finding the proper maxima, the inflection points on a curve at which the curvature change sign also need to be found from the second derivative, since the sign of the curvature is always the same as the sign of the second derivative. This means that there is a buried maximum under the curvature change point. The false maxima, as a consequence of fluctuations in the measurement, can be deleted. After choosing all the proper maxima, an estimation of Gaussian functions performed in arbitrary sequence during the deconvolution program would fit to the reality only in that case when they have had no any influence on each other.

2.4 Excited State Measurements

2.4.1 Introduction

Fluorescence occurs when a molecule absorbs photons from the UV-visible spectrum (200-900 nm), causing a transition to a high-energy electronic state and then emits photons as it returns to its initial state, in less than 10^{-9} s. Some energy, within the molecule, is lost through heat or vibration so that the emitted energy is less than the exciting energy; *i.e.* the emission wavelength is always longer than the excitation wavelength. The difference between the excitation and emission wavelengths is called the Stokes shift. Emission occurs predominantly from the lowest singlet state (S_1) and is independent of the excitation wavelength. Emission spectra are determined by measuring the variation in emission intensity as a function of wavelength for a fixed excitation wavelength. However, the excitation spectra are determined by measuring the emission intensity at a fixed wavelength, while varying the excitation wavelength.

The fluorescence lifetime and quantum yield are the most important characteristics of a fluorophore. The fluorescence quantum yield is defined as the ratio of the number of photons emitted to the number of photons absorbed. Fluorescence lifetime refers to the average time available for the fluorophore individual relaxation processes leading to the relaxed S_1 state.

2.4.2 Optical System of Fluorometer and General Protocol for Data Acquisition

Emission spectra were measured on Photon Technology International (PTI) Quantamaster 6000 spectrofluorometer equipped with a continuous xenon arc lamp as the excitation source. The emitting light was collected 90° to the excitation beam and detected by a Hammamatsu R-928 photomultiplier tube (PMT) in photon counting mode. The PMT was housed in a water-cooled PMT housing supplied by Products for Research Inc. The optical layout is show in Figure 2-3. All spectroscopic measurements were recorded using 1.0 cm quartz cuvette supplied by Starna, measuring the solvent and cell

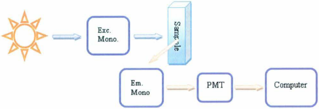

Figure 2-3. Optical system of Quantamaster 6000 spectrofluorometer.

first, and then dissolving the sample in solvent for emission measurements. Emission spectra were corrected for instrument response and light loss using correction factors supplied by the manufacturer.

Relative quantum yield were measured in deoxygenated chloroform or toluene solutions at 25°C where $A < 0.2$ at the λ_{exc} and compared to a standard sample of quinine bisulfate in 0.1M aqueous sulfuric acid solution for which $\phi_{std} = 0.52$ at $\lambda_{exc} = 350$ nm. Relative quantum yields were calculated using eq 2-16, where A is a solution absorbance, I the emission intensity, n the refraction index of the solvent and the subscript *un* and *std* refer to the unknown and standard respectively.[5]

$$\phi_{em} = \phi_{std}\left(\frac{A_{std}}{A_{un}}\right)\left(\frac{I_{un}}{I_{std}}\right)\left(\frac{n_{un}}{n_{std}}\right)^2 \qquad (2\text{-}16)$$

2.4.3 Data Analysis: Emission Spectral Fitting

2.4.3.1 Introduction

The purpose of emission spectrum analysis is to investigate the nature of band shapes of emission spectra including the distribution of intensity within the vibrational bands of emission spectra, the band shapes of these vibrational envelopes, and their relation to the rate of nonradiative processes in which the Franck-Condon principle applies. From the shapes of vibrational bands, the information of intramolecular vibration can be obtained, and from the areas under vibrational bands the Franck-Condon factors of intramolecular vibration can be determined. The theory for emission spectral fitting is presented in Chapter 1 (Section 1.3.2.4). The important result for the theoretical analysis is that the factors are incorporated in the Franck-Condon weighted density states. Franck-Condon weighted density states can be determined from the emission spectra using the protocols described by Kober et al.[6,7] from which the theory for nonradiative decay was recast into parameters that could be experimentally determined.

2.4.3.2 The Basics of Spectral Fitting

Although a spectrometer is used to find the spectrum of a source, what is obtained from the spectrometer is not the actual spectrum, but rather photon counts (C) within specific instrument channels, (*I*). The true fluorescence emission spectrum is a plot of intensity of fluorescence, expressed as quanta per unit frequency interval, against frequency or wavenumber. Therefore, if Q represents the total number of quanta (of all frequencies) of fluorescence emitted per unit time, then represents the intensity at any frequency, v, and the plot of dQ/dv against v is the true fluorescence emission spectrum. The observed spectrum is related to the actual spectrum of the source $f(E)$, such as:

$$C(I) = \int_0^\infty f(E)\,R(I,E)dE \qquad (2\text{-}17)$$

where $R(I,E)$ is the instrumental response and is proportional to the probability that an incoming photon of energy E will be detected in channel I. The emission spectral data are normally recorded in the form of energy units (microwatts) per unit wavelength interval, *i.e.* $dE/d\lambda$.[8] To convert to quanta per unit wavelength interval, this must be first multiplied by the corresponding wavelength (λ), *i.e.* $(dE/d\lambda)\cdot\lambda$. The factor of λ arises from:

$$\frac{dE}{d\lambda}=\frac{dQ\cdot v}{d\lambda}=\frac{dQ}{d\lambda}\cdot\frac{c}{\lambda}=c\cdot\frac{dQ}{d\lambda}\cdot\frac{1}{\lambda} \tag{2-18}$$

To convert to quanta per unit frequency interval, it must be multiplied again by λ^2. Therefore, the equation for this conversion is

$$\frac{dQ}{dv}=\frac{dE}{d\lambda}\lambda^3 \tag{2-19}$$

where λ^2 factor arises from the relation $\lambda = c/v$. Therefore,

$$\frac{dQ}{dv}=\frac{dQ}{d\lambda}\cdot\frac{d\lambda}{dv}=\frac{dQ}{d\lambda}\cdot\frac{d\lambda}{d(c/\lambda)}=-\frac{dQ}{d\lambda}\cdot\frac{\lambda^2}{c} \tag{2-20}$$

Ideally, the actual spectrum of a source, *f(E)*, can be determined by inverting eq 2-17, thus deriving *f(E)* for a given set of *C (I)*. However, this is not possible in general because inversions tend to be non-unique and unstable to small changes in *C (I)*.

The alternative is nonlinear least-squares analysis that is a numerical procedure for estimating a set of parameters of an equation, so that this equation will describe a particular set of data points. These procedures work by successive approximation; that is to try to create a parameterized model spectrum, $f_m(E)$, which can be described in terms of a few parameters and then give an estimate of the values for the parameters to match it to the data obtained by the spectrometer. For each *f(E)*, a model spectrum $f_m(E)$ is calculated and then gives values to the model parameters. The nonlinear least-squares algorithm returns a more accurate approximation. This procedure is applied iteratively until the theoretical model fits the observed data. These values are referred to as the best-fit parameters. The theoretical model spectrum, $f_m(E)$, with the best-fit parameters is considered to be the best-fit model.

The method of nonlinear least squares is built on the hypothesis that the optimum description of a set of data is one which minimizes the weighted sum of squares of deviations, Δy, between the data, y_i, and the fitting function f. All nonlinear least-squares parameter estimation procedures have inherent basic assumptions. These are:

1. All of the experimental uncertainties of the data must be attributable to the dependent variables (those values are actually measured by the experimental protocol).
2. The experimental uncertainties of the dependent variables must follow a Gaussian (normal or bell-shaped) distribution.
3. No systematic uncertainties can exist in either the dependent, or independent variables (those values can be controlled by appropriate settings of the instrumentation or sample preparation).
4. The model function is the correct mathematical description of the data.
5. There must be a sufficient number of data points to yield a good random sampling of the parent population of residuals.
6. The data points must be independent observations.

A way of demonstrating the consistency of a model in terms of accounting for observed experimental behavior is to examine the residuals in order to confirm or deny these assumptions. Residuals are the differences between the observed experimental data and the fitting function evaluated at the maximum-likelihood values of the parameters. Because the photon flux model usually includes shape parameters that make the model nonlinear, the minimization is done via the Levenberg-Marquardt algorithm. To fit the data, the parameters of the model function are varied so as to minimize the deviation between the model and data obtained by the spectrometer, as determined by the χ^2 function.

$$\chi^2 = \sum_{i=1}^{n} \frac{1}{\sigma_i^2} [y_i - f(x_i)]^2 \qquad (2\text{-}21)$$

where n is the number of data points, σ_i^2 is "variance" related to the measurement error for y_i. y is the independent variable, and x is the dependent variable, and f is the assumed relationship between x and y. y_i is the "observed mean", and $f(x_i)$ is the "predicted mean".

For each parameter, a guess value must be inputted and a variation status selected as to whether the parameter value is to be varied to optimize the fit or held fixed. After the fit is done, the value of χ^2, the number of degrees-of-freedom of the data and model, and the model parameters and their uncertainties will be displayed. The estimated parameter uncertainties are obtained from the covariance matrix, which is based upon the derivatives for χ^2 with respect to the model parameters. The covariance matrix is also output, normalized so that values range from -1 (complete anti-correlation) to 0 (uncorrelated) to +1 (complete correlation).

The goodness-of-fit of the theoretical model is determined when χ^2 is minimized. The χ^2 statistics provides a well-known goodness-of-fit criterion for a given number of degrees of freedom (v, which is calculated as the number of channels minus the number of model parameter). If χ^2 exceeds a critical value, $f_m(E)$ is not an adequate model for $C(I)$. Generally, the reduced χ^2 is approximately equal to one. A reduced χ^2 is much less than one indicating that the errors on the data have been over-estimated. When the data used in the fit are not particularly good, the goodness-of-fit is not only dependent on the reduced χ^2. In such a case, many different models with adequate fits can be found. Therefore, the choice of the correct model is a matter of scientific judgment.

2.5 The Time-Resolved Fluorescence

2.5.1 Introduction

Three common techniques used in time-resolved fluorescence spectroscopy are the stroboscopic technique (strobe), the time-correlated single photon counting technique (TCSPC) and the frequency modulation or phase shift technique (phase). The first two are time-domain techniques while the last one is a frequency-domain technique. The time-domain techniques, *i.e.* the strobe and TCSPC, are very similar in what they measure and in the way data are analyzed. The differences are mainly in the hardware; they use different detection electronics and different pulsed light sources, although some light sources can be used with both techniques. The time-domain techniques are direct techniques. Fluorescence decay curves (*i.e.* fluorescence intensity as a function of time) are measured directly and the researcher has full advantage of seeing the physical mechanism during the course of the experiment. Frequently, a qualitative judgment about a particular mechanism can be made by examining raw decay data and a proper fitting function can be thus selected.

In this thesis, all fluorescence lifetimes were measured by the stroboscopic technique based on PTI nitrogen/dye lasers. The shortest lifetime that can be measured with a lifetime instrument depends on the temporal pulse width, pulse stability and electronic response.

2.5.2 Experimental Set-up and Data Acquisition

The stroboscopic technique utilizes a pulsed light source (a laser or an LED) and measures the fluorescence intensity at different time delays after the pulse, as shown in Figure 2-4. As a result, a fluorescence decay curve is collected. The laser is triggered by the software/interface with the repetition rate up to 20 Hz controlled by the user. The optical pulse from the dye laser (or optional frequency doubler) is fed by a single optical fiber to the sample compartment and excites the sample. In order to eliminate any potential jitter (*i.e.* the uncertainty between the time the laser is triggered and the time it actually fires), a photodiode (Pd) is placed in front of the laser and the pulse from the Pd is routed to a digital delay gate generator (DGG) unit, which outputs a delayed TTL pulse.

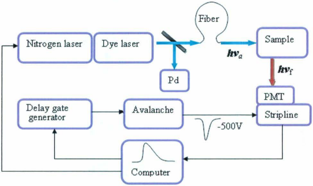
Fiber
Nitrogen laser
Dye laser
$h\nu_a$
Sample
$h\nu_f$
Pd
PMT
Delay gate generator
Avalanche
Stripline
-500V
Computer

Figure 2-4. Block diagram of an N_2/dye laser-based stroboscopic system.

The DGG is under computer control and the value of the TTL pulse delay is determined in the acquisition software. The delayed pulse triggers an avalanche circuit, which provides a narrow high voltage pulse (ca. -500V) for the detection circuitry. This pulse creates the gain and the temporal discrimination gate for the photomultiplier. Scanning the gate (time delay) across the fluorescence decay allows the acquisition of fluorescence intensity as a function of time. One of the advantages of the stroboscopic technique is the ability to utilize low repetition, inexpensive lasers, such as PTI's nitrogen/dye laser, which can provide virtually continuous excitation wavelength range from 235 to over 990 nm with the optional frequency doubler.

To obtain the fluorescence lifetime, the profile of instrument response function (excitation pulse) has to be measured in addition to the fluorescence decay because the laser (lamp) pulse has a finite temporal width, which distorts the intrinsic fluorescence response from the sample. This distortion is known as convolution. In a typical experiment, the instrument response function (IRF) is measured by using a scattering solution in a companion measurement prior to determining the fluorescence decay of the sample.

2.5.3 Time-Resolved Data Analysis

Convolution. Analysis is performed by convoluting the IRF with a model function (e.g. a single exponential decay or a double exponential decay or some other function) and then comparing the result with the experimental decay. This is done by an iterative numerical procedure until the best agreement with the experimental decay curve is achieved. In any fluorescence lifetime instrument with pulsed excitation, at any given emission wavelength, the free decay of fluorescence $F(t)$ will be distorted by the finite width of the excitation pulse (Figure 2-5). The observed fluorescence decay data, $F(t)$, is a convolution of the instrument response function $R(t)$, and the intensity of fluorescence decay function $D(t)$ of the sample. The mathematical description is expressed as:[9-11]

$$F(t) = \int_0^t R(t - t')\, D(t')dt' \qquad (2\text{-}22)$$

where $R(t)$ is the instrument response function (IRF), also known as the excitation pulse curve. $F(t)$ is the experimentally determined decay intensity at time t and $D(t)$ is a function assumed to describe the fluorescence dynamics of the sample. The analysis of the data involves the determination of the best values for the parameters in $D(t)$.

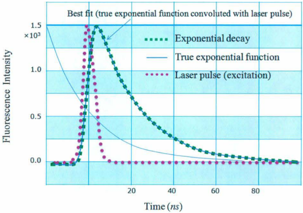

Figure 2-5. Experimental laser profile decay (dot functions) and the best numerical fit in a typical time-domain experiment. The true exponential function represents the model decay, *i.e.* a hypothetical decay if the laser pulse was infinitely narrow.

The fluorescence decay was fitted to a delta function generated decay at time t, and can be adequately represented by a sum of exponential decays:

$$D(t) = \sum_i a_i \exp\left(\frac{-t}{\tau_i}\right) \qquad (2\text{-}23)$$

In this expression, τ_i is the *i*th decay time, and a_i is the pre-exponential factor of the *i*th component. This fitting function allows for negative a_i's so that rise times can also be determined with this program. To remove the convolution distortion and calculate the time-resolved emission spectra, the experimental $R(t)$ is used to determine the parameters (e.g. the lifetime) of the fitting function $D(t)$ by using a procedure known as iterative reconvolution, which employed nonlinear least square regression by Marquardt's algorithm for parameter optimization.[12-14]

Curve Fitting Procedure. The fitting procedure is based on the Marquardt algorithm where the experimental data are compared to a model decay convoluted with the IRF. Because the method is a statistical fitting method, which usually involves linearization of the fitting function and least squares solution, large data sets must be used to insure validity. Least square fitting produces a set of calculated points, which describes the experimental set. The calculated values are optimized by minimizing the weighted sum of the squares of deviations of the calculated points, $D(i)_{\mathrm{calc}}$, from the experimental ones, $F(i)_{\mathrm{exp}}$, according to eq 2-24, for all i channels of data. That is the reduced chi-square (χ^2), is minimized.

$$\chi^2 = \frac{1}{N-n-1}\sum_i^n \frac{\left[D(i)_{calc} - F(i)_{exp}\right]^2}{\sigma(i)^2} \qquad (2\text{-}24)$$

where N is the number of data channels, n is the number of fitting parameters, and σ is the standard deviation. The fitting function, $D(i)_{\mathrm{calc}}$, is optimum when the χ^2 is minimized. Strictly, eq 2-24 is valid only when the Gaussian approximation is valid and the variance of the calculated *i*th data point is zero. Therefore, sufficient counts must be collected to provide approximate Gaussian statistics.

For multi-exponential models, the minimization of χ^2 is done with respect to either the decay parameter itself or both the decay parameter and the pre-exponential factor. In practice, initial choices for decay parameter(s) τ_i and pre-exponential(s) a_i are chosen by the user that establishes an initial functional form for the decay function $D(t)$ (eq 2-23). The initial guesses are used to calculate $D(i)$, and determine χ^2. Partial derivatives of the calculated points with respect to the initial guesses are calculated, and they are used in a simple series expansion of the linearized function $D(i)$ to provide a set of matrix equations, which are solved to generate a new set of parameters, incremented from the initial set. In this manner, new values are reconvoluted until the χ^2 value converges to a minimum.

The best fit is determined when chi-square is minimized. Acceptable values tend to be near 1 for ideal Poisson distributed data. For good results, χ^2 is between 0.9 and 1.2. Values too low (~ 0.75 or lower) are symptoms of too small a data set for a meaningful fit, while high values (> 1.5) indicate significant deviation from the degree of exponentially fitted.[15,16]

Goodness of Fit. In addition to the chi-square value, a number of statistical parameters have been developed to assist in determining the quality of the analysis. The first parameter is reduced χ^2 as discussed above. Others are:

Randomness of the Residual Pattern. The residual R_i is the difference between the calculated fit and the real data at t_i. Weighted residuals r_i are the products of R_i

and W_i, *i.e.* $r_i = R_i \cdot W_i$ and should range from about -3.3 to 3.3. W_i is a weighting factor, which normally corresponds to the standard deviations in the R_i. Weighted residuals are more sensitive at long times than unweighted residuals.

Autocorrelation Function of the Weighted Residuals.[17] This function is calculated from eq 2-25

$$C_{r_j} = \frac{1}{m}\sum_{i=n_1}^{n+m-1} r_i r_{i+j} \Big/ \frac{1}{n_3}\sum_{i=n_1}^{n_2} (r_i)^2 \qquad (2\text{-}25)$$

where $n_3 = n_2 - n_1 + 1$, n_1 and n_3 are the first and last channels chosen to do the calculation. An upper limit is set at $j = n_3/2$ to allow for maximal testing of a finite data set. By definition $C_{r_0} = 1$. For the remaining points, C_{r_j} should form a flat band of high frequency low amplitude noise about zero.

Durbin-Watson Parameter.[18,19] This parameter was introduced by Durbin and Watson to test whether a certain type of serial correlation exists in residuals, defined as:

$$DW = \sum_{i=n_1+1}^{n_2} (r_i - r_{i-1})^2 \Big/ \sum_{i=n_1}^{n_2} (r_i)^2 \qquad (2\text{-}26)$$

where the other parameters are defined above. The fit is likely satisfactory if the value of *DW* is greater than 1.7, 1.75, 1.8 for single, double and triple exponential fit respectively.[20]

Runs Test Parameter. This parameter determines the number of positive and negative groups or runs of the residuals as defined as:

$$z = \frac{zn}{\sqrt{(zd)}} \qquad (2\text{-}27)$$

where

$$zn = (nn + np) - \frac{(2 \times nvn \times nvp)}{nvn + nvp} + 1 \qquad (2\text{-}28)$$

$$zd = \frac{2 \times nvn \times nvp \ \times (2 \times nvn \times nvp - nvn - nvp)}{(nvn - nvp)^2 \times (nvn + nvp - 1)} \qquad (2\text{-}29)$$

and np is the number of positive transitions, and nn is the number of negative transitions, nvn is the number of negative residuals, and nvp is the number of positive residuals. A value of $z > -1.96$ indicates a satisfactory fit at the 95% confidence level.[21]

These criteria enable the user to decide whether the fitting model adequately describes the experimental data or a different fitting function is required.

2.6 Transient Absorption Spectroscopy

2.6.1 Introduction

Laser flash photolysis is a technique of transient spectroscopy and transient kinetic studies, in which a short pulse of light is used for excitation of sample that has been placed in the optical path of a spectrometer. This intense light pulse creates short-lived photo-excited intermediates such as excited states, radicals and ions. The result of this interaction can be either a transient absorption or an emission process. The use of a laser for sample excitation gives the technique the specificity of single wavelength excitation, nanosecond time resolution, and the high reproducibility of pulsed light output from the analyzing source that permits routine generation of time-resolved spectra over these timescales.

Time resolved absorption spectra can be generated in kinetic mode laser flash experiments by automatic scanning through a pre-defined spectral range and subsequent data slicing. This technique requires many laser shots, in particular when high spectral resolution is required. The laser interaction with the sample often results in irreversible changes and this necessitates sample replacement for each individual measurement. In addition, many measurements are required to be done in the absence of oxygen and so the samples either need to be degassed using the classical freeze-pump-thaw method or by purging using an inert gas.

2.6.2 Theoretical Background

2.6.2.1 Principles of Transient Absorption

Transient Absorption Spectroscopy is essentially the "absorption spectrum of an absorption spectrum". The measurements are based on the well-known Beer-Lambert absorption law:

$$I(\lambda) = I_0(\lambda) \times 10^{-c\varepsilon(\lambda)l} \qquad (2\text{-}30)$$

where I_0 is the intensity of the light of a particular wavelength λ directed at a sample solution, I is the intensity of the transmitted light. c is the concentration of absorbing molecules (in M), ε is the molar extinction coefficient of these molecules (in $M^{-1}cm^{-1}$), and l is the path length traversed through the sample (in cm). The *OD* (optical density) or alternatively *A* (absorbance) is defined as: $-\log(I/I_0)$, therefore

$$OD(\lambda) = c\varepsilon(\lambda)l \qquad (2\text{-}31)$$

When a mixture of absorbing molecules is present, the following expression can simply be used:

$$OD(\lambda) = \sum_i c_i\varepsilon_i(\lambda)l \qquad (2\text{-}32)$$

In transient absorption measurements, changes in absorption (Δ*OD*) are measured by a difference in detected intensity Δ*I* between I_1 and I_2 before and after the start of the induced processes. If the change is small (Δ*I*/*I* <<1), the following useful approximation can be made:[22]

$$\Delta OD = -\log(I_2/I_0) - \log(I_1/I_0) = -\log(I_2/I_1) = -\log(1 + \Delta I/I_1)$$

$$= -0.434\ln(1 + \Delta I/I_1) \approx -0.434\,\Delta I/I_1 \qquad (2\text{-}33)$$

Eq 2-33 indicates that Δ*OD* is directly proportional to the change in absorption. Therefore, it is important to choose an appropriate concentration to perform optimal experiments. Δ*OD* increases when the concentration is increased, but this limits the amount of detected light. Therefore, high concentrations should be avoided, and as a rule of thumb, an optimal *OD* around 0.5 at the excitation or detection wavelength will be good for a pump-probe experiment. When an entire wavelength region is probed, *OD* values of up to 1 or even higher are preferred in order to get good signal/noise ratios over the entire wavelength region.

2.6.2.2 Data Acquisition

The absorption changes (Δ*OD*) are recorded using a spectrally continuous xenon lamp (probe source) forming the background in a single beam absorption spectrometer. The probe source is operated in a pulsed mode to enhance the photon flux for measurements in short time ranges and in a continuous mode for slower reactions or longer lived species. Laser flash photolysis is applicable to liquid and solid samples. Liquid samples are usually measured in a cuvette with the pump beam and the probe beam overlapping orthogonally. Solid samples that may be in the form of a powder in a cuvette or a film are generally studied in a diffuse reflectance setup. In either case, the sample in a cuvette or a film is attached to a vertical sample stage so that the sample position can be readily adjusted in vertical or lateral directions.

The sample being investigated is exposed to an intense laser pump pulse, which creates the transient species, and the probe source, which forms the background for the time dependant absorption measurement. For time scales in the microsecond and nanosecond range, the required high background level of the probe light is created by the intense flash from the pulsed xenon lamp, which reaches a sufficiently flat plateau after some stabilization period. This plateau level represents the pre-photolysis background level of the transmitted light through the sample. At a pre-set time after lamp triggering, when the pulse plateau is flat, the excitation laser is triggered to create the transient species under investigation (Figure 2-6). The absorption of the transient species is usually

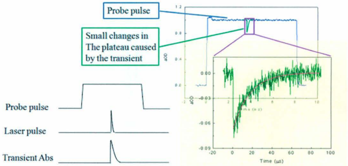

Figure 2-6. Left: The relative timing of the laser, flash lamp pulses and the transient absorption signal. Right: the output from the flash lamp (rear window) as detected at the photomultiplier (PMT). Inset is an expansion of the signal showing the decrease in light detected at the PMT due to short-lived species produced by the laser pulse.

time dependent and produces a time dependent change in the transmission of the sample. After recording the time dependent transmission of the sample, the optical density change is calculated using the level of the background light as 100% and the baseline measurement as 0%. The change in optical density, ΔOD, can be analyzed using exponential least squares fitting algorithms, resulting in transient lifetimes or rate constants.

2.6.2.3 Excited State Absorption, Photobleaching, and Stimulated Emission

In transient absorption, the presence of the transient species can cause the sample to have either increased or decreased levels of absorption relative to the absorption of the ground state species (positive ΔOD and negative ΔOD respectively). When the ground state molecules are promoted to an excited state or undergo a reaction, there will be a depletion of the absorbing molecules, which lose their ground state absorption. Concomitantly, a different or increased absorption is created that is associated with different species, for example, a reaction product, a molecule that has accepted or donated an electron, or a molecule that is in the excited state and shows excited state absorption (ESA). In addition, a reduction in the measured optical density is also associated with sample emission. A molecule in the excited singlet state can emit light to return to the ground state by spontaneous emission or stimulated emission (SE) induced by the probe light, giving rise to an apparent additional bleaching. A schematic energy level system of a chromophore and corresponding transient absorption are shown in Figure 2-7.

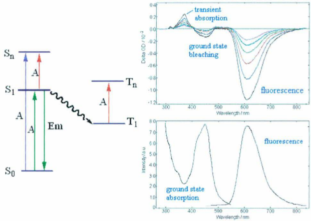

Figure 2-7. Diagram of the energy levels of a chromophore (left), and the corresponding transient absorption (right).

2.6.3 Experimental Setup and Data Acquisition

2.6.3.1 Nanosecond Transient Configuration

Excitation Source. The excitation light used was the third harmonic (355 nm) of a neodymium-doped yttrium aluminum garnet (Nd:YAG) laser (Quantel, Brilliant *ω*) with a duration of 5-8 ns. The repetition rate of the laser was 20 Hz. The intensity of the pump light was 9.5 mJ/cm^2.

Probe Source. The analyzing light was obtained from a 150W xenon arc lamp. The lamp runs in conventional cw mode with its operating current increased significantly for a few milliseconds when increased photon flux is required. The laser and analyzing light beams, intersecting at right angles, passed through a quartz cell with 1 cm^2 cross section. To record processes between 1 ns and 1 μs, a high intensity for the probe light in a short time is required which can be produced by a pulsed xenon flash lamp. When slower reactions or longer lived species are being measured, the pulsing action is disabled and the continuous light source is used in regular cw mode. To minimize heating and actinic effects, a mechanical shutter is placed between the probe lamp and the sample. It opens shortly before the excitation pulse arrives and closes after the time interval of interest.

Monochromator. After the probe beam passes through the sample, it is normally focused into the entrance slit of a monochromator, which is equipped with a diffraction grating, and then the single wavelength of emission can be selected by varying the angle between the incident and dispersed beam. Light exiting a typical monochromator is ideally monochromatic but usually contains extraneous wavelengths. However, stray light does not pose a serious problem in nanosecond transient spectroscopy because the probe source is generally a high-intensity arc lamp.

Detector System. Conversion of an optical signal to an electronic signal is generally accomplished with the use of optomechanical detectors, such as the conventional photomultiplier tube (PMT). PMTs contain focusing electrodes that direct electrons emitted by the photo-emissive cathode to an electron multiplier (dynodes) for cascade secondary emission electron multiplication. The multiple electrons are then collected by an anode as an output signal. Using an electron multiplier results in high detector sensitivity in the UV/Vis/NIR regions. A RCA IP28 photomultiplier was used for single-wavelength detection of transient absorption (Applied Photophysics) and provides the fast time response needed in nanosecond experiments. The PMT can be coupled to digital oscilloscope, and the signals from PMT were displayed and recorded as a function of time on a Tektronix 500MHz oscilloscope (1 GS/s sampling rate), which employ an analog-to-digital (A/D) converter that is interfaced to a computer.

2.6.3.2 Optical Layout of Transient Absorption System

The nanosecond transient absorption system for the experiments described in this thesis is schematically represented in Figure 2-8.

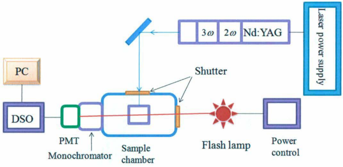

Figure 2-8. Schematical representation of nanosecond transient absorption system.

Kinetic measurements were obtained by averaging multiple results to improve the signal-to-noise ratio. The data were initially fitted to an appropriate exponential decay function using software provided by Applied Photophysics and then analyzed by Origin software. The transient absorption was obtained from a series of oscilloscope traces measured using the same solution in a point-by-point manner with respect to the wavelength using the Origin software. The samples were deaerated by passing pure nitrogen gas for 20 min through the solutions prior to each experiment. Absorption spectra were taken before and after excited state measurements to assess the photostability of the sample. Samples were routinely changed after minimal spectral changes were observed.

2.6.4 Data Analysis

Instrument Response Function. In transient absorption measurements, the recorded trace is a convolution of the studied kinetics and the instrument response function. Theoretically, infinitely short light pulses of one particular wavelength would be ideal for pump-probe measurements. However, from the Heisenberg uncertainty principle $\Delta E \cdot \Delta t \geq h/2\pi$, it is clear that these cannot be obtained due to the finite width of the excitation pulse. In addition, because of the imperfections in the laser, additional broadening to 20 nm can also take place.[23,24] This instrument function in "slow" measurements is due to the finite response time of the detection system and the width of the exciting pulse. In "fast" experiments this instrument function is determined entirely by the cross correlation function $G(t)$ of the pump and probe pulse:[22]

$$G(t) = \int_{-\infty}^{\infty} I_{pump}(t')I_{probe}(t-t')dt \qquad (2\text{-}34)$$

The instrument function is considered as a set of closely spaced "delta functions" (extremely short pulses), all giving rise to the same kinetic curve but with different starting points and different amplitudes. In order to remove the convolution of instrument response function, the kinetic trace is then fitted to a sum of decay curves with the same decay parameters and with different starting points and starting heights, according to the shape of the instrument function. The fitting function is expressed as:

$$\Delta OD(t) = \int_0^t G\,(t - t')\Delta OD'(t')dt' \qquad (2\text{-}35)$$

where the measured change in absorption $\Delta OD(t)$ is a convolution of $G(t)$ and the real absorption change $\Delta OD'(t')$ that has to be recovered from the measured signal. An accurate determination of the instrument function is required. For "slow" real-time experiments (slower than 1 ns) this convolution is usually not necessary because the pulses are either too short on the relevant time scales or measurements immediately after the excitation are not possible at all due to a burst of scattering (or fluorescence) during and immediately after the pulse.

Analysis of Kinetics. In general, two types of information that can be obtained from nanosecond absorption spectroscopy: single wavelength detection (kinetic mode) and full spectrum accumulation (spectral mode). All transient absorption data reported in this thesis are kinetic measurements. Full-wavelength experiments are most suitable for detection of spectral dynamics and intermediate states and can be obtained by multiple scans at various time delays. Kinetic data are often obtained using the single-wavelength approach because the information of interest is the variation of intensity with time. The transient data obtained from nanosecond time-resolved absorption spectroscopy using single-wavelength methods is generally interpreted by iterative reconvolution based on the Marquardt fitting algorithm.[25] The fitting of transient absorption traces can involve non-exponential, single-exponential, and multi-exponential assumptions, which have a general expression as:

$$\Delta OD(\lambda, t) = \sum_i \Delta OD_i\,(\lambda)\exp(-t/\tau_i) \qquad (2\text{-}36)$$

where $\Delta OD\,(\lambda, t)$ is the difference in OD between time t and infinite time. $\Delta OD_i\,(\lambda)$ is the amplitude of a component with a lifetime $\tau_i\,(k = 1/\tau)$ at a wavelength λ, varying with wavelength. The quality of the fits was assessed using a reduced χ^2 criterion and plots of weighted residuals. In general, one can decide how many independent decay components are needed to describe the observed kinetics by closely inspecting the residuals (difference between measured and fitted curves).

2.7 Global Kinetic Analysis

2.7.1 Introduction

For all types of multi-wavelength spectrophotometric investigation, raw data were processed by use of the program SPECFIT/32$^{\text{TM}}$, which is a multivariate data analysis program for modeling and fitting chemical kinetics and a variety of equilibrium titration 3D data sets. Generally, the methodology of the program SPECFIT/32$^{\text{TM}}$ is using the underlying chemical model and its nonlinear parameters to generate concentration profiles for each of the colored species, and then the initial parameter estimates are refined via the Levenberg-Marquardt procedure to minimize the least squares residuals between the 3D data set and the model system.[26] This methodology relies on several specialized mathematical procedures that optimize the least squares minimization.

There are several advantages in measuring and analysing multi-wavelength data as compared to selecting single-wavelengths: (1) the ability to extract predicted spectra of unknown intermediates; (2) more reliable parameter estimates than single-wavelength fits; (3) the ability to constrain fits with known molar absorptivity spectra.

2.7.2 Theory of nonlinear least-squares fitting of Multivariate Absorption Data

2.7.2.1 Multivariate absorption data and Beer–Lambert's law

With modern instrumentation, multivariate data are readily available. The typical example is the diode array spectrophotometer, which typically deliver absorption readings for a total of 1024 wavelengths. For each value of the independent variable (e.g. time) a complete spectrum is acquired and this type of measurement results in data can be stored as rows in a matrix Y. The matrix Y then has the dimensions $n \times l$ where n is the number of experimental points and l the number of wavelengths (or equivalent) at which the spectra were taken.

According to Beer-Lambert's law, the absorbance of a system at one particular wavelength l at time t is the sum of the contributions from all absorbing components. The contribution from each species to the absorbance is linearly proportional to the concentration and the optical path length (the distance travelled through the solution by the incident light beam). If the path length and absorptivity constant are expressed by the single constant $\varepsilon_i(\lambda)$, then Beer-Lambert's law and each element in Y is represented by eq 2-37 (for nc absorbing species).

$$y(t,\lambda) = c_1(t)\varepsilon_1(\lambda) + c_2(t)\varepsilon_2(\lambda) + \cdots + c_{nc}(t)\varepsilon_{nc}(\lambda) = \sum_{i=1}^{nc} c_i(t)\varepsilon_i(\lambda) \qquad (2\text{-}37)$$

When spectra are arranged according to the matrix Y, eq 2-37 can be expressed using matrix notation:[26]

$$Y = CA + R \qquad (2\text{-}38)$$

The columns of the matrix C contain the concentration profiles c_i of the nc absorbing species at the nt measurement times. The rows of the matrix A contain the molar absorptivities $\varepsilon_i(\lambda)$ for each species at the $n\lambda$ measured wavelengths. However, because of the inherent noise in any measured data, the matrix Y cannot be perfectly represented by the product of C and A, and this difference is captured in the matrix of residuals R. Therefore, each element in Y is the product of the corresponding row in C and column in A plus the noise component in the matrix R. In a fitting procedure, those matrices C and A are determined which best represent the original matrix Y. Generally, the least-squares criterion is used to define the optimum.

2.7.2.2 The Singular Value Decomposition

Experimental 3D data sets frequently contain measurements at many more wavelengths than the number of colored components that are represented by the colorimetric changes for the equilibrium or kinetic system under study. The drawbacks of multichannel detection become evident. The large number of data points to be handled, and the large number of parameters to be fitted which includes the nonlinear ones and the matrix A of linear parameters. To resolve these problems, the method of Singular Value Decomposition (SVD)[26-28] is used to reduce the wavelength-time spectral data matrix Y to the factor analytical form,

$$Y = USV \qquad (2\text{-}39)$$

where U (Nm×Ne) and V (Ne×Nw) are sets of orthogonal (linearly independent) concentration and spectral eigenvectors ($U^tU = VV^t = 1$) respectively. S (Ne) is a set of singular (weighting) factors. Nm is number of measurements (scans), Nw is number of wavelengths in the scans, and Ne is number of significant eigenvectors. The matrix product $Y = USV$ is the least squares best estimator of the original 3D data set (Y).

The basic steps of data reduction through SVD are briefly repeated: Y in eq 2-38 is replaced by its SVD eq 2-39 to yield

$$Y = CA + R = USV \qquad (2\text{-}40)$$

post-multiplication with V^t will give

$$YV^t = CAV^t + RV^t = US \qquad (2\text{-}41)$$

Eq 2-40 is effectively a projection of R, Y, and A into the subspace defined by V. The projections RV^t and AV^t are conveniently renamed as $R'$and A'. YV^t is renamed as, Y' thus, eq 2-41 can be rewritten as

$$Y' = CA' + R' \qquad (2\text{-}42)$$

Comparing eq 2-42 with its original, eq 2-38, the reduction of the sizes of Y, A, and R to Y', A', and $R'$is considerable, which have only Ne columns rather than the original 1024. The SVD method produces a linearly independent set of (Ne) eigenvectors with all of the colorimetric information for the experiment, plus some additional noise eigenvectors, that can be excluded from further consideration. This is a very useful representation because the product ($U \times S$) contains the evolutionary information for the colored components. Therefore, they are often referred to as the concentration eigenvectors. Indeed, these are the input data used by the global fitting procedure.[27,29]

2.7.2.3 Elimination of Linear Parameters

The task of the fitting algorithm is to determine the set of parameters for which the fit is optimal. The longer the list of parameters the more difficult the fit and the more likely there are strong correlations. Therefore, it is crucial to recognize that the matrix A is composed of linear parameters that can be computed explicitly and there is no need to pass them through the non-linear optimization routine.[26] Successful modeling of experimental 3D data sets is significantly enhanced by the elimination of the linear (amplitude) information from the global fitting procedure. Once the nonlinear (model) parameters have been optimized, the spectral information for the colored species can be obtained by application of matrix methods to the multivariate solution of Beer's law.

The matrix inverse (M^{-1}) is the most common numerical method for solving systems of linear equations, although a number of other methods exist for special cases. For any matrix C as defined by the rate or equilibrium constants, the best corresponding matrix A can be computed as

$$\hat{A} = C^{+}Y \qquad (2\text{-}43)$$

where C^{+} is the so called pseudo-inverse of the matrix C, and it can be calculated as

$$C^{+} = (C^{t}C)^{-1}C^{t} \qquad (2\text{-}44)$$

where C is a square matrix that is also non-singular (*i.e.* neither the rows nor the columns are linearly dependent). C^{t} is the matrix transpose of C. This substitution of A by $\hat{A}$ dramatically reduces the number of parameters to be fitted iteratively to those defining the matrix C (rate or equilibrium constants).

2.7.2.4 Nonlinear Least-Squares Fit

The task of the fitting algorithm is to find that, hopefully unique, set of parameters for which the measured data Y and their calculated values Y_{calc} are as similar as possible.

The differences between Y and Y_{calc} are called the residuals R, expressed as:

$$R = Y - Y_{calc} = Y - C\hat{A} \qquad (2\text{-}45)$$

The residuals are defined as a function of the non-linear parameters. The sum of squares of the residuals matrix, ssq, is defined as:[29]

$$ssq = \sum_{i}\sum_{j} R_{i,j}^{2} \qquad (2\text{-}46)$$

The parameters are non-linear because the relationship between the parameters and the residuals is not linear.

One of the most commonly chosen methods of non-linear regression is the Levenberg-Marquardt method.[30,31] This method is a gradient method, which means it relies on calculation of the derivative of the function being optimized (the residuals). These derivatives are collected in the Jacobian J.

$$J = \frac{\delta R}{\delta P} \qquad (2\text{-}47)$$

Starting from an initial set of guessed values for the parameters, the iterative refinement of the parameters is given by the following formula. The shift vector ΔP is computed and added to the vector parameter.

$$\Delta P = -J^{+}R = -(J'J)^{-1}J'R \qquad (2\text{-}48)$$

Convergence is checked by comparing the new sum of squares with the previous one. If improvement is below a certain threshold, *i.e.* the shift in the parameters resulted in no further improvement of the ssq value, then the process is terminated and the results are reported. In the case of divergence, the modification was suggested by Marquardt based on the ideas of Levenberg. It basically consists of suitably increasing the diagonal elements of the Hessian matrix ($H=J^tJ$) by a certain number, the Marquardt parameter *mp*, and prior to its inversion as shown in eq 2-49.

$$\Delta P = -(H + mp \times I)^{-1} J^t r(P_0) \qquad (2\text{-}49)$$

where I is the identity matrix. Increasing the Marquardt parameter shortens the shift vector and directs it to the direction of steepest descent. Once the ssq converges, the magnitude of the Marquardt parameter is reduced and eventually set to zero when the break criterion is reached.

2.7.3 Error Estimates and Correlation Coefficients

The estimation for the standard deviations of the fitted parameters is contained in the inverse of the Hessian matrix $(J^tJ)^{-1}$. The standard error σ_i in parameter p_i is given by

$$\sigma_i = \sigma_Y \sqrt{h_{i,j}^{-1}} \qquad (2\text{-}50)$$

$h_{i,j}^{-1}$ is the i-th diagonal element of the inverted Hessian matrix H^{-1} and σ_Y is the standard deviation of the residuals R given by

$$\sigma_Y = \sqrt{\frac{ssq}{nt \times n\lambda - (n\lambda + nc \times nk)}} \qquad (2\text{-}51)$$

where $nt \times n\lambda - (n\lambda + nc \times nk)$ is the number of degrees of freedom. This equals the number of experimental values, the number of elements in R ($nt \times n\lambda$), minus the number of fitted parameters ($np + nc \times n\lambda$, that is the number of non-linear and linear parameters). If H is normalized to one in the diagonal elements, the off-diagonal element

$h_{i,j}$ of the normalized H is the correlation coefficient between the parameter i and j. For example, the Hessian matrix resulting from the global analysis of kinetic data of SC-$(C_{60})_2$ (will be discussed in Chapter 4) is shown as following:

```
[PARAMETER COEFFICIENTS]

1  0  0  0  0
0  0  1  0  0
0  0  0  1  0
0  0  0  0  1
```

All correlation coefficients between the parameter i and j (off-diagonal elements $h_{i,j}$) are equal to 0. As the value of the correlation coefficient approaches to unity, parameters are correlated. High correlation between parameters means that the two parameters cannot be distinguished from one another and one needs to be removed from the fit.[27,29,32]

2.8 References

(1) Zhou, N.; Wang, L.; Thompson, D. W.; Zhao, Y. *Org. Lett.* **2008**, *10*, 3001-3004.

(2) Zhou, N.; Wang, L.; Thompson, D. W.; Zhao, Y. *Tetrahedron Lett.* **2007**, *48*, 3563-3567.

(3) OriginPro 7.0 ed.; Microcal Software Inc.: Northampton, 2003.

(4) Schäffer, B.; Lorinczy, D. *J. Therm. Anal. Cal.* **2005**, *82*, 531-535.

(5) Coe, B. J.; Friesen, D. A.; Thompson, D. W.; Meyer, T. J. *Inorg. Chem.* **1996**, *35*, 4575-4584.

(6) Kober, E. M.; Meyer, T. J. *Inorg. Chem.* **1984**, *23*, 3877-3886.

(7) Kober, E. M.; Caspar, J. V.; Lumpkin, R. S.; Meyer, T. J. *J. Phys. Chem.* **1986**, *90*, 3722-3734.

(8) Parker, C. A.; Rees, W. T. *Analyst* **1961**, *85*, 587-600.

(9) O'Connor, D. V.; Ware, W. R.Andre, J. C. *J. Phys. Chem.* **1979**, *83*, 1333-1343.

(10) McKinnon, A. E.; Szabo, A. G.Miller, D. R. *J. Phys. Chem.* **1977**, *81*, 1564-1570.

(11) Kees Vos, A. H.; Antonie J.; Visser,W. G. *Eur. J. Biochem.* **1987**, *165*, 55-63.

(12) http://www.pti-nj.com/LaserStrobe/LaserStrobe.html; Photon Technology International, 2005.

(13) Photon Technology International Inc., 2005.

(14) Sau, A. K.; Chen, C.-A.; Cowan, J. A.; Mazumdar, S.Mitra, S. *Biophys. J.* **2001**, *81*, 2320-2330.

(15) James, D. R.; Ware, W. R. *Chem. Phys. Lett.* **1986**, *126*, 7-11.

(16) James, D. R.; Siemiarczuk, A.; Ware, W. R. *Review Scientific Instruments* **1992**, *63*, 1710-1716.

(17) Grinvald, A.; Steinberg, I. Z. *Anal. Biochem.* **1974**, *59*, 583-598.

(18) Durbin, J.; Watson, G. S. *Biometrika* **1950**, *37*, 409-428.

(19) Durbin, J.; Waton, G. S. *Biometrika* **1951**, *38*, 159-178.

(20) O'Connor, D.; Phillips, D. *Time-Correlated Single Photon Counting*; Academic Press: London, 1984.

(21) Hamburg, M. *Basic Statictics*; Brace Harcourt Jovanovich: New York, 1985.

(22) van Amerongen, H.; van Grondelle, R. *Methods in Enzymology* **1995**, 201-226.

(23) Hastings, G.; Durrant, J. R.; Barber, J.; Porter, G.; Klug, D. R. *Biochemistry* **1992**, *31*, 7638-7647.

(24) Durrant, J. R.; Hastings, G.; Hong, Q.; Barber, J.; Porter, G.; Klug, D. R. *Chem. Phys. Lett.* **1992**, *188*, 54-60.

(25) Chen, E.; Chance, M. R. In *Metallobiochemistry Part C: Spectroscopic and Physical Methods for Probing Metal Ion Environments in Metalloenzymes and Metalloproteins*; Volume 226 ed.; Academic Press, 1993, pp 119-147.

(26) Maeder, M.; Zuberbuehler, A. D. *Anal. Chem.* **1990**, *62*, 2220-2224.

(27) Binstead, R. A.; Jung, B.; Zuberbühler, A. D.; 2000-2005 Spectrum Software Associates ed.; Spectrum Software Associates: Marlborough.

(28) Wall, M. E.; Rechtsteiner, A.; Rocha, L. M. In *A Practical Approach to Microarray Data Analysis*; Berrar, D. P., Dubitzky, W., Granzow, M., Eds.; Kluwer: Norwell, MA, 2003, pp 91-109.

(29) Norman, S.; Maeder, M. *Crit. Rev. Anal. Chem.* **2006**, *36*, 199 - 209.

(30) Marquardt, D. W. *J. Soc. Ind. Appl. Math.* **1963**, *11*, 431-441.

(31) Levenberg, K. Q. *Appl. Math.* **1944**, *2*, 164-168.

(32) Puxty, G.; Maeder, M.; Hungerbühler, K. *Chemometrics and Intelligent Laboratory Systems* **2006**, *81*, 149–164.

Chapter 3

Radiative and Non-radiative Processes of OPV/OPE Chromophores

Overview

The ultimate goal in this chapter is the quantitative understanding of the structural, electronic and vibronic parameters of π-conjugated OPV/OPE bridges, as well as the substituent and orientation effects on the photophysical properties.

3.1 Introduction........111

3.1.1 Conducting Polymers........111

3.1.2 Bonding in π-Conjugated Polymers........112

3.1.3 Conformation and Structural Dynamics........118

3.1.4 Matrix Effect........120

3.2 Results........125

3.2.1 Overview........125

3.2.2 Ground State Conformation and FMO Calculations........126

3.2.3 Absorption and Band Assignments........127

3.2.3.1 Absorption Spectral Deconvolution........128

3.2.3.2 TD-DFT Band Assignments of Multi-electron States.......130

3.2.4 Excited States: Chromophoric Bridges........131

3.2.4.1 Photochemistry........131

3.2.4.2 Radiative Decay: Electronic Structure........133

3.2.4.3 Emission Spectral Fitting........135

3.3 Discussions........139

3.3.1 OPV/OPE as Chromophores: Substituent Effect........139

3.3.2 Electronic Coupling Between Donor and Acceptor via the Bridge......146

3.3.3 Low Frequency Torsional Modes, Evidence for Quadratic Coupling...150

3.3.4 Excited State Decay: Non-Radiative Decay and Energy Gap Law......153

3.4 Conclusions........155

3.5 References........156

3.1 Introduction

3.1.1 Conducting Polymers

The discovery of electron conducting carbon-based medium in 1965 by two Australian physicists went unnoticed despite the fact that paper was published in *Nature*. In 1976, conducting carbon-based polymers were "re-discovered" by Shirakawa, MacDiarmid and Heeger.[1,2] Interests in these conducting polymers were transformed from a laboratory curiosity to new key technological applications when Tang and VanSlyke reported an electro-luminescent (EL) device based on aluminum *tris*(8-hydroxyquinolate) (Alq_3).[3]

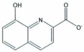

8-hydroxyquinolate

Soon after that, Friend at Cambridge reported the π-conjugated polymer, poly(*p*-phenylene vinylene) (PPV), could be fabricated into light emitting diode (LED's). The organic light emitting diode was constructed by successive deposition of a thin film of the emissive polymer by spin coating techniques onto a transparent conductive anode such as ITO (indium-tin-oxide) supported on glass. On the top of the active polymer layer is the cathode consisting of a vacuum-deposited metal layer, as shown in Figure 3-1.[4] Double charged injection by application of a forward bias voltage results in the formation of an electron/hole pair. The formed singlet-excited state emits a photon by radiative decay to the ground state. The OLED shown above relies on charge carrier dynamics such as inter-

and intra-molecular electron/hole or exciton formation and dissociation dynamics within a polymer or inter-chain hopping.

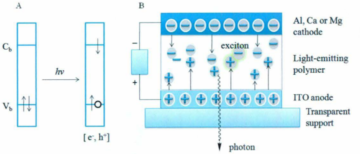

Figure 3-1. (A) Band gap excitation illustrating the formation of exciton, (B) Schematic presentation of a single-layer EL device adapted from ref[4].

The pioneering work of Friend illustrates one of the key conceptual advances toward the development of molecular electronics. The proof of concept experiments that illustrated the feasibility of molecular electronics came out of a collaboration between Mark Reed and James Tour.[5-7] The connection between charge carrier dynamics in conventional silicon semiconductors *vs.* molecular assemblies is discussed in section 3.1.2 below.

3.1.2 Bonding in π-Conjugated Polymers

Terminology. Electronic materials with electrical, magnetic and optical properties originated from the study of solid-state materials primarily by condensed matter physicists. The materials involved were metals or ionic solids, structures with infinite, three-dimensional lattices and no discrete building blocks. These are quite different from the molecular-based systems that dominate organic/inorganic chemistry. Organic materials are "molecules", where the molecular origins are clear and the weak intermolecular interactions whether they are a truly molecular solid with well-defined molecules held together in a molecular lattice by relatively weak interaction, or a polymer. Since the fundamental terminology and conceptual foundation for the field of electronic materials were developed by scientists with very different perspectives from that of an organic chemist, there is a correspondence between a variety of molecular and solid state terms as given in Table 3-1.

Table 3-1. Correspondence between a variety of molecular and solid state terms.[8]

Molecular	Solid State
Molecular orbital	Crystal orbital or bond orbital
HOMO	Valence band; top = Fermi level(Ef)
LUMO	Conduction band
HOMO-LUMO gap	Band gap (Eg)
LCAO-MO	Tight binding
Jahn-Teller distortion	Peierls distortion
Unpaired spin	Magnetic
Paired spin	Non-magnetic

Band Structure Theory and Charge Carrier Dynamics. From a theoretical point of view, the conjugated polymer can be approximated by an infinite linear system, and the electronic structure can be interpreted within the band theory framework in terms of a quasi-one-dimensional tight binding model. The "traditional" theoretical approach to photo-generation of carriers in low mobility materials involves the initial creation of bound geminate electron hole (e^-, h^+) pairs (excitons). However, in semiconductor polymers, the dominant "electronic" excitations are inherently coupled to distortions in the polymer backbone by the electron-phonon interaction, analogous to electron-vibrational coupling for electronic transitions in molecular systems.[9] As a result, the excitation in semi-conducting polymers is not consistent with the exciton model.[10,11] Photo-excitation across the π-π* band gap creates the self-localized, nonlinear excitations of conducting polymers: solitons (in degenerate ground-state systems), polarons and bipolarons (in non-degenerate ground state systems) as shown in Figure 3-2.[12,13] When the ground state

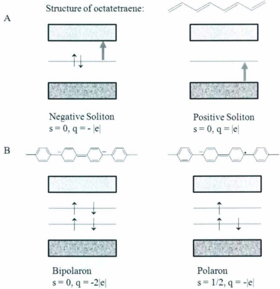
A
Structure of octatetraene:
Negative Soliton
s = 0, q = - |e|
Positive Soliton
s = 0, q = |e|
B
Bipolaron
s = 0, q = -2|e|
Polaron
s = 1/2, q = -|e|

Figure 3-2. (A) Band diagrams for positive and negative solitons with associated electronic transitions. (B) Schematic picture of a negative bipolaron in PPP and band diagram for a negative bipolaron (left); Schematic picture of a polaron in PPP and band diagram of an electron polaron (right), adapted from ref 13.

is non-degenerate, as in the poly(*p*-phenylenevinylene) (PPV) or poly(*p*-phenylene) (PPP), charged polaron pairs can either separate as mobile charged polarons or form bound polaron-excitons, *i.e.* neutral bipolarons bound by a combination of their Coulomb attraction and their shared distortion. Photoluminescence can be described in terms of the radiative decay of polaron-excitons.

Molecular Orbital Theory. The electronic structure for conjugated systems of finite size (oligomers or short polymer chains) can also be described with molecular orbital theory based on one-electron (e.g. Hückel or Hartree-Fock) treatment. The full systems are described as single large molecules. The electronic structure is interpreted in terms of individual molecular orbitals (MOs). Take a simple example of octatetraene (Figure 3-3), there is a highest occupied molecular π orbital (HOMO). Above it there exists a gap in the range of 1.5 eV to 3.0 eV and it extends up to the next level, the lowest unoccupied molecular π orbital (LUMO). Photo-excitation results in the redistribution of electron density in the ground state to that of the excited state with absorption energy given by

$$E_{abs} = E_o + \lambda_{vib} + \Delta E_{el} \qquad (3\text{-}1)$$

where E_{abs} is absorption energy, λ_{vib} is the vibrational reorganization energy and ΔE_{el} is the interelectronic repulsion energy.[9] In the weakly coupled limit, the coupling between the HOMO and LUMO is negligible and ΔE_{el} is neglible. The lowest energy electronic transition for octatetraene is the strongly allowed $1A_g \rightarrow 1B_u$, and corresponds to a transition from the highest occupied MO (HOMO) to the lowest unoccupied MO (LUMO). The "band gap" excitation in conjugated polymers populates the lowest energy excited singlet state, and the relaxation is a radiative $1B_u \rightarrow 1A_g$ emission, which repopulate the ground state.

However, in longer chains, where the π-bonds are spread over several nuclear coordinates, ΔE_{el} starts to become an important contribution to the band gap energy. As a result, configuration interaction (CI) has to be taken into account, thus, the electronic configuration is described by a linear combination of transitions between different orbitals (more precisely between the corresponding spin-adapted electronic wavefunctions).[9] For example, in polyenes the singly excited HOMO to LUMO + 1 or HOMO - 1 to LUMO configurations and the doubly excited HOMO to LUMO configuration strongly mix and result in the $2A_g$ state being located below the $1B_u$ state (Figure 3-3).

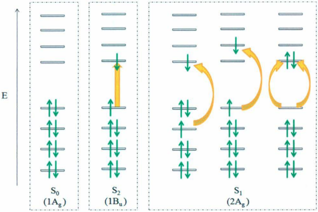

Figure 3-3. The main electronic configurations contributing to the ground state S_0 and the lowest singlet excited states S_1 and S_2.

There is an extremely important conceptual connection between the electron transfer in a bulk semiconductor, or a wire and the electron transfer in a polymer chain. The notion of a molecular wire is difficult to pin down since the electron transfer in long chain polymers do not display ohmic behavior. For example, a piece of copper wire is highly conductive due to its very low resistance. The conductance (g) is an extensive property as the conductance is inversely proportional to the resistance (R) and R is proportional to the length of the wire. Electron transfer between a bridged donor and acceptor is an intensive property because the rate constant for electron transfer (k_{ET}) is independent of the size.

Thermal non-adiabatic electron transfer across a molecular bridge or polymeric chain and conductance (R^{-1}) in a copper wire both depend on quantum-mechanical tunneling. Given that the rate constant for electron transfer ($k_{ET} = f(V)$) in molecular assemblies and the current ($I = f(V)$) in an ohmic copper wire both depend on the driving force, the current in a molecular assembly is given by

$$I = -e\, k_{ET}(eV) \qquad (3\text{-}2)$$

and the electron transfer rate constant is given by

$$k_{ET} \approx \exp\left(\frac{-eV}{2k_BT}\right) \qquad (3\text{-}3)$$

leads to the expression

$$g = \frac{1}{R} = \frac{dI}{dV} = \left(\frac{e^2}{2k_BT}\right) k_{ET} \qquad (3\text{-}4)$$

The relationship of conductance with the rate constant for electron transfer is an important contribution because in principle the magnitude of k_{ET} can be manipulated through synthetic control. If true, once the electron transfer parameters of a given system are known, energy between the HOMO and LUMO of a conjugated polymer may be engineered.[14]

3.1.3 Conformation and Structural Dynamics

Conjugated oligomers/polymers are a class of materials that are exceedingly useful in optoelectronic devices. Light excitation of the band gap (HOMO → LUMO transition) leads to the direct formation of an electron hole pair (e^-, h^+) or a bound exciton. The optical properties of conducting polymers have been extensively studied, yet, some issues still remain unresolved. Some of the issues, which are important to device applications, are the energetics and the associated dynamical processes that lead to the dissociation of a bound exciton into separated charge carriers. The binding energetics of a bound localized exciton range from as little as 0.1 eV up to as large as 1.0 eV.[15]

There have been two main branches of theoretical approaches to electronic properties of conjugated polymers and oligomers. One is using the band picture of delocalized electronic states to exploit a solid-state physics band theory. Another is using the picture of exciton to exploit the language of molecular spectroscopy derived from the isolated phenyl ring. A first remarkable feature of the optical spectra of PPV or oligomers and their derivatives is the presence of strong vibronic coupling. From the theoretical simulation of absorption and emission spectra, the presence of a vibronic progression with relaxation energy on the order of 0.15-0.2 eV in the long chain indicates that the electronic excitation produces a localized geometry relaxation around it (which extends over 20 Å) and as such can hardly be related to a pure transition from HOMO to LUMO.[16] For the longer chains, the transitions from HOMO - n to LUMO + n (n = 1, 2 ...)

are significantly mixed.

In order to understand the nature of upper lying excited states that have a strong coupling with the ground state, the absorption spectrum of an isolated PPV oligomer has been theoretically simulated including the effect of Coulomb interaction as shown in Figure 3-4.[16] Two types of excited states can be clearly distinguished from the simulated spectrum. The first type is the excited states with Gaussian distributions, centered on the hole position (not necessarily on the site where the hole is located due to the nature of the molecular orbitals contributing to the description of the excited states) and extending over a few repeat units (I, II, IV absorption bands). In these transitions, the photo-generated electron and hole are bound by Coulomb attraction and these states are mainly polarized along the direction parallel to the chain axis.[17,18] The effective binding radius of the exciton associated with these lowest energy electronic transitions is approximately 30 Å (on the order of five phenylene rings).[13] In addition to these weakly bound excitons, there

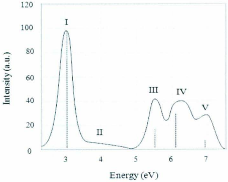

Figure 3-4. INDO/SCI simulated linear absorption spectrum of the OPV oligomer.[16]

are two other transitions (III, V absorption bands) from an occupied delocalized level to an unoccupied localized level (D → L*) or vice versa (L → D*). The resulting bound state has a binding energy of ~ 0.8 eV, and is a more tightly bound exciton (separated by a few phenylene rings). Such states are polarized mostly perpendicularly to the long chain axis. Under these conditions, the charge-transfer character is a favorable element for a fast dissociation of the exciton.

3.1.4 Matrix Effects

The experimental body of work concerning the study of conducting polymers, molecular constructs containing conjugated components, *etc.*, is extensive and widely varying due to the broad based interest and commercial potential for these materials. As such, the reported experimental conditions are extremely divergent ranging from spin-coated films, films comprised of differing blends of conducting polymers and dopants as well as solutions where the polymeric species may possess primary, secondary and tertiary structures, giving a glimpse of the rich conformational and morphological properties of these compounds.

In the work described below, the compounds have been synthesized and extensively characterized. The reported properties of these assemblies, in this work (see below) were determined in dilute solutions. The possibility still exists that intermolecular interactions such as excimer formation, aggregation, and the formation of colloidal properties may occur leading to inter and intramolecular processes, *i.e.* the formation of supramolecular adducts which may display properties quite distinct from individual components. The focus in this work has been to characterize the ground and excited state properties of the assemblies under dilute conditions where intermolecular interactions are minimal.

It is useful at this juncture to describe some of the more prominent intermolecular processes and interactions that have been documented in other π-conjugated assemblies. These are outlined below.

Interchain interactions modify the optical and electronic behavior of conjugated polymers. A number of experimental studies have highlighted the influence of interchain interactions when going from dilute solutions to the solid state.[19-22] In another case, *i.e.* in composites of conducting polymers and fullerene for photovoltaic applications, the discovery of charge transfer critically depending on charge separation of the photoexcited electron-hole pair over chains of different nature has attracted much attention on the understanding of interchain interaction effects in π-conjugated systems.

Interchain interactions have been probed in terms of the distance of interchain separation. For short interchain distances (*d*), *i.e.* *d* much shorter than the length of the molecule, the interaction between the conjugated chains, which varies with structure and morphology, results in either interchain charge-transfer-type coupling or interchain exciton-transfer-type coupling.[23]

Interchain Charge Transfer. The charge-transfer properties strongly depend on the extent of electronic coupling. The approximation of transfer integrals for electron (hole) transfer in two interacting oligomers (M_a and M_b) in organic semiconductors is given by KT-ESD approach (Koopmans' theorem)[24-26]

$$V = \frac{E_{L+1(H)} - E_{L(H-1)}}{2} \qquad (3\text{-}5)$$

where $E_{L+1(H)}$ and $E_{L(H-1)}$ are the energies of the LUMO + 1 and LUMO (HOMO and HOMO - 1) levels taken from the closed-shell configuration of the neutral state of a (M_a - M_b). The electronic coupling strongly depends on the mode of packing and decay exponentially with intermolecular distance. This simply explains the exponential decay of intermolecular overlap between the π orbitals when two oligomers are pulled apart. The electronic couplings can vary by as much as a factor of 3-4 between 3.4 and 4.0 Å, that is, within the typical range of intermolecular distances found in organic conjugated crystals and thin films.

The dynamics of photoinduced interchain electron transfer has been fully characterized with a study in hetero-junction of conducting polymers (as donors, D) and buckminsterfullerene (C_{60}) or its derivatives (as acceptor, A), as shown in Figure 3-5. The photoinduced electron-transfer reaction is energetically favorable because the excess energy is readily taken up by promoting the hole to a higher energy state in the π* orbital. Once the photoexcited electron is transferred to an acceptor unit, the resulting cation

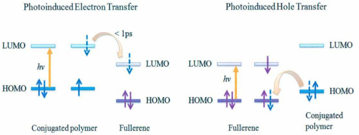
Photoinduced Electron Transfer
Photoinduced Hole Transfer
< 1ps
LUMO
hν
HOMO
LUMO
HOMO
Conjugated polymer
Fullerene
LUMO
hν
HOMO
Fullerene
LUMO
HOMO
Conjugated polymer

Figure 3-5. Molecular orbital energy diagram for photoinduced (left) electron (e^-) transfer and; (right) hole (h^+) transfer between semiconducting polymers and C_{60}.

radical in the conjugated polymer backbone is relatively stable. This results from the delocalized nature of the π-electrons.

Interchain Exciton Coupling. A great amount of theoretical and experimental research has been carried out for π-conjugated polymers on their solid-state photophysics. It is recognized that the fluorescence behavior will reflect the interchain exciton couplings, which is mediated by Coulombic coupling between transition densities on the separate chains. Since the presence of external fluorescence quenchers generally dictates the observed fluorescence quantum yield for systems in condensed phases when interchain exciton migration is present, the larger fluorescence quenching might reflect more efficient exciton migration to non-fluorescent energy traps (energetic and conformational disorder with some segments of comparatively low energy) in the solid films. In general, energy transfer between an excited chromophore and an acceptor molecule can occur by direct energy transfer (e.g. by a long-range dipole-dipole coupling up to 100 Å) or in a multistep mechanism consisting of intrachain energy migration (short-range incoherent hopping) on the polymer chain to a site close to the acceptor, followed by short-range energy transfer to the acceptor.

Interchain π-Stacking. *π-Stacked Aggregation* involving intimate π-π stacking of two or more chromophores in the ground state increases the number of chromophores in the direct vicinity of the quencher that favors dipole-dipole induced interchain exciton migration to the non-emissive energy traps, thereby enhancing the quenching efficiency. In addition, interaction between the conjugated chains leads to a splitting of the HOMO and LUMO levels of the isolated molecule into gerade and ungerade molecular orbitals that are fully delocalized over the whole complex (Figure 3-6). This usually leads to bathochromic shifts or new peaks in the spectra.

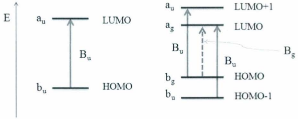

Figure 3-6. Energy levels of molecular orbitals for the isolated chain (left), and a cofacial dimer in the case of strong interaction (right).

π-stacked excimer, a pair of identical planar molecules in a cofacial arrangement, is formed as a result of attractive interactions arising upon the excitation of one of the molecules, which have a repulsive interaction in the ground state. An important aspect is that the emission spectrum of the excimer is red-shifted and the absence of vibronic feature with respect to that of the monomer and in many cases, the dual emission of the monomer and the excimer is observed. Typically, excimer formation occurs when the aromatic planes of the molecules are separated by 3-4 Å.

3.2 Results

3.2.1. Overview

The main structural motifs and geometries of the hydrogen terminated OPV/OPE co-oligomers (abbreviated as π-B) are illustrated in Scheme 3-1. One of the major themes explored in the studies described in this dissertation is the quantitative understanding of the structural, electronic and vibronic parameters that govern the excited state dynamics in the hybrid π-conjugated OPV/OPE co-oligomers. These OPV/OPE co-oligomers possess large absorption cross-sections in the UV-Vis spectral range and are the dominant light absorbing units for the chromophore-quencher C_{60}-(π-B)$_n$-C_{60} assemblies discussed in the next chapter. The characterization of the ground and excited state properties of these π-conjugated OPV/OPE co-oligomers is a prerequisite to understanding the photo-induced electron and energy transfer mechanisms in the C_{60}-(π-B)$_n$-C_{60} adducts.

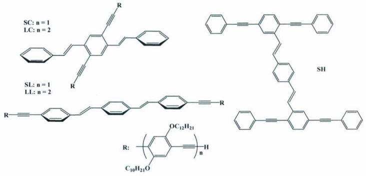

Scheme 3-1. Structure of hydrogen terminated OPV/OPE co-oligomers.

3.2.2. Ground State Conformation and FMO Calculations

The ground state structures and electronic properties of **SL** and **SC** OPV/OPE hybrid oligomers were calculated using both Hartree-Fock and density functional theory (DFT) methods.[1] The structures optimized at the HF/6-311G (d) level were used for subsequent single point calculations. The optimized structures of **SL** at different theoretical levels consistently give a planar, linear π-framework, in which the OPV unit adopts the *trans* conformation. The ground state structure of the isomeric **SC** where the 1, 2, 4, and 5 positions of the central phenyl ring bear substituents exhibits a twisted *trans* phenylenevinylene framework, with the OPE branch being virtually planar. The non-planarity of the OPV moiety of **SC** is presumably a result of the combination by steric and electronic interactions between the OPV/OPE substituents that are difficult to assess. The structures optimized at the HF/6-311G (d) level were used for subsequent single point calculations.

The frontier molecular orbital (FMO) properties for the linear and cruciform oligomers were calculated at HF/6-311G (d) level as shown in Figure 3-7. The HOMO and LUMO orbitals of **SL** are extensively distributed along the entire π-framework of the molecule, and the HOMO-LUMO gap is calculated as $E_g = 8.162$ eV. In slight difference, the HOMO and LUMO of **SC** are more populated at the central phenyl ring with a slight larger band gap of $E_g = 8.526$ eV.

---

[1] (a) The calculations were performed by Dr. Yuming Zhao and are included here for completeness. The pendant alkyloxy groups of the two molecules were replaced by OH groups to minimize the computational costs.

(b) *Chem. Eur. J.* Submitted.

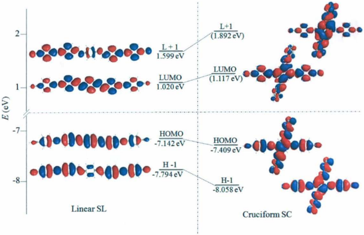
2
1
-7
-8
E (eV)
L + 1
1.599 eV
LUMO
1.020 eV
HOMO
-7.142 eV
H -1
-7.794 eV
Linear SL
L+1
(1.892 eV)
LUMO
(1.117 eV)
HOMO
-7.409 eV
H-1
-8.058 eV
Cruciform SC

Figure 3-7. FMO plots and energies for linear and cruciform OPV/OPE oligomers **SL** (left) and **SC** (right) calculated at the HF/6-311G (d) level. Note that the pendent alkyloxy groups were replaced by OH groups to save the computational time.

3.2.3 Absorption

UV-Visible spectral data for OPV/OPE oligomers and model sample 1,4-Bis-decyloxy-2-dec-1-ynyl-5-ethynyl-benzene **(DEB)** along with relevant literature data for comparative purposes are summarized in Table 3-2. Comparative UV-Visible spectra for the **SL**, **SC** and **SH** isomers respectively are shown in Figure 3-8. The OPV/OPE oligomers possess rich electronic spectroscopic properties. The UV-Vis absorption spectral envelopes for the OPV/OPE hybrid oligomers are broad and exhibit structure characterized by a number of resolved peaks and shoulders due to several underlying overlapping transitions and their vibronic components. The energetics and oscillator strengths of the underlying transitions that define the spectral envelope depend on the topology of the assembly, *i.e.*

linear (**SL**) *vs.* cruciform (**SC**), the number of (π-B)$_n$ spacers, and the nature of the terminal groups R (R = H, or C_{60}) and the attachment points for substituents.

Table 3-2. Absorption spectral data for OPV/OPE oligomers and model samples in $CHCl_3$.

Compound	SL	SC	LL	LC	SH	DEB	DSB	BPEB
$\lambda_{max}^{S_0\to S_1}$, nm	401	390	411	410	386	346	356	322
ε (×10^4 $M^{-1}cm^{-1}$)	1.1	5.4	41	3.2	3.8	0.71	6.74	4.98
$E_{op}^{S_0\to S_1}$, cm^{-1}	24,900	25.600	24,300	24,400	25,900	28,900	28,100	31,100

DSB:1, 4-distyrylbenzene.[27] BPEB: 1, 4-bis(phenylethynylene)benzene. [28]

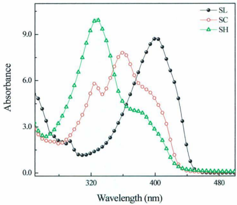

Figure 3-8. Absorption spectra of **SL**, **SC** and **SH** in $CHCl_3$ at 298 (± 3) K. The absorption spectra have been arbitrarily scaled to illustrate the most important differences.

3.2.3.1 Absorption Spectral Deconvolution

A more extensive analysis of the absorption spectral data through spectral deconvolution of the band envelopes for **SL** and **SC** coupled to time dependent density functional theory (TD-DFT) calculations was undertaken. The analysis described below is revealing in terms of understanding the electronic transitions and their different oscillator strengths as well as transition energies, which accrue from the specific orbital and spin parentage inherent in the ground and excited state wavefunctions. The absorption spectrum may be mathematically described as a function given by $A = f(\lambda)$. Recasting the absorption spectrum as a function of energy, $A = f(\bar{\nu})$, where $\bar{\nu}$ is the energy of the transition, followed by Gaussian deconvolution of the absorption spectrum provides the oscillator strength (f_{osc}) of the transitions and detailed information regarding electronic structure.[2] In this work, the energies and the number of bands required to fit the UV-Vis spectra for **SL** and **SC** were calculated from the first and second derivatives of the absorption spectrum. The band maxima were identified by the first and second derivatives,

$$\frac{dA(\bar{\nu})}{d(\bar{\nu})} = 0 \; and \; \frac{d^2(A(\bar{\nu}))}{d(\bar{\nu})^2} = 0 \qquad (3\text{-}6)$$

The criterion was satisfied and provides independent assessment of the number and energies of the underlying transitions that make up the spectral envelope.[29,30] The energies for each of the transitions were fixed and only the bandwidths of the individual Gaussians were allowed to vary to achieve an adequate fit. The results of the deconvolution procedure, the calculated and the observed spectral envelopes for **SL** and **SC** are shown in Figures 3-9 respectively. The fitted spectra and experimental spectra are seen to be in good agreement, *as the low energy side of the absorption band fits are adequately modeled in the deconvolution analyses.* However, cautious interpretation of the data is warranted as the residuals from the comparison between the calculated and experimental start to exhibit structure at higher energy.

---

[2] Spectral fitting or Franck-Condon line shape analyses of absorption and emission band envelopes using a multi-Gaussian model coupled to an iterative simplex or Levenberg-Marquadt non-linear least squares minimization procedures may be problematic due to several reasons. These include: the number of parameters used in the fits may give rise to several equivalent fits due to the number of shallow minima on the error surface; mathematical correlation between parameters which preclude a physical interpretation; and the difficulty in assessing the errors in the fitting parameters. The best strategy is to determine as many key parameters from experimental data such that the number of floating parameters is minimized in the fitting procedure.

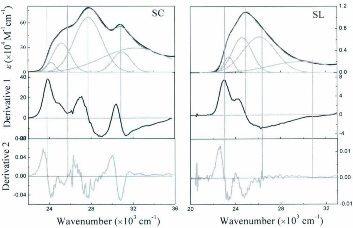

Figure 3-9. Gaussian deconvolution of OPV/OPE oligomers **SL** and **SC**.

3.2.3.2 TD-DFT Band Assignments of Multi-electron States

The TD-DFT calculations were performed on the structures optimized at the HF/6-311G (d) level (*vide supra*) to determine the transition energies, and the orbital parentage of the five lowest lying excited states for **SL** and **SC** respectively. The calculated transition energies, oscillator strengths from the TD-DFT calculations and the comparative data from the deconvolution analysis of absorption spectra are compiled in Table 3-3.

Table 3-3. UV-Vis spectral assignments for co-oligomers **SL** and **SC** based on TD B3LYP/6-31G (d) calculations.

Entry	Calculated[a]	Experimental	Contribution of electronic transitions	
	$\bar{\nu}$ (cm^{-1}); f_{osc}	$\bar{\nu}$ (cm^{-1}); f_{osc}	MO Characters	Coefficient (%)
SL		23420; 1.35×10^{-2}	$n \rightarrow \pi^*$	88
	23420; 3.550	24631; 6.01×10^{-2}	HOMO → LUMO	92
SC		24213(sh); 5.72×10^{-2}	unassigned	
	27773; 0.914	25445; 3.22×10^{-1}	$n \rightarrow \pi^*$	87
	27625; 0.176	26810; 8.60×10^{-1}	HOMO → LUMO	95
	29940; 2.304 33223; 0.185	27701; 2.35×10^{-1} 30934; 2.34×10^{-1}	H-1→LUMO HOMO → L+1	32 54

[a] Only transitions with oscillator strength (f) greater that 0.1 are taken into account.

3.2.4 Excited States: Chromophoric Bridges

3.2.4.1 Photochemistry

It is important to establish the photostability of the OPV/OPE assemblies prior to the characterization of the excited state properties, given the well-known *trans-cis* photoisomerization in stilbene, eq 3-7.

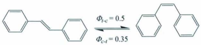

(3-7)

The *trans-cis* isomerization and *vice versa* may be accessed via direct irradiation or radiationless or "non-vertical" process using a triplet sensitizer.[31,32] The process where the $^3(\pi\pi^*)$ based transient state (abbreviated ^{3}t*) undergoes a conversion to a perpendicular triplet $^3p^*$ which possesses a twisted geometry about the olefin bond. The $^3p^*$ state may relax back to the ground state or result in the isomerization. Other photo-induced isomerization mechanisms include as the formation of a diradical species across the olefin bond. The quantum yield for photoinduced isomerisation ($\Phi_p < 0.001$) is greatly reduced in 1, 4-distyrylbenzene (DSB) relative to stilbene.[31,33]

Spectral changes as a function of irradiation time for **SC** in $CHCl_3$ solution are shown in Figure 3-10. The observation of photochemistry in **SC** is consistent with an isomerization process; however, quantitatively the process is much less efficient than that found in stilbene ($\Phi_{t\text{-}c}$ = 0.5 or $\Phi_{c\text{-}t}$ = 0.35 ($\lambda_{exc} = 313$ nm)). There are a number of possible isomer products that may form during the photolysis of **SC**, *i.e.* *EE*-DSB → *EZ*-DSB → *ZZ*-DSB (Scheme 3-2).[34]

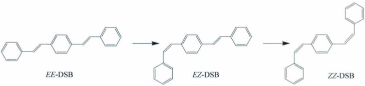

Scheme 3-2. Photoinduced isomerization of DSB with broadband white light excitation.

The observation of analogous photochemistry for **SC** would be reasonable given the literature precedence; however, the products have not yet been fully characterized.[3] When **SC** is terminated with C_{60} forming the **SC-(C$_{60}$)$_2$** assembly the photochemistry is significantly attenuated which allowed the acquisition of the transient absorption difference spectrum using 355 nm pulsed excitation, described in Chapter 4.[35]

---

[3] Wang, L.; Zhang, N.; Zhao, Y. Thompson, D. W. Manuscript in preparation.

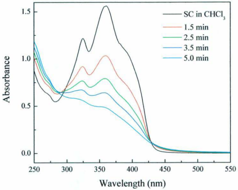

Figure 3-10. Photoinduced isomerization of **SC** in N_2 saturated $CHCl_3$ solution at 298 (± 3 K) using broadband white light excitation. The spectral changes are shown at the time intervals indicated in the top right corner of the spectra.

3.2.4.2 Radiative Decay: Electronic Structure

Steady-state UV-Visible and emission spectral data, quantum yields and excited state lifetime data of OPV/OPE oligomers are summarized in Table 3-4. Comparative emission spectra for the **SL**, **SC** and **SH** isomers respectively are shown in Figure 3-11.

As shown in Figure 3-11, emission spectra of **SC** and **SH** have very close λ_{max} at 428 nm and 425 nm respectively, but the emission of **SL** is red shifted with λ_{max} at 445 nm. Emission from **SL** and **SH,** both of them having terminal substituents, exhibit well-resolved vibronic structures with $\hbar\omega$ = 1310 cm^{-1} for **SH** and 1420 cm^{-1} for **SL.** However, the emission spectrum of **SC,** with central substituents at 2, 5 positions, is weakly structured with $\hbar\omega$ = 1300 cm^{-1}. Comparing the spectral profiles, **SC** with the central

Table 3-4. Absorption and emission data for OPV/OPE oligomers in $CHCl_3$ at 298 ± 3K.

Entry	SL	SC	LL	LC	SH	LH
$\lambda_{max}^{S_0\rightarrow S_1}$, nm	401	390	411	410	386	376
ε ($\times 10^4$ $M^{-1}cm^{-1}$)	1.1	5.4	41	3.2	3.8	0.46
$E_{op}^{S_0\rightarrow S_1}$, cm^{-1}	24,900	25,600	24,300	24,400	25,900	26,600
$\lambda_{em}^{S_1\rightarrow S_0}$, nm	445 710	428 725	456 710	452 725	425	439
$E_{em}^{S_1\rightarrow S_0}$, cm^{-1}	22,500 14,100	23,400 13,800	21,900 14,100	22,100 13,800	23,500	22,800
E_{abs} - E_{em}, cm^{-1}	2470	2210	2400	2270	2380	3820
$\phi_F^{S_1\rightarrow S_0}$	0.63	0.96	0.89	0.96	0.49	0.54
τ_F, ns (k_d, s^{-1})	1.0 (1.0×10^9)	2.7 (3.7×10^8)	<0.50 (2×10^9)	1.1 (9.0×10^8)	1.2 (8.3×10^8)	2.0 (5.0×10^8)
k_r, s^{-1}	5.3×10^8	3.6×10^8	1.8×10^9	8.7×10^8	4.1×10^8	2.7×10^8
k_{nr}, s^{-1}	3.1×10^7	1.5×10^7	2.2×10^8	3.6×10^7	4.2×10^8	2.3×10^8

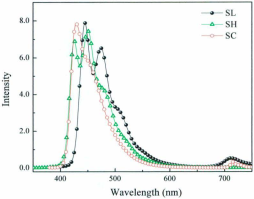

Figure 3-11. Emission spectra of **SL**, **SC** and **SH** in $CHCl_3$ at 298 (±3) K. The emission spectra have been arbitrarily scaled to illustrate the most important differences.

substituents is predicted to be more strongly coupled system than **SL** and **SH** with terminal substituents. In addition, the 0-0 vibronic transition is the strongest component for **SL** and **SC**, and the emission spectra of **SH** is not 0-0 peaked.

3.2.4.3 Emission Spectral Fitting

The emission spectra of the OPV/OPE oligomers were analyzed by the single, average mode Franck-Condon line shape analysis as described in Chapter 1, and the fitting example is shown in Figure 3-12. The form of equation is given by[4]

$$I(\bar{\nu}) = \sum_{\upsilon=0}^{\upsilon=5} \left\{ \left(\frac{E_0 - \upsilon\hbar\omega}{E_0} \right)^3 \cdot \left(\frac{S^{\upsilon}}{\upsilon!} \right) \cdot \exp\left[-4\ln 2 \left(\frac{\bar{\nu} - E_0 + \upsilon\hbar\omega}{\Delta\bar{\nu}_{1/2}} \right) \right] \right\} \qquad (3\text{-}8)$$

where E_0 is the energy gap for the $\upsilon = 0$ to $\upsilon' = 0$ transition. It is valid in the weak coupling limit, $E_0 \gg S\hbar\omega$, low temperature limit, $\hbar\omega \gg k_BT$, and assumes quantum spacing is same in the ground and excited states. The average mode is a weighted average of all the modes that are coupled to the transition given by eq 3-9.

$$\hbar\omega = \sum_j S_j \hbar\omega \Big/ \sum_j S_j \qquad (3\text{-}9)$$

The spectral fitting parameters E_0, S, $\Delta\bar{\nu}_{1/2}$ and $\hbar\omega$ are listed in Table 3-5. These parameters can be used to calculate the vibrational overlap factors for non-radiative

---

[4] Two modes fitting:

$$I(\bar{\nu}) = \sum_{\upsilon_M=0}^{5} \sum_{\upsilon_L=0}^{15} \left\{ \left(\frac{E_{00} - \upsilon_M\hbar\omega_M - \upsilon_L\hbar\omega_L}{E_0} \right)^3 \cdot \left(\frac{S_M^{\upsilon_M}}{\upsilon_M!} \right) L(\upsilon_L) \cdot \exp\left[-4\ln 2 \left(\frac{\bar{\nu} - E_{00} + \upsilon_M\hbar\omega_M + \upsilon_L\hbar\omega_L}{\Delta\bar{\nu}_{1/2}} \right) \right] \right\}$$

$$L(\upsilon_L) = S_L^{\upsilon_L} \left(\frac{X^m m!}{(m + \upsilon_L)!} \right) \left[\sum_{l=0}^{\infty} \frac{(m + \upsilon_L)!\,(-S_L)^l}{(m - l)!\,(l + \upsilon_L)!\,m!} \right]^2, (\upsilon_L \geq 0)$$

decay ln[FC(calc)] by using eq 3-10 in the limit of a single medium-frequency acceptor mode.[36] For OPV/OPE oligomers, S and $\hbar\omega$ are the average values for contributions from a series of stretching modes mainly C=C and C≡C in character.[37,38] The solvent and low frequency stretching and torsional modes treated classically are included in $\Delta\bar{\nu}_{1/2}$.

$$\ln[\mathrm{FC(calc)}] = -\frac{1}{2}\left[\frac{\hbar\omega E_0}{(1000cm^{-1})}\right] - S - \left(\frac{\gamma E_0}{\hbar\omega}\right) + (\gamma+1)^2\left(\frac{\Delta\bar{\nu}_{1/2}}{\hbar\omega}\right)^2 / 16\ln 2 \qquad (3\text{-}10)$$

In eq 3-10, E_0, $\hbar\omega$ and $\Delta\bar{\nu}_{1/2}$ are in cm^{-1} and γ is given by,

$$\gamma = \ln\left(\frac{\mathrm{E_0}}{S\hbar\omega}\right) - 1 \qquad (3\text{-}11)$$

Calculated values for ln[FC(calc)] are listed in Table 3-5, they are related to the rate constant for nonradiative decay, k_{nr}, by,

$$\ln(k_{nr}) = \ln\beta_0 + \ln[\mathrm{FC(calc)}] \qquad (3\text{-}12)$$

β_0 contains the vibrationally induced electronic coupling matrix element, which dynamically couples the initial and final electronic states. $\ln\beta_0$ is given by

$$\ln\beta_0 = \left(\frac{c_k^2\omega_k\sqrt{\pi/2}}{1000}\right) \qquad (3\text{-}13)$$

and

$$\left(\Delta\bar{\nu}_{1/2}\right)^2 = \left(\Delta\bar{\nu}_{1/2}\right)_0^2 + \lambda_o 16k_{\mathrm{B}}T\ln 2 \qquad (3\text{-}14\text{ a})$$

In this case, the intrinsic bandwidth $\left(\Delta\bar{\nu}_{1/2}\right)_0$ is assumed much smaller than $\Delta\bar{\nu}_{1/2}$. The magnitude of $\Delta\bar{\nu}_{1/2}$ can be experimentally determined by the temperature dependence studies, which lies outside the scope of this investigation. Within the assumptions stated above, eq 3-14 a is reduced to

$$\left(\Delta\bar{\nu}_{1/2}\right)^2 = \lambda_o 16k_{\mathrm{B}}T\ln 2 \qquad (3\text{-}14\text{ b})$$

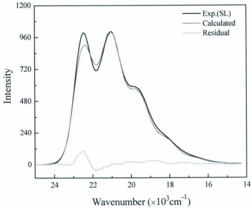

Figure 3-12. The result from the emission spectral fitting analysis for **SL** by eq 3-8. The observed emission spectrum for **SL** in $CHCl_3$ solution at 298±3K is shown in black. The calculated spectra using eq 3-8 with E_0 = 22,937 cm^{-1}, S_m = 1.27, $\Delta\bar{\nu}_{1/2}$ = 423 cm^{-1} and $\hbar\omega$ = 1450 cm^{-1} is shown in red. The residual is shown in green. The fit is seen to be adequate even though there is structure in the residuals shown in green. The largest deviation is found at 23,000 cm^{-1} and the deviation accounts for < 10 % of the integrated intensity.

Table 3-5. The spectral fitting parameters for OPV/OPE oligomers.

Entry	E_{em} (cm^{-1})	E_0 (cm^{-1})	S_m	S_l	$\Delta\bar{\nu}_{1/2}$ (cm^{-1})	$\hbar\omega$ (cm^{-1})	E_{abs}-E_{em} (cm^{-1})	λ_t (cm^{-1})	λ_{vib} (cm^{-1})	λ_o (cm^{-1})	ln[FC]	γ
SC	23,400 21,100	23,200	1.10		1260	1300	2280	1140	1430	686	-41.1	1.79
LC	22,100 20,700	21,900	0.85		1220	1450	2270	1140	1230	644	-37.4	1.88
SL	22,500 21,200 14,100	22,900	1.27	2.11	423	1450	2470	1240	1840	713	-33.9	1.52
LL	21,900 20,600 19,100	22,100	1.03	1.07	809	1450	2400	1200	1490	614	-35.3	1.69
SH	23,500 22,200 20,800	23,500	1.70		1260	1350	7050	3530	2290	695	-33.0	1.33
LH	22,800 21,500	23,400	1.40	2.63	782	1550	3820	1910	2170	266	-30.7	1.38

3.3 Discussion

The modular synthetic methodologies employed here allow systematic variation of key structural components in the {R-(π-B)$_n$-[OPV]$_{C/L}$-(π-B)$_n$-R} assembly. For example the length of the linear assemblies and the backbone of the cruciforms can be extended by placing OPE spacers (denoted as (π-B)$_n$, where n is the number of spacers) between the central OPV fragment and the terminal group R (where R= H or C_{60}).

3.3.1 OPV/OPE as Chromophores: Substituent Effect

Model Compounds

1,4-Bis-decyloxy-2-dec-1-ynyl-5-ethynyl-benzene (DEB). The absorption and emission spectra of monomeric DEB is shown in Figure 3-13. The absorption spectrum of DEB is dominated by an intense structured band at 335 nm (ε = 8010 M^{-1}cm^{-1}, E_{op}= 29,900 cm^{-1}) with a well-defined shoulder at 346 nm (ε ~ 7900 M^{-1}cm^{-1}, E_{op} = 29,900

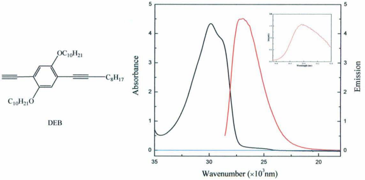

Figure 3-13. Absorption (black) and emission (red) spectra for DEB in N_2 saturated $CHCl_3$ solution at 298 (± 3) K. The emission was obtained following λ_{exc} = 335 nm excitation. Insert: emission at 715 nm.

cm^{-1}) assigned to a $S_0 \rightarrow S_1$ transition. There is a low intensity absorption $n \rightarrow \pi*$ that tails out past 400 nm. Light excitation into the $S_0 \rightarrow S_1$ transition leads to an intense emission band at 367 nm (ϕ_f = 0.62, E_{em} = 27,250 cm^{-1}) assigned to a $S_1 \rightarrow S_0$ radiative transition ($\tau \sim$ 2 ns). The weak emission band at 715 nm tentatively assigned to a $T_1 \rightarrow S_0$ phosphorescence.

1,4-Bis(phenylethynyl)benzene (BPEB) and Oligo(*p*-phenyleneethynylene)s (OPEs).

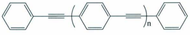

BPEP: n = 1

Figure 3-14. Structure of 1,4-bis(phenylethynyl)benzene (BPEB) and oligo(*p*-phenylene-ethynylene)s (OPEs).

The UV-Vis spectrum of BPEB features a series of partially resolved absorption bands between 250 and 350 nm, with a sharp band-edge at the red end of the absorption profile. The fluorescence shows some vibrational fine structure with peaks at 346, 362, and 375 nm, tailing to the red.[28] OPEs exhibit intense absorption in the UV-Visible, which shifted to the low energy values with increasing chain length of the OPEs. OPEs are also highly emissive. The optical spectra of OPEs are characterized by a substantial asymmetry between absorption and fluorescence, together with a very small Stokes shift. These effects have been explained in terms of torsional disorder and quadratic coupling between the ground and the first singlet excited states, which will be discussed later.[39,40]

1,4-distyrylbenzene (DSB) and Oligo(*p*-phenylenevinylene)s (OPVs). 1, 4-distyryl-benzene (DSB) possesses C_{2h} symmetry and the lowest energy absorption band is assigned to a highly allowed $1A_g \rightarrow 1B_u$ ($\pi \rightarrow \pi^*$) or $S_0 \rightarrow S_1$ transition (Figure 3-15). Once formed the $\pi \rightarrow \pi^*$ excited state decays with $\Phi_{em} \sim 1$ ($\tau \sim 1$ ns) with little or no Stokes shift.

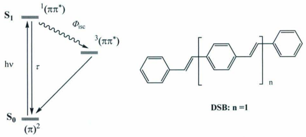

Figure 3-15. Energy diagram and structure of DSB and OPVs.

Increasing the number of styryl units from n = 1 for DSB to n = 10 does not significantly change the shape of the absorption band envelope which retains the vibronic structure, however, a systematic decrease in the energy of $S_0 \rightarrow S_1$ transition as n is increased.[41] The observation of a systematic red shift in absorption energy as the number of monomers, n, incorporated into the oligomer increases is often observed and is ascribed to the increased electron delocalization which lowers the energy of the $\pi \rightarrow \pi^*$ transition. The interpretation that delocalization in oligomers decreases the transition energy is not quite correct.

The dipole allowed $\pi \rightarrow \pi^*$ transition occurs from the HOMO to next highest molecular orbital, in this case it is often inferred that the acceptor MO is the LUMO which remains unperturbed. This would be correct if the compound was undergoing a one-electron reduction as given by

$$\mathrm{DSB} + e^- \longrightarrow [\mathrm{DSB}]^{-\cdot} \qquad (3\text{-}15)$$

and the HOMO is filled. The optical transition generates a bound exciton, where the hole (h^+) left in the HOMO, which generates a Coulombic attraction to the electron and reduces the excitation energy. Therefore, the commonly held notion that as the conductive polymer increases in size, the concomitant decrease in the band gap energy is due to delocalization of the excited electron is incorrect. The exciton frequency ω with increasing n is given by

$$\omega\,(n) = \omega_o + \frac{\Delta\omega}{n} \qquad (3\text{-}16)$$

where ω_o is the frequency of the monomer.

Distyrylbenzene: Terminal Substituents [DSB $(\mathrm{R_{T\text{-}1}})_2$] *vs.* Central Substituents [DSB(2,5-$\mathrm{R_{M\text{-}1}}$)$_2$]. The asymmetry between the absorption and emission spectra in OPE is also observed in oligo(*p*-phenylenevinylene)s. The exciton model for nonlinear quadratic coupling of the torsional motions to the electronic transition as discussed above also accounts for this anomalous feature for OPVs.

In the search for blue-light-emitting materials, the relationship between the molecular geometry and the optical properties of oligo(*p*-phenylenevinylene)s have been investigated both theoretically and experimentally.[18,42-46] Due to the well-defined chemical structure together with their improved solubility and processibility, *trans, trans*-distyrylbenzene (DSB) and their derivatives, oligo(*p*-phenylenevinylene)s with short chain lengths, have been synthesized as the model to investigate their absorption, luminescence and electronic properties. Based on the absorption and fluorescence spectra of the DSB derivatives with alkoxy substituents, DSB derivatives can be classified into two groups: terminal substituted and central substituted DSB. The absorption spectra of DSB with terminal substituents are weakly structured, while those with central substituents are composed of two structureless broad bands with the peak energies of ~3.2 and 3.7 eV.[44] Therefore, substitution to the terminal phenyl rings is predicted to be much less effective, irrespective of the number of substituents. Furthermore, structureless spectral profiles observed for central substituted DSB indicate that each vibronic level is strongly coupled into the torsional motion and result in the significant broadening of each vibronic band. According to the quadratic coupling model, this suggests that DSB with central substituents have non-planar conformations in solution. Unlike the absorption spectra, emission spectra with well-resolved vibronic structures are observed for all DSB derivatives other than DSB with 2, 5-alkoxy substituents.

In order to investigate the influence of substituents in the terminal phenylene rings of DSB, the derivatives with electron withdrawing and/or electron donating substituents at the *ortho-*, *meta-* and *para-* positions of the terminal phenylene subunits are classified into two groups. One is symmetrically substituted DSB (with two donors or two acceptors) at *para-* (*ortho-* or *meta-*) position, and the other is asymmetrically substituted DSB (with one donor and one acceptor) at *para-* (*ortho-* or *meta-*) position. The asymmetrically substituted DSB shows a significant shift towards longer wavelengths, and its vibronic features are not clearly visible.[46,47] Such a red shift is consistent with the fact that donating substituents will increase the HOMO energy and withdrawing substituents will lower the LUMO energy level, resulting in a smaller energy gap (Figure 3-16). The

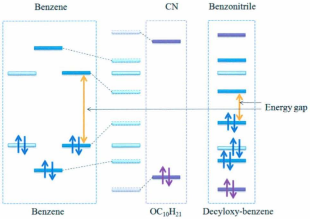

Figure 3-16. MO diagram for substituted DSB by application of perturbation.

excitation for asymmetrically substituted DSB is generally dominated by the intramolecular charge-transfer excitation, which gives a strong absorption spectrum and usually is featureless and rather symmetrical (will be discussed in Chapter 5 and 6). The emission spectrum of asymmetrically substituted DSB is more red shifted with no vibronic features. The peak broadening is possibly due to the dipole-dipole interaction among the polar molecules and interaction with the surrounding solvent. For the symmetrically substituted DSB, both absorption and emission show vibronic structures, which are very similar to that of unsubstituted DSB. With respect to the influences of substituents in the terminal phenylene subunits, the *meta*-DSB derivative exhibits a relatively blue shift in the optical transition spectra for the absorption and emission as compared to the *para*- and *ortho*-DSB derivatives.[27,48-50] Therefore, *para*- and *ortho*-substituents have the stabilization effect, which is indicated by the plot of absorption energy *vs.* $\sigma(p)$ as shown in Figure 3-17. With respect to the emission energy, substituents are less effective. This is consistent with the evidence that the molecular structure of the excited state is more constrained to a planar geometry.

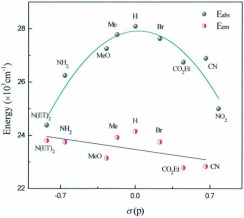

Figure 3-17. Dependence of optical energy (E_{abs} and E_{em}) for DSB on Hammet $\sigma(p)$. Data from ref 27.

To study the vibronic structure in more detail for central and terminal substituted DSB, the Franck-Condon band shape analysis shows that the 0-0 vibronic transition is the strongest component and the 0-0 vibronic transition energy for central substituted DSB are lower than those for terminal substituted DSB.[51] Similar to what is observed for the absorption spectra, all emission spectra are 0-0 peaked ($S < 1$) and the vibronic components have slightly narrower bandwidths than that for the absorption, which indicates that there is a steeper potential surface for torsional motions in the excited state than in the ground state. The primary evidence to support this conclusion is that the vibronic structure is more pronounced in the fluorescence spectrum than in the absorption spectrum.

3.3.2 Electronic Coupling Between Donor and Acceptor via the Bridge

Electronic Coupling. One of the important themes explored in this work is the relationship between the extent of π bonding and the molecular donor and/or acceptor components that make up the assembly as well as the resulting electronic properties. In the weak coupling limit, the donor and acceptor components in the assembly display properties that are linear combinations of the component fragments.[52] In the other extreme where the donor and acceptor components are strongly coupled, the energetics of chemical bonds between the donor and acceptor are significantly enhanced and the properties of the assemblies are quite distinct from those of the components. The extent of coupling is dominated by the nature and the extent of π bonding interactions. In conjugated systems such as poly-(*p*-phenylenevinylene), the π bonding orbitals are spread over several nuclear coordinates, whereas σ bonds tend to be localized between two nuclear coordinates in the assembly. The ramifications of the bonding arrangements are central to the electronic structure and the physical properties of the assembly. Therefore, using the criteria listed above, the linear assemblies lie in the weakly coupled limit in the ground state based on the similar shape and energetics of the spectral band envelopes.

The cruciform systems appear to be strongly coupled systems as evidenced by the dramatic variation of **SC** and **LC** absorption spectra respectively (Figure 3-18).

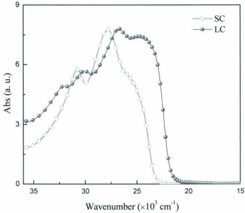

Figure 3-18. Absorption spectra of **SC** (o) and **LC** (●) obtained in $CHCl_3$ at 298 ± 3 K.

Electronic Excited States. The spectrum of **SL** obtained in $CHCl_3$ solution at 298 ± 3 K displays two resolved bands at 401 nm (24,900 cm^{-1}; $\varepsilon(\bar{\nu}) = 1.1 \times 10^4 M^{-1} cm^{-1}$) and 293 nm (34,100 cm^{-1}; $\varepsilon(\bar{\nu}) = 2.5 \times 10^3 M^{-1} cm^{-1}$); whereas **SC** has a prominent shoulder at 390 nm (25,600 cm^{-1}; $\varepsilon(\bar{\nu}) = 5.4 \times 10^4 M^{-1} cm^{-1}$) and two resolved bands at 360 nm (24,900 cm^{-1}; $\varepsilon(\bar{\nu}) = 7.8 \times 10^4 M^{-1} cm^{-1}$) and 324 nm (30,900 cm^{-1}; $\varepsilon(\bar{\nu}) = 5.4 \times 10^4 M^{-1} cm^{-1}$). A cursory inspection of the band envelopes for **SL** and **SC** indicates that the visible spectra are dominated by $\pi \rightarrow \pi^*$ transitions ($S_0 \rightarrow S_n$) as the extinction coefficients are consistent with electric dipole allowed transitions.

The single configuration of one electron absorption model has provided a basis for understanding $\pi \rightarrow \pi^*$ electronic transitions as a transition of an electron from a ground state occupied molecular orbital to an anti-bonding acceptor orbital, *i.e.* an $S_0 \rightarrow S_1$ transition to form the Franck-Condon excited state. A more extensive analysis of the absorption spectral data through spectral deconvolution of the band envelopes for **SL** and **SC** coupled to time dependent density functional (TD-DFT) calculations was undertaken. The analysis described below is revealing in terms of understanding the electronic transitions and their different oscillator strengths as well as transition energies that accrue from the specific orbital and spin parentage inherent in the ground and excited state wavefunctions. The TD-DFT results suggest that a more sophisticated model is required to explain electronic transitions. The electronic transitions for **SL** and **SC** possess intensities consistent with electric dipole allowed $\pi \rightarrow \pi^*$ transitions ($\varepsilon(\bar{\nu}) > 10^3$ M^{-1} cm^{-1}), and there is good agreement between the experimental and calculated transition energies especially for the HOMO-LUMO band gaps.

The calculated FMO plots shown in Figure 3-7 encompass both the OPV and OPE components and thus the electronic transitions between donor and acceptor MO's cannot be viewed as a superposition of the spectroscopic properties of the individual components. It is not valid for the cruciform systems that the electronic coupling arguments for the ground state in the weakly coupled limit are commonly made for systems even with extensive π bonding. Following the discussion outlined by McCusker,[53] the ground and excited state energetics as well as the corresponding transitions between states are best described as composite multi-electronic donor (designated (ϕ_0)) and virtual acceptor (designated (ϕ_v)) states. The orbital parentage for the $\phi_0 \rightarrow \phi_v$ optical excitations are predicated on the fractional composition of FMO's that define ϕ_0 and ϕ_v. A cursory analysis of the electron density maps clearly show the shape of spectral envelopes for **SL** and **SC** are due to a several underlying $\phi_0 \rightarrow \phi_v$ optical excitations (Figure 3-19).

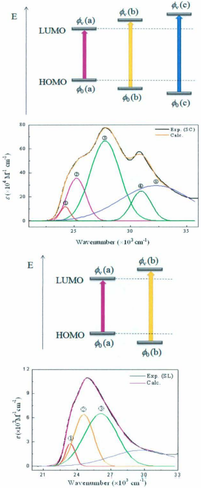

② $(\pi\pi^*)_1$ ϕ_0 (a) → ϕ_v (a)

HOMO → LUMO

③ $(\pi\pi^*)_2$ ϕ_0 (b) → ϕ_v (b)

H-1 → LUMO (59%)

HOMO → L+1 (36%)

④ $(\pi\pi^*)_3$ ϕ_0 (c) → ϕ_v (c)

H-1 → LUMO (32%)

HOMO → L+1 (54%)

⑤ $(\pi\pi^*)_4$ ϕ_0 (d) → ϕ_v (d)

H-1 → L+1 (91%)

② $(\pi\pi^*)_1$ ϕ_0 (a) → ϕ_v (a)

HOMO → LUMO

③ $(\pi\pi^*)_2$ ϕ_0 (b) → ϕ_v (b)

H-1 → L+1 (76%)

HOMO → L+2 (16%)

Figure 3-19. The shape of spectral envelope of **SC** (top), and **SL** (bottom) along with several underlying $\phi_0 \rightarrow \phi_v$ optical excitations.

3.3.3 Low Frequency Torsional Modes, Evidence for Quadratic Coupling

Conformational Dynamics. Oligo(*p*-phenyleneethynylene)s (OPEs) are well documented.[39,54,55] Other than essential feature of asymmetry, the absorption spectra of OPEs show an unusual change in shape with oligomer length. The absorption band associated with the $S_0 \rightarrow S_1$ transition is broad and structureless, while the corresponding fluorescence band is narrower and structured. In addition, the Stokes shift between absorption and emission bands is very small. These effects have been explained in terms of the nonlinear quadratic coupling of the torsional motions to the electronic transition (Figure 3-20).[56,57]

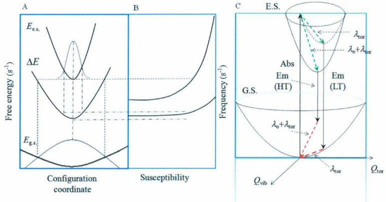
A
B
C
$E_{e.s.}$
ΔE
$E_{g.s.}$
Free energy (s^{-1})
Configuration coordinate
Susceptibility
Frequency (s^{-1})
E.S.
G.S.
λ_{tor}
$\lambda_o+\lambda_{tor}$
Abs
Em (HT)
Em (LT)
$\lambda_o+\lambda_{tor}$
λ_{tor}
Q_{tor}
Q_{vib}

Figure 3-20. Quadratic-coupling model. A: The ground state ($E_{g.s.}$) and excited state ($E_{e.s.}$) potentials are harmonic, leading to Gaussian equilibrium population distributions in both the ground and excited states. The potentials have different curvatures, but are not displaced, leading to a quadratic coupling ΔE. B: The absorption and emission spectra result from projecting the ground and excited state populations, respectively, onto the coupling. Both spectra have a sharp cutoff at low frequency, but they have different high-frequency tails (upper, absorption; lower, emission). Reproduced from ref [56]. C: Representation of the quadratic coupling in three-dimension.

The spectral asymmetry between the absorption and emission spectra of these two state systems have been ascribed to significant conformational changes between the ground and excited states of these materials (Figure 3-21). More constrained to a planar geometry in the excited state is due to the effect of quinoidal/cumulenic configurations. Therefore, the $S_0 \rightarrow S_1$ absorption spectrum is generated from many superimposed torsionally excited initial states and gives rise to broad subbands. In the excited electronic state, the rotation barrier of the phenyl rings is substantially higher than that in the ground electronic state. Therefore, the excited state relaxes toward a planar structure, and this causes the emission spectrum to be narrower than the absorption spectrum and to be vibrationally resolved.

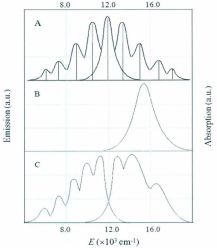

Figure 3-21. Vibrational transitions in absorption and emission within the harmonic Condon approximation. (A) coupling in a double-bond stretching mode, (B) coupling in a ring-torsional mode, (C) coupling in both modes, adapted from ref 58.

The effect of torsional disorder on the fluorescence intensity is also strongly dependent on the nature of the substituent on the phenyl groups. This has been qualitatively discussed in term of the excitonic nature of the S_1 state.[54] For linear and cruciform OPV/OPE oligomers discussed in this thesis, the phenyl moiety has two alkoxy substituents at 2 and 5 *meta-* positions where two alkoxy substituents are in *para-* position to each other. In this case, the $S_0 \rightarrow S_1$ transition dipole moment of alkoxy substituted phenyleneethynylene (ROPE) has been reported not to be aligned along the long-axis of the molecule defined by the triple bond. If the molecule is torsionally disordered, the short-axis components of the monomeric transition dipoles are randomly oriented and then cancel. Therefore, the total dipole moment is only from the contribution of the long-axis components (Figure 3-22). However, if the oligomer is planar, both the long- and short-axis components interact and the total dipole moment will be larger than that with torsional disorder. Considering the bulkiness of $C_{10}H_{21}O$ substituents, such a planar

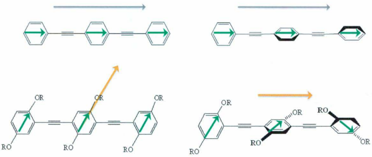

Figure 3-22. The exciton model for OPEs (top) and RO substituted OPEs (bottom). The short arrows are the transition dipole moments of the monomeric units and the long arrows are the transition dipole moment of the oligomers, adapted from ref [54].

geometry is strongly disfavored by steric hindrance relatively to the other, and then the oscillator strength of the OPE would no longer depend on the torsional disorder.

3.3.4 Non-radiative Decay and Energy Gap Law

The increased energy gap results in a decrease in the non-radiative decay rate constant as predicted qualitatively by the energy gap law in the form,

$$(\tau)^{-1} \approx k_{nr} \propto \exp\left(\frac{\gamma E_0}{S\hbar\omega_M}\right) \qquad (3\text{-}17)$$

By using the quantitative relationship in eq 3-17 and the spectral fitting parameters in Table 3-5, the analysis indicates that the fundamental photophysical behavior of the DSB excited state is essentially unchanged by the placement of substituents in 1,4 positions. Excited state decay kinetics and inefficient photochemistry in solution is evidence for a related pattern of photophysical events in stilbene, and DSB as proposed above, following its formation by photoinduced *cis-trans* isomerization.

Electronic Coupling in Rotamers. Steric interaction leads to a dihedral angle between rings. When the rings are in a perpendicular position with dihedral angle being 90°, there is no steric interaction, but the perpendicular position can also decouple the olefin P_z orbitals from the other P_z orbitals in the phenylene ring. Steric interaction varies with torsion about the single bond between phenylene and vinylene subunits. In eq 3-18,

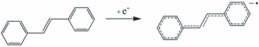

(3-18)

the reduction of the stilbene leading to the population of the $\pi*$ level results in the reduction of a single ring, which then cause the bond length change (Δq) and electron-electron repulsion. To minimize Δq and electron-electron repulsion, the ring will undergo resonance stabilization, which spreads the excited electron in the π* over a large set of nuclear coordinates. For stilbene, the resonance stabilization derived from the linear combination of two P_z orbitals, one from the phenylene and the other from the olefin subunit, is given by

$$\langle 2P_z|2P'_z\rangle = K^2\left(\frac{2a}{Z} - L\right)[\exp(-ZL/2a)]\cos\theta \qquad (3\text{-}19)$$

Where *K* is a constant, *a* is the Bohr radius, *L* is distance between the atoms and θ is the angle between the z-axes. L is the bond length, about 1.35 Å. Eq 3-19 reveals that the electronic coupling between the phenylene and vinylene subunit fluctuates with the torsion angle, as shown in Figure 3-23.

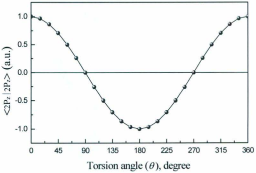

Figure 3-23. Plot of the electron-electron repulsion *vs.* torsional angles in stilbene.

3.4 Conclusions

Detailed analysis of the absorption and emission spectra of cruciform (**SC**), linear (**SL**) and H-mer (**SH**) has been performed and the data show the following trends.

1. The absorption spectral manifolds arise due to a superposition of underlying $\pi \rightarrow \pi*$ transitions that are best described as composite multi-electronic donor and acceptor states.
2. The pattern of transitions and the orbital contribution for each transition observed for **SC**, **SL** and **SH** are similar in energy, but the intensities of the underlying absorption bands depend on the placement of the OPE components.
3. The absorption bands are broadened due to a distribution of rotamers in the ground state. The asymmetry between the absorption and the emission spectra are consistent with the quadratic coupling model of Berg.
4. Spectral fitting of the emission bands shows:
   - ➢ S_m (Huang Rhys Factor) systematically decreases as more OPE monomers are introduced to lengthen the bridge.
   - ➢ With OPE incorporated $\hbar\omega$ increases due to the participation of C≡C vibrational modes in the excited state decay.
   - ➢ The electron redistribution in the excited state does not dramatically change the dipole moments $\Delta\vec{\mu}$. Therefore, the solvent reorganization energy is small.

3.5 References

(1) Shirakawa, H.; Louis, E. J.; MacDiarmid, A. G.; Chiang, C. K.; Heeger, A. J. *Chem. Commun.* **1977**, 578-580.

(2) Chiang, C. K.; Fincher, C. R.; Park, Y. W.; Heeger, A. J.; Shirakawa, H.; Louis, E. J.; Gau, S. C.; MacDiarmid, A. G. *Phys. Rev. Lett.* **1977**, *39*, 1098-1101.

(3) Tang, C. W.; VanSlyke, S. A. *Appl. Phys. Lett.* **1987**, *51*, 913-915.

(4) Grimsdale, A. C.; Chan, K. L.; Martin, R. E.; Jokisz, P. G.; Holmes, A. B. *Chem. Rev.* **2009**, *109*, 897-1091.

(5) Reinerth, W. A.; Joneslly, L.; Burgin, T. P.; Zhouz, C.-W.; Muller, C. J.; Deshpande, M. R.; Reed, M. A.; Tour, J. M. *Nanotechnology* **1998**, *9*, 246-250.

(6) Reed, M. A.; Zhou, C.; Muller, C. J.; Burgin, T. P.; Tour, J. M. *Science* **1997**, *278*, 252-254.

(7) Zhou, C.; Deshpande, M. R.; Reed, M. A.; Jones, L.Tour, J. M. *Appl. Phys. Lett.*, *71*, 611-613.

(8) Anslyn, E. V.; Dougherty, D. A. *Modern physical organic chemistry*; University Science: Sausalito, Calif., 2006.

(9) Endicott, J. F. In *Electron Transfer in Chemistry*; Wiley-VCH: Toronto, 2001; Vol. 1 Principles, Theories, Methods, and Techniques, pp 238-267.

(10) Patil, A. O.; Heeger, A. J.; Wudl, F. *Chem. Rev.* **1988**, *88*, 183-200.

(11) Tretiak, S.; Saxena, A.; Martin, R. L.Bishop, A. R. *Proc. Natl. Acad. Sci. U.S.A.* **2003**, *100*, 2185-2190.

(12) Brédas, J. L.; Street, G. B. *Acc. Chem. Res.* **2002**, *18*, 309-315.

(13) Heeger, A. J. *Angew. Chem. Intl. Ed.* **2001**, *40*, 2591-2611.

(14) Nitzan, A.; Ratner, M. A. *Science* **2003**, *300*, 1384-1389.

(15) Brédas, J.-L.; Cornil, J.; Beljonne, D.; dos Santos, D. A.; Shuai, Z. *Acc. Chem. Res.* **1999**, *23*, 267-276.

(16) Cornil, J.; Beljonne, D.; Heller, C. M.; Campbell, I. H.; Laurich, B. K.; Smith, D. L.; Bradley, D. D. C.; Müllen, K.; Brédas, J. L. *Chem. Phys. Lett.* **1997**, *278*, 139-145.

(17) Rice, M. J.; Gartstein, Y. N. *Phys. Rev. Lett.* **1994**, *73*, 2504-2507.

(18) Chandross, M.; Mazumdar, S.; Liess, M.; Lane, P. A.; Vardeny, Z. V.; Hamaguchi, M.; Yoshino, K. *Phys. Rev. B* **1997**, *55*, 1486-1496.

(19) Amrutha, S. R.; Jayakannan, M. *J. Phys. Chem. B* **2008**, *112*, 1119-1129.

(20) Lacroix, J. C.; Chane-Ching, K. I.; Maquere, F.; Maurel, F. *J. Am. Chem. Soc.* **2006**, *128*, 7264-7276.

(21) Pu, K.-Y.; Qi, X.-Y.; Yang, Y.-L.; Lu, X.-M.; Li T.-C. ; Fan, Q.-L.; Wang, C.; Liu, B.; Chan, H. S. O.; Huang, W. *Chem. Eur. J.* **2008**, *14*, 1205-1215.

(22) Hutten, P. F. v.; Krasnikov, V. V.; Hadziioannou, G. *Acc. Chem. Res.* **1999**, *32*, 257-265.

(23) Bittner, E. R.; Karabunarliev, S.; Herz, L. M. *J. Chem. Phys.* **2007**, *126*, 191102-191104.

(24) Troisi, A.; Orlandi, G. *J. Phys. Chem. A* **2006**, *110*, 4065-4070.

(25) Lu, S. Z.; Li, X. Y.; Liu, J. F. *J. Phys. Chem. A* **2004**, *108*, 4125-4131.

(26) Coropceanu, V.; Cornil, J.; da Silva Filho, D. A.; Olivier, Y.; Silbey, R.; Brédas, J. L. *Chem. Rev.* **2007**, *107*, 926-952.

(27) Nakatsuji, S.; Matsuda, K.; Uesugl, B. Y.; Nakashima, K.; Akiyama, S.; Katzerb, G.; Fabian, W. *J. Chem. Soc. Perkin Trans.* **1991**, 861-867.

(28) Nakatsuji, S.; Matsuda, K.; Uesugi, B. Y.; Nakashima, K.; Akiyama, S.; Fabian, W. *J. Chem. Soc. Perkin Trans* **1992**, 755-758.

(29) Schäffer, B.; Lorinczy, D. *J. Therm. Anal. Cal.* **2005**, *82*, 531-535.

(30) Kong, H.; Ye, F.; Lu, X.; Guo, L.; Tian, J.Xu, G. *Journal of Chromatography A 2nd International Symposium on Comprehensive Multidimensional Gas Chromatography* **2005**, *1086*, 160-164.

(31) Dattelbaum, D. M.; Itokazu, M. K.; Iha, N. Y.; Meyer, T. J. *J. Phys. Chem. A* **2003**, *107*, 4092-4095.

(32) Waldeck, D. H. *Chem. Rev.* **1991**, *91*, 415-436.

(33) Catalan, J.; Saltiel, J. *J. Phys. Chem. A* **2001**, *105*, 6273-6276.

(34) Xie, Z.; Yang, B.; Liu, L.; Mao, L.; Li, P.; Gheng, G.; Liu, S. *J. Phys. Org. Chem.* **2005**, *18*, 962.

(35) Zhou, N.; Wang, L.; Thompson, D. W.; Zhao, Y. *Tetrahedron Lett.* **2007**, *48*, 3563-3567.

(36) Katz, E. N.; Mecklenburg, S. L.; Graff, D. K.; Chen, P. Y.; Meyer, T. J. *J. Am Chem. Soc.* **1994**, *98*, 8959-8961.

(37) Caspar, J. V.; Westmoreland, T. D.; Allan, G. H.; Bradley, P. G.; Meyer, T. J.; Woodruff, W. H. *J. Am. Chem. Soc.* **1984**, *106*, 3492-3500.

(38) Kober, E. M.; Caspar, J. V.; Lumpkin, R. S.; Meyer, T. J. *J. Phys. Chem.* **1986**, *90*, 3122-3134.

(39) Beeby, A.; Findlay, K.; Low, P. J.; Marder, T. B. *J. Am. Chem. Soc.* **2002**, *124*, 8280-8284.

(40) Sluch, M. I.; Godt, A.; Bunz, U. H. F.; Berg, M. A. *J. Am. Chem. Soc.* **2001**, *123*, 6447-6448.

(41) Strobl, G. *The Physics of Polymers, Concepts for Understanding Their Structures and Behaviours*; 3rd Ed ed.; Springer-Verlag: New York, 2007.

(42) Yang, B.; Xie, Z.; Zhang, H.; Xu, H.; Hanif, M.; Gu, X.; He, F.; Yu, J.; Ma, Y.; Shen, J.; Liu, X.; Feng, J. *Chem. Phys.* **2008**, *345*, 23-31.

(43) Baraldi, I.; Ginocchietti, G.; Mazzucato, U.; Spalletti, A. *Chem. Phys.* **2007**, *337*, 168-176.

(44) Ichino, Y.; Ni, J. P.; Ueda, Y.; Wang, D. K. *Synthetic Metals* **2001**, *116*, 223-227.

(45) Wang, B.-C.; Chang, J.-C.; Pan, J.-H.; Xue, C.; Luo, F.-T. *Journal of Molecular Structure: THEOCHEM* **2003**, *636*, 81-87.

(46) Tao, Y.; Donat-Bouillud, A.; D'Iorio, M.; Lam, J.; Gorjanc, T. C.; Py, C.; Wong, M. S. *Synthetic Metals* **2000**, *111-112*, 417-420.

(47) Solntsev, K. M.; McGrier, P. L.; Fahrni, C. J.; Tolbert, L. M.; Bunz, U. H. F. *Org. Lett.* **2008**, *10*, 2429-2432.

(48) Renak, M. L.; Bartholomew, G. P.; Shujun Wang; Ricatto, P. J.; Lachicotte, R. J.; Bazan, G. C. *J. Am. Chem. Soc.* **1999**, *121*, 7787-7799.

(49) Busht, T. E.; Scott, G. W. *J. Phys. Chem.* **1981**, *85*, 146-148.

(50) Stalmach, U.; a, H. D.; Meier, H.; Gebhardt, V.; Haarer, D.; Bather, A.; Schmidt, H.-W. *Optical Materials* **1998**, *9*, 77-81.

(51) Pond, S. J. K.; Rumi, M.; Levin, M. D.; Parker, T. C.; Beljonne, D.; Day, M. W.; Brédas, J. L.; Marder, S. R.; Perry, J. W. *J. Phys. Chem. A* **2002**, *106*, 11470-11480.

(52) Y. Lei; Buranda, T.; Endicott, J. F. *J . Am. Chem. Soc.* **1990**, *112*, 8820-8833.

(53) McCusker, J. K. *J.Phys. Chem. A* **2002**, *106*, 7399-7406.

(54) Duvanel, G.; Grilj, a.; Schuwey, A.; Gossauerb, A.; Vauthey, E. *Photochem. Photobiol. Sci.* **2007**, *6*, 956-963.

(55) Maoa, G.; Oritaa, A.; Fenenkob, L.; Yahirob, M.; Adachib, C.; Oteraa, J. *Mater. Chem. Phys.* **2009**, *115*, 378-384.

(56) Liu, L. T.; Yaron, D.; Sluch, M.; Berg, M. A. *J. Phys. Chem. B* **2006**, *110*, 18844-18852.

(57) Liu, L. T.; Yaron, D.; Berg, M. A. *J. Phys. Chem. C* **2007**, *111*, 5770-5782.

(58) Karabunarliev, S.; Bittner, E. R.; Baumgarten, M. *J. Chem Phys.* **2001**, *114*, 5863-5870.

Chapter 4

Electron Transfer *vs.* Energy Transfer in Bisfullerene Terminated OPV/OPE Oligomers

Overview

The goal of this chapter is to understand the structural, electronic and vibronic parameters that govern the photo-induced electron and energy transfer in the π*-bridged* C_{60} *Systems* $[A\text{-}(\pi\text{-}B)_{C/L}\text{-}A]$.

4.1 Introduction....................163

4.1.1 The Electron Transfer Mechanism in Donor-Bridge-Acceptor Systems....................163

4.1.2 Exponential Distance Dependence of Bridge-Mediated Electron Transfer....................165

4.1.3 Solvent Mediated Superexchange in Donor-Bridge-Acceptor Molecule.168

4.1.4 Effect of the Donor-Bridge Energy Gap on the ET Mechanism.......... 172

4.1.5 Effect of Torsional Motion on ET Rates....................175

4.1.6 Effect of Donor- Acceptor Orientation on ET Rates....................176

4.1.7 Covalently Linked System Containing Fullerene (C_{60}) 177

4.1.8 π-Conjugated Oligomers or Derivatives as Bridges....................179

4.1 Results....................182

4.2.1 Structure of OPV/OPE Oligomers and Bisfullerene Terminated Assemblies....................182

4.2.2 Radiative Processes of DEB and DEB-C_{60}....................183

4.2.3 Radiative Processes of SC-$(C_{60})_2$ and LC-$(C_{60})_2$....................187

4.2.4 Transient Absorption of SC-$(C_{60})_2$ and LC-$(C_{60})_2$....................190

4.2.5 Radiative Processes of SL-$(C_{60})_2$ and LL-$(C_{60})_2$....................194

4.2.6 Transient Absorption of SL-$(C_{60})_2$ and LL-$(C_{60})_2$....................197

4.2.7 Global Kinetic Analysis....................201

4.2 Discussions....................213

4.3.1. The Effect of Varying Donor-Acceptor Distance 213

4.3.2. Back Electron Transfer or Charge Recombination..........................218

4.3.3. Orientation Effect..221

4.2 Conclusions...225

4.3 References..226

4.1 Introduction

The absorption of sunlight by plants and bacteria initiates photosynthesis, which eventually results in the conversion of carbon dioxide and water into carbohydrates, oxygen, and energy (ATP). The energy absorption, transduction and the stepwise electron transfer over a series of redox-active cofactors are controlled through a series of spatially arranged chromophores that are electronically coupled to produce a trans-membrane gradient such that energy is converted into an electrochemical potential in the form of charge separation across the cell membrane. To develop synthetic and engineering methods for extending the biological processes to synthetic systems, spatial precision is critical to this energy transfer process and therefore extensive work has explored the synthesis and characterization of modular architectures where photoactive components are linked together covalently in a precise manner.[1-3] Applying organic or inorganic synthetic methodologies to covalently couple donor and acceptor molecules eliminates the limitation of diffusion. It also allows one to systematically probe how the chain architecture, distance between donor and acceptor, and differences in their energy levels affect energy transfer and charge separation.

4.1.1 The Electron Transfer Mechanism in Donor-Bridge-Acceptor Systems

Designing and developing effective molecular electronic devices and polymeric electron-transfer materials depends on understanding the details of the electron-transfer mechanism. Intense experimental and theoretical efforts have been devoted to exploring the mechanism of bridge-mediated long-range charge transfer (donor-bridge-acceptor, DBA) where the separation of the donor (D) and acceptor (A) greatly exceeds the range of direct donor-acceptor electronic overlap. How does the rate of charge transfer depend on the nature of the bridge connecting the donor and the acceptor? It has been long recognized that charge transfer in a donor-bridge-acceptor system may proceed via two distinct mechanisms or a combination of these mechanisms.[4-11] In the configuration where the bridge-state energy is higher than the donor/acceptor-state energy, electron transfer occurs by quantum-mechanical tunneling from the donor to the acceptor. The role of the bridge is to mediate the electronic coupling V_{DA} between the donor and acceptor. This is known as the superexchange mechanism. On the contrary, when the donor/acceptor and bridge energies are on the order of k_BT, the bridge acts as a quantum wire and the electron hops from one site to its nearest neighbor and then through the whole bridge, ultimately reducing the acceptor. This sequential electron transport mechanism is known as the hopping mechanism. The effects of the bridge, the energy gap between the donor/acceptor and the bridge, the reorganization energies, and the temperature on the competition between these two mechanisms have been investigated. Only recently was the partially coherent hopping mechanism introduced as an intermediate between the two conventional mechanisms.[12-14] The partially coherent hopping mechanism includes pathways that make incoherent and coherent jumps between states in a single path, and it is different from the superexchange pathways where bridges function solely as a virtual bridge. Therefore, charge transfer processes that are dominated by pathways through any bridge state in the system are referred as a through-bridge mechanism. For a system with more than one consecutive bridge state, the through-bridge mechanism consists of the incoherent nearest neighbor hopping pathways and the next-nearest neighbor hopping pathways.[15]

4.1.2 Exponential Distance Dependence of Bridge-Mediated Electron Transfer

The dynamics of photoinduced ET in D-B-A systems are known to depend on the length and nature of the bridge.[16,17] The ET rate is governed by the through-bond electronic coupling V_{DA} and displays an exponential dependence on the D-A distance described by eq 4-1. The derivation of the exponential relationship can be presented in several ways; in a chemical context, McConnell, who used perturbation theory to discuss superexchange mixing of donor and acceptor sites by intervening orbitals, gave the first important derivation.[18]

$$k_{ET}(r_{DA}) = k_o \exp(-\beta r_{DA}) \qquad (4\text{-}1)$$

where k_o is a temperature-dependent prefactor, r_{DA} is the D-A separation, and β characterizes the steepness of the experimental distance dependence. The values of β for D-B-A systems vary with the nature of the bridge. The distance dependence of k_{ET} originates from both the electronic coupling and the Franck-Condon vibrational overlap factors in eq 4-2,

$$k_{ET}(r_{DA}) = \frac{2\pi}{\hbar}|V_{DA}(r_{DA})|^2\mathrm{FC}(r_{DA}) \qquad (4\text{-}2)$$

and it is difficult (experimentally) to separate the contribution from the vibrationally induced electronic coupling and vibrational overlap in $\mathrm{FC}(r_{DA})$. The electronic coupling is of the exchange type and is related to orbital overlap; it is generally believed to decay exponentially with distance r_{DA} and is characterized by the decay exponent β^c (eq 4-3).

$$|V_{DA}(r_{DA})|^2 = |V_{DA}^o|^2\exp\left(\frac{-\beta^c\, r_{DA}}{2}\right) \qquad (4\text{-}3)$$

In eq 4-3, V_{DA}^{o} is the electronic coupling at contact distance, and β^{c} is an attenuation factor characteristic of the intervening medium. The Franck-Condon factors may also introduce distance dependence to the ET rate (for example, through the distance dependence of reorganization energy), so β and β^{c} do not need to be identical. In addition, the electronic coupling also depends on the interactions among bridge units and the inverse of the energy gap between the relevant bridge and donor states, expressed as:

$$V_{DA}(r_{DA}) = \frac{V_{DB}V_{BA}}{\Delta E}\left(\frac{v_{mn}}{\Delta E}\right)^{m-1} \qquad (4\text{-}4)$$

where ΔE is the energy gap between the donor and bridge unit, v_{mn} is the nearest neighbor interaction element, and m is the repeating number of identical units of the bridge. From the McConnell model, the value of β^{c} is expected to vary with the donor-bridge energy gap as described in eq 4-5.

$$\beta^{c} = \frac{2}{r_o}\ln\left|\frac{\Delta E}{v_{mn}}\right| \qquad (4\text{-}5)$$

where r_o is the (hypothetical) length of the repeating unit of the bridge. In the limit where $v_{mn}/\Delta E \ll 1$, the exponential distance dependence is predicted by eq 4-4. In D-B-A systems with π-conjugated bridges, it is difficult to dissect the bridge into well-defined chain units and the validity of eq 4-3 and 4-4 might be questioned. In general, the value of β^{c} is regarded as the bridge-specific parameter. However, β^{c} is not a bridge specific parameter for π-conjugated bridges. Albinsson *et al.* have experimentally investigated the bridge mediated electronic coupling in D-B-A systems with different bridging structures. In parallel to the experimental studies, they also developed DFT-based quantum mechanical method to calculate the electronic coupling for ET and triplet energy transfer

(TET). Calculating the values of V_{DA} for oligo(*p*-phenyleneethynylene) (OPE) bridges with edge-edge separation between 12 and 37 Å (m = 2-5) and the linear fit of $\ln V_{DA}$ *vs.* r_{DA} gave the β^c values. This shows that β^c is sensitive to the appended donor and acceptor, and thus is not a bridge-specific parameter as described in eq 4-5.[19] The approximate exponential dependence on distance found for the OPE bridges was also observed for oligo(thiophene) (OTP) and oligo(*p*-phenylenevinylene) (OPV) bridges.[20] However, for the bridges with non-aromatic repeating structures, oligo(ethylene) (OE), phenyl end capped oligo(ethylene) (Ph-OE), oligo(vinylene) (OV), and phenyl end capped oligo(vinylene) (Ph-OV), different behavior was observed and show distinct non-exponential distance dependence.[19] Clearly, the McConnell superexchange model cannot be used for these bridges.

In contrast to the superexchange mechanism, the bridge is dissected into subunits, which is demanded in the electron hopping mechanism. The electronic interaction between the donor, the bridge, and the acceptor can be divided into several components: the interaction of the donor with the first unit of the bridge V_{DB_1}, the successive interactions of two different bridging units $V_{B_1B_2}$, $V_{B_2B_3}$..., and finally the interaction between the last bridging unit and the acceptor V_{B_nA}. The electronic coupling between two redox sites connected by a single covalent bridge is given by eq 4-6.[21]

$$V_{DA} = V_{DB_1} V_{B_nA} \sum \alpha_{B_{l\upsilon}} \alpha_{B_{n\upsilon}} / (E_D - E_{B\upsilon}) \qquad (4\text{-}6)$$

where V_{DB_1}, V_{B_nA} are the coupling elements between the orbitals of the donor/acceptor and the atomic orbitals of the adjacent bridge atoms, B_1 and B_n, respectively. $\alpha_{B_{l\upsilon}}$, and $\alpha_{B_{n\upsilon}}$ are the orbital coefficients of the υth bridge molecular orbitals at the atoms bonded to D and A. E_{Bv} is the energy of the vth molecular orbital of the bridge, and the summation is over the molecular orbitals of the bridge. Applying the Gamow tunneling model,[22] which describes the electronic interaction between two centers in terms of a single tunneling barrier of width r_{DA} and height ΔE, the electronic coupling is given by:

$$V_{DA} = \frac{\alpha}{\Delta E}\exp\left(-m\sqrt{\Delta E}\, r_{DA}\right) \qquad (4\text{-}7)$$

where α is a system specific parameter related to the donor-bridge coupling but not dependent on r_{DA}, and m is related to the effective mass of the virtual tunneling electron(s). Eq 4-7 can qualitatively describe the anomalous behavior of the OE, Ph-OE, OV, and Ph-OV bridges as well as the normal exponential behavior of the OPE, OPV, and OTP bridges.

From eq 4-7, the electronic coupling increases rapidly with small values of ΔE. This behavior is expected because at near degeneracy the energy gap is so small that this might lead to very strong electronic mixing between the donor and the bridge. In such a situation ($\Delta E < 3000$ cm^{-1}), a non-coherent hopping mechanism is difficult to avoid and the rate for ET is no longer dictated by the direct superexchange mechanism between the donor and acceptor, but through a relay mechanism involving the density of states populated at the bridge.[23]

In summary, ET in D-B-A systems is governed by the superexchange mechanism for shorter bridges and by the sequential hopping mechanism for longer bridges. The ET rate of coherent superexchange exponentially decreases with the distance between states while the ET rate of incoherent hopping is more or less independent on the distance.

4.1.3 Solvent Mediated Superexchange in Donor-Bridge-Acceptor Molecule

In the superexchange mechanism, indirect mixing of the donor and acceptor wavefunctions through the orbitals located between the donor and acceptor may enhance long distance electron transfer (or simply charge transfer for either charge). This raises the possibility that solvent molecules may also mediate electron transfer. For electron transfer reactions in the nonadiabatic limit, the rate constant of electron transfer, k_{ET}, is given by

$$k_{ET} = \frac{2\pi}{\hbar}|V|^2 FCWD \qquad (4\text{-}8)$$

$|V|$ is the donor/acceptor electronic coupling, and FCWD is the Franck-Condon weighted density of states, which accounts for the nuclear rearrangement that must precede the electron tunneling event. The single mode semiclassical expression for the FCWD model interacts with the solvent classically and treats solute vibrations using a single effective medium- or high-frequency (or averaged) mode. The rate constant is expressed as:

$$k_{ET} = \frac{2\pi}{\hbar}|V|^2 \frac{1}{\sqrt{4\pi\lambda_o k_B T}} \sum_{n=0}^{\infty} \exp(-S)\frac{S^n}{n!} \exp\left\{-\left[(\lambda_o + \Delta G^o + nh\nu)^2/4\lambda_o k_B T\right]\right\} \qquad (4\text{-}9)$$

This equation describes the electron transfer rate constant using four principle parameters: ΔG^o (the change in Gibbs free energy of reaction), λ_o (low-frequency primarily solvent reorganization energy), λ_i (medium- or high-frequency primarily solute reorganization energy), ν (the effective frequency of the quantum mechanical mode), and $|V|$ (donor/ acceptor electronic coupling). S (the Huang-Rhys factor) is defined as:

$$S = \frac{\lambda_i}{h\nu} \qquad (4\text{-}10)$$

λ_i and ν can be estimated from the analysis of charge-transfer absorption and emission spectra.[24,25]

Solvent can mediate electron transfer in superexchange process by enhancing the total electronic coupling, $|V|$.[26-29] Napper *et al.* demonstrated that the electronic coupling for C-shaped molecules in solvent with more positive electron affinities (more readily accept an electron) is larger than that in solvent with more negative electron affinities (less readily accept an electron). The electronic coupling $|V|$ in an solvent-mediated superexchange process is given by:[29]

$$|V| = \frac{H_{D^*S}H_{SA}}{E_{D^+S^-A} - E_{D^*SA}} \qquad (4\text{-}11)$$

where E_{D^*SA} and $E_{D^+S^-A}$ are the energies of the transition state and the vertically displaced superexchange state (D^+S^-A). H_{D^*S} and H_{SA} are the donor/solvent and solvent/acceptor exchange integrals, respectively. A solvent with more positive values of $\mathrm{EA_v}$ (vertical electron affinities) is predicted to stabilize the superexchange state D^+S^-A and the total electronic coupling depends on the energetic difference between $E_{D^+S^-A}$ and E_{D^*SA}. In addition, the value of the electronic coupling is also dependent on the ability of the solvent molecules to be oriented between the donor and the acceptor to maximize the $|V|$. The more highly substituted solvents are less accessible to geometries with good electronic wavefunction overlap between the donor and acceptor, and then less effective for mediating electron transfer.[29]

Electron transfer reactions involve changes in the overall charges in the donor and acceptor moieties. The stability of the charged species depends on the nature of the solvent, which undergo rotational and translational motions to partially screen the charge and energetically stabilize the redox-separated state. The rate constant of electron transfer given by eq 4-9 can be modulated by the Franck-Condon factor that depends on the reaction free energy, solvent reorganization energy, and nuclear vibrational frequency. Both the reaction free energy and the solvent reorganization energy are functions of the solvent, therefore, the electron transfer rate constant also depends on the solvent.[30-32] For the electron transfer in a high polar solvent, a dielectric continuum model for the solute-solvent interaction is used to estimate ΔG^o and λ_o. In the continuum model, the charge-separated state is treated as a point dipole $\vec{\mu}$ embedded in a spherical cavity and the solvent is treated as a continuum with bulk dielectric properties. The solvent reorganization energy (λ_o) is given by a modification of the Born equation.[26]

$$\lambda_o(cont) = \frac{\mu^2}{\alpha_o^3}\left(\frac{\epsilon_s - 1}{2\epsilon_s + 1} - \frac{n^2 - 1}{2n^2 + 1}\right) \qquad (4\text{-}12)$$

where α_o is the effective cavity radius, ϵ_s is the static dielectric constant of the solvent, and n is the refractive index of the solvent. The Gibbs free energy is given by

$$\Delta G^o = \Delta G^o_{vac} - \left(\frac{\mu^2}{\alpha_o^3}\right)\left(\frac{\epsilon_s - 1}{2\epsilon_s + 1}\right) \qquad (4\text{-}13)$$

where ΔG^o_{vac} is the reaction Gibbs free energy in the absence of solvation.

For weak dipolar solvents and especially for aromatic solvents where quadrupole interactions are important, Matyushov developed a molecular approach that treats the solute and solvent molecules as polarizable spheres with embedded point dipole moments, and, in the case of an aromatic solvent, with an embedded point quadrupole moment. The reorganization energy is expressed as a sum of three terms:

$$\lambda_o = \lambda_e + \lambda_{ind} + \lambda_{disp} \qquad (4\text{-}14)$$

where λ_o is the solvent reorganization arising from electrostatic interactions, λ_{ind} is the contribution from induction forces, and λ_{disp} from dispersion interactions. The reaction free energy is given as a sum of four components.

$$\Delta G^o = \Delta G^o_{vac} + \Delta G^o_e + \Delta G^o_{ind} + \Delta G^o_{disp} \qquad (4\text{-}15)$$

where ΔG^o_{vac} is defined as above and the other three terms are from solvation effects. The electrostatic and induction terms, ΔG^o_e and ΔG^o_{ind} make the dominant contributions to the solvent reorganization energy and the dispersion term ΔG^o_{disp} plays a minor role and may be neglected.

4.1.4 The Effect of the Donor-Bridge Energy Gap on the ET Mechanism

Electron transfer reactions in donor-bridge-acceptor molecules that occur by means of superexchange interaction depend on the vertical energy gap separating the donor and the bridge. This dependence modulates the electronic coupling matrix element for ET, and hence the ET rate. The governing mechanism changes from incoherent hopping to partially coherent hopping and eventually to coherent superexchange as the donor-bridge energy gap becomes large. A perturbative calculation of the electron tunneling matrix element V_{DA} described by McConnell dependent on electronic coupling constants between nearest neighbor states and the energy gap can estimate the effective superexchange coupling constant. However, it is unclear how these parameters determine the dominant type of overall transfer mechanism.

To explore the electron-transfer mechanism as a function of the donor-bridge energy gap while the electronic coupling strength between the states remaining as a constant, Marcus theory and ion pair energetics based on the electrostatic interaction can be used for analysis. An accurate assessment of the free energies of the ion pairs, ΔG^o_{IP}, can be calculated by using an expression derived by Weller based on the Born dielectric continuum model.[33,34] This model employs the redox potentials of the donor and acceptor determined in a polar solvent along with the Born solvation energies of both ions in the low polarity solvent of interest, given by

$$\Delta G^o_{IP} = e(E_{OX} - E_{RED}) - \frac{e^2}{4\pi\epsilon_0\epsilon_s R_{DA}} + \frac{e^2}{8\pi\epsilon_0}\left(\frac{1}{2R_D} + \frac{1}{2R_A}\right)\left(\frac{1}{\epsilon_s} - \frac{1}{\epsilon_s'}\right) \qquad (4\text{-}16)$$

where E_{OX} and E_{RED} are the oxidation potential of the donor and the reduction potential of the acceptor, e is the charge of the electron, ϵ_s is the static dielectric constant of the solvent used for the spectroscopic measurements, and ϵ_0 is the dielectric constant of the solvent used for the electrochemical measurements. R_{DA} is the distance from center-to-center of the donor and acceptor, and R_D and R_A are the spherical radii of the donor and acceptor, respectively. The free energies for the CS reactions are determined from ΔG^o_{IP} using eq 4-16 and eq 4-17.

$$\Delta G^o_{CS} = \Delta G^o_{IP} - E^D_{00} \qquad (4\text{-}17)$$

$$\Delta G^o_{CR} = -\,\Delta G^o_{IP} \qquad (4\text{-}18)$$

where E^D_{00} is the lowest excited-state energy of the donor, which is derived from the average energy of the 0-0 absorption and fluorescence maxima of the donor. The energy scale used in these equations assumes that zero corresponds to the energy of the ground state molecule. Again from dielectric continuum theory,[35] Marcus showed that λ_o can be approximated from eq 4-19:

$$\lambda_o = \frac{e^2}{4\pi\epsilon_o}\left(\frac{1}{2R_D} + \frac{1}{2R_{DA}} - \frac{1}{R_{DA}}\right)\left(\frac{1}{\epsilon_\infty} - \frac{1}{\epsilon_s}\right) \qquad (4\text{-}19)$$

where ϵ_∞ is the optical dielectric constant of the solvent and the remaining parameters are defined above. The temperature dependence of λ_o is due to that of ϵ_∞ and ϵ_s as well as the change of solvent viscosity as a function of temperature. Semiclassical electron transfer theory shows that the electron transfer rate constant, k_{ET}, depends on the electronic coupling matrix element V_{DA} for the reaction and the free energy of reaction ΔG^o as expressed by eq 4-9. Therefore, eq 4-9, along with eqs 4-16 ~19 can be used to estimate the k_{CS}.

The true value of ΔE might not be known, as it includes virtual states of the bridge, but could be approximated by calculations.[36,37] The suggested ΔE can been calculated as

$$\Delta E = e(E_{OX}^D - E_{RED}^B) - E_{00}^D \qquad (4\text{-}20)$$

At the simplest level of analysis, the photo-initiated, long distance CS in a D-B-A system can be viewed as the movement of an electron between the LUMOs of the donor, bridge, and acceptor. Photon absorption results in the promotion of an electron from the HOMO of the donor into its LUMO, and then electron moves to the LUMO of the acceptor with the assistance of the LUMO of the bridge. In the superexchange mechanism, the bridge LUMO acts as a virtual state with no significant electronic population during the ET. In the hopping mechanism, the electron will physically locate at the bridge for a short time before appearing in the LUMO of the acceptor. Two general methods can be employed for estimating the LUMO energies for donor and bridge.[37,38] First, by using the pairing theorem, the LUMO energy of an organic molecule can be approximated as the sum of its excited state energy and oxidation potential. The second method for calculating the LUMO energies of the donor and bridge uses semi-empirical molecular orbital calculations.

From the analysis, the conclusion can be drawn that the donor-bridge energy gap can play a significant role in the ET dynamics of molecular D-B-A systems. This energy gap usually plays a role in V_{DA}, the electronic coupling matrix element between the donor and acceptor. Conventional wisdom holds that the ET reaction in intramolecular D-B-A molecules occurs by a superexchange mechanism that uses virtual orbitals of the bridge. When the donor-bridge energy gap becomes smaller, reaching a critical value, the donor-to-acceptor ET reaction changes from a superexchange mechanism to a charge hopping mechanism.[39]

In addition, using redox potentials to calculate ΔE may yield an underestimation of this barrier because ΔE is calculated from the energy of the relaxed radical species whereas the true energy barrier concerns the unrelaxed energy levels. The electron or hole never resides on the bridge in superexchange process, but tunnels through it. The difference between the virtual level and those calculated from redox potentials and the E_{00}^{D} level is small if ΔE is large. Conversely, the difference between the true barrier and the calculated one can become significant if ΔE is small.

4.1.5 Effect of Torsional Motion on ET Rates

The exact nature of the electron-transfer excited states is sensitive to the torsion angles in the donor/bridge and bridge/acceptor pairs.[40,41] Torsional motions will primarily affect the electronic coupling between adjacent electronic sites, and will impart an angular dependence to V_{mn} (m, n nearest neighbors) by

$$V_{mn} = V_{mn}^{o} cos\phi \qquad (4\text{-}21)$$

where ϕ is the torsional angle and V_{mn}^{o} is the electronic coupling between sites m and n at $\phi = 0^{o}$. If ϕ is temperature dependent, this will impart a temperature dependence to V_{DA} that may override the normal Arrhenius-like temperature dependence of k_{ET} expected from semiclassical ET theory. Since the electron transfer is sensitive to the torsional motion, the rate of electron transfer may be controlled primarily by intramolecular torsions. These molecular motions can have a profound effect on the ability of conjugated molecules to transport an electron for a long distance.[42]

4.1.6 Effect of Donor-Acceptor Orientation on ET Rates

Rapid electron transfer requires optimizing the parameters in eq 4-9 that are a function of the molecular design. The electronic coupling of the reactant state and the product state, $|V|$, is a function of the overlap of the donor and the acceptor orbitals. This in turn depends on the energetic, spatial geometric and the symmetry factors. In most covalently linked donor-acceptor systems, the electronic coupling via a superexchange interaction may be partitioned into a through-bond component that involves the bonds of the bridge between the donor and acceptor, a direct through-space interaction between the donor and acceptor, and a superexchange interaction through the intervening solvent molecules between the donor and acceptor moieties. Therefore, the orientation dependence of the electron transfer rate is due to a combination of through-space and through-solvent couplings.[30,31,43,44]

4.1.7 Covalently Linked System Containing Fullerene (C_{60})

A significant challenge for artificial photosynthesis is to achieve a long-lived charge separation state and prevent the charge recombination. One way to address this challenge is to integrate successive energy gradients into covalently linked molecular assemblies that will quickly shuttle electrons away from the excitation site to more stable sites. Fullerene (C_{60}) as the electron acceptor has recently be used to construct such assemblies.[45] The combination of C_{60} with π-conjugated oligomers for the construction of donor-C_{60} arrays is of particular interest. The unique three-dimensional structure of C_{60} and the facile electron acceptance (up to six electrons) make it a good candidate as the electron acceptor with the first reduction potential similar to that of benzoquinones, which are typical electron acceptors in both natural and artificial photosynthetic systems.

In the natural photosynthetic reaction center, the forward electron transfer is regulated to be much faster than the back electron transfer, resulting in the production of long-lived final charge-separated state with an almost 100% quantum yield. The reorganization energy (λ) has a decisive impact on the realization of such a situation. To optimize the efficiency of forward electron transfer *vs.* back electron transfer, the Marcus parabolic curve for electron transfer gives an insight into the importance of reorganization energy. As the free energy change (ΔG_{ET}^{o}) becomes more negative, the electron transfer rate increases (normal region) until it reaches a maximum point where $-\Delta G_{ET}^{o} = \lambda$. However, as the free energy change becomes more negative, the electron transfer rate decreases (inverted region). For the photosynthetic electron transfer, λ is optimized for each electron transfer process. That is, the forward electron transfer proceeds under optimal conditions near the maximum point of the Marcus parabola, whereas the highly exergonic and energy-wasting process of back electron transfer is shifted into the inverted region. In conventional photosynthetic models such as porphyrin-quinone and diporphyrin dyads, the reorganization energy is controlled mainly by the surrounding solvent. Given two electron transfer systems in which the controlling factors, the free energy change and the electronic coupling, are identical, a smaller reorganization energy would make the forward and back electron transfer processes with a smaller λ faster and slower, respectively, than the corresponding processes with a larger λ as shown in Figure 4-1.[46]

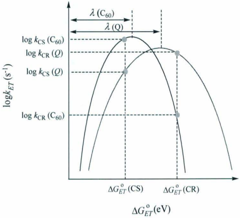

Figure 4-1. Parabolic curves for electron transfer of donor-C_{60} and donor-quinone systems.

Donor-acceptor systems containing C_{60} feature relatively rapid photoinduced charge separation and relatively slow charge recombination.[47,48] Such behavior is rationalized by either large electronic coupling for the photo-induced charge separation and a small one for the charge recombination or a small reorganization energy.[49,50] The reorganization energy is the sum of a solvent term (λ_o) and a vibrational term (λ_i). The unit charge in $C_{60}^{\cdot-}$ is highly delocalized over the three-dimensional carbon framework of C_{60}, so that the charge density of each carbon in $C_{60}^{\cdot-}$ is much smaller than that of typical two-dimensional π acceptors, causing the solvent reorganization energy of C_{60} to be smaller. Solvent reorganization energy is a function of charge separation distance and solvent polarity (eq 4-19). To realize the smallest reorganization energy in artificial photosystems, the solvent reorganization energy is expected to decrease when the donor and acceptor are fixed in close proximity and solvent polarity decreases. In addition, similar small reorganization energies are obtained for C_{60}-based donor-acceptor systems in the solid state. These systems also demonstrate the charge recombination to yield the triplet excited state, rather than the molecular ground state.[51,52] Therefore, C_{60} is a potential component for constructing artificial photosynthetic systems.

4.1.8 π-Conjugated Polymers or Derivatives as Bridges

In π-conjugated polymers, the chemical bonding leads to one unpaired electron (the π-electron) per carbon atom in which the carbon orbitals are in the sp^2p_z configuration and the orbitals of successive carbon atoms along the backbone overlap. Therefore, π-bonding leads to electron delocalization along the backbone of the polymer, and this electronic delocalization provides the "highway" for charge mobility along the backbone of the polymer chain. The electronic structure in conducting polymers is determined by the chain symmetry (*i.e.* the number and kind of atoms within the repeat unit). As a result, such polymers can exhibit semiconducting or even metallic properties. The discovery of photoinduced electron transfer in composites of π-conjugated polymers possessing electron donating properties and fullerene C_{60}, having an electron accepting character, opened a number of new opportunities for π-conjugated polymers.[53-55] These studies demonstrated that the electron transfer rate ($>10^{13}$ s^{-1}) is several orders of magnitude larger than any competing decay process, and the quantum efficiency of the electron transfer process is close to unit.[56-60] Once the photoexcited electron is transferred to an acceptor unit, the resulting cation radical species on the conjugated polymer backbone is relatively stable.[60] The forward to reverse asymmetry of the photoinduced charge separation in the π-conjugated polymer-C_{60} system is remarkable; this asymmetry is orders of magnitude greater than that observed in the photosynthesis of green plants. Using π-conjugated polymers in conjunction with a molecular electron acceptor to achieve the long-lived charge separation is based on the stability of the photoinduced nonlinear excitations (such as polarons) on the conjugated polymer backbone. A comprehensive study was undertaken on the theoretical investigation of electronic structure and photophysical properties of π-conjugated polymers such as oligo(*p*-phenylenevinylene)s (OPV) and oligo(*p*-phenyleneethynylene)s (OPE).[61,62] OPEs have a high fluorescence quantum yield and are considered to be less conjugated than OPVs due to the presence of the carbon-carbon triple bonds.[63] The introduction of alkyl or alkyloxy groups at the peripheral positions of OPV is shown to modify the photophysical behavior of the compounds.[62] Hybrid conjugated aromatic polymers, having carbon-carbon double and triple bonds, could be of interest because they combine high quantum yields of fluorescence as found for OPE with suitability and stability as found in the case of OPV. Therefore, it is reasonable to consider electron transfer from the photoexcited π-conjugated polymer to C_{60}.

4.2 Results

4.2.1 Structure of OPV/OPE Oligomers and Bisfullerene Terminated Assemblies

The modular synthetic methodologies described in the previous chapter allowed the systematic variation of key structural components in the H terminated OPV/OPE chromophoric bridges. The placement of C_{60} in the assemblies yields new chromophore-quencher dyads that possess dumb-bell topologies as illustrated in Scheme 4-1.

The chromophore-quencher assemblies consist of two parts, an OPV/OPE chromophoric bridge and a C_{60} electron acceptor. These systems undergo photoinduced electron/energy transfer cascades to yield charge-separation states as well as other excited state products. In this chapter the systematic steady state and time resolved spectroscopic investigations conducted on the OPV/OPE family of chromophore-quencher are described. The detailed analyses of the spectroscopic data provide insight into the factors that dictate

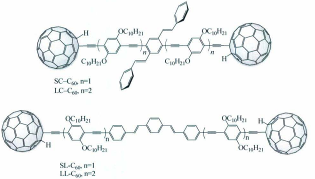

Scheme 4-1. The structure of OPV/OPE oligomers and bisfullerene terminated OPV/OPE oligomers.

the excited state dynamics from which correlations between the structure and electronic properties may be derived.

4.2.2 Radiative Processes of DEB and C_{60}-DEB

The Absorption and Emission of 1,4-Bis-decyloxy-2-dec-1-ynyl-5-ethynyl-benzene (DEB). The absorption and emission spectra of DEB are shown in Figure 4-2. Briefly, light excitation into the $S_0 \rightarrow S_1$ transition at 346 nm gives rise to an intense emission at 367 nm (27,250 cm^{-1}) with ϕ_{em}= 0.62 and a lifetime of ~ 2 ns reasonably assigned to a $S_1 \rightarrow S_0$ fluorescence band. There is another radiative transition at 715 nm, assigned to $T_1 \rightarrow S_0$ phosphorescence band.

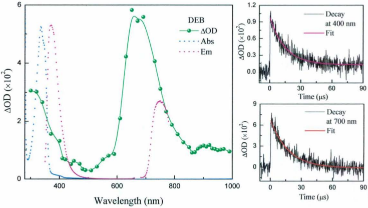

Figure 4-2. The transient absorption difference spectrum of DEB (•) obtained immediately following pulsed laser excitation at 355 nm (5 ns fwhm) in N_2 saturated $CHCl_3$ solution at 298 ($\pm$ 3) K. The solid green line is for illustrative purposes only. Also plotted is absorption (blue dot line) and emission (red dot line) spectra of DEB respectively in N_2 saturated $CHCl_3$ solution at 298 ($\pm$ 3) K. The corrected emission spectra was acquired with λ = 350 nm excitation, and normalized with the absorption maxima of the $S_0 \rightarrow S_1$ for illustrative purposes.

Transient Absorption of DEB. Also shown in Figure 4-2 is the transient absorption difference spectrum (TA) obtained at $t = 0$ following pulsed laser excitation at 355 nm. The DEB transient absorption difference spectrum is characterized by two prompt positive absorptions at ~ 350 nm (28,600 cm^{-1}) and 630 nm (15,900 cm^{-1}) respectively. The spectrum evolves in time and returns to the baseline with single exponential decay kinetics independent on the monitoring wavelength. Non-linear least square analyses of the time resolved absorption data using eq 4-22.

$$\Delta A_t = \Delta A_0 \exp(-kt) + y_0 \qquad (4\text{-}22)$$

where ΔA_t and ΔA_0 are changes in transient absorbance at time t and 0 after flash, k the decay rate constant, and y_0 an appropriate fixed number close to the asymptotic value of ΔA_t variable for large t values. The analyses yield the observed rate constant $k = 2.5\ (\pm\ 0.5)\times10^5\ \mathrm{s}^{-1}$ ($\tau = 4\ (\pm\ 0.8)\ \mu\mathrm{s}$), assigned to ^{3}DEB* based excited state decay. Two transient absorption bands are assigned to $T_1 \rightarrow T_n$ at $\lambda_{max}^{\Delta OD} = 350$ nm, and a lower energy $T_1 \rightarrow T_2$ at $\lambda_{max}^{\Delta OD} = 630$ nm. The combination of steady state and time-resolved absorption and emission spectroscopic data are consistent with the suggested mechanistic model shown in Figure 4-3. The spectroscopic observation of a long-lived triplet state in the absence of an obvious source of spin-orbit coupling provides evidence that the alkoxy substituents play a significant role in the excited state relaxation of the S_1 state by mediating intersystem crossing to the triplet state as shown in eq 4-23 (El-Sayed's rules). The $n \rightarrow \pi^*$ transition is clearly resolved in the ground state absorption spectrum at ~ 400 nm.

$$^1(\pi,\pi)^* \longrightarrow {}^1(n,\pi)^* \longrightarrow {}^3(\pi,\pi)^* \qquad (4\text{-}23)$$

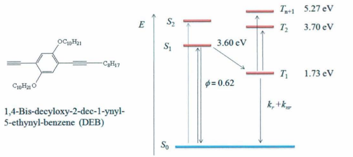
OC10H21
C8H17
C10H21O
1,4-Bis-decyloxy-2-dec-1-ynyl-5-ethynyl-benzene (DEB)
E
S2
S1
S0
3.60 eV
φ = 0.62
Tn+1 5.27 eV
T2 3.70 eV
T1 1.73 eV
kr + knr

Figure 4-3. Schematic energy level diagram illustrating the energetics of the singlet and triplet states.

The Absorption and Emission of C_{60}-DEB. The absorption spectrum of C_{60}-DEB in Figure 4-4 is adequately modeled as a linear combination of the DEB and C_{60} respectively. This suggests a weak electronic interaction between DEB and C_{60} in the

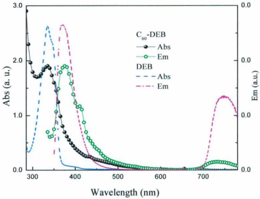

Figure 4-4. Absorption (•) and emission (o) spectra of C_{60}-DEB acquired in N_2 saturated $CHCl_3$ at 298 (± 3) K in comparison with the absorption (blue dot line) and emission (green dot line) acquired under the same condition.

ground state, in agreement with other analogous systems described by Schuster[64] and Tour.[65,66] DFT calculations by Zhao are consistent with the HOMO localized on DEB and LUMO on C_{60}.[67] Emission at 715 nm is assigned to $^1C_{60}^*$ excited state decay with a lifetime about 1.5 ns, in agreement with the reported lifetime for pristine $^1C_{60}^*$.[68,69] Based on the ϕ_F for DEB and C_{60}-DEB, the DEB based emission is significantly quenched ($\phi_F(C_{60}-DEB)/\phi_F\,(DEB) \approx 10^{-4}$).

Franck-Condon (FC) Excited State. The FC state possesses the electronic structure of the $^1(\pi,\pi)^*$ state, but the nuclear and solvent coordinates are still in the ground state configurations as electronic motion is much faster than the vibrational or nuclear motion. The Stokes shift between the absorbing and emitting states is given by

$$E_{abs} - E_{em} = 2\,\lambda_t \qquad (4\text{-}24)$$

where λ_t is the total reorganization energy, which is the sum of the vibrational (λ_{vib}) and solvent (λ_o) reorganization energies respectively. The Stokes shift of ~ 3100 cm^{-1} is consistent with the transition with high charge transfer character between the ground state and the lowest-lying excited state.

Transient Absorption of C_{60}-DEB. The transient absorption difference spectrum for C_{60}-DEB obtained in N_2 saturated $CHCl_3$ solution following 335 nm (5 ns fwhm) pulsed laser excitation is shown in Figure 4-5. Immediately following excitation, there are at least four prompt positive transient absorptions, two of which are well resolved with $\lambda_{max}^{\Delta OD}$ at 400 nm (25,000 cm^{-1}) and 730 nm (13,700 cm^{-1}). Another two relatively weak absorptions are at 500 nm (20,000 cm^{-1}) and 600 nm (16,700 cm^{-1}) respectively. All

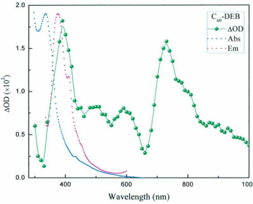

Figure 4-5. Absorption spectrum (blue dot line) and emission (red dot line) spectra of DEB-C_{60} respectively in N_2 saturated $CHCl_3$ solution at 298 (± 3) K. The corrected emission spectra was acquired with λ = 350 nm excitation, and normalized with the absorption maxima of the $S_0 \rightarrow S_1$ for illustrative purposes as in Figure 4-2. Also plotted is the transient absorption difference spectrum of DEB-C_{60} (green •) obtained immediately following 355 nm pulsed excitation in N_2 saturated $CHCl_3$ solution at 298 (± 3) K. The solid green line is for illustrative purposes only.

absorption bands decay with single exponential kinetics to pre-excitation values independent on the monitoring wavelength. The absorption at 600 nm is assigned as $T_1 \rightarrow T_2$ transition of DEB by comparison with the difference spectrum of DEB (Figure 4-3). The other three absorptions at 400, 500 and 730 nm are assigned as the excited state absorption of ${}^3C_{60}^*$.[69,70]

4.2.3 Radiative Processes of SC-$(C_{60})_2$ and LC-$(C_{60})_2$

Absorption Spectra. The absorption spectra of bisfullerene terminated OPV/OPE cruciform oligomers are shown in Figure 4-6. The spectra of SC/LC-$(C_{60})_2$ closely correspond to a superposition or linear combination of the individual spectra of OPV/OPE

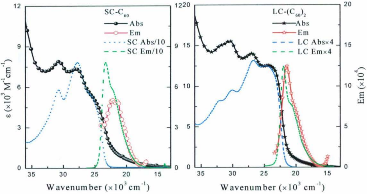

Figure 4-6. (Left) The absorption and emission spectra of SC-$(C_{60})_2$ (Abs●, Em○) in comparison with that of SC (dot line). (Right) LC-$(C_{60})_2$ (Abs ★, Em ☆) in comparison with that of LC (dot line) measured in $CHCl_3$ at 298±3K.

oligomers and C_{60}, *i.e.* the $\pi \rightarrow \pi^*$ transitions of the oligomer bridge and the typical absorptions of the C_{60} at ca. 300-350 nm (33,300 - 28,580 cm^{-1}) and a weak tail beyond 500 nm (20,000 cm^{-1}). The consequence of weak electronic interactions between the molecular components of the assemblies in the ground state was introduced in Chapter 3. Based on the spectroscopic data for OPV/OPE assemblies and the C_{60} terminus, the electronic properties of C_{60} are not dramatically altered when bonded to the OPV/OPE bridges. Comparing the spectra of SC/LC-$(C_{60})_2$ derivatives with those of their oligomer bridges, it is clear that the $\pi \rightarrow \pi^*$ transition of the SC/LC-$(C_{60})_2$ derivatives show little or no spectral shifts, suggesting an absence of significant energetic perturbations in the ground state. However, the absorption intensities of the π-bridges vary dramatically depending on the system. The absorptivity of SC-$(C_{60})_2$ was significantly decreased by the factor of 10 in comparison with the absorptivity of SC. On the other hand, the absorptivity of LC-$(C_{60})_2$ is increased by the factor of 4 when compared with that of LC. Figure 4-6 also shows that the absorption of OPV/OPE above 450 nm (22,220 cm^{-1}) is negligible. Therefore, the excitation of 350 - 450 nm (28,570-22,220 cm^{-1}) for SC/LC-$(C_{60})_2$ will result in almost selective excitation of the OPV/OPE moiety. The difference of f_{osc} will be addressed below.

Emission Spectra. The emission spectra of SC/LC-$(C_{60})_2$ are shown in Figure 4-6, and spectral data are summarized in Table 4-1. OPV/OPE oligomers SC and LC are highly emissive, with quantum yields of 0.96 for both SC and LC. The emission from triplet state is observed at 725 nm (13,800 cm^{-1}) for both SC and LC. For bisfullerene terminated oligomer SC-$(C_{60})_2$, the emission from singlet excited state $C_{60}-{}^1(\pi\text{-}B)^*_{SC}-C_{60}$ resulted from the exclusive OPV/OPE excitation is relatively red shifted ~ 10 -15 nm, and close to completely quenched ($\phi \approx 10^{-4}$) by energy transfer to the acceptor C_{60}. The evidence to support the energy transfer process is from the ultrafast kinetic data, which show the decay rate of $C_{60}-{}^1(\pi\text{-}B)^*_{SC}-C_{60}$ is the same as the rate of $C_{60}-(\pi\text{-}B)_{SC}-{}^1C^*_{60}$ formation.[1] The emission at 710 nm from the singlet excited state, $C_{60}-(\pi\text{-}B)_{SC}-{}^1C^*_{60}$, formed by energy transfer is also significantly quenched with a lifetime less than 300 ps, which is very close to the detection limit of the laser system. Compared with the lifetime of pristine C_{60} (S_1), 1.2 ns,[68] the lifetime of $C_{60}-(\pi\text{-}B)_{SC}-{}^1C^*_{60}$ is dramatically attenuated presumably due to an increase in k_{nr} competitive nonradiative decay processes. In

---

[1] The author thanks Prof. Nikolai Tkachenko for ultrafast data prior to publication.

LC-$(C_{60})_2$ assembly, the emission from the singlet excited state, $C_{60} - {}^1(\pi\text{-}B)^*_{LC} - C_{60}$, from the direct OPV/OPE bridge excitation, is significantly quenched ($\phi < 10^{-3}$). However, a definitive statement regarding the spectroscopy and the lifetime of the assembly is not possible as a trace amount of highly emissive bridge precursor as impurity may dominate. The emission from the singlet excited state, $C_{60} - (\pi\text{-}B)_{LC} - {}^1C^*_{60}$, which is formed by the excited state energy transfer to C_{60}, has a lifetime 1.2 ns.

Table 4-1. Comparative absorption and emission spectral data for SC-$(C_{60})_2$, SC and LC-$(C_{60})_2$, LC measured in $CHCl_3$ at 298 ± 3 K.

Entry	SC-$(C_{60})_2$	SC	LC-$(C_{60})_2$	LC
$\lambda_{max}^{S_0 \to S_1}$, nm	403(sh)	390	415	403
ε ($\times 10^4$ $M^{-1}cm^{-1}$)	0.60	5.4	13	3.2
$E_{op}^{S_0 \to S_1}$, cm^{-1}	24,800	25,600	24,100	24,800
$\lambda_{em}^{S_1 \to S_0}$, nm	451 710, $({}^1C^*_{60})$	428 725, ${}^3(SC)^*$	464 710, $({}^1C^*_{60})$	452 725, ${}^3(LC)^*$
$E_{em}^{S_1 \to S_0}$, cm^{-1}	22,200 14,100	23,400 13,800	21,600 14,200	22,100 13,700
E_{abs}-E_{em}, cm^{-1}	2460	2280	2550	2270
$\phi_F^{S_1 \to S_0}$	~ 10^{-4}	0.96	$\leq 10^{-3}$	0.96
τ_F, ns ($k_{d,}$ s^{-1})	2.6^a (3.8×10^8) <0.30 (3.3×10^9)	2.7 (3.7×10^8)	1.0^a 1.0×10^9) 1.2 (8.3×10^8)	1.1 (9.0×10^8)
$k_{r,}$ s^{-1}	3.8×10^4	3.6×10^8	1.0×10^6	8.7×10^8
$k_{nr,}$ s^{-1}	3.8×10^8	1.0×10^7	1.0×10^9	3.6×10^7

a. Trace amount of bridge precursor mask the lifetime of bisfullerene derivative.

4.2.4 Transient Absorption of Bisfullerene Terminated Derivatives SC/LC-$(C_{60})_2$

The difference spectra of transient absorption of SC-$(C_{60})_2$ and LC-$(C_{60})_2$ were acquired in N_2 saturated $CHCl_3$ 298±3K following excitation at 355 nm (fwhm: 5 ns). The laser pulse in the TA experiment is sufficiently intense such that SC undergoes photoinduced isomerization or possibly other reactions, which have not been characterized. Due to the facile photochemistry of SC, the transient absorption spectrum of SC cannot be acquired in solution. The difference spectra for SC-$(C_{60})_2$ and LC-$(C_{60})_2$ *vs.* LC are shown in Figure 4-7 and Figure 4-8. The transient absorption decays are fitted to the single exponential decay function as eq 4-22.

$$\Delta A_t = \Delta A_0 \exp(-kt) + y_0 \qquad (4\text{-}22)$$

All parameters are as defined above.

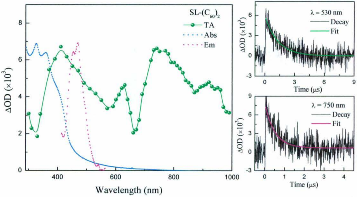

Figure 4-7. Nanosecond transient absorption spectrum of SC-$(C_{60})_2$ (green •) obtained immediately following 355 nm pulsed excitation in N_2 saturated $CHCl_3$ solution at 298 (± 3) K. The absorption (blue dot line) and emission (red dot line) are for comparison.

The transient absorption difference spectrum at $t = 0$ for SC-$(C_{60})_2$ in N_2 saturated $CHCl_3$ leads to the formation of at least four discernable transient absorptions, two of which are very broad with maxima at 410 nm (24,390 cm^{-1}) and 750 nm (13,330 cm^{-1})

respectively. The transient lifetime for the absorption at $\lambda_{max}^{\Delta OD}$ = 410 nm is ~ 3 ± 0.5 μs. This transient absorption is assigned to the radical anion $C_{60}^{-\cdot}$.[70] The absorption with $\lambda_{max}^{\Delta OD}$ at 750 nm has a lifetime about 600 ± 50 ns, which decays by the same single exponential kinetics ($k_D = (1.5 \pm 0.5)\times10^6$ s^{-1}) as the absorption band after 880 nm (11,360 cm^{-1}). These two transient species are assigned as $OPV^{+\cdot}$ and $C_{60}^{-\cdot}$ respectively from the charge-separation state $C_{60}-OPE-OPV_{SC}^{+\cdot}-OPE-C_{60}^{-\cdot}$.[34,71,72] The absorption at 630 nm (15,870 cm^{-1}) has a relatively long lifetime about 20 μs ($k_D = \sim5.0\times10^4$ s^{-1}), with the single exponential decay kinetics. This transient absorption is assigned as the excited state absorption $T_1 \rightarrow T_2$ localized on OPE, which is verified by comparison with the transient absorption spectrum of C_{60}-DEB and DEB described in Section 4.2.2. The transient absorptions at 410 and 750 nm do not return to the pre-excitation level. The presence of a long-lived transient species is evident by the small amplitude of transient absorption at t = 50 μs (inserted decay trace at 750 nm of Figure 4-7). The interpretation of the data is complicated due to the wavelength dependent kinetics. The triplet state, $^3C_{60}^*$, has similar absorption as that of $C_{60}^{-\cdot}$ in the visible region, and it also shows absorption at 740 nm.[70,73] Due to the superposition of the transient absorptions from both $^3C_{60}^*$ and $C_{60}^{-\cdot}$, the decay kinetics at 410 and 740 nm have a very slow component, which has the same lifetime as the transient with absorption at 400 and 740 nm from C_{60}-DEB. With reference to the transient absorption spectrum of C_{60}-DEB, the slow components at 410 and 740 nm are assigned primarily as the $^3C_{60}^*$ based excited state absorption.

The transient absorption spectrum of LC (Figure 4-8) exhibits a great resemblance to the transient absorption spectrum of DEB. Following 355 nm excitation of LC in N_2

saturated $CHCl_3$, two transient absorptions at ~ 400 nm (25,000 cm^{-1}) and 700 nm (14,300 cm^{-1}) are observed at $t = 0$, which returned to baseline with the single exponential decay kinetics independent on the monitoring wavelength. Non-linear least square analysis gave $k = 6.0 \pm 0.5 \times 10^4$ s^{-1} ($\tau = 10 \pm 0.8$ μs). The transient absorption spectrum is assigned to $^3OPE^*$ based excited state absorption, which is characterized by two prominent bands of $T_1 \rightarrow T_n$ at $\lambda_{max}^{\Delta OD}$ = 400 nm (25,000 cm^{-1}), and a lower energy $T_1 \rightarrow T_2$ at $\lambda_{max}^{\Delta OD}$ = 700 nm (14,300 cm^{-1}). This assignment is also supported by comparing with the transient absorption spectrum of the reference compound DEB.

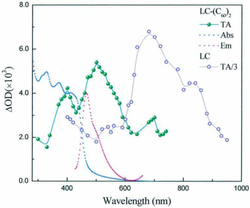

Figure 4-8. Nanosecond transient absorption spectrum of LC-$(C_{60})_2$ (green •) obtained immediately following 355 nm pulsed excitation in N_2 saturated $CHCl_3$ solution at 298 (± 3) K. The absorption (blue dot line) and emission (red dot line) are for comparison.

The transient absorption of LC-$(C_{60})_2$ displays a very different spectrum from that of SC-$(C_{60})_2$. As shown in Figure 4-8, the strong absorption with maximum at 500 nm (20,000 cm^{-1}) has a lifetime about 1.3 ± 0.5 μs, which is assigned as $T_1 \rightarrow T_n$ absorption of

^{3}OPV*.[74] Two other transient absorptions with maxima at 400 and 700 nm decay with τ ~ 5 ± 0.5 μs. With reference to the $T_1 \rightarrow T_n$ absorption of $^3C_{60}^*$ from SC-$(C_{60})_2$ and C_{60}-DEB, the absorptions at 400 nm and 700 nm are assigned to the absorption of $^3C_{60}^*$. The excited state ^{3}OPE* also displays absorption above 700 nm, verified by the transient absorption spectrum of LC. Therefore, the absorption above 700 nm possibly is the superposition of absorption from both ^{3}OPE* and $^3C_{60}^*$ or both of which require these two excited states to be in rapid equilibrium on the time scale of the excited state decay. In comparison with the transient absorption spectrum of SC-$(C_{60})_2$, it is clear that there is no sign of a charge-separation state in LC-$(C_{60})_2$ that persists on the ns time scale.

4.2.5 Radiative Processes of SL-$(C_{60})_2$ and LL-$(C_{60})_2$

Absorption Spectra. The absorption spectra of the SL/LL-$(C_{60})_2$ in dilute $CHCl_3$ solution (Figure 4-9) closely correspond to the superposition of the absorption spectra

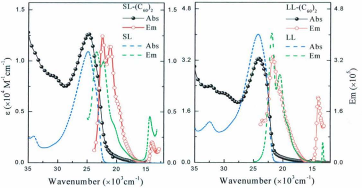

Figure 4-9. The absorption and emission spectra of SL-$(C_{60})_2$ (Abs ●, Em ○) in comparison with that of SL (dot line), and LL-$(C_{60})_2$ (Abs ●, Em ○) in comparison with that of LL (dot line) measured in $CHCl_3$ at 298 ± 3K.

from individual OPV/OPE linear bridges and C_{60}. The $\pi \rightarrow \pi*$ transitions occur at 404 nm (24,750 cm^{-1}) for SL bridge and 414 nm (24,155 cm^{-1}) for LL bridge. SL/LL-$(C_{60})_2$ display the typical absorptions of the C_{60} at ca. 300-350 nm (33,300-28,580 cm^{-1}) and a weak tail beyond 500 nm (20,000 cm^{-1}). The covalently linked fullerene and OPV/OPE oligomer maintain the electronic properties of the separated molecules. The $\varepsilon(\bar{\nu})$ of SL-$(C_{60})_2$ is very close to the $\varepsilon(\bar{\nu})$ of SL, but the $\varepsilon(\bar{\nu})$ of LL-$(C_{60})_2$ increased by the factor of 10 in comparison with the $\varepsilon(\bar{\nu})$ of LL. The absorption of SL/LL after 450 nm (22,000 cm^{-1}) is negligible. Therefore, the excitation of 350-450 nm (28,570-22,220 cm^{-1}) for SL/LL-$(C_{60})_2$ will result in almost selective excitation of the OPV/OPE bridges.

Emission Spectra. The emission spectra of bisfullerene terminated OPV/OPE linear oligomers are shown in Figure 4-9, and spectral data are summarized in Table 4-2. OPV/OPE linear bridges are highly emissive with quantum yield of 0.63 and 0.89 for SL and LL, respectively. The singlet excited state, OPV/OPE (S_1), decays radiatively to the ground state and nonradiatively via two pathways, $S_1 \xrightarrow{k_{nr}} S_0$ and intersystem crossing to the triplet state OPV/OPE (T_1). The lifetimes (τ) of the singlet excited state is 1.2 ns for SL and < 500 ps for LL. For SL-$(C_{60})_2$, the emission from the bridge singlet excited state, $C_{60} - {}^1(\pi\text{-}B)^*_{SL} - C_{60}$, that resulted from the exclusive OPV/OPE excitation is considerably quenched ($\phi \approx 10^{-3}$) by energy transfer to the acceptor C_{60} via a dipole-dipole resonance interaction. The evidence to support the energy transfer process is the ultrafast kinetic data, which shows the decay rate of ${}^1(\pi\text{-}B)^*_{SC}$ is the same as the rate of ${}^1C^*_{60}$ formation.[2]

---

[2] The author thanks Prof. Nikolai Tkachenko for ultrafast data prior to publication.

Table 4-2. Comparative absorption and emission spectral data for SL-$(C_{60})_2$, SL and LL-$(C_{60})_2$, LL measured in $CHCl_3$ at 298±3 K.

Entry	SL-$(C_{60})_2$	SL	LL-$(C_{60})_2$	LL
$\lambda_{max}^{S_0\rightarrow S_1}$, nm	404	401	414	411
ε ($\times10^4$ $M^{-1}cm^{-1}$)	1.4	1.1	33	4.1
$E_{op}^{S_0\rightarrow S_1}$, cm^{-1}	24,800	24,900	24,160	24,300
$\lambda_{em}^{S_1\rightarrow S_0}$, nm	453 711 ($^1C_{60}^*$)	445 710 $^3(SL)^*$	460 710 $^1C_{60}^*$)	456 710 $^3(LL)^*$
$E_{em}^{S_1\rightarrow S_0}$, cm^{-1}	22,100 14,100	22,500 14,100	21,700 14,100	21,900 14,100
E_{abs}-E_{em}, cm^{-1}	2670	2470	2420	2400
$\phi_F^{S_1\rightarrow S_0}$	~10^{-3}	0.63	< 10^{-3}	0.89
τ_F, ns (k_d, s^{-1})	<1.6> (6.0×10^8)[a] <0.30 (3.3×10^9)	1.2 (8.3×10^8) 20000 (5.0×10^4)	1.0(1.0×10^9)[a] 1.5 (6.7×10^8)	<0.50 (2.0×10^9) 4000 (2.5×10^5)
k_r, s^{-1}	6.0×10^5	5.2×10^8	1.0×10^6	1.8×10^9
k_{nr}, s^{-1}	6.0×10^8	3.1×10^8	1.0×10^9	2.0×10^8

a. Trace amount of bridge precursor mask the lifetime of bisfullerene derivative.
$D(t) = a_1 \exp(-t/\tau_1) + a_2 \exp(-t/\tau_2)$, $\langle\tau\rangle = a_1\tau_1/(a_1 + a_2) + a_2\tau_2/(a_1 + a_2)$.

The emission from the singlet excited state, $C_{60} - (\pi\text{-}B)_{SL} - {}^1C_{60}^*$, formed by energy transfer is also significantly quenched. The lifetime of $C_{60} - {}^1(\pi\text{-}B)_{SL}^* - C_{60}$ is obscured by a trace amount of precursor SL as impurity, and the lifetime of $C_{60} - (\pi\text{-}B)_{SL} - {}^1C_{60}^*$ is less than 300 ps. The excitation of OPV/OPE bridges in LL-$(C_{60})_2$ results in a close to completely quenched fluorescence from $C_{60} - {}^1(\pi\text{-}B)_{LL}^* - C_{60}$ by energy transfer to the acceptor, C_{60}. The emission from $C_{60} - (\pi\text{-}B)_{SL} - {}^1C_{60}^*$ formed by energy transfer decays radiatively to the ground state with a lifetime of 1.5 ns.

4.2.6 Transient Absorption of Bisfullerene Terminated Derivatives SL/LL-$(C_{60})_2$

SL and SL-$(C_{60})_2$. The transient absorption difference spectra of SL and SL-$(C_{60})_2$

acquired in N$_2$ saturated CHCl$_3$ at 298 ± 3K following pulsed laser excitation at 355 nm are shown in Figure 4-10 and Figure 4-11. The transient absorption difference spectrum of SL shows the ground state depletion at 400 nm (25,000 cm^{-1}), which is due to the loss of ground state absorption, in good match with the absorption spectrum of the original solution. This suggests that little or no chemical change occurs upon the laser excitation. A second negative band observed after 700 nm (14,285 cm^{-1}), which decays by the single exponential kinetics with $k = (5.0 \pm 0.5) \times 10^4\ s^{-1}$, is assigned as the triplet emission. This is in agreement with the emission spectrum as shown in the red dot line. In addition, another absorption with high intensity at $\lambda_{max}^{\Delta OD}$ = 500 nm has a lifetime about 1.0 ± 0.5 μs, which is assigned as $T_1 \rightarrow T_n$ absorption of ^{3}OPV*.[74] The broad absorption from 550 nm (18,180 cm^{-1}) to 660 nm (15,150 cm^{-1}) with a lifetime τ = 1.5 ± 0.5 μs is assigned as the $T_1 \rightarrow T_n$ absorption of ^{3}OPE*, with reference to the transient absorption spectra of DEB and LC.

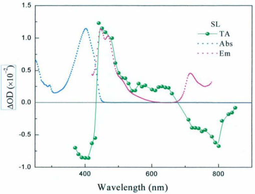

Figure 4-10. The transient absorption difference spectrum of SL (green •) obtained in N$_2$ saturated CHCl$_3$ solution at 298 (± 3) K immediately following 355 nm pulsed excitation. The absorption (blue dot line) and emission (red dot line) are for comparison.

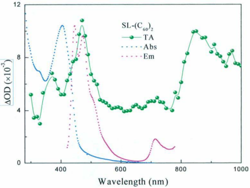

Figure 4-11. The transient absorption difference spectrum of SL-(C_{60})$_2$ (green •) obtained in N_2 saturated $CHCl_3$ solution at 298 (± 3) K immediately following 355 nm pulsed excitation. The absorption (blue dot line) and emission (red dot line) are for comparison.

The transient absorption difference spectra of SL-(C_{60})$_2$ displays a very similar profile as that of SC-(C_{60})$_2$, which exhibits at least four clearly resolved transient absorption bands. The maxima of two intense absorption bands are at 470 nm (21,300 cm^{-1}) and 840 nm (11,900 cm^{-1}). The transient species with absorption at 470 nm decays by the single exponential kinetics with $k_D = (7.0 \pm 0.5) \times 10^5\ s^{-1}$ ($\tau = 1.0 \pm 0.5\ \mu s$). With reference to the transient absorption of SL, this absorption band is assigned as $T_1 \rightarrow T_n$ absorption of $^3OPV^*$. The transient absorption at $\lambda_{max}^{\Delta OD} = 840$ nm decays with the same single exponential kinetics with $k_D = (2.5 \pm 0.5) \times 10^6\ s^{-1}$ ($\tau = 400 \pm 50$ ns) as the absorption band after 880 nm (11,360 cm^{-1}). These two transient species with $\lambda_{max}^{\Delta OD}$ at 840 nm and after 880 nm are assigned as $OPV^{+\cdot}$ and $C_{60}^{-\cdot}$, respectively, from the charge separation state $C_{60}-DEB-OPV_{SL}^{+\cdot}-DEB-C_{60}^{-\cdot}$. As known from the transient absorption spectrum of SC-$(C_{60})_2$ and the literature,[70] $C_{60}^{-\cdot}$ also shows an absorption at ~ 400 nm, but the lifetime of the transient with absorption at 380 nm (26,300 cm^{-1}) is about 2.0 ± 0.5 μs, relatively longer than the lifetime of $C_{60}^{-\cdot}$. With reference to the transient absorption spectra of C_{60}-DEB and SC-$(C_{60})_2$, $^3C_{60}^*$ also exhibits very similar absorption as $C_{60}^{-\cdot}$ in visible region, other than the absorption at ~ 740 nm as discussed above. Therefore, the absorption with $\lambda_{max}^{\Delta OD}$ at 380 nm is assigned as the superposition of absorption from both $C_{60}^{-\cdot}$ and $^3C_{60}^*$. As shown in Figure 4-9, the spectrum shows an extended absorption from 550 nm (18,200 cm^{-1}) to 660 nm (15,200 cm^{-1}), which decays by the single exponential kinetics with $k_D = (5.0 \pm 0.5)\times10^5\ s^{-1}$. This absorption band is assigned as $T_1 \rightarrow T_n$ absorption of $^3OPE^*$, with reference to the transient absorption spectra of LC and DEB.

LL and LL-$(C_{60})_2$. The transient absorption difference spectra of LL and LL-$(C_{60})_2$ were acquired under the same conditions as described above and shown in Figure 4-12 and Figure 4-13 respectively. The spectrum of LL displays a very similar profile as that of SL, with ground state bleaching at 400 nm (25,000 cm^{-1}), another negative band after 700 nm (14,285 cm^{-1}), and two absorption bands with $\lambda_{max}^{\Delta OD}$ at 470 nm (21,280 cm^{-1}) and 920 nm (10,640 cm^{-1}). The ground state depletion is in good match with the absorption spectrum of the original solution, suggesting little or no chemical change upon the laser excitation. Referring to the band assignment of SL, the negative band after 700 nm (14,285 cm^{-1}) which decays by the single exponential kinetics with $k = (2.5 \pm 0.5)\times10^5\ s^{-1}$ is assigned as the triplet emission. The intense absorption at $\lambda_{max}^{\Delta OD} = 470$ nm with a lifetime about 1.5 ± 0.5 μs is assigned as $T_1 \rightarrow T_n$ absorption of $^3OPV^*$.[74] The weak absorption with $\lambda_{max}^{\Delta OD}$ at 920 nm has a very long lifetime with $\tau = 10 \pm 0.5\ \mu s$. This

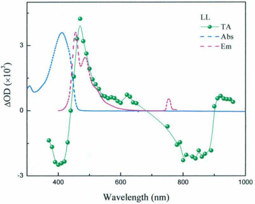

Figure 4-12. The transient absorption difference spectrum of LL (green •) obtained in N_2 saturated $CHCl_3$ solution at 298 (± 3) K immediately following 355 nm pulsed excitation. The absorption (blue dot line) and emission (red dot line) are for comparison.

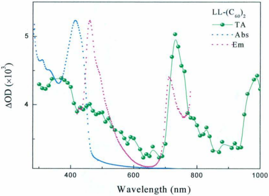

Figure 4-13. The transient absorption difference spectrum of LL-$(C_{60})_2$ (green •) obtained in N_2 saturated $CHCl_3$ solution at 298 (± 3) K immediately following 355 nm pulsed excitation. The absorption (blue dot line) and emission (red dot line) are for comparison.

transient absorption remains unassigned because it has a small ΔOD and is mixed with the triplet emission at ~ 800 nm - 900 nm, preventing the definitive assignment.

The transient absorption difference spectrum of LL-$(C_{60})_2$ (Figure 4-13) exhibits absorption in the entire visible region with two distinct sharp bands at 730 nm (13,700 cm^{-1}) and 950 nm (10,200 cm^{-1}), and another relatively broad band at 350nm (28,600 cm^{-1}). In comparison with the transient absorption difference spectra of LL, the absorption at 730 nm probably originates from ${}^3C_{60}^*$. With reference to C_{60}-DEB, and SC-$(C_{60})_2$, ${}^3C_{60}^*$ exhibits absorption at 400, 500 and 730 nm, and then the transient absorption at 730 nm is assigned as the excited state absorption of ${}^3C_{60}^*$. The broad absorption at 350 nm is assigned as $T_1 \rightarrow T_n$ absorption of ${}^3OPE^*$ by comparing with the reference compound DEB. The low energy sharp band at 950 nm is probably from the $T_1 \rightarrow T_2$ absorption of ${}^3OPE^*$, because DEB and LL display transient absorption at the same spectral region.

4.2.7 Global Kinetic Analysis

The spectral-kinetic data were processed by using the program SPECFIT/32 (Spectrum Software Associate, Marlborough, MA 01752, U.S.A.). The methodology of the program SPECFIT/32 as described in Chapter 2 relies on the method of Singular Value Decomposition (SVD) and nonlinear regression modeling by the Levenberg-Marquardt method. The experimental wavelength-time spectral data matrix (Y) is first reduced to a much smaller basis set of concentration (U×S) and spectroscopic (V) eigenvectors by Singular Value Decomposition, where the matrix product, $Y = U \times S \times V$, is the least squares best estimator of the original data matrix.[75,76] Generally, there will be as many eigenvectors as there are spectra or abscissa points in each spectrum, whichever is the less, *i.e.* the original data matrix is a highly over-determined system. However, SVD reduces the wavelength-time spectral data matrix (Y) to much smaller basis set of concentration (U×S) and spectroscopic (V) eigenvectors with significant eigenvectors containing all of the spectral and evolutionary information from the original data set. The remaining eigenvectors contain only experimental noise and can be eliminated from further consideration without the loss of information. After SVD, a global multivariate least-squares regression method is applied to fit the concentration (U×S) eigenvector basis set in the subspace spanned by V to an appropriate model of Y = CA, where the matrix C contains the concentration profiles and A represents the molar absorptivities of spectra. The concentration profiles for complex kinetic systems are solved within SPECFIT/32 by numerical integration of a user-defined set of differential rate equations. The results of such kinetic fits return both globally optimized rate constants and predicted spectra of the colored species.

In some cases, *i.e.* global analyses of equilibrium constants for metal coordination and protonation in Chapter 6, the program will be used with known molar absorptivity spectra of initial species in order to constrain the fit and in this way, more reliable spectra will be returned for those predicted species from the fit.

Global Kinetic Analysis of SC-(C_{60})$_2$. The transient absorption difference spectral changes of SC-(C_{60})$_2$ with time following 355 nm laser excitation is shown in Figure 4-14. At long wavelength after 700 nm, the transient absorptions assigned as charge-separation state, $C_{60}-\mathrm{OPE}-\mathrm{OPV}_{SC}^{+\cdot}-\mathrm{OPE}-C_{60}^{-\cdot}$, recombine to the ground state

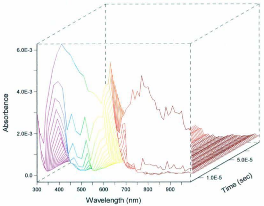

Figure 4-14. The transient absorption difference spectral changes of SC-$(C_{60})_2$ with time in N_2 saturated $CHCl_3$ solution at 298±3K after 355 nm laser excitation.

relatively faster than any other processes. The middle red absorption assigned as the triplet excited state absorption localized at OPE is the slowest process returning to the baseline. The high-energy absorptions from 300 to 550 nm are the superposition of transient absorptions of $^3OPV^*$, $C_{60}^{-\cdot}$ and $^3C_{60}^*$. The rate of the charge recombination is much faster than the rate of triplet state decaying, therefore, at the early time, the rate constant of the charge recombination dominates. The SVD of the data set revealed that the overall processes were far more complicated. As shown in Figure 4-15, the SVD revealed the presence of five significant spectral and time domain eigenvectors, which correspond to the four distinct kinetic processes as identified from the transient absorption difference spectrum. The tenth spectral eigenvector (V) was consistent with the line spectrum of the lamp source of the probe beam and the corresponding temporal changes

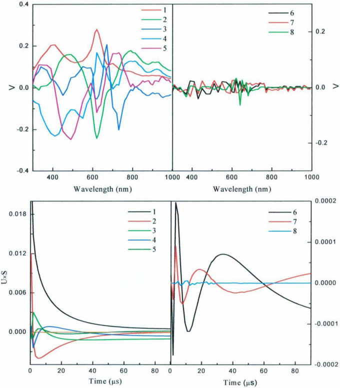

Figure 4-15. Singular value decomposition of the spectral-kinetic data matrix **Y** in Figure 4-14 for the first eight temporal eigenvectors from U x S.

(U x S) most likely arise from changes in lamp intensity.[76,77] Two of the remaining eigenvectors contain some structures, which is possibly factored from the less than 5% photochemical products given the extensive photolysis during the course of data acquisition. The photochemistry associated with SC-$(C_{60})_2$ was found to be significantly attenuated relative to SC by using the broadband white light excitation described in Chapter 3. Nevertheless, small changes in the steady state absorption spectrum of ~ 5% photoproducts are enough to generate spectral eigenvectors. The remaining eigenvectors contained only random noise that could be factored from the data. The SVD of the data set revealed the presence of four species, each of which has a distinct transient absorption difference spectrum. The analysis was found to be consistent with the kinetic model as described in Figure 4-16. Three distinct transient intermediates indicated in blue are formed in the laser pulse, consistent with the ultrafast flash photolysis experiment described above. The four spectrally different transient species are indicated in red in Figure 4-16. The colorless species is defined as the ground state shown in green in Figure 4-16. A global fit to this model gives the rate constant $k_1 = 1.3 \times 10^6\ s^{-1}$, assigned to the rate constant of charge recombination (k_{CR}). The single exponential kinetic data obtained at ~ 800-950 nm region

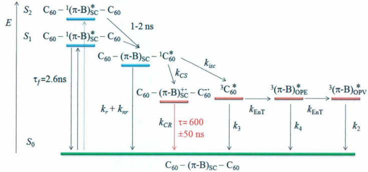
E
S_2 $C_{60}-{}^1(\pi\text{-B})^*_{SC}-C_{60}$
S_1 $C_{60}-{}^1(\pi\text{-B})^*_{SC}-C_{60}$
1-2 ns
$C_{60}-(\pi\text{-B})_{SC}-{}^1C^*_{60}$
k_{isc}
k_{CS}
τ_f=2.6ns
$C_{60}-(\pi\text{-B})^{+\cdot}_{SC}-C^{-\cdot}_{60}$
${}^3C^*_{60}$
${}^3(\pi\text{-B})^*_{OPE}$
${}^3(\pi\text{-B})^*_{OPV}$
$k_r + k_{nr}$
k_{EnT}
k_{EnT}
k_{CR} τ= 600 ±50 ns
k_3
k_4
k_2
S_0
$C_{60}-(\pi\text{-B})_{SC}-C_{60}$

Figure 4-16. Schematic energy level diagram showing excitation, energy transfer, intersystem crossing, charge separation, and charge recombination in the SC-$(C_{60})_2$ system. ${}^3(\pi\text{-B})^*_{OPV}$ is the triplet excited state localized on OPV, ${}^3(\pi\text{-B})^*_{OPE}$ is the triplet excited state localized on OPE, and ${}^3C^*_{60}$ is an abbreviation of $C_{60}-(\pi\text{-B})_{SC}-{}^3C^*_{60}$.

are consistent with the results derived from global analysis. The rate constant $k_2 = 6.0 \times 10^4$ s^{-1}, defined as the rate constant for ^{3}OPV* decay in the model of global analysis, is very close to the decay rate constant ($k_D = 5.8 \times 10^4$ s^{-1}) derived from the transient absorption data at around 450 nm to 550 nm absorption. The rate constant for $^3C^*_{60}$ decay is defined as k_3 in the global fit model. The fourth rate constant returned from global fit is $k_4 = 4.1 \times 10^3$ s^{-1}, defined as the rate constant for the decay of ^{3}OPE*, which has a relatively large discrepancy from the rate constant as derived from the transient absoption data $k_D = 5.0 \times 10^4$ s^{-1}. The possible reason for this large discrepancy is due to the set time base not being long enough for the decay traces to return to the baseline. As seen from Figure 4-14, the absorption in the red region is still above the baseline when approaching to the end of time base. The multi-wavelength spectral data for the global analysis program consist in the same data matrix, *i.e.* the same data points for different wavelengths. If the set time base is long enough for the slowest process, much information will be lost for the fast components. In summary, even if with the large discrepancy for the slow process, more than 95% of the data are fitted in a good agreement with the results as determined from the transient absorption data as shown in Figure 4-17.

Another criterion for the goodness of the global fit is the the variance-covariance matrix (H) of the parameters. The diagonal elements contain the information of the parameter variances and the off-diagonal elements the parameter covariances. Usually, the matrix H is normalized to one in the diagonal elements, and the off-diagonal element $h_{i,j}$ of the normalized H is the correlation coefficient between parameter i and j. If the value of the correlation coefficient is close to one, the parameters are mathematically correlated. High

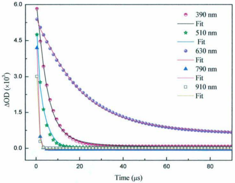

Figure 4-17. Representative decay traces show the goodness of global fitting for the defined kinetics model as in Figure 4-14 for SC-$(C_{60})_2$.

correlation between parameters means that these two parameters cannot be distinguished from one another and one needs to be removed from the fit. As output in the fitting result, all off-diagonal elements are equal to zero, which indicates that all kinetic processes are not correlated and intepretation of the kinetic data is tenable.

Together with the kinetic information, the global fit returns the predicted spectra of four colored species and the concentration profiles as shown in Figure 4-18. Due to the poor signal/noise ratio from 10 nm scan step between traces, the predicted spectra are smoothed by adjacent 5 points average, in agreement with the assigned absorption bands with reference to the spectra of model compounds DEB and C_{60}-DEB. The concentration changes of these four colored transients and the colorless ground state vary linearly with the values of rate constants for kinetic processes over the time course. The small value of the rate constant k_4 corresponds to the slow change of concentration for the colored species defined as $^3OPE^*$ in the global fit model.

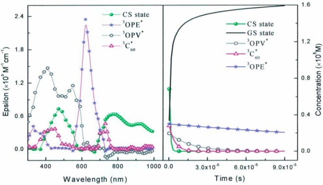

Figure 4-18. Predicted transient absorption spectra for four colored species and the concentration profiles obtained from global fit for SC-$(C_{60})_2$.

Global Kinetic Analysis of LC-$(C_{60})_2$ The transient absorption difference spectral changes of LC-$(C_{60})_2$ with time following 355nm laser excitation is shown in Figure 4-19.

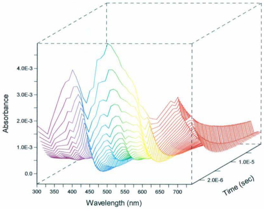

Figure 4-19. The transient absorption difference spectral changes of LC-$(C_{60})_2$ with time in N_2 saturated $CHCl_3$ solution at 298±3K after 355 nm laser excitation.

It is evident that there are no fast processes as revealed from the transient absorption data. The SVD shows the presence of four significant spectral and time domain eigenvectors, which correspond to the three distinct kinetic processes as identified from the transient absorption spectrum as shown in Figure 4-20. The fifth spectral eigenvectors (V) and the corresponding temporal changes (U x S) are also shown in Figure 4-20, which are completely random, consistent with the line spectrum of the lamp source from the probe

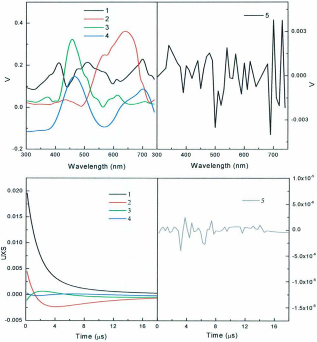

Figure 4-20. Singular value decomposition of the spectral-kinetic data matrix Y in Figure 4-19. (top) The first five spectral eigenvectors V and (bottom) the first five temporal eigenvectors from U x S.

beam as noted above. The remaining eigenvectors contain random noise that could be factored from the data. The SVD of the data set reveals the presence of three spectrally distinct transient species, which is consistent with the kinetic model as illustrated in Figure 4-21. Three transient intermediates indicated in blue are formed in the laser pulse. Three spectrally different transient species are indicated in red. The colorless species is defined as the ground state shown in green. A global fit to this model returned a rate constant k_1 = 5.1 × 10^5 s^{-1}, defined as the rate constant for the decay of $C_{60}-(\pi\text{-}B)_{LC}-{}^3C_{60}^*$, very close to the one (k = 5.0 ± 0.5 × 10^5 s^{-1}) derived from the non-linear least square analysis of the time resolved transient absorption at 400 nm, assigned as the $C_{60}-(\pi\text{-}B)_{LC}-{}^3C_{60}^*$based absorption. The rate constants k_2 (2.6 × 10^5 s^{-1}) and k_3 (7.3 × 10^4 s^{-1}) are also in agreement with those from the transient absorption data, identified as the decay rate constants of${}^3(\pi\text{-}B)_{OPV}^*$ and ${}^3(\pi\text{-}B)_{OPE}^*$ respectively.

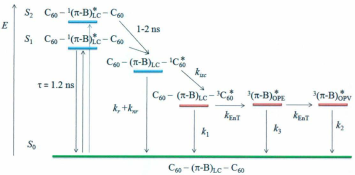
E
S_2 $C_{60}-{}^1(\pi\text{-}B)_{LC}^*-C_{60}$
S_1 $C_{60}-{}^1(\pi\text{-}B)_{LC}^*-C_{60}$
1-2 ns
$C_{60}-(\pi\text{-}B)_{LC}-{}^1C_{60}^*$
k_{isc}
τ = 1.2 ns
$C_{60}-(\pi\text{-}B)_{LC}-{}^3C_{60}^*$
${}^3(\pi\text{-}B)_{OPE}^*$
${}^3(\pi\text{-}B)_{OPV}^*$
k_r+k_{nr}
k_{EnT}
k_{EnT}
k_1
k_3
k_2
S_0
$C_{60}-(\pi\text{-}B)_{LC}-C_{60}$

Figure 4-21. Schematic energy level diagram showing excitation, energy transfer, intersystem crossing in LC-$(C_{60})_2$ system. ${}^3(\pi\text{-}B)_{OPV}^*$ is the triplet excited state localized on OPV, ${}^3(\pi\text{-}B)_{OPE}^*$ is the triplet excited state localized on OPE.

All off-diagonal elements of the parameter variance-covariance matrix H are equal to zero. Therefore, these three kinetic processes are independent on each other and each of them is a necessary step for the kinetics model.

Along with the kinetic information, the global fit returns the predicted spectra for these three observed colored species and the corresponding concentration profiles as shown in Figure 4-22. Due to the poor signal/noise ratio from 10 nm scan step between traces, the predicted spectra are smoothed by adjacent 5 points average. The concentration changes of these three colored transient species and the colorless ground state vary linearly with the values of rate constants for these three distinct kinetic processes over the time course.

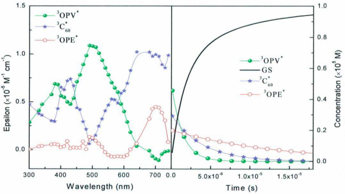

Figure 4-22. Predicted transient absorption spectra for three colored species and the concentration profiles obtained from global fit for LC-$(C_{60})_2$.

All other kinetic data are analyzed by the same program and self-defined kinetic models. The goodness of fitting is assessed by the significant spectral eigenvectors, the parameter variance-covariance matrix H, and comparing the fitting with the experimental decay traces at different wavelengths. All results of global kinetic analyses other than SL-$(C_{60})_2$ are summarized in the appendix or supplemental material. The result for SL-$(C_{60})_2$ is presented here for the purpose of discussion described in next section.

Global kinetic analysis of SL-$(C_{60})_2$ reveals that four colored species and a colorless ground state are involved in the kinetic processes. Based on the kinetic information from the global fit and the transient absorption data, the kinetic model for SL-$(C_{60})_2$ is given in Figure 4-23. In OPV/OPE linear bridged bisfullerene system, due to the orientation effect, the lifetime for charge-separation state is shortened to 400 ± 50 ns. In addition, the photophysics of linear bridged system is different from that of cruciform bridged systems.

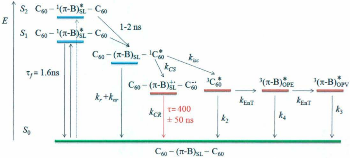
E
S_2 $C_{60}-{}^1(\pi\text{-B})^*_{SL}-C_{60}$
S_1 $C_{60}-{}^1(\pi\text{-B})^*_{SL}-C_{60}$
1-2 ns
$C_{60}-(\pi\text{-B})_{SL}-{}^1C^*_{60}$
k_{isc}
k_{CS}
τ_f = 1.6ns
$C_{60}-(\pi\text{-B})^{+\cdot}_{SL}-C^{-\cdot}_{60}$
$^3C^*_{60}$
$^3(\pi\text{-B})^*_{OPE}$
$^3(\pi\text{-B})^*_{OPV}$
k_r+k_{nr}
k_{EnT}
k_{EnT}
k_{CR}
τ = 400 ± 50 ns
k_2
k_4
k_3
S_0
$C_{60}-(\pi\text{-B})_{SL}-C_{60}$

Figure 4-23. Schematic energy level diagram showing excitation, energy transfer, intersystem crossing, charge separation, and charge recombination in the SL-$(C_{60})_2$ system. $^3(\pi\text{-B})^*_{OPV}$ is the triplet excited state localized on OPV, $^3(\pi\text{-B})^*_{OPE}$ is the triplet excited state localized on OPE, and $^3C^*_{60}$ is an abbreviation of $C_{60}-(\pi\text{-B})_{SL}-{}^3C^*_{60}$.

4.3 Discussion

4.3.1 The Effect of Varying Donor-Acceptor Distance

In OPV/OPE cruciform system, the emission from $^1(\pi\text{-B})^*_{\mathrm{SC}}$ (ϕ_{em}= 0.96) is almost completely quenched when the electron/energy acceptor C_{60} is covalently tethered. The lifetime of the bridge singlet excited state as determined from the time-resolved fluorescence is comparable to the bridge precursor $^1(\pi\text{-B})^*_{\mathrm{SC}}$, presumably due to a trace amount of highly emissive bridge precursor as impurity masking the radiative transition from $C_{60} - {}^1(\pi\text{-B})^*_{\mathrm{SC}} - C_{60}$ to $C_{60} - (\pi\text{-B})_{\mathrm{SC}} - C_{60}$. However, the lifetime of $C_{60} - (\pi\text{-B})_{\mathrm{SC}} - {}^1C^*_{60}$ is significantly reduced when compared to the lifetime of pristine $^1C^*_{60}$.[78] The spectroscopic signature assignable to $C_{60} - (\pi\text{-B})^{+\cdot}_{\mathrm{SC}} - C^{-\cdot}_{60}$ was detected in the transient absorption spectrum (see Figure 4-6). The charge separation is competitive with intersystem crossing with a $C^{-\cdot}_{60}$ spectral maker at $\lambda^{\Delta OD}_{max}$ ~ 900 - 1000 nm. As the charge recombination (CR) process is the only deactivation process in this time regime with k_{obsd} = $(1.5 \pm 0.5)\times10^6\ \mathrm{s}^{-1}$, the lifetime of the charge-separated state will be the inverse of the measured rate constant for the charge recombination process as eq 4-25.

$$\tau_{CS} = 1/k_{CR} \qquad (4\text{-}25)$$

The calculated lifetime for the charge-separated state is 600 ± 50 ns based on the global analysis.

In principle, the electron transfer can take place directly from the initially excited state $^1(\pi\text{-B})^*_{\mathrm{SC}}$, but it can also occur indirectly in a two-step process via an intermediate state $C_{60} - (\pi\text{-B})_{\mathrm{SC}} - {}^1C^*_{60}$, which is formed by energy transfer from $^1(\pi\text{-B})^*_{\mathrm{SC}}$ to C_{60}. The emission lifetime of $C_{60} - (\pi\text{-B})_{\mathrm{SC}} - {}^1C^*_{60}$ measured at 715 nm is less than 300 ps, very close to the detection limit. Therefore, even with deconvolution from the laser pulse, the lifetime has significant uncertainty and $\tau \leq 300$ ps. The observed rate constant for emission quenching is significantly larger than the decay rate constant from pristine $^1C_{60}^*$ to C_{60}. As discussed above the signal marker for $C_{60}^{-\cdot}$ observed in transient absorption difference spectrum is the absorption band at ~ 900 - 1000 nm (Figure 4-7). Taken together the short emission lifetime and the observation of signal for $C_{60}^{-\cdot}$ is consistent with a mechanism where the electron transfer occurs after singlet energy transfer to form the $^1C_{60}^*$ state. Therefore, the rate constant for the intramolecular charge separation (k_{CS}) can be calculated from eq 4-26,[79]

$$k_{CS} = \frac{1}{\tau(\mathrm{SC}-(\mathrm{C}_{60})_2)} - \frac{1}{\tau\,(\mathrm{C}_{60})} \qquad (4\text{-}26)$$

where, $\tau(\mathrm{SC}\text{-}(\mathrm{C}_{60})_2)$ is the lifetime of the fullerene emission from $\mathrm{C}_{60}-(\pi\text{-B})_{\mathrm{SC}}-{}^1\mathrm{C}_{60}^*$ and $\tau(\mathrm{C}_{60})$ is the lifetime of pristine $^1\mathrm{C}_{60}^*$ (1.2 ns).[78] When an indirect mechanism is operative, the electron transfer reaction occurs in less than 400 ps ($k_{\mathrm{CS}} = 2.5\times10^9$ s^{-1}).

It is evident the formation of the bridged radical ion pair, $\mathrm{C}_{60}-(\pi\text{-B})_{\mathrm{LC}}^{+\cdot}-\mathrm{C}_{60}^{-\cdot}$, is attenuated as the bridge length increases. The emission from the bridge singlet excited state, $\mathrm{C}_{60}-{}^1(\pi\text{-B})_{\mathrm{LC}}^*-\mathrm{C}_{60}$, is also significantly quenched due to the energy transfer to form $\mathrm{C}_{60}-(\pi\text{-B})_{\mathrm{LC}}-{}^1\mathrm{C}_{60}^*$. After the formation of $\mathrm{C}_{60}-(\pi\text{-B})_{\mathrm{LC}}-{}^1\mathrm{C}_{60}^*$, it will undergo charge separation or intersystem crossing to form $\mathrm{C}_{60}-(\pi\text{-B})_{\mathrm{LC}}-{}^3\mathrm{C}_{60}^*$, a kinetic competition that depends on ΔG^o and λ. The intersystem crossing, $S_1 \rightarrow T_1$, efficiently produce $\mathrm{C}_{60}-(\pi\text{-B})_{\mathrm{LC}}-{}^3\mathrm{C}_{60}^*$ within ~ 1 ns after the formation of $\mathrm{C}_{60}-(\pi\text{-B})_{\mathrm{LC}}-{}^1\mathrm{C}_{60}^*$.[80] $\mathrm{C}_{60}-(\pi\text{-B})_{\mathrm{LC}}-{}^3\mathrm{C}_{60}^*$ will relax to the ground state $\mathrm{C}_{60}-(\pi\text{-B})_{\mathrm{LC}}-\mathrm{C}_{60}$, or by Dexter energy transfer form $C_{60}-OPE-OPV_{LC}-{}^3OPE^*-C_{60}$ and $C_{60}-OPE-{}^3OPV^*-OPE-C_{60}$. Due to the small energy difference between the two triplet states, $C_{60}-(\pi\text{-}B)_{LC}-{}^3C_{60}^*$ and ${}^3OPE^*$, these two states are dynamically coupled given by eq 4-27.[81-83]

$$C_{60}-(\pi\text{-}B)_{LC}-{}^3C_{60}^* \overset{K}{\rightleftharpoons} C_{60}-OPE-OPV_{LC}-{}^3OPE^*-C_{60} \qquad (4\text{-}27)$$

The observed kinetics will be exponential as these two states presumably interconvert rapidly on the time scale of excited state decay, and the transient absorption spectra will be linear combination of the difference spectra by equilibrium constant.

The quantum yields and fluorescence lifetimes of LC and LC-$(C_{60})_2$ (Table 4-1) can be used to estimate the rate constants for the energy transfer (k_{EnT}) via the relation:[84]

$$k_{EnT} = \left(\frac{\phi(\text{LC})}{\phi(\text{LC}-(C_{60})_2)} - 1\right)/\tau(\text{LC}) \qquad (4\text{-}28)$$

where $\frac{\phi(\text{LC})}{\phi(\text{LC}-(C_{60})_2)}$ is the quenching ratio and $\tau(\text{LC})$ is the lifetime of the S_1 state of LC. The calculated rate constant for energy transfer process is extremely fast and occurs within about 2 ps ($k_{EnT} \sim 10^{12}\ s^{-1}$)

In OPV/OPE linear systems, the pattern of the excited state dynamics is similar to that in cruciform systems described in Section 4.2.6. The charge separation is very efficient as shown in Figure 4-9. The charge recombination (CR) process competes with no other deactivation process, and the lifetime of the charge-separated state calculated from eq 4-25 is about 400 ± 50 ns. The lifetime of charge separation state is shorter than the lifetime in SC-$(C_{60})_2$ because of the chromophore orientation effect which will be discussed in section 4.3.4. In the linear system SL-$(C_{60})_2$, the charge separation also occurs indirectly in a two-step process via an intermediate state $C_{60}-(\pi\text{-}B)_{SL}-{}^1C_{60}^*$.

This is evident from the measured lifetime of $C_{60}-(\pi\text{-}B)_{SL}-{}^{1}C_{60}^{*}$, less than 300 ps. The rate constant of this indirect charge separation (k_{CS}) calculated from eq 4-26 is 2.5×10^{9} s^{-1}, which means the charge separation occurs in less than 400 ps.

In LL-$(C_{60})_2$, there is no evidence for the formation/decay of an intramolecular charge separation state. After direct excitation of the OPV/OPE linear bridge, the Förster energy transfer to form $C_{60}-(\pi\text{-}B)_{LL}-{}^{1}C_{60}^{*}$ significantly quenches the emission from $C_{60}-(\pi\text{-}B)_{LL}^{*}-C_{60}$. The rate constant for energy transfer calculated from eq 4-28 is 1.8×10^{12} s^{-1}, which is extremely fast and occurs within less than 1 ps. After the formation of $C_{60}-(\pi\text{-}B)_{LL}-{}^{1}C_{60}^{*}$, it will undergo charge separation or intersystem crossing to form $C_{60}-(\pi\text{-}B)_{LL}-{}^{3}C_{60}^{*}$, a kinetic competition that depends on ΔG^{o} and λ. The pattern of the kinetic processes is similar to that in cruciform systems as described above albeit with some differences in the rate constants.

The rate constants for energy transfer (k_{EnT}), indirect charge separation (k_{CS}), and charge recombination (k_{CR}) for bisfullerene terminated OPV/OPE oligomers are summarized in Table 4-3. The energy gap between the donor and bridge can be estimated from the emission spectral fitting data as listed in Table 3-5.

The rate constant for bridge mediated electron transfer is distance dependent and characterized by an attenuation factor β, eq 4-29.

$$k_{ET} \propto |V_{DA}|^{2} \propto \exp(-\beta R_{DA}) \qquad (4\text{-}29)$$

where R_{DA} is the donor-acceptor edge-to-edge distance. The magnitude of β depends on the electronic structure of the bridge (ν), the length of a repeating unit of the bridge (R_o),

Table 4-3. Fluorescence quenching of $\phi(\pi-\mathrm{B})/\phi$, rate constants for energy Transfer (k_{EnT}), indirect charge separation (k_{CS}), charge recombination (k_{CR})[a], the energy and the redox potential of donor.

Entry	$\frac{\phi(\pi-\mathrm{B})}{\phi}$	k_{EnT} (s^{-1})	$\frac{\phi(C_{60})}{\phi}$	k_{CS} (s^{-1})	k_{CR} (s^{-1})	E_{00} (cm^{-1})	E_{ox}(GS) (cm^{-1})	E_{ox}(ES) (cm^{-1})
SC-$(C_{60})_2$	9.6×10^2	3.6×10^{12}	> 4	$> 2.5\times10^9$	1.5×10^7	23,340	13,310	-10,030
LC-$(C_{60})_2$	9.6×10^2	5.0×10^{11}	1	-	-	21,950	12,580	-9,370
SL-$(C_{60})_2$	6.3×10^2	5.3×10^{11}	> 4	$> 2.5\times10^9$	2.5×10^7	22,360	10,240	-12,120
LL-$(C_{60})_2$	8.9×10^2	1.8×10^{12}	1	-	-	22,130	10,240	-11,890

[a] Rate constants for energy transfer (k_{EnT}), indirect charge separation (k_{CS}), and direct charge recombination (k_{CR}) calculated from eqs 4-26, 4-28, and 4-25, respectively. Redox potentials were measured by Dr. Yuming Zhao, and are included here is for the discussion.

and on the energy difference, ΔE, between the donor and bridge subunit localized states according to eq 4-30.

$$\beta = \frac{2}{R_0} \ln\left(\frac{\Delta E}{\nu}\right) \qquad (4\text{-}30)$$

The dependence of the ET rate constant on the energy gap, ΔE_{DB}, between the donor and the bridge could be separated from the dependence on the donor-acceptor distance (R), by comparing the systems with the same donor-acceptor distance. However, for both short bridge systems SC-$(C_{60})_2$ and SL-$(C_{60})_2$ and long bridge systems LC-$(C_{60})_2$ and LL-$(C_{60})_2$, the energy gap between the donor and the bridge in SC-$(C_{60})_2$ (or LC-$(C_{60})_2$) is very close to the energy gap in SL-$(C_{60})_2$ (or LL-$(C_{60})_2$). It is difficult to rationalize the dependence of electron transfer rate on the energy gap. This will be elaborated on in Chapter 5 for donor-substituted systems in which the donor groups have a significant impact on the energy gap.

With respect to the distance dependence of the electron transfer rate, it can be separated from the dependence of the energy gap by comparing the systems with the relatively same energy gap. In OPV/OPE cruciform and linear systems, the energy gap between the donor and the bridge is comparable to each other, and the rate of electron transfer decreases exponentially with distance. For LC-$(C_{60})_2$ and LL-$(C_{60})_2$, the bridge repeating unit is 2, and the rate of electron transfer becomes negligible in comparison with the other processes. Therefore, there is no evidence for the charge-separated state detected in the transient absorption spectrum. On the contrary, the charge-separated state is detected in SC-$(C_{60})_2$ by the transient absorption of $C_{60}^{-\cdot}$.

4.3.2 Back Electron Transfer or Charge Recombination

After the photo-induced electron transfer generating a charge-separated state, a charge recombination process brings the systems back to the ground state. The CR process was studied by monitoring the decay of $C_{60}^{-\cdot}$ at 950 nm in transient absorption. As there are no other deactivation processes competing with the recombination, the rate constant for charge recombination is calculated as the inverse of the measured lifetimes of $C_{60}^{-\cdot}$. The lifetimes corresponding to the charge separation states are 600 ± 50 ns for SC-$(C_{60})_2$ and 400 ± 50 ns for SL-$(C_{60})_2$. The calculated rate constants for charge recombination are $1.5\times10^7\ s^{-1}$ for SC-$(C_{60})_2$ and $2.5\times10^7\ s^{-1}$ for SL-$(C_{60})_2$. In the classical limit, the rate constant k_{ET} is given by[85,86]

$$k_{ET} = \nu_{ET} \exp\left\{-\left[\frac{(\lambda + \Delta G^o)^2}{4\lambda RT}\right]\right\} \qquad (4\text{-}31)$$

where λ is the sum of intramolecular, λ_i, and solvent, λ_o, reorganization energies. The overall free energy change, $\Delta G°$, for charge separation was calculated by eqs 4-32 and

4-33 using the electrochemical redox data:[33,87]

$$-\Delta G_{CR}^{o} = E_{OX} - E_{RED} - \Delta G_s \qquad (4\text{-}32)$$

$$-\Delta G_{CS}^{o} = E_{00} - (-\Delta G_{CR}) \qquad (4\text{-}33)$$

where E_{OX} is the first oxidation potential of the OPV/OPE bridge, and E_{RED} is the first reduction potential of the fullerene. E_{00} is the energy of the 0-0 transition between the lowest excited state and the ground state of the OPV/OPE, evaluated from the fluorescence emission peaks, and ΔG_s refers to free energy of solvation, calculated by using the "dielectric continuum model" according to eq 4-34.

$$\Delta G_s = \frac{e^2}{4\pi\epsilon_0\epsilon_S R_{CC}} \qquad (4\text{-}34)$$

where R_{CC} is the center-to-center distance of the positive and negative charges in the charge-separated state. ϵ_S is the relative permittivity of the solvent, -*e* is the elemental charge, and ϵ_0 is the vacuum permittivity. In the limit of weak electronic coupling between the electron donor and acceptor, the nonadiabatic limit, the barrier crossing frequency, ν_{ET} is the electron tunneling frequency, ν_e. It is related to λ and the electron transfer matrix element, $\hat{H}_{DA}$, as shown in eq 4-35. $\hat{H}_{DA}$ is the resonance energy arising from orbital mixing between the donor and acceptor orbitals.[85,86]

$$\nu_{ET} = \nu_e = \frac{2\pi \hat{H}_{DA}^2}{\hbar}\sqrt{\frac{1}{4\pi\lambda RT}} \qquad (4\text{-}35)$$

The calculated $\hat{H}_{DA}$ from eq 4-35 are summarized in Table 4-4.

For SC-$(C_{60})_2$ and SL-$(C_{60})_2$, the total reorganization energy is 2440 ± 10 cm^{-1}, but the driving forces are different by 0.050 eV, and the rate constants for the charge

Table 4-4: The electron transfer matrix elements calculated from the overall free energy change between states, reorganization energy and redox potentials.[a]

Entry	k_{CS} (s^{-1})	k_{CR} (s^{-1})	λ_t (cm^{-1})	ΔG^o_{CS} (cm^{-1})	ΔG^o_{CR} (cm^{-1})	$\frac{\Delta G^o_{CS}}{\lambda_t}$	ν_{ET} (cm^{-1})	$\hat{H}_{DA}$ (cm^{-1})
SC-$(C_{60})_2$	$> 2.5\times10^9$	1.5×10^7	2450	-4557	-18783	1.86	2.2×10^{10}	4.0
LC-$(C_{60})_2$	-	-	2879	-4046	-17904	1.40		
SL-$(C_{60})_2$	$> 2.5\times10^9$	2.5×10^7	2435	-3165	-19195	1.30	3.3×10^9	1.5
LL-$(C_{60})_2$	-	-	1813	-9060	-13070	5.00		

[a] Redox potentials were measured by Dr. Y. Zhao, and are included here for the discussion.

recombination differ by a factor of 10. The ratio of $\Delta G^o/\lambda_t$ is 1.86 for SC-$(C_{60})_2$ and 1.30 for SL-$(C_{60})_2$ respectively and the charge recombination reaction lies in the inverted region. LC-$(C_{60})_2$ should have a rate constant of 5.1×10^6 s^{-1} based on the reorganization energy and a driving force of -17904 cm^{-1}, assuming by the extrapolation to calculate k_{CR} for LC-$(C_{60})_2$ is correct. The plot of $\ln k_{nr}$ *vs.* ΔG^o has a negative slope, based on the assumption the electronic coupling is sufficient in LC-$(C_{60})_2$ for electron transfer. The data given in Table 4-4 show $\hat{H}_{DA}$ ~ 4.0 cm^{-1} for SC-$(C_{60})_2$ and 1.5 cm^{-1} for SL-$(C_{60})_2$, which is sufficient for the charge separation for SC-$(C_{60})_2$ and SL-$(C_{60})_2$.

The fact that LC-$(C_{60})_2$ does not yield a charge separation is presumably due to an attenuation of $\hat{H}_{DA}$. It follows that the extra spacer impedes k_{CS} as $\hat{H}_{DA}$ is lowered by a longer distance between the electron donor OPV and the electron acceptor C_{60}. The mechanism for the transduction of the electron is presumably superexchange, which is dependent on the donor-acceptor separation distance. The extra spacer places the donor OPV and the acceptor C_{60} further apart and then the electron transfer by superexchange is attenuated.

In the classical limit, the activation barrier is given by the free energy and the total reorganization energy plus the contribution of distortions to the reaction profile induced by strong electronic coupling. In the semiclassical model developed by Sutin, Brunshwig and Creutz, the semiclassical model introduces the parameters to correct for electron transfer via a tunneling mechanism because in the inverted region the thermal population is insufficient to overcome the barrier. The quantum model then imposes wavefunctions that extend beyond the arbitrary energy of the ground state reactant and product harmonic oscillators. The molecule must find a route from which the electron density can be transferred to the product of vibrationally excited state in the ground state with the conservation of energy and angular momentum.

Within the context of the Fermi Golden rule, the reorganization energy and energetics are incorporated in Franck-Condon factor. The wavefunctions of ground and excited states are electronically orthogonal. Therefore, to have the electron transfer between two states, there must involve molecular vibrations that break the orthogonality and provide the electronic pathway to return to the ground state. The molecular vibrations that break the orthogonal nature are known as promoting modes. The promoting modes distort the symmetry of the electronically excited state configuration and couple the excited state electron density to the high vibrational level of the ground state. Promoting modes generally are symmetrically allowed transitions, which have been probed by using resonance Raman spectroscopy. Within the context of one mode approximation, that is all averaged vibrational modes and the quantum spacing is an average of the different vibration energetics.

4.3.3 Orientation Effect

The kinetic processes in OPV/OPE linear systems are similar to the processes in cruciform systems. However, the efficiency of intersystem crossing is increased by the orientation effect involving $^1(n,\pi*) \rightarrow {}^3(\pi,\pi)*$ (El-Sayed's rules shown in Figure 4-24).[88,89] In OPV/OPE linear oligomers, the transition moment is along the molecular axis, and excitation involves the OPE fragment, which is indicated from the emission spectral fitting parameter, $\hbar\omega$ = 1450 cm^{-1}. Intersystem crossing is facilitated by coupling a change in spin angular momentum with a change in orbital angular momentum on converting a $^1(n,\pi)*$ state to a $^3(\pi,\pi)*$ state, which has emission at 710 nm for SL and at 725 nm for SC (Figure 4-25).

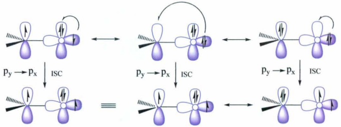

Figure 4-24. Intersystem crossing by coupling a change in spin angular momentum with a change in orbital angular momentum on converting a $^1(n,\pi)*$ state to a $^3(\pi,\pi)*$ state. Reproduced from ref 88.

For alkoxy substituted OPV/OPE oligomers, S_1 and T_1 are $(n,\pi)*$, while T_2 is $(\pi,\pi)*$. Theoretically, transitions between states of different multiplicity ($\Delta S \neq 0$) are strictly forbidden, but practically they are partly allowed due to the spin-orbit coupling. Therefore, the $S_1 \rightarrow T_1$ transition may occur via a direct spin-orbital coupling of S_1 to the

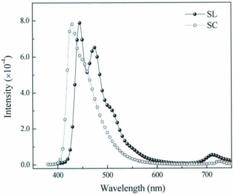

Figure 4-25. Orientation effect on intersystem crossing to convert a $^1(n,\pi)^*$ state to a $^3(\pi,\pi)^*$ state for SC *vs.* SL.

upper vibrational level of T_1 or via the spin-orbital coupling of S_1 to an upper T_n state followed by $T_n \rightarrow T_1$ internal conversion. The uppermost T_n level cannot be more than 1000 cm^{-1} above the S_1 state, otherwise the contribution of the $S_1 \rightarrow T_n$ channel to k_{ST} would be negligible. To calculate the rate constant k_{ST}^n, the empirical Robinson-Frosch equation can be used:

$$k_{ST}^n \sum (S_1 \rightarrow T_n) \approx 10^{12} \left|\beta_{S_1T_n}^n\right|^2 \exp\left(-0.25E_{S_1T_n}^{0.4}\right) \qquad \text{(4-36)}$$

where $\beta_{S_1T_n}^n = \langle \psi_{S_1} | \hat{H}_{SO} | \psi_{T_n} \rangle$ is the matrix element of the spin-orbit coupling between the S_1 and the T_n states, and $E_{S_1T_n}$ is the energy gap between S_1 and T_n levels, expressed in cm^{-1}. The exponential factor in eq 4-36 approximates the Franck-Condon factor depending on the energy gap, $E_{S_1T_n}$, which can be evaluated from the spectroscopic analyses. The value of the spin-orbit coupling matrix element is determined by the types of symmetry of the S_1 and T_n states, which cannot, as yet, be directly evaluated. For alkoxy substituted OPV/OPE oligomers, the mixing of S_1 and T_1 is symmetry forbidden, but the mixing of S_1 and T_2 is symmetry allowed. Therefore, based on the assumption that the process of the internal conversion for the S_1 level is negligible, the rate constants of the $S_1 \rightarrow T_1$ process can be estimated from the experimental data according to eq 4-37.[90]

$$k_{ST} = (1 - \phi_F)/\tau_S \qquad (4\text{-}37)$$

From the spectroscopic data in Table 4-1 and Table 4-2, the calculated values of k_{ST} are 2.6×10^8 s^{-1} for SL and 1.5×10^7 s^{-1} for SC. The energy gap between S_1 and T_n levels estimated from the spectroscopic data is 9570 cm^{-1} for SC and 8385 cm^{-1} for SL. From eq 4-36, the calculated value of the spin-orbit coupling matrix is 0.26 for SC and 2.8 for SL.

4.4 Conclusions

1. The charge separation and charge recombination for short bridged systems SC-$(C_{60})_2$ and SL-$(C_{60})_2$ lie in the inverted region, but the charge recombination is more deeply down in the inverted region. Therefore, the rate constant for charge recombination is much smaller than the forward charge separation.
2. The long bridged systems LC-$(C_{60})_2$ and LL-$(C_{60})_2$ do not yield a charge separation state after photon capture, which is due to an attenuation of $\widehat{H}_{DA}$ with increasing the donor-acceptor separation distance.
3. Due to the orientation effect, the charge separation in SL-$(C_{60})_2$ is less efficient than in SC-$(C_{60})_2$.

4.5 References

(1) Szacilowski, K.; Macyk, W.; Drzewiecka-Matuszek, A.; Brindell, M.; Stochel, G. *Chem. Rev.* **2005**, *105*, 2647-2694.

(2) Devadoss, C.; Bharathi, P.; Moore, J. S. *J. Am. Chem. Soc.* **1996**, *118*, 9635-9644.

(3) Davis, W. B.; Svec, W. A.; Ratner, M. A.; Wasielewski, M. R. *Nature* **1998**, *396*, 60-63.

(4) Okada, A.; Chernyak, V.; Mukamel, S. *J. Phys. Chem. A* **1998**, *102*, 1241-1251.

(5) Speiser, S. *Chem. Rev.* **1996**, *96*, 1953-1976.

(6) Davis, W. B.; Wasielewski, M. R.; Ratner, M. A.; Mujica, V.; Nitzan, A. *J. Phys. Chem. A* **1997**, *101*, 6158-6164.

(7) Felts, A. K.; Pollard, W. T.; Friesner, R. A. *J. Phys. Chem.* **1995**, *99*, 2929-2940.

(8) Oevering, H.; Paddon-Row, M. N.; Heppener, M.; Oliver, A. M.; Cotsaris, E.; Verhoeven, J. W.; Hush, N. S. *J. Am. Chem. Soc.* **1987**, *109*, 3258-3269.

(9) Petrov, E. G.; May, V. *J. Phys. Chem. A* **2001**, *105*, 10176-10186.

(10) Ramakrishna, S.; Willig, F.; May, V. *Chem. Phys. Lett.* **2002**, *351*, 242-250.

(11) Goldsmith, R. H.; DeLeon, O.; Wilson, T. M.; Finkelstein-Shapiro, D.; Ratner, M. A.; Wasielewski, M. R. *J. Phys. Chem. A* **2008**, *112*, 4410-4414.

(12) Zhang, H.; Li, X.-Q.; Han, P.; Yu, X. Y.; Yan, Y. *J. Chem. Phys.* **2002**, *117*, 4578-4584.

(13) Henderson, P. T.; Jones, D.; Hampikian, G.; Kan, Y.; Schuster, G. B. *Proc. Nat. Acad. Sci. U. S.A.* **1999**, *96*, 8353-8358.

(14) Sim, E. *J. Phys. Chem. B* **2005**, *109*, 11829-11835.

(15) Sim, E.; Kim, H. *J. Phys. Chem. B* **2006**, *110*, 16803-16807.

(16) Bixon, M.; Jortner, J. *Adv. Chem. Phys.* **1999**, *106*, 35-202.

(17) Skourtis, S. S.; Beratan, D. N. *Adv. Chem. Phys.* **1999**, *106*, 377–452.

(18) McConnell, H. M. *J. Chem. Phys.* **1961**, *35*, 508-515.

(19) Mattias P. ; Eng, B. A. *Angew. Chem. Int. Ed.* **2006**, *45*, 5626-5629.

(20) Eng, M. P.; Albinsson, B. *Chem. Phys.* **2009**, *357*, 132-139.

(21) Ogawa, M. Y.; James F, W.; Young, Z.; MiUer, J. R.; Isied, S. S. *J. Phys. Chem.* **1993**, *97*, 11456-11463.

(22) Gamov, G. *Nature* **1928**, *122*, 805-806.

(23) Davis, W. B.; Svec, W. A.; Ratner, M. A.; Wasielewski, M. R. *Nature* **1998**, *396*, 60-63.

(24) Zeng, Y.; Zimmt, M. B. *J. Phys. Chem.* **1992**, *96*, 8395-8403.

(25) Marcus, R. A. *J. Phys. Chem.* **1989**, *93*, 3078-3086.

(26) Cave, R. J.; Newton, M. D.; Kumar, K.; Zimmt, M. B. *J. Phys. Chem.* **1995**, *99*, 17501-17504.

(27) Han, H.; Zimmt, M. B. *J. Am. Chem. Soc.* **1998**, *120*, 8001-8002.

(28) Kumar, K.; Lin, Z.; Waldeck, D. H.; Zimmt, M. B. *J. Am. Chem. Soc.* **1996**, *118*, 243-244.

(29) Napper, A. M.; Read, I.; Kaplan, R.; Zimmt, M. B.; Waldeck, D. H. *J. Phys. Chem. A* **2002**, *106*, 5288-5296.

(30) Wiederrecht, G. P.; Watanabe, S.; Wasielewski, M. R. *Chem. Phys.* **1993**, *176*, 601-614.

(31) Sinks, L. E.; Wasielewski, M. R. *J. Phys. Chem. A* **2003**, *107*, 611-620.

(32) Weiss, E. A.; Ahrens, M. J.; Sinks, L. E.; Ratner, M. A.; Wasielewski, M. R. *J. Am. Chem. Soc.* **2004**, *126*, 9510-9511.

(33) Rehm, D.Weller, A. *Israel Journal of Chemistry* **1970**, *8*, 259-271.

(34) Neuteboom, E. E.; Meskers, S. C. J.; Hal, P. A. V.; van Duren, J. K. J.; Meijer, E. W.; Janssen, R. A. J.; Dupin, H.; Pourtois, G.; Cornil, J.; Lazzaroni, R.; Brédas, J. L.; J. Beljonne, D. *J . Am. Chem. Soc.* **2003**, *125*, 8625-8638.

(35) Marcus, R. A. *Annu. Rev. Phys. Chem.* **1964**, *15*, 155-196.

(36) Harriman, A.; Heitz, V. a.; Sauvage, J. P. *J. Phys. Chem.* **1993**, *97*, 5940-5946.

(37) Wiberg, J.; Guo, L.; Pettersson, K.; Nilsson, D.; Ljungdahl, T.; Martensson, J.; Albinsson, B. *J. Am. Chem. Soc.* **2007**, *129*, 155-163.

(38) Davis, W. B.; Ratner, M. A.; Wasielewski, M. R. *Chem. Phys.* **2002**, *281*, 333-346.

(39) Bixon, M.; Jortner, J. *J. Am. Chem. Soc.* **2001**, *123*, 12556-12567.

(40) Davis, W. B.; Ratner, M. A.; Wasielewski, M. R. *J. Am. Chem. Soc.* **2001**, *123*, 7877-7886.

(41) Pourtois, G.; Beljonne, D.; Cornil, J.; Ratner, M. A.; Brédas, J. L. *J. Am. Chem. Soc.* **2002**, *124*,

4436-4447.

(42) Giaimo, J. M.; Gusev, A. V.; Wasielewski, M. R. *J. Am. Chem. Soc.* **2002**, *124*, 8530-8531.

(43) Sakata, Y.; Tsue, H.; O'Neil, M. P.; Wiederrecht, G. P.; Wasielewski, M. R. *J. Am. Chem. Soc.* **1994**, *116*, 6904-6909.

(44) Lukas, A. S.; Bushard, P. J.; Wasielewski, M. R. *J. Phys. Chem. A* **2002**, *106*, 2074-2082.

(45) Sanchez, L.; Herranz, M.; Martin, N. *Journal of Materials Chemistry* **2005**, *15*, 1409-1421.

(46) Imahori, H.; Mori, Y.; Matano, Y. *J. Photochem. Photobiol. C: Photochem. Rev.* **2003**, *4*, 51-83.

(47) Hiroshi, I.; Kiyoshi, H.; Tsuyoshi, A.; Masanori, A.; Seiji, T.; Tadashi, O.; Masahiro, S.; Yoshiteru, S. *Chem. Phys. Lett.* **1996**, *263*, 545-550.

(48) Imahori, H.; Sakata, Y. *Eur. J. Org. Chem.* **1999**, 2445-2457.

(49) Williams, R. M.; Koeberg, M.; Lawson, J. M.; An, Y.-Z.; Rubin, Y.; Paddon-Row, M. N.; Verhoeven, J. W. *J. Org. Chem.* **1996**, *61*, 5055-5062.

(50) Moore, T. A.; Moore, A. L.; Gust, D. *Phil. Trans. R. Soc. Lond. B* **2002**, *357*, 1481-1498.

(51) Watanabe, N.; Furusho, Y.; Takata, T.; Araki, Y.; Ito, O. *Angew. Chem.* **2003**, *115*, 705-707.

(52) Liddell, P. A.; Sumida, J. P.; N., M. A.; Noss, L.; Seely, G. R.; Clark, K. N.; Moore, A. L.; Moore, T. A.; Gust, D. *Photochem. Photobiol.* **1994**, *60*, 537-541.

(53) Sariciftci, N. S.; Smilowitz, L.; Heeger, A. J.; Wudl, F. *Science* **1992**, *258*, 1474-1476.

(54) Wolffs, M.; Hoeben, F. J. M.; Beckers, E. H. A.; Schenning, A. P. H. J.; Meijer, E. W. *J. Am. Chem. Soc.* **2005**, *127*, 13484-13485.

(55) Panda, P.; Veldman, D.; Sweelssen, J.; Bastiaansen, J. J. A. M.; Langeveld-Voss, B. M. W.; Meskers, S. C. J. *J. Phys. Chem. B* **2007**, *111*, 5076-5081.

(56) Kraabel, B.; Lee, C. H.; McBranch, D.; Moses, D.; Sariciftci, N. S.; Heeger, A. J. *Chem. Phys. Lett.* **1993**, *213*, 389-394.

(57) Brabec, C. J.; Zerza, G.; Cerullo, G.; De Silvestri, S.; Luzzati, S.; Hummelen, J. C.; Sariciftci, S. *Chem. Phys. Lett.* **2001**, *340*, 232-236.

(58) Kraabel, B.; Hummelen, J. C.; Vacar, D.; Moses, D.; Sariciftci, N. S.; Heeger, A. J.; Wudl, F. *J. Chem. Phys.* **1996**, *104*, 4267-4273.

(59) van Hal, P. A.; Janssen, R. A. J.; Lanzani, G.; Cerullo, G.; Zavelani-Rossi, M.; De Silvestri, S. *Chem. Phys. Lett.* **2001**, *345*, 33-38.

(60) Smilowitz, L.; Sariciftci, N. S.; Wu, R.; Gettinger, C.; Heeger, A. J.; Wudl, F. *Phys. Rev. B* **1993**, *47*, 13835-13842.

(61) Schenning, A. P. H. J.; Tsipis, A. C.; Meskers, S. C. J.; Beljonne, D.; Meijer, E. W.; Brédas, J. L. *Chem. Mater.* **2002**, *14*, 1362-1368.

(62) Seixas de Melo, J.; Pina, J.; Burrows, H. D.; Di Paolo, R. E.; Maçanita, A. L. *Chem. Phys.* **2006**, *330*, 449-456.

(63) Swager, T. M.; Gil, C. J.; Wrighton, M. S. *J. Phys. Chem.* **1995**, *99*, 4886-4893.

(64) Vail, S. A.; Schuster, D. I.; Guldi, D. M.; Isosomppi, M.; Tkachenko, N.; Lemmetyinen, H.; Palkar, A.; Echegoyen, L.; Chen, X.; Zhang, J. Z. H. *J. Phys. Chem. B* **2006**, *110*, 14155-14166.

(65) Zhao, Y.; Shirai, Y.; Slepkov, D. A.; Alemany, L. B.; Sasaki, T.; Hegmann, F. A.; Tour, J. M. *Chem. Eur. J.* **2005**, 3643-3658.

(66) Shirai, Y.; Osgood, A. J.; Zhao, Y.; Yao, Y.; Saudan, L.; Yang, H.; Yu-Hung, C.; Sasaki, T.; Morin, J.-F.; Guerrero, J. M.; Kelly, K. F.; Tour, J. T. *J. Am. Chem. Soc.* **2006**, *128*, 4854-4864.

(67) Wang, L.; Zhang, N.; Zhao, Y.; Thompson, D. W. *Manuscript in preparation.*

(68) Sun, Y. P.; Wang, P.; Hamilton, N. B. *J. Am. Chem. Soc.* **1993**, *115*, 6378-6381.

(69) Williams, R. M.; Zwier, J. M.; Verhoeven, J. W. *J. Am. Chem. Soc.* **1995**, *117*, 4093-4099.

(70) Kamat, P. V.; Bedja, I.; Hotchandanit, S. *J. Phys. Chem.* **1994**, *98*, 9137-9142.

(71) Peeters, E.; van Hal, P. A.; Knol, J.; Brabec, C. J.; Sariciftci, N. S.; Hummelen, J. C.; Janssen, R. A. J. *J. Phys. Chem. B* **2000**, *104*, 10174-10190.

(72) Ramos, A. M.; Meskers, S. C. J.; vanHal, P. A.; Knol, J.; Hummelen, J. C.; Janssen, R. A. J. *J. Phys. Chem. A* **2003**, *107*, 9269-9283.

(73) Sauve, G.; Dimitrijevie, N. M.; Kamat, P. V. *J. Phys. Chem.* **1995**, *99*, 1199-1203.

(74) Ginocchietti, G.; Cecchetto, E.; Cola, L. D.; Mazzucato, U.; Spalletti, A. *Chem. Phys.* **2008**, *352*, 28-34.

(75) Binstead, R. A.; Jung, B.Zuberbühler, A. D.; 2000-2005 Spectrum Software Associates ed.; Spectrum Software Associates: Marlborough, 2000.

(76) Stultz, L. K.; Binstead, R. A.; Reynolds, M. S.; Meyer, T. J. *J. Am. Chem. Soc.* **1995**, *117*, 2520-2532.

(77) Stultz, L. K.; Huynh, M. V. H.; Binstead, R. A.; Curry, M.; Meyer T. J. *J. Am. Chem. Soc.* **2000**, *122*, 5984-5996.

(78) Sun, Y.-P.; Wang, P.; Hamilton, N. B. **1993**, *J. Am. Chem. Soc.*, 6378-6381.

(79) Debreczeny, M. P.; Wasielewski, M. R.; Shinoda, S.; Osuka, A. *J. Am. Chem. Soc.* **1997**, *119*, 6407-6414.

(80) Fraelich, M. R.; Weisman, R. B. *J. Phys. Chem.* **1993**, *97*, 11145-11147.

(81) Gevaert, M.; Kamat, P. V. *J. Phys. Chem.* **1992**, *96*, 9883-9888.

(82) Thompson, D. W.; Fleming, C. N.; Myron, B. D.; Meyer, T. J. *J. Phys. Chem. B* **2007**, *111*, 6930-6941.

(83) Wielopolski, M.; Atienza, C.; Clark, T.; Guldi, D. M.; Martìn, N. *Chem. Eur. J.* **2008**, *14*, 6379-6390.

(84) van Hal, P. A.; Knol, J.; Langeveld-Voss, B. M. W.; Meskers, S. C. J.; Hummelen, J. C.; Janssen, R. A. J. *J. Phys. Chem. A* **2000**, *104*, 5974-5988.

(85) Alstrum-Acevedo, J. H.; Brennaman, M. K.; Meyer, T. J. *Inorg. Chem.* **2005**, *44*, 6802-6827.

(86) Meyer, T. J.; Taube, H. *Comprehensive Coordination Chemistry, The Synthesis, Reactions, Properties and Applications of Coordination Compounds. Electron-Transfer Reactions*; Pergammon Press: Oxford U.K., 1987; Vol. 1.

(87) D'Souza, F.; Chitta, R.; Gadde, S.; McCarty, A. L.; Karr, P. A.; Zandler, M. E.; Sandanayaka, A. S. D.; Araki, Y.Ito, O. *J. Phys. Chem. B* **2006**, *110*, 5905-5913.

(88) Turro, N. J.; Ramamurthy, V.; Scaiano, J. C. *Principles of Molecualr Photochemistry: An Introduction*; University Science Books, 2009.

(89) Anslyn, E. V.; Dougherty, D. A. *Modern physical organic chemistry*; University Science: Sausalito, Calif., 2006.

(90) Korshunov, L. I.; Shatrov, V. D.; Kuznetsov, V. S.; Rachek, V. F.; Mikhailov, u. A.; Batekha, I. G.; El'tsov, A. V. *J. Appl. Spec.* **1980**, *33*, 1115-1119.

Chapter 5

Radiative, Non-radiative Processes of OPV/OPE Chromophore with Donor Substituents and Derivative Bisfullerene Terminated Oligomers

Overview

The goal of this chapter is to understand the donor substituent effect on the structural, electronic and vibronic parameters that govern the photo-induced electron and energy transfer in the donor substituted (π-B)-bridged C_{60} Systems (A-[π-$(D)B_C]_n$-A).

5.1 Introduction....233

5.1.1 Twisted Intramolecular Charge Transfer (TICT)....234

5.1.2 Planar Intramolecular Charge Transfer (PICT)....236

5.1.3 Wagged Intramolecular Charge Transfer (WICT)....238

5.1.4 Rehybridized Intramolecular Charge Transfer (RICT)....240

5.1.5 Excited-State Structural Relaxation in Donor Acceptor Substituted Stilbenes....240

5.1 Results: Radiative Processes....246

5.2.1. Structure of OPE/OPV Oligomers with Donor Substituents....246

5.2.2. Absorption and Emission of OPE/OPV Oligomers with Donor Substituents....247

5.2.3. Transient Absorption of OPE/OPV Oligomers with Donor Substituents..254

5.2.4. Absorption and Emission of Bisfullerene Terminated Oligomers....256

5.2.5. Transient Absorption of Derivative Bisfullerene Terminated Oligomers..260

5.2 Discussions....263

5.3.1. Substituent Effect....263

5.3.2. The Effect of Varying Donor-Acceptor Distance and the Interplay with the Energy-gap Dependence....269

5.3.3. The Distance and Energy-gap Dependence of Energy Transfer....273

5.3.4. Back Electron Transfer or Charge Recombination....274

5.3 Conclusions....277

5.4 References....278

5.1 Introduction

The photoinduced intramolecular charge transfer (ICT) in the excited state is an important transition due to their potential application such as non-linear optical materials for data storage, laser dyes, optical switches, pH and ion detectors, fluorescence sensors, etc.[1-4] Photoinduced intramolecular charge transfer may also play a significant role for generating sustained charge separation by efficient intramolecular charge transfer (ICT) in photochemical-energy utilization.[5-7]

Organic molecules consisting of electron donor and electron acceptor groups linked by a conjugated π-electron system (D-π-A) have attracted considerable attention due to the complexity of the excited state manifolds and dynamics. The observation of dual emission by Lippert et al.[8] and the recognition that R_2N substituted chromophores undergo conformational changes resulting in the twisted intramolecular charge transfer (TICT) significantly challenged the existing paradigms for the excited state relaxation in aromatic chromophores.[9] In view of their close relationship to photochemical energy utilization and other application, a convincing and clear analysis of the electronic and geometrical structure before and after the primary step of charge transfer needs to be delineated. With regard to the mechanistic aspects of photophysics and photochemistry of D-π-A molecules, many hypotheses have been formulated in competition with the simple and initially convincing explanation given by Lippert et al. Currently, the leading monomolecular models may be divided into four classes based on the conformation of the excited states: TICT (twisted intramolecular charge transfer), WICT (wagged intramolecular charge transfer),[10,11] in which a pseudo Jahn-Teller coupling to form a planar

CT (PICT) state,[12] and RICT (rehybridization intramolecular charge transfer).[13,14]

5.1.1 Twisted Intramolecular Charge Transfer (TICT)

Electronic excitation generally planarizes the system and thus increases the charge delocalization to reduce the electron-electron repulsion and bond lengths change due to the population of $\pi*$ orbital,[15,16] Some D-A systems have been found to undergo torsional motion about the D-A bond, resulting in the formation of a twisted charge-separation state with an orthogonal conformation between the donor and acceptor. The first clearly recognized and most discussed example of twisted intramolecular charge transfer is 4-(*N,N*-dimethylamino)benzonitrile (DMABN). In the absence of any excited state reaction, two fluorescence bands were observed in a variety of solvents, from the weakly polar dialkyl ethers and toluene to the highly polar alkyl cyanides and alcohols. The intensity and energetics of the emission bands strongly depended on the solvent polarity and temperature. Only one fluorescence band appears in non-polar solvents, originating from the ^1L_b ($^1B_2$) state, and later named by different authors as B fluorescence (F_B), normal fluorescence (F_N), or locally excited fluorescence (LE). In polar solvents, a long wavelength emission band grows in relative intensity, which was assigned to the second singlet excited state (^1La), while the intensity of the first band decreases with increasing polarity of the solvent.[8,17] After studying the dual fluorescence of DMABN and its derivatives, Grabowski and coworkers proposed an intramolecular conformational change occurred, with the F_B band assigned to an approximately coplanar structure and the F_A to an excited state charge transfer conformation with a highly twisted NMe_2 group as illustrated in Figure 5-1.[9] The torsional motion accompanying intramolecular charge transfer, a rather widespread phenomenon, was proposed as a successor of the so-called locally excited (LE) state through the twisting of the D-A bond.

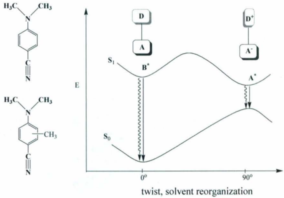

Figure 5-1. Structure of substituted DMABN and adiabatic reaction pathway for TICT.

The nature of the adiabatic reaction pathway, which connects the S_1 local excited species to the S_1 charge transfer emitting state, has been discussed extensively in the experimental and theoretical literature.[18-23] The S_1 reaction coordinate that involves the twist of the amino group relative to the benzene ring has often been postulated to be the origin of the "TICT mechanism" (Figure 5-1). If a TICT forming molecule possessing a planar ground state is electronically excited, the structure of the excited state adopts a twisted conformation characterized by red-shifted emission or non-radiative decay with an enhanced rate constant. The efficiency of this relaxation process as well as the position of the emission band strongly depends on the molecular environment.[24] The formation of the TICT state results in the formation of an excited state dipole moment, which is energetically stabilized in polar solvents as reflected in the D_S constant of the solvent.

It is often assumed that the essential difference between the TICT and the other ICT models for molecules such as DMABN consists of the absence of electronic coupling between the amino and benzonitrile groups in the TICT state, leading to an increased lifetime for charge separation in the TICT state. In WICT, RICT, and PICT states to be discussed below, the electron donor (D) and acceptor (A) substituents of DMABN are both electronically coupled to the phenyl group. Therefore, the usual assumption is that the N-phenyl bond has a single-bond character in TICT, while it has a double bond character in PICT. However, several calculations have found a quinoidal TICT state on S_1,[25-27] as manifested in the VB structure.[28] The intrinsic electronic coupling between the amino group and the benzene ring is large in both PICT and TICT structures.

5.1.2 Planar Intramolecular Charge Transfer (PICT)

Based on the absence of a linear correlation between the maximum of the CT emission band, $h\nu_{max}$ (CT), and the redox potentials of the electron donor (D) and acceptor (A) subunits in DMABN,[29,30] it has been concluded that a strong electronic coupling exists between the amino and benzonitrile subunits. This is in clear contradiction of the principle of minimum overlap of the TICT model. Clearly, DMABN cannot be treated as a D (NR_2) and an A (CN) group separated by a phenyl ring, which plays the role of an inert molecular spacer. Therefore, the TICT model has been challenged by several other alternative models, and the most important one is the planar ICT (PICT) state suggested by Zachariasse and coworkers.[29,31-33]

In support of the PICT model, some indirect experimental approaches based on time-resolved resonance Raman[34] and infrared measurements[35,36] to unravel the ICT molecular structure have been reported, but which were interpreted as giving support to the TICT model. A direct determination of the molecular structure for the ICT state in crystalline 4-(diisopropylamino)benzonitrile (DIABN) from picosecond X-ray diffraction has been reported by Zachariasse et al. Spectroscopic results suggest that an ICT state with a lifetime of 3 ns is produced upon photoexcitation of DIABN molecules in a crystalline powder. X-ray diffraction (XRD) experiments with a time resolution of 70 ps show that the torsional angle of the diisopropylamino group with respect to the plane of the phenyl ring of DIABN decreases from 14° in the electronic ground state to 10° in the equilibrated ICT state. Therefore, the ICT state of DIABN in the crystal lattice has an effectively planar structure.[18] Recently, the interpretation of these time-resolved X-ray diffraction experiments of DIABN crystal powder has been questioned based on experiments in which the ICT state of DIABN was prepared by the direct excitation of the crystal powder with 400 nm laser light with excitation energy around 6000 cm^{-1} below that of S_1.[37] Under such strongly endothermic conditions, an *anti*-Stokes process, S_1 can normally only be populated by two-photon absorption.[38] A more common and simple experimental approach to obtain structural information of ICT states is to use model compounds, for which the structure is assumed to be known. The intramolecular charge transfer with planarized 4-cyanofluorazene (FPP4C) and its flexible counterpart 4-cyano-N-phenylpyrrole (PP4C) were investigated, both of them showing a similar dual emission from a locally excited (LE) and an intramolecular charge transfer (ICT) state.[39] The fluorescence and time-resolved spectra were similar, suggesting that the ICT states of

FPP4C and PP4C have similar structure with a high degree of planarity (Figure 5-2). It is clear that a perpendicular twist of the D and A subunits in a donor/acceptor molecule is not a requirement for efficient ICT in the excited state.

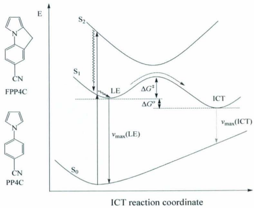

Figure 5-2. Structure and potential energy surfaces for the ground state S_0 and the excited states S_1, S_2, LE, and ICT for planar FPP4C and flexible PP4C.

5.1.3 Wagged Intramolecular Charge Transfer (WICT)

The TICT model to explain the structural and molecular nature of the red shifted second emission band of DMABN and its dual fluorescent derivatives appears to be flawed based on the observations made for F4PPC and PP4C. Gorse and Pesquer suggested the wagged intramolecular charge transfer to challenge the necessity of this twist to obtain the ICT state that is responsible for the dual fluorescence.[11] According to the authors, WICT is the pyramidalization of the dimethylamino nitrogen which change from planar (sp^2) to pyramidal (sp^3) hybridization of the dimethylamino nitrogen (Figure 5-3).

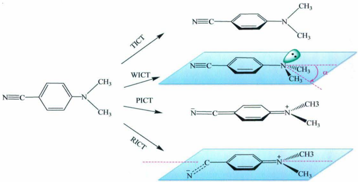

Figure 5-3. Schematic representation of WICT in comparison with TICT, PICT and RICT.

The pyramidalization of the dimethylamine nitrogen can also decouple the nitrogen lone pair orbital from the acceptor π subsystem, which would lead to an increase in the positive charge on the dimethylamino group and, hence, to a larger value of the dipole moment of the intramolecular charge transfer state. To ascertain if the dual fluorescence can be interpreted in terms of WICT state, theoretical calculations have been carried out on DMABN using both semiempirical and ab initio methods.[11,13,40,41] The calculations suggest that the dual fluorescence may be a consequence of a dynamically coupled TICT and LE which are distorted with respect to one another with a kinetic barrier, $\Delta G^{\neq}$. If true, the relative distribution of the LE and TICT states will be solvent and temperature dependent. Furthermore, the calculations predicted an energy minimum at a twist angle of about 60^{o}, but not the fully twisted (perpendicular) structure for the lowest excited state. On the other hand, the dual fluorescence phenomena cannot be solely related to the presence of a WICT state mainly because the polar WICT state is too high in energy and no minimum exists along the reaction coordinate.

5.1.4 Rehybridized Intramolecular Charge Transfer (RICT)

Rehybridization of the carbon atom of cyano group from sp to sp^2 is due to the charge transferred to it from the dimethylamino group, resulting in an in-plane bent structure of the acceptor group, which is the key feature of the rehybridized ICT (RICT) model (Figure 5-3). The RICT model was proposed based on the results of ab initio CI single optimizations by identifying a corresponding excited state minimum with strong charge transfer character.[13,14] However, this RICT state is 19.6 kcal/mol higher in energy than the TICT state and is furthermore associated with a large barrier (17.6 kcal/mol) which is not surprising given the significant changes in bonding required for a reconfiguration of sp → sp^2.[40] Thus, even in polar solvents the TICT pathway for DMABN is thermodynamically and kinetically favored against the RICT reaction. Moreover, the RICT hypothesis would not help to explain ample evidence for analogues of DMABN in which the CN group is replaced by such substituent as -CHO, $-COCH_3$, -COOR, or-$CONR_2$, or those in which the whole benzonitrile acceptor is replaced by the pyridine or pyrimidine ring. Therefore, the RICT hypothesis remains unsupported by the experimental data.

5.1.5 Excited-State Structural Relaxation in Donor-Acceptor Substituted Stilbenes

TICT based dual fluorescent systems have been applied in the design of ratiometric fluorescent chemosensors,[4,42,43] nonlinear optical materials,[44] and electro-optical switches.[45] In addition, the TICT concept has inspired the design of ground state twisted zwitterionic D-A systems possessing very large polarizability properties.[46,47] The fluoroionophoric behavior for the neutral probes is characterized by an "off-on" photoinduced electron transfer (PET)-like fluorescence intensity in response to a switching from a twisted intramolecular charge transfer to a planar intramolecular charge transfer state. *trans*-Aminostilbenes are D-A molecules that could undergo both *trans-cis* isomerization and TICT formation in the singlet excited state ($^1t^*$). The structural effect on the interplay of these two types of torsional motions is still controversial.

Different mechanistic interpretations for the formation and deactivation of the TICT state of aminostilbenes have been proposed. Recent experimental data reveal that substituents play an important role in determining the relative energy levels of the excited states and thus the resulting decay pathways. Earlier spectroscopic studies on *N,N*-dialkyl substituted *trans*-4-aminostilbenes (Figure 5-4), including the parent molecule (DS), *trans*-4-(*N,N*-dimethylamino)-4′-cyanostilbene (DCS), *trans*-4-(*N,N*-dimethylamino)-4′-nitrostilbene (DNS), *trans*-4,4′-tetramethyldiaminostilbene (DDS), have led to the proposition of a common TICT state resulting from the twisting of the anilino(D)-styryl

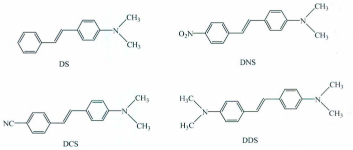

DS

DNS

DCS

DDS

Figure 5-4. Structure of *N,N*-dialkyl substituted *trans*-4-aminostilbenes.

(A) C-C bond.[48-50] The emissive nature of the TICT state was attributed to either a large vibronic mixing with the other allowed states or an incomplete twisting of the single bond (*i.e.*, twisted angle < 90°). However, several significant issues were raised regarding the nature of the emissive state as a planar or a twisted configuration coupled with the necessity of a TICT state to rationalize the photochemical properties of aminostilbenes.[51-53] Yang et al. reported systematic studies on the excited state properties of *N*-aryl-substituted *trans*-4-aminostilbenes and the related model compounds, which have provided an opportunity for exploring and testing the participation of TICT states in the excited state decay of aminostilbenes.[16,54-58] It has been shown that the electron donor strength plays an important role in observing emission from a TICT state for aminostilbene and its derivatives. Compared with the *N*,*N*-dialkyl derivatives (e.g. DS), the *N*-aryl-substituted *trans*-4-aminostilbenes have inherently greater fluorescence quantum yields and longer fluorescence lifetimes due to the prominent "amino conjugation effect", which can be a useful probe for differentiating a TICT from a PICT state for *trans*-4-aminostilbenes.[16,57]

Based on the nature of ICT states in acetonitrile, *N*-aryl-substituted *trans*-4-aminostilbenes are classified into three different groups (Groups I-III), which possess a PICT, a stilbenyl-anilino C-N bond TICT, a DMABN-like TICT, and a styryl-anilino C-C bond TICT state, respectively. Like the parent *trans*-4-aminostilbene, **1H** and **1Me** display a single fluorescence emission band with large value of Φ_f. The sum of $\Phi_f + 2\Phi_{tc}$ is 1.0 within experimental error in both polar and non-polar solvent. Apparently, the excited singlet decay is mainly via fluorescence and torsion of the central double bond for **1H** and **1Me** (Group I). A two-state model (^{1}t* (PICT) and ^{1}p*) is sufficient to account for the photochemical behavior (Figure 5-5).[58] In addition, the studies of solvent effect on Φ_f and $2\Phi_c$ indicate that both D-only and D-A substituted *trans*-stilbenes have larger barriers for the double bond torsion in more polar solvents.[16] With regard to the photo-isomerization mechanism, the *trans-cis* double bond torsion in the lowest singlet excited state (S_1) encounters an energy barrier (E_a) before it reaches a surface minimum with a perpendicular geometry ($^1p^*$) (Figure 5-6).[59,60] The $^1p^*$ state then undergoes an efficient surface jump $S_1 \rightarrow S_0$ due to the conical intersection, which accounts for a fraction of ~ 0.5 for the decay of $^1p^*$ to the *trans* (β) and *cis* ($1-\beta$)isomer (e.g., $\beta = 0.46$ for *trans*-stilbene).

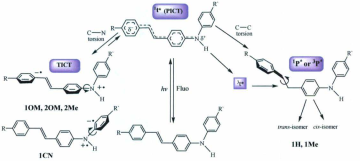

R=H, R`=H: **1 H**
R=H, R`=CH_3: **1 Me**
R=H, R`=OCH_3: **1OMe**
R=H, R`=CN: **1CN**

R=CN, R`=H: **2 H**
R=CN, R`=CH_3: **2 Me**
R=CN, R`=OCH_3: **2OMe**
R=CN, R`=CN: **2CN**

Figure 5-5. Photodynamic scheme proposed for *N*-aryl substituted *trans*-4-amino-stilbenes. States $^1t^*$, $^3t^*$, $^1p^*$, $^3p^*$, PICT, and TICT refer to the singlet and triplet excited states of the *trans* isomer and those of the C-C twisted perpendicular states and the planar and twisted intramolecular charge transfer states, respectively. Reproduced from ref [58].

The dual fluorescence was observed for **1CN** (Group II) with a low quantum yield in polar solvents, which differentiates them from the other *N*-aryl-substituted *trans*-4-

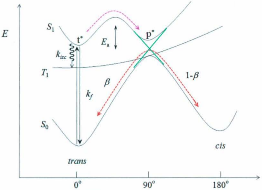

Figure 5-6. Simplified potential energy surface for the lowest electronic states of *trans*-aminostilbenes. The dash arrows show the *trans*→*cis* photoisomerization pathway along the S_1 state.

aminostilbene derivatives of Group I. The discrepancies in fluorescence properties between **1H** (or **1Me**) and **1CN** disappear when the rotation of the aniline-benzonitrilo C-N was inhibited, indicating the formation of a DMABN-like TICT state by twisting the anilino-benzonitrilo C-N bond should be temperature dependent. The weak emission property observed for the TICT state is consistent with the forbidden nature of the fluorescence, and a broad TICT emission is in accord with a broad distribution of conformers with varied twisted angles around the C-N single bond.[16] Therefore, a three-state model (^{1}t*, ^{1}p*, and TICT) is required to describe the excited state properties for **1CN**. The ^{1}t*(PICT) states result from photoinduced charge transfer from the aminostilbene as the electron donor to the phenylnitrile. The introduction of an electron-withdrawing cyano group in the donor apparently reduces its electron-donating power and then inhibits the formation of a DMABN-like TICT state for **1CN** (Figure

5-5).[58] For aminostilbenes **1CN**, the TICT state has an opposite charge-transfer direction from the PICT state, and thus, facile charge redistribution is required for initiating the changes in nuclear coordinate and the reorientation of the solvent dipoles.

The common photochemical properties observed for **1OM** and **2OM** (Group III) is the dramatic changes in Φ_f as a function of solvent, which closely resemble the group II molecules and could also be described by three-state model (^{1}t*, ^{1}p*, and TICT) with an overlapped emission from the ^{1}t* and the TICT states. However, the introduction of strong electron-donating methoxy substituent results in a stronger amino donor than that in the other derivatives of aminostilbenes, so that the structure of TICT state for **1OM** and **2OM** is very different from that for **1CN**, resulted from the twisting of the stilbenyl (A)-anilino (D) C-N bond and the direction of ICT (Figure 5-5). Independent on the bond involved in the TICT state, TICT state formation in both cases of Group II and Group III have the common features of broad fluorescence spectra and a low quantum yield for both fluorescence and isomerization.

5.2 Results

5.2.1 Structure of OPE/OPV Oligomers with Donor Groups and Bisfullerene Terminated Assemblies

The free energy change for charge separation and the reorganization energetics are two of key parameters for the optimization of photoinduced charge separation (CS) and charge recombination (CR) processes. Ideally, by manipulating CS to be close to the top of the Marcus normal region ($\Delta G^o \approx \lambda_t$) and CR deeply down to the inverted region ($\Delta G^o \gg \lambda_t$), under these energy constraints, CS is barrierless and the rate constant for CR will decrease as ΔG^o increases. This is a matter of great importance to select a donor-acceptor pair with suitable redox potentials and excitation energy, matching with small reorganization energetics. As discussed in Chapter 3, the main structural geometries of the OPV/OPE oligomers are two-dimensional cruciform. The redox potential of OPV could be adjusted by the introduction of donor and/or acceptor groups to the *para*-positions.[61] In this chapter, the excited state dynamics of bisfullerene terminated OPV/OPE oligomers with donor substituents will be investigated and compared with unsubstituted OPV/OPE systems (Chapter 4). The structures and numbering key for the main structural geometries of the OPV/OPE oligomers with donor substituents are illustrated in Scheme 5-1.

In the sections below, the ground and excited state properties of the OPV/OPE bridge with donor groups will be first described, followed by the results of bisfullerene terminated systems conducted in this study.

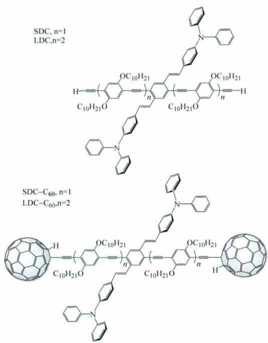
SDC, n=1
LDC,n=2
N
$OC_{10}H_{21}$
$OC_{10}H_{21}$
H
H
n
n
$C_{10}H_{21}O$
$C_{10}H_{21}O$
N
SDC–C_{60}, n=1
LDC–C_{60},n=2
N
H
$OC_{10}H_{21}$
$OC_{10}H_{21}$
n
n
$C_{10}H_{21}O$
$C_{10}H_{21}O$
H
N

Scheme 5-1. Structures of donor substituted OPV/OPE oligomers and bisfullerene terminated derivatives.

5.2.2 Absorption and Emission of OPV/OPE Oligomers with Donor Groups

Absorption Spectra. The absorption spectra of bis(diphenylamino)-substituted cruciform DSC and DLC are shown in Figure 5-7. The spectral envelopes arise from overlapping transitions that differ in the molecular orbital parentage and their vibronic component. The data of optical properties for DSC and DLC and comparative data for OPV/OPE analogous SC and LC are summarized in Table 5-1.

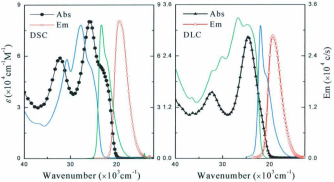

Figure 5-7. (Left) The absorption and emission spectra of DSC (Abs ●, Em ○) in comparison with that of SC (solid line), and (right) DLC (Abs ▲, Em △) in comparison with that of LC (solid line) measured in N_2 saturated $CHCl_3$ at 298 ± 3K.

Table 5-1. Absorption and emission data of DSC and DLC and comparative data for SC and LC in N_2 saturated $CHCl_3$ at 298±3 K.

Entry	DSC	SC	DLC	LC
$\lambda_{max}^{S_0\rightarrow S_1}$, nm	435	390	406	403
ε($\times 10^4$ M^{-1}cm^{-1})	5.1	5.4	2.8	3.2
$E_{op}^{S_0\rightarrow S_1}$, cm^{-1}	23,000	25,600	24,600	24,800
$\lambda_{em}^{S_1\rightarrow S_0}$, nm	515	428	514	452
$E_{em}^{S_1\rightarrow S_0}$, cm^{-1}	19,400	23,400	19,500	22,100
E_{abs}-E_{em}, cm^{-1}	3570	2280	5170	2270
$\phi_F^{S_1\rightarrow S_0}$	0.80	0.96	0.46	0.96
τ_F, ns (k_d, s^{-1})	1.8 (5.6×10^8)	2.7 (3.7×10^8)	2.2 (4.5×10^8)	1.1 (9.0×10^8)
k_r, s^{-1}	4.4×10^8	3.6×10^8	2.1×10^8	8.7×10^8
k_{nr}, s^{-1}	1.5×10^7	1.5×10^7	2.4×10^8	3.6×10^7

As shown in Figure 5-7, the absorption spectrum of SC in $CHCl_3$ is similar to the spectrum observed for 1,4-distyrylbenzene with analogous substituents in the 2 and 5 positions of the central benzene.[62] The 0-0 absorption peak is clearly visible at 390 nm (25,640 cm^{-1}), and the absorption maximum is at 360 nm (27,780 cm^{-1}). Another transition to a high-energy excited state is at 320 nm (31,250 cm^{-1}). The introduction of *N,N*-diphenylamino groups into the 4 and 4' positions of the two terminal phenyl rings in DSC results in a considerable red shift for the absorption maximum to 387 nm (25,840 cm^{-1}), and the 0-0 absorption peak to 435 nm (22,990 cm^{-1}). Such a red shift suggests substantial interactions between the *N,N*-diphenylamino groups and distyrylbenzene. On the contrary, the high-energy band is blue shifted to 309 nm (32,360 cm^{-1}), possibly due to another transition to a high-energy excited state with configurations all localized in the triphenylamine moiety.[63]

As investigated in Chapter 3 by TD-DFT, the HOMO and LUMO of SC spread over the entire molecule, and are superimposable upon each other. Therefore, the HOMO → LUMO transitions of unsubstituted short cruciform SC are characterized by $\pi\rightarrow\pi^*$ transitions. Introducing donor groups into each end of distyrylbenzene will result in different electron densities due to the inductive effects of NR_2 substituents with the HOMO and LUMO into distyrylbenzene and bisphenylethynylene branch respectively.[64] The HOMO and LUMO become localized and the electronic excitation will result in a transition with a large degree of charge transfer character.

In contrast with the short oligomer series, the 0-0 transition of LC is red shifted to 403 nm (24,810 cm^{-1}), and the absorption maximum is at 373 nm (26,810 cm^{-1}). The intensity ratio of 0-0 *vs.* 0-1 transition is relatively higher than the intensity ratio in SC, suggesting that the structure of Franck-Condon state is less distorted in LC. Bis(diphenylamino)-substituted long cruciform DLC gives rise to a pronounced absorption shoulder at $\sim 450 - 500$ nm. The absorption maximum at 406 nm (24,630 cm^{-1}), and the high-energy absorption band at 309 nm show very little spectral shifts in comparison with the absorption spectrum of LC (312 nm).[1]

Emission Spectra. The emission maxima (λ_{em}), Stokes shift ($E_{abs} - E_{em}$), quantum yield and lifetime data are summarized in Table 5-1. The emission spectra of SC and LC are much narrower than the absorption spectra, and also display a vibronic structure with $\hbar\omega = 1250$ cm^{-1} which is attributed to the C=C stretching mode of the distyrylbenzene. In addition, the emission spectra of both SC and LC display a large intensity ratio of 0-0 *vs.* 0-1 band, but the intensity distribution of the vibronic components is different from the absorption spectra. According to the Franck-Condon principle, the structural distortions in the excited state of a compound are small, accordingly the 0-0 transition is dominant and the intensity of 0-0 *vs.* 0-1 increases as Δq (bond distortion) decreases.

The emission spectra of DSC and DLC display a significant red shift to 515 nm (19,420 cm^{-1}) with a shoulder at 550 nm (18,180 cm^{-1}). The large Stokes shifts observed for DSC (3570 cm^{-1}, 0.44 eV) and DLC (5170 cm^{-1}, 0.64 eV) are diagnostic for a radiative transition with a high degree of charge transfer character. Other evidence for CT comes from the solvent dependence studies described below and a significant difference in resolving vibronic progressions, presumably due to solvent broadening. The results are consistent with analogues described elsewhere.[65] The presence of electron donating groups (NR_2) in 4,4`-positions of distyrylbenzene results in significant redistribution of electron density expected for an ICT band.[64,66] The shape of emission spectral envelopes for DSC and DLC is independent on the excitation wavelength and the fluorescence decays display single-exponential kinetics independent on the monitoring wavelength.

---

[1] More detailed understanding of these spectral properties requires expensive TD-DFT and ab initio calculations and the results will be disclosed in the future.

The excited state dynamics for DSC and DLC are distinctly different from the well-known charge transfer molecule 4-(*N,N*-dimethylamino)benzonitrile (DMABN),[67] The spectroscopy of DMABN displays weak emission from the locally excited (LE) state in contrast to DSC where the emission is observed in polar solvents. However, the deconvolution of emission profiles of both DSC and DLC in $CHCl_3$ gives two bands with different half bandwidth, $\Delta\bar{\nu}_{1/2}$, together with the single-exponential fluorescence decay, suggesting there is a rapid dynamical coupling between two emitting species PICT and TICT on the time scale of excited state decay.

Fluorescence Quantum Yields and Lifetimes. Quantum yields of bis(diphenyl-amino)-functionalized cruciform DSC and DLC are relatively lower than that of SC and LC, which is opposite to the "amino conjugation effect" described by Yang *et al.*.[63] The introduction of *N,N*-diphenyl substituents to 4-aminodistyrylbenzenes leads to a more planar ground state geometry about the nitrogen atom, a conformational change suggested from the theoretical calculation.[63] Such a constrained geometry results in a significant overlap of the amine lone pair electrons into the π-bonding molecular orbitals of the arene ring. If this is true, the planar ${}^1t^*$ state should be energetically stabilized relative to the perpendicular ${}^1p^*$ state. The net result would be an increased thermal barrier between ${}^1t^*$ and ${}^1p^*$ with a concomitant decrease in k_{nr} due to a decrease in non-radiative deactivation pathways. However, the emission quantum yield decreases and a significant red shift in emission, as a consequence of energy gap law, nonradiative pathways (vibronic coupling) become more accessible with a small energy separation in the weak coupling limit. The rate constants for radiative (k_r) and nonradiative (k_{nr}) decays are correlated with the fluorescence quantum yield (Φ) and lifetime (τ) by eq 5-1 and eq 5-2.

$$\Phi = \frac{k_r}{k_r + k_{nr} + \sum_i k_i} \qquad (5\text{-}1)$$

$$\tau = (k_r + k_{nr})^{-1} \qquad (5\text{-}2)$$

The fluorescence lifetime and quantum yield are dependent on k_{nr}. With a decreasing energy gap, k_{nr} exponentionally increases. Consequently, quantum yields for DSC and DLC decrease with the decreasing energy separation.

Emission Spectral Analysis. Emission spectral profiles were analyzed by application of Franck-Condon analysis as described in Chapter 2. Vibronic contributions are included as a single, averaged mode of quantum spacing $\hbar\omega$ and the electron-vibrational coupling constant S. The electron-vibrational coupling constant (Huang-Rhys factor) is related to the change in equilibrium displacement between states. The spectral fitting parameters are reported in Table 5-2. The emission spectra and the calculated fits for DSC and DLC are shown in Figure 5-8. The bandwidth at half-height for each vibronic component, $\Delta\bar{\nu}_{1/2}$, is related to the solvent reorganizational energy, λ_o by

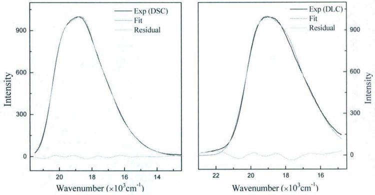

Figure 5-8. Emission spectral fitting for DSC (left) and DLC (right) measured in $CHCl_3$ at 298±3K.

Table 5-2. Emission spectral fitting parameters for the spectra of DSC and DLC measured in $CHCl_3$ at 298±3K.

Entry	DSC	SC	DLC	LC
E_{em}, cm^{-1}	19,400	23,400	19,500	22,100
E_0, cm^{-1}	19,800	23,200	19,500	22,000
S	1.32	1.10	1.07	0.85
$\Delta\bar{\nu}_{1/2}, \mathrm{cm}^{-1}$	1590	1260	1940	1220
$\hbar\omega, \mathrm{cm}^{-1}$	1320	1300	1550	1450
E_{abs}-E_{em}, cm^{-1}	3570	2280	5170	2270
λ_t, cm^{-1}	1790	1140	2590	1140
λ_{vib}, cm^{-1}	1742	1430	1660	1230
λ_o, cm^{-1}	1100	690	1636	644
In[(FC)]	-30.5	-41.1	-27.2	-37.4
γ	1.43	1.79	1.88	1.46

$$(\Delta\bar{\nu}_{1/2})^2 = 16k_B T\lambda_o \ln 2 \qquad (5\text{-}3)$$

The solvent reorganization energy can be calculated from eq 5-3, reported in Table 5-2. For DSC and DLC, the solvent reorganization energies are much larger than those of SC and LC.

The solvent dependence of the emission spectrum is expected and is characteristic of the charge transfer transition. The microscopic origin for solvent dependence is due to a formation or change of dipole moment; low dielectric solvents destabilize the excited state and high dielectric solvents stabilize the excited state.

5.2.3 Transient Absorption of OPE/OPV Oligomers with Donor Substituents

The transient absorption difference spectra of the excited states and intermediates involved in the electron transfer steps were acquired in N_2 saturated $CHCl_3$ following laser flash excitation at 355 nm. The difference spectra for DSC and DLC are shown in Figure 5-9 and Figure 5-10. The transient absorption decays are fitted to the single exponential decay function,

$$\Delta A_t = \Delta A_0 \exp(-kt) + y_0 \qquad (5\text{-}3)$$

with ΔA_t and ΔA_0 changes in transient absorbance at time *t* and 0, respectively, *k* the decay rate constant, and y_0 an appropriate fixed number close to the asymptotic value of ΔA_t variable for large *t* values. These spectra are important for the identification of charge separation state in transient absorption experiments.

The transient absorption difference spectra of DSC and DLC have the similar profiles. The 355 nm pulsed laser excitation of DSC and DLC in N_2 saturated $CHCl_3$ leads to the formation of an intense transient absorption at $\lambda_{max}^{\Delta OD}$ = 490 nm (20,410 cm^{-1}). The

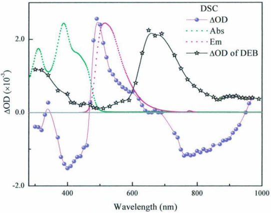

Figure 5-9. Transient absorption difference spectrum of DSC in comparison with the transient absorption difference spectrum of DEB, together with Abs (green dot line) and Em (red dot line) in N_2 saturated $CHCl_3$ at 298±3 K.

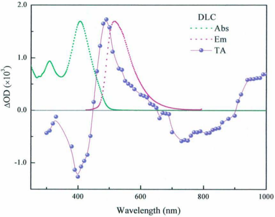

Figure 5-10. Transient absorption difference spectrum of DLC in comparison with Abs (green dot line) and Em (red dot line) in N_2 saturated $CHCl_3$ at 298 ± 3 K.

transient lifetime is ~ 2.0 μs, which decays by the single exponential kinetics ($k_D = 5.0 \times 10^5$ s^{-1}). The transient absorption is assigned to the excited state absorption of $T_1 \rightarrow T_n$ localized on OPV.[68,69] In Figure 5-9, the transient absorption difference spectrum of DEB is also shown for the comparison. After laser excitation, the transient absorption spectra of both DSC and DLC displayed the ground state depletion at ~ 300 - 480 nm (33,330 - 20,830 cm^{-1}), which are in a good match with the UV-Vis spectra of the original solution. Apparently, little or no chemical change occurs upon laser excitation. In addition, another negative band with $\lambda_{max}^{\Delta OD}$ ~ 700 to 900 nm (14,280 - 11,110 cm^{-1}) which decays by the single exponential kinetics with $k_D = 5.0 \times 10^5$ s^{-1} is tentatively assigned as triplet emission.

5.2.3 Absorption and Emission of Derivative Bisfullerene Terminated Oligomers

Absorption Spectra. The absorption spectra of bisfullerene terminated OPE/OPV oligomers are shown in Figure 5-11. The spectra of DSC/DLC-$(C_{60})_2$ display collective

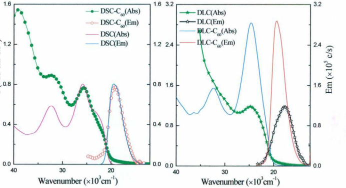

Figure 5-11. The absorption and emission spectra of DSC-$(C_{60})_2$ (Abs ●, Em ○) in comparison with that of DSC (solid line), and DLC-$(C_{60})_2$ (Abs ★, Em ☆) in comparison with that of DLC (solid line) measured in N_2 saturated $CHCl_3$ at 298±3K.

spectral properties of the two individual components, *i.e.* the $\pi \rightarrow \pi*$ transitions of the oligomer bridges and the characteristic absorptions of C_{60} at ~ 300 - 350 nm (33,300 - 28,570 cm^{-1}) along with a weak tail beyond 500 nm (20,000 cm^{-1}). Comparing the absorption spectra of DSC/DLC-$(C_{60})_2$ with those of their oligomer bridges DSC/DLC, it is clear that $\pi \rightarrow \pi*$ transitions of DSC/DLC-$(C_{60})_2$ show little or no spectral shifts, indicating an absence of significant electronic coupling in the ground state. There is no evidence for charge transfer from the bridge to the acceptor C_{60} in the ground state spectra. The absorptivity of DLC-$(C_{60})_2$ was significantly decreased by the factor of 10.

Emission Spectra. The emission spectra of bisfullerene terminated oligomers in comparison with the emission spectra of donor substituted OPE/OPV precursors are shown in Figure 5-11. The emission maxima (λ_{em}), Stokes shift ($E_{abs} - E_{em}$), quantum yield and lifetime for DSC-$(C_{60})_2$ and DLC-$(C_{60})_2$ in comparison with those of DSC and DLC are summarized in Table 5-3. The emission maximum of DSC-$(C_{60})_2$ at 525 nm (19,050 cm^{-1}) is ca. 10 nm red-shifted relative to that of DSC, and the emission of ${}^1C_{60}^*$ appears at 710 nm (14,085 cm^{-1}).[70] In comparison with DLC, the emission maximum of DLC-$(C_{60})_2$ is further red-shifted to 562 nm (17,800 cm^{-1}), and ${}^1C_{60}^*$ emits at 710 nm, which is masked by the tailing of emission at 562 nm.

Fluorescence Quantum Yield and Lifetime. OPE/OPV oligomers are highly emissive, with quantum yield close to unit. The introduction of donor substituents into the OPV branch reduces the quantum yield as nonradiative pathways become more accessible with a small energy separation as predicted from the non-radiative decay theory. However, the fluorescence of bisfullerene terminated oligomers is significantly quenched by the

Table 5-3. The absorption and emission data of DSC-(C_{60})$_2$ and DLC-(C_{60})$_2$ in comparison with those of DSC and DLC measured in $CHCl_3$ at 298±3 K.

Entry	DSC-(C_{60})$_2$	DSC	DLC-(C_{60})$_2$	DLC
$\lambda_{max}^{S_0\rightarrow S_1}$, nm	391	435	405	406
ε ($\times 10^4$ $M^{-1}cm^{-1}$)	8.1	5.1	0.30	2.8
$E_{op}^{S_0\rightarrow S_1}$, cm^{-1}	25,600	23,000	24,700	24,600
$\lambda_{em}^{S_1\rightarrow S_0}$, nm	525 710	515	562 710	514
$E_{em}^{S_1\rightarrow S_0}$, cm^{-1}	19,100 14,100	19,400	17,800 14,100	19,500
E_{abs}-E_{em}, cm^{-1}	6530	3570	6890	5170
$\phi_F^{S_1\rightarrow S_0}$	1.3×10^{-3}	0.80	$\leq10^{-3}$	0.46
τ_F, ns	4.8 (525)^a 3.9 (710)	1.8	4.8 (562)^a 3.8	2.0
k_r, s^{-1}	2.4×10^8	4.4×10^8	2.1×10^8	4.4×10^8
k_{nr}, s^{-1}	2.4×10^{11}	1.5×10^7	2.1×10^{11}	1.1×10^8

a. Trace amount of bridge precursor mask the lifetime of bisfullerene derivative.

magnitude of 10^3, indicating the involvement of competitive photoinduced energy/electron transfer pathways for the excited state deactivation. The emission lifetimes of oligomer bridges and $^1C_{60}^*$ are 4.8 and 3.9 ns respectively, which are relatively longer than the lifetimes of DSC/DLC and pristine C_{60} (1.2 ns).[70]

Emission Spectral Analysis. Emission spectral profiles were analyzed by the same methodology as described before. The experimental along with the fitted spectra are shown in Figure 5-12, and the spectral fitting parameters are reported in Table 5-4. In comparison with the donor substituted oligomer bridges, it is obvious that the solvent reorganization energy for thebisfullerene terminated oligomer is much larger than that of

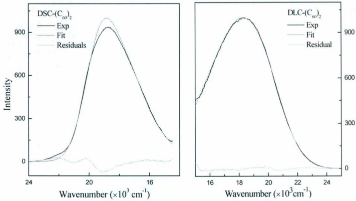

Figure 5-12. Emission spectral fitting for DSC-$(C_{60})_2$ (left) and DLC-$(C_{60})_2$ (right) in $CHCl_3$ at 298±3K.

Table 5-4. Emission spectral fitting parameters of DSC-$(C_{60})_2$ and DLC-$(C_{60})_2$ in $CHCl_3$ at 298±3K.

Entry	DSC-$(C_{60})_2$	DSC	DLC-$(C_{60})_2$	DLC
E_{em}, cm^{-1}	19,000 14,080	19,400	19,800	19,500
E_0, cm^{-1}	19,200	19,800	19,800	19,500
S	0.82	1.32	1.58	1.07
$\Delta\bar{\nu}_{1/2}, \mathrm{cm}^{-1}$	2460	1590	3230	1940
$\hbar\omega, \mathrm{cm}^{-1}$	1900	1320	1750	1550
E_{abs}-E_{em}, cm^{-1}	6590	3570	7050	5170
λ_t, cm^{-1}	3290	1790	3530	2590
λ_{vib}, cm^{-1}	1360	1740	2770	1660
λ_o, cm^{-1}	2360	1100	4820	1640
ln[(Fcalc)]	-23.9	-30.5	-19.9	-27.2
γ	1.52	1.43	0.97	1.88

the bridge precursor, indicating a long distance ICT, but further evidence to support the ICT requires transient absorption data. The electron-vibrational coupling constant or Huang- Rhys factor (*S*), which is related to the change in the equilibrium displacement between the ground and excited states, of DSC-$(C_{60})_2$ is larger than that of DLC-$(C_{60})_2$. This is opposite to the trend that has been demonstrated by the OPE/OPV oligomers with donor substituents.

5.2.5 Transient Absorption of Derivative Bisfullerene Terminated Oligomers

Transient absorption difference spectra for DSC-$(C_{60})_2$ and DLC-$(C_{60})_2$ were acquired in N_2 saturated $CHCl_3$ following pulsed laser excitation at 355 nm. The difference spectra of DSC-$(C_{60})_2$ and DLC-$(C_{60})_2$ are shown in Figure 5-13 and 5-14. The transient absorption decays are fitted to the single exponential decay function as eq 5-3.

The 355 nm pulsed laser excitation of DSC-$(C_{60})_2$ in N_2 saturated $CHCl_3$ leads to the transient absorption in the entire visible region with two discernable bands at 400 nm (25,000 cm^{-1}) and 520 nm (19,230 cm^{-1}) respectively, which resembles the transient absorption difference spectrum of LC-$(C_{60})_2$. The transient absorption at $\lambda_{max}^{\Delta OD}$ = 520 nm has a lifetime ~ 3.0 μs, which is assigned to the excited state absorption of $T_1 \rightarrow T_n$ localized on OPV.[68,69] The other transient absorption with $\lambda_{max}^{\Delta OD}$ at 400 nm decay with τ ~ 0.5 μs. With reference to $T_1 \rightarrow T_n$ absorption of ${}^3C_{60}^*$ from LC-$(C_{60})_2$ and C_{60}-DEB, the absorption at 400 nm is assigned to the excited state absorption of ${}^3C_{60}^*$.

The transient absorption of DLC-$(C_{60})_2$ displays a very different spectrum from that of DSC-$(C_{60})_2$. As shown in Figure 5-14, it has a very intense absorption with $\lambda_{max}^{\Delta OD}$ at 490 nm (20,410 cm^{-1}) with the transient lifetime ~ 1.3 μs and decaying by single

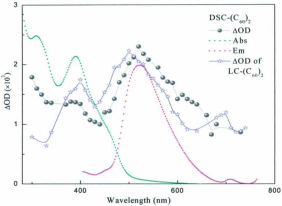

Figure 5-13. Transient absorption difference spectrum of DSC-$(C_{60})_2$ (•) in comparison with Abs (green dot line) and Em (red dot line) and TA of LC-$(C_{60})_2$ (☆) in N_2 saturated $CHCl_3$ at 298±3 K.

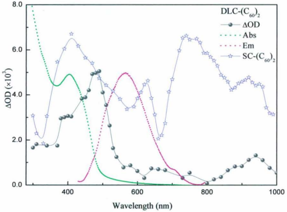

Figure 5-14. Transient absorption difference spectrum of DLC-$(C_{60})_2$ (•) in comparison with Abs (green dot line) and Em (red dot line) and TA of SC-$(C_{60})_2$ (☆) in N_2 saturated $CHCl_3$ at 298±3 K.

exponential kinetics ($k_D = 7.0 \times 10^5\ s^{-1}$). This transient absorption is assigned to the excited state absorption $T_1 \rightarrow T_n$, which is localized on OPV.[71] The relatively weak absorption at ~ 800 - 1000 nm with the lifetime ~ 1.0 μs is possibly from the C_{60} radical anion and the diphenylamino radical cation.[72] DLC-$(C_{60})_2$ also displays discernable transient absorptions at 400 nm (25,000 cm^{-1}) and 700 nm (14,285 cm^{-1}), which is assigned as a $^3C_{60}^*$ based excited state absorption with reference to the transient absorption difference spectra of the model compounds C_{60}-DEB and SC-$(C_{60})_2$.

5.3 Discussions

5.3.1 Substituent Effect

Intramolecular Charge Transfer. Electronic conjugation in two-dimensional (2D) settings offers an opportunity to spatially separate molecular orbitals that fundamentally affect the ground and excited state electronic properties. The 2D cruciforms regulate the mixing of localized and delocalized components of the electronic structures associated with cross-linking. Cruciform chromophores as discussed in Chapter 3 display two distinct molecular axes with either similar or dissimilar electronic properties. Attaching donor and/or acceptor substituents to cruciforms at suitable positions can lead to independent electronic shifts of HOMO and LUMO into opposite directions or delocalized over the entire molecule (Figure 5-15). The HOMO and LUMO of cruciform (SC) without donor and/or acceptor substituents spread overall the molecule. The introduction of donor substituents at each end of distyrylbenzene reallocates the HOMO and LUMO into distyrylbenzene and bisphenylethynylene branch respectively (Figure 5-15), which results in an ICT after photon capture.[64] This is in agreement with the experimental results that the absorption and emission of both DSC and DLC have substantial red shifts with a loss of fine structure for emission spectra.

Further evidence to support the ICT is the study of solvent dependence as shown in Figure 5-16. The emission spectra displayed a dramatic red shift with the increasing dielectric constant of the solvent, consistent with expectations of dielectric continuum theory. The vibrational structure is observed in toluene, but the spectra are broad in chloroform and completely structureless in more polar solvents, providing evidence for

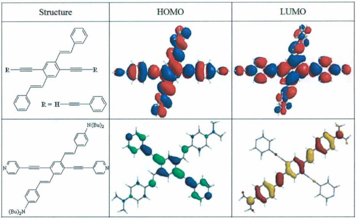
Structure
HOMO
LUMO
R
R
R = H
N(Bu)2
N
N
(Bu)2N

Figure 5-15. FMOs for cruciform calculated with HF/6-311G(d) and donor substituted one calculated with B3LYP 6-31G//6-31G (d, p) using Spartan.[64]

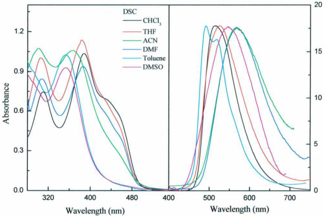

Figure 5-16. Solvent dependence of absorption and emission for donor substituted cruciform at 298±3K.

the charge transfer character of the fluorescent singlet. In addition, there are significant changes in the absorption spectra as a function of solvent polarity, which appears to stabilize the ground state.

Molecular Structure. The nature of substituents has a great influence on the structure of ground and excited states, and then plays a significant role on the photophysical and photochemical properties. ZINDO calculations on *trans*-4-(*N,N*-diphenylamino)stilbene suggests that the fluorescent state, particularly in the region of the central double bond is less distorted, indicating a reduced role for the central double bond in the lowest excited state consistent with the population of $\pi*$ orbitals and a reduction in the force constant.[63] Optimized geometries for the ground and excited states indicate that *trans*-4-(*N,N*-diphenylamino)stilbene adopts completely planar structures about the N atom (*i.e.* a sp^2 character for the N atom), with dihedral angle $\theta = 56^{\circ}$ between the two *N*-phenyl planes of the amine group (Figure 5-17). ^{13}C NMR measurements by Meier[61]

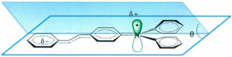

Excited state

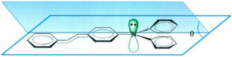

Ground state

φ (=360°) is defined as the sum of bond angles about N atom.

Figure 5-17. Optimized geometries for the ground and excited states of *trans*-4-(*N,N*-diphenylamino)stilbene adapted from ref 63.

also demonstrated that the dipolar quinoid resonance structure seems to be appropriate for stilbene in the ground state S_0 and the first excited singlet state S_1 based on the valence bond (VB) model. As a test of the proposed structure, the binding constants of H^+ and Ag^+ should be attenuated (Chapter 6). There is no detectable change in the absorption and emission spectra consistent with expectations based on the VB model.

The Electronic Origin of the Dual Fluorescence. The emission maximum of DSC and DLC are red shifted to λ_{max} = 515 nm (19,420 cm^{-1}) with a shoulder at ~ 550 nm (18,180 cm^{-1}) as illustrated in Figure 5-7. The energy difference between two peaks is ~1200 cm^{-1}, as expected for the vibronic progressions from C=C stretching modes. However, the Gaussian deconvolution analyses indicate that these two bands have different half bandwidths ($\Delta\bar{\nu}_{1/2}$), *i.e.* 1560 and 2655 cm^{-1} for DSC and 1613 and 2750 cm^{-1} for DLC as shown in Figure 5-18. If the assignment that there exist two emitting

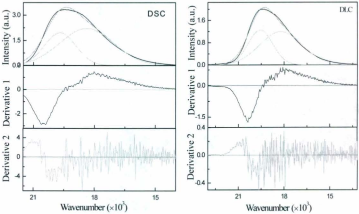

Figure 5-18. Emission band shape analysis by Gaussian deconvolution for DSC and DLC.

states or conformers is correct, then there must be a dynamically coupled interconversion between two states rapid on the time scale for the excited state decay as the single exponential decay kinetics was observed.

The electronic origin of the dual fluorescence has been proposed as different models, *i.e.* TICT (twisted intramolecular charge transfer),[41] WICT (wagged intramolecular charge transfer),[10] in which a pseudo Jahn-Teller coupling to form a planar CT (PICT) state is assumed,[12] and RICT (rehybridization intramolecular charge transfer).[13,14] The TICT or PICT model was identified as being due to the CT state in which the benzene ring is distorted to an antiquinoid (AQ) or a quinoid (Q) structure, respectively. However, a different CT state in dimethylaminobenzonitrile (DMABN) was identified and confirmed in which the benzene ring assumes a quinoid structure, with the dimethyl amino group is 90° twisted with respect to the benzene ring.[26,27] To resolve the TICT/PICT debate, another model was proposed by modeling the structure of the acceptor as a derivative of the benzene anion radical.[73] The benzene ring as the principal electron acceptor leads to four different lowest lying electronic excited states in these systems: two of them are principally of LE nature, whereas the other two are CT-types as shown in Figure 5-19. The LE states are due to transitions from the benzene HOMOs to the benzene LUMOs, and two CT states with similar energies but different symmetries arise from an electron transfer from the HOMO of the amino group to two of the nearly degenerate benzene LUMOs 3a and 3b.

The donor orbitals of an amino substituent are p orbitals possessing b-type symmetry in the C_2 symmetry group. Placing an electron in the 3b orbital, a radical anion

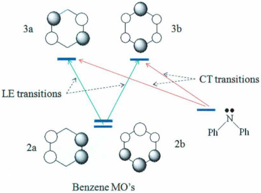

Figure 5-19. MO diagram and optical transitions from the ground state.

with ^2B symmetry is formed, and this radical anion has a quinoid structure with a minimum in the planar form. If an electron is transferred into the 3a MO, the formed radical anion with ^2A symmetry has an anti-quinoid structure (an AQ structure). In AQ structure, the distance between the two bonded central carbon atoms in the benzene ring is longer than in benzene. Therefore, the AQ structure with a minimum at the perpendicular form has a larger dipole moment than the quinoid structure. This perpendicular geometry is preferred in polar solvents. Depending on the substituents, *i.e.* *N*,*N*-diphenylamino as donor, the planar conformation of CT excited state is lower in energy than that of the LE state, and dual fluorescence can be observed also from the planar structure. In non-polar solvent, if the LE state is much lower in energy than two CT states so that no dual fluorescence is expected.

5.3.2 EIT *vs.* EnT: The Effect of Varying Donor-Acceptor Distance and the Interplay with the Energy gap Dependence for Electron Transfer

For OPV/OPE cruciform systems discussed in Chapter 4, the formation of the radical ion pair, $C_{60}-(\pi\text{-B})_{SC}^{+\cdot}-C_{60}^{-\cdot}$, was detected in the transient absorption difference spectrum of Figure 4-6, indicating the charge separation is very efficient with a $C_{60}^{-\cdot}$ spectral maker at 900 - 1000 nm. The calculated lifetime for the charge separation state is 600 ± 50 ns. However, there is no detectable spectroscopic evidence for the formation of radical ion pair, $C_{60}-(\pi\text{-B})_{LC}^{+\cdot}-C_{60}^{-\cdot}$, as the bridge length increases. The emission from the bridge singlet excited state, $C_{60}-{}^{1}(\pi\text{-B})_{LC}^{*}-C_{60}$, is also significantly quenched due to the Förster energy transfer to form $C_{60}-(\pi\text{-B})_{LC}-{}^{1}C_{60}^{*}$. After the formation of $C_{60}-(\pi\text{-B})_{LC}-{}^{1}C_{60}^{*}$, the system will undergo charge separation or intersystem crossing to form $C_{60}-(\pi\text{-B})_{LC}-{}^{3}C_{60}^{*}$, a kinetic competition dependent on ΔG^{o} and λ.

In donor substituted OPV/OPE cruciforms, the emission are characterized by an intramolecular charge transfer from diphenylamino to OPV subunit. The introduction of acceptor C_{60} to the donor substituted OPV/OPE oligomers changes the coefficient distribution of the FMOs. The reduced overlap between the HOMO and LUMO is consistent with the unusually long emissive lifetime. The reduced quantum yield of the charge transfer band is correlated with the decreased energy gap. In $C_{60}-(\pi\text{-B})_{DSC}-C_{60}$, the emission from ${}^{1}(\pi\text{-B})_{DSC}^{*}$ is significantly quenched. The excited state absorption of bridge $T_1 \rightarrow T_n$ at 480 nm resulting from the intersystem crossing is shown in Figure 5-13. It is obvious there is no spectroscopic evidence of a charge separation state in $C_{60}-(\pi\text{-B})_{DSC}-C_{60}$ at least on the ns time scale as shown in Figure 5-13. The rate constant for energy transfer estimated from eq 4-28 is extremely fast and occurs within ~ 5 ps. The photophysical processes in $C_{60}-(\pi\text{-B})_{DSC}-C_{60}$ system after the excitation of the OPV/OPE oligomer is illustrated in Figure 5-20.

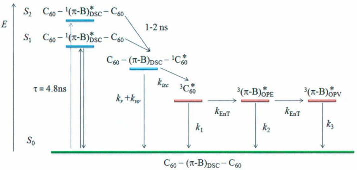
E
S_2 $C_{60}-{}^1(\pi\text{-B})^*_{DSC}-C_{60}$
S_1 $C_{60}-{}^1(\pi\text{-B})^*_{DSC}-C_{60}$
1-2 ns
$C_{60}-(\pi\text{-B})_{DSC}-{}^1C^*_{60}$
τ = 4.8ns
k_r+k_{nr}
k_{isc}
${}^3C^*_{60}$
${}^3(\pi\text{-B})^*_{OPE}$
${}^3(\pi\text{-B})^*_{OPV}$
k_{EnT}
k_{EnT}
k_1
k_2
k_3
S_0
$C_{60}-(\pi\text{-B})_{DSC}-C_{60}$

Figure 5-20. Schematic energy level diagram showing excitation, energy transfer, intersystem crossing after excitation of OPE/OPV oligomer in DSC-$(C_{60})_2$ system.

In $C_{60}-(\pi\text{-B})_{DLC}-C_{60}$, the charge transfer from diphenylamino to C_{60} has been detected in transient absorption difference spectrum (Figure 5-14) as the excited state absorption of $C_{60}^{\bullet-}$ at $\lambda^{\Delta OD}_{max} = 950$ nm. The emission from ${}^1(\pi\text{-B})^*_{DLC}$ is also significantly quenched by energy transfer to C_{60}. When the indirect mechanism is operative, the electron transfer reaction occurs in ~ 1-2 *ns* ($k_{CS} = 6\times10^8\ s^{-1}$) calculated by eq 4-26.

The rate for charge separation (CS) has been shown to have exponential distance dependence following eq 4-29 with attenuation factor *β*.

$$k_{ET} \propto |V_{DA}|^2 \propto \exp(-\beta R_{DA}) \qquad (4\text{-}29)$$

The magnitude of *β* is given by eq 4-30.

$$\beta = \frac{2}{R_0} \ln\left(\frac{\Delta E}{\nu}\right) \qquad (4\text{-}30)$$

All parameters are as defined in Chapter 4. The rate constants for energy transfer (k_{EnT}), indirect charge separation (k_{CS}), and charge recombination (k_{CR}) for the bisfullerene terminated OPV/OPE oligomers are summarized in Table 5-5. The energy gap between the donor and bridge can be estimated from the emission spectral fitting data as listed in Table 5-2 and 5-4.

Table 5-5. Fluorescence quenching of $\phi(\pi\text{-B})/\phi$, rate constants for energy transfer (k_{EnT}), indirect charge separation (k_{CS}), charge recombination (k_{CR})[a], the energy and the redox potential of donor.

Entry	$\frac{\phi(\pi\text{-B})}{\phi}$	k_{EnT} (s^{-1})	$\frac{\phi(C_{60})}{\phi}$	k_{CS} (s^{-1})	k_{CR} (s^{-1})	E_{00} (cm^{-1})	E_{ox}(GS) (cm^{-1})	E_{ox}(ES) (cm^{-1})
SC-$(C_{60})_2$	9.6×10^{3}	3.6×10^{12}	>4	2.5×10^{9}	1.7×10^{7}	23,240	13,310	-9,930
LC-$(C_{60})_2$	9.6×10^{1}	5.0×10^{11}	1	-	-	21,470	12,580	-8,900
DSC-$(C_{60})_2$	8.0×10^{2}	2.0×10^{11}	1	-	-	19,200	8,750	-10,450
DLC-$(C_{60})_2$	4.6×10^{2}	9.3×10^{11}	1.5	6.0×10^{8}	1.0×10^{6}	19,765	9,110	-10,655

[a] Rate constants for energy transfer (k_{EnT}), indirect charge separation (k_{CS}), and direct charge recombination (k_{CR}) calculated from eqs 4-28, 4-26, and 4-25, respectively. Redox potentials were measured by Dr. Yuming Zhao, and included here for the discussion.

The dependence of the ET rate constant on the energy gap, ΔE_{DB}, between the donor and the bridge could be separated from the dependence on the donor-acceptor distance (R) by comparing the systems with the same donor-acceptor distance. For short bridge systems SC-$(C_{60})_2$ and DSC-$(C_{60})_2$, the ΔE_{DB} (2750 cm^{-1}) in DSC-C_{60} is larger than the ΔE_{DB} (2230 cm^{-1}) in SC-$(C_{60})_2$, assuming in the week coupling limit and E_{B}(OPE) = -7700 cm^{-1}.[74] From eq 4-29 and 4-30, the rate of electron transfer increases with the decreasing ΔE_{DB}. For donor substituted OPV/OPE systems, the ΔE_{DB} is large in comparison with the OPV/OPE cruciform systems. Therefore, the forward electron transfer will be slow compared with other kinetic processes, and then no evidence for the charge separation state is detected in the transient absorption difference spectrum. On the contrary, the indirect electron transfer is very efficient in SC-$(C_{60})_2$. The charge separation state lives long enough to be detected by the transient absorption of $C_{60}^{\cdot-}$ after 900 nm. For long bridge systems LC-$(C_{60})_2$ and DLC-$(C_{60})_2$, the dependence of electron transfer rate on the energy gap is opposite to the trend as established in the short bridge systems. The ΔE_{DB} (1200 cm^{-1}) of LC-$(C_{60})_2$ is smaller than the ΔE_{DB} (2955 cm^{-1}) of DLC-$(C_{60})_2$. Based on eqs 4-29 and 4-30, the k_{CS} for LC-$(C_{60})_2$ should be greater than the k_{CS} for DLC-$(C_{60})_2$. However, there is no detectable spectroscopic evidence for the charge separation state in LC-$(C_{60})_2$ due to the kinetic competition between the charge separation and the intersystem crossing from ${}^1C_{60}^{*}$ to ${}^3C_{60}^{*}$, which is dependent on ΔG^o and λ (discussed in Chapter 4). For DLC-$(C_{60})_2$, both the charge separation and charge recombination slow down with increasing the energy gap, and possibly the charge recombination rests in the inverted region with $k_{CR} < k_{CS}$. Therefore, the charge separation state is detected by the transient absorption of $C_{60}^{\cdot-}$ after 900 nm. With regard to the relatively low efficiency, the electron transfer rate is also dependent on the separation distance between the donor and the acceptor.

With respect to the distance dependence of the electron transfer rate, it can be separated from the dependence of the energy gap by comparing the systems with a similar energy gap. The energy gap between the donor and the bridge in SC-$(C_{60})_2$ is very close to the energy gap in DLC-$(C_{60})_2$, and the rate of electron transfer decreases exponentially with distance. For DLC-$(C_{60})_2$, the bridge repeating unit is 2, and the rate of electron transfer becomes very slow in comparison with the other processes. As a result, the charge separation state is detected in transient absorption difference spectrum, but with a very low efficiency. When the bridge repeating unit is 1 in SC-$(C_{60})_2$, the charge separation becomes very efficient as the intensity of transient absorption band from $C_{60}^{\cdot-}$ becomes very high as shown in Figure 5-14.

For LC-$(C_{60})_2$ and DSC-$(C_{60})_2$ systems, the energy gap is dramatically decreased by comparing with the energy gap in SC-$(C_{60})_2$ and DLC-$(C_{60})_2$ systems, and the contribution of the energy gap plays a dominant role. Therefore, the forward and back electron transfer become very fast, and the lifetime of the charge separation state is not long enough to be detected at least on the ns time scale.

5.3.3 The Distance and Energy-gap Dependence of Energy Transfer

The electronic coupling for the non-radiative energy transfer process can be divided into a Coulomb and an exchange part. The mechanism for the Coulomb part is dependent on resonance between two oscillating dipoles, and the overlap between the donor fluorescence spectrum and the absorption spectrum of the acceptor plays an important role. The dipole-dipole term for the allowed transition is described in Chapter 1, and for the convenience, is represented here again.

$$k_{EnT}^{d-d} = \frac{9000(\ln 10)\kappa^2 \phi_D J_{\text{Förster}}}{128\pi^5 N_A n^4} \frac{1}{\tau_D^o} \left(\frac{1}{R_{DA}}\right)^6 \qquad (5\text{-}6)$$

The exchange contribution depends on the overlap between the wavefunctions of the donor and acceptor. Since there is no direct molecular orbital overlap between the donor OPV and the acceptor C_{60}, the forward energy transfer is through the Förster mechanism by resonance between two oscillating dipoles. However, the backward energy transfer from the triplet excited state ${}^3C_{60}^*$ formed by intersystem crossing to ${}^3(\pi\text{-}B)_{SC}^*$ is through the Dexter mechanism. The Dexter energy transfer depends on the overlap between the wavefunctions of the donor and acceptor. Since the molecular orbital overlap at sufficiently large separation decreases exponentially with increasing separation distance, the Dexter energy transfer rate is expressed as

$$k_{EnT}^{EX} \propto J \cdot \exp\left(\frac{-2R_{DA}}{L}\right) \qquad (5\text{-}7)$$

From Table 5-5, it is evident that the forward energy transfer in a short bridge system, *i.e.* SC-$(C_{60})_2$, is more efficient than in a long bridge system, LC-C_{60}. In donor substituted OPV/OPE systems, the Förster energy transfer also becomes less efficient with the increasing distance. For DSC-$(C_{60})_2$, energy transfer to the acceptor C_{60} forming ${}^1C_{60}^*$ is very proficient, but no charge separation state is detected because the electron transfer is also dependent on the energy gap between the donor and the bridge. The large energy gap eliminates the charge separation process. The back energy transfer forming the excited triplet state ${}^3(\pi\text{-}B)_{DSC}^*$ is an indication of the high efficiency of energy transfer to the acceptor C_{60}.

5.3.4 Back Electron Transfer or Charge Recombination

Subsequent to the photoinduced generation of the charge separation state, a charge recombination process brought the systems back to the ground state. The CR process was studied by monitoring the decay of $C_{60}^{\cdot-}$ at 950 nm in transient absorption spectrum. As there is no other deactivation processes competing with the charge recombination, the rate constant for charge recombination is derived from the fitting of single exponential decay trace of the $C_{60}^{-\cdot}$. The smaller the energy gap between the donor and the bridge, the faster the charge separation and charge recombination.

The free energy change and reorganization energy are the key parameters to govern the photoinduced CS and CR processes. The most special factor for electron transfer of fullerenes is the small reorganization energy. The free energy change for the CS process ($-\Delta G_{CS}$) in SC-$(C_{60})_2$ calculated by the Rehm-Weller equation is around - 0.75 eV, and the total reorganization energy (λ_t) estimated from the emission spectral fitting is ~ 0.33 eV. The free energy change for the CR process ($-\Delta G_{CR} = 2.1$ eV) is much greater than the λ_t value. The forward CS is down to the inverted region of the Marcus parabola, but the CR is more deeply down to the inverted region with $k_{CR} \ll k_{CS}$. The relatively fast forward electron transfer will accelerate the photoinduced charge separation. The free energy changes and reorganization energies for the forward and back electron transfer in other systems are summarized in Table 5-6.

Table 5-6. Rate constants for forward and back electron transfer, driving forces, reorganization energies and electronic coupling constants for SC/LC-$(C_{60})_2$ and DSC/DLC-$(C_{60})_2$ systems.

Entry	k_{CS} (s^{-1})	k_{CR} (s^{-1})	λ_t (cm^{-1})	ΔG_{CS}^{o} (cm^{-1})	ΔG_{CR}^{o} (cm^{-1})	$\frac{-\Delta G_{CS}^{o}}{\lambda_t}$	ν_{ET} (cm^{-1})	$\hat{H}_{DA}$ (cm^{-1})
SC-$(C_{60})_2$	2.5×10^{9}	1.7×10^{7}	2554	-4557	-18783	1.86	2.2×10^{10}	4.0
LC-$(C_{60})_2$	-	-	2879	-4046	-17904	1.40	-	-
DSC-$(C_{60})_2$	-	-	3721	-6520	-12660	1.75	-	-
DLC-$(C_{60})_2$	6.0×10^{8}	1.0×10^{6}	7318	-6538	-13410	0.88	6.6×10^{8}	0.90

For DLC-$(C_{60})_2$, the forward electron transfer is in the normal region with $-\Delta G^o_{CS} < \lambda_t$, but the charge recombination is in the inverted region with $-\Delta G^o_{CR} \gg \lambda_t$. Therefore, the rate of charge separation is much greater than the rate of charge recombination, and thus the spectroscopic evidence for charge separation state is shown in the transient absorption spectrum as $C_{60}^{\cdot-}$ based absorption after 900 nm. For LC-$(C_{60})_2$ and DSC-$(C_{60})_2$ systems, both charge separation and charge recombination are in the inverted region. Compared with SC-$(C_{60})_2$, the large donor-acceptor separation distance in LC-$(C_{60})_2$ dramatically reduces the electronic coupling term. For DSC-$(C_{60})_2$, even with the short donor-acceptor separation distance, the electronic coupling term V_{DA} is also decreased due to the large energy gap as given by eq 4-7,

$$V_{DA} = \frac{\alpha}{\Delta E}\exp\left(-m\sqrt{\Delta E}\, r_{DA}\right) \qquad (4\text{-}7)$$

Therefore, a kinetic competition between the charge separation and intersystem crossing is favorable for the formation of ${}^3C_{60}^*$ in both LC-$(C_{60})_2$ and DSC-$(C_{60})_2$ systems.

5.4 Conclusions

1. The charge separation and charge recombination for short bridged system DSC-$(C_{60})_2$ are in the inverted region. The electronic coupling term V_{DA} is also decreased due to the large energy gap (high tunneling height). Therefore, the kinetic competition between the charge separation and intersystem crossing is favorable for the formation of $^3C_{60}^*$.
2. In the long bridged system DLC-$(C_{60})_2$, the forward ET is in the Marcus normal region and the back ET is in the inverted region. The relatively fast forward ET will accelerate the charge separation upon photoexcitation.
3. The introduction of *N,N*-diphenylamino groups to distyrylbenzene significantly increases the energy gap between the donor and the bridge, and then attenuates the electronic coupling term V_{DA}. The efficiency of charge separation is reduced with the attenuated electronic coupling.

5.5 References

(1) Ghosh, S.; Chakraborty, A.; Kar, S.; Guchhait, N. *J. Luminescence* **2009**, 482-491.

(2) Grabowski, Z. R.; Rotkiewicz, K.; Rettig, W. *Chem. Rev.* **2003**, *103*, 3899-4032.

(3) Kim, J.; Morozumi, T.; Kurumatani, N.; Nakamura, H. *Tetrahedron Lett.* **2008**, *49*, 1984-1987.

(4) Liu, Y.; Han, M.; Zhang, H.-Y.; Yang, L.-X.; Jiang, W. *Org. Lett.* **2008**, *10*, 2873-2876.

(5) Rettig, W. *Angew. Chem. Int. Ed. Engl.* **1986**, *25*, 971-988.

(6) E. Lippert; Rettig, W.; Bonacic-Koutecky, V.; Heisel, F.Miehe, J. A. *Adv. Chem. Phys.* **1987**, *68*, 1.

(7) Bhattacharyya, K.; Chowdhury, M. *Chemical Reviews* **2002**, *93*, 507-535.

(8) Lippert, E.; Luder, W.; Boos, H. *Advances in Molecular Spectroscopy*; Pergamon Press: Oxford, 1962.

(9) Rotkiewicz, K.; Grellmann, K. H.; Grabowski, Z. R. *Chem. Phys. Lett.* **1973**, *19*, 315-318.

(10) Zachariasse, K. A.; Haar, T. v. d.; Hebecker, A.; Leinhos, U.; Kuhnle, W. *Pure & Appl. Chem.* **1993**, *65*, 1745-1750.

(11) Gorse, A.-D.; Pesquer, M. *J. Phys. Chem.* **1995**, *99*, 4039-4049.

(12) Schuddeboom, W.; Jonker, S. A.; Warman, J. M.; Leinhos, U.; Kuehnle, W.; Zachariasse, K. A. *J. Phys. Chem.* **1992**, *96*, 10809-10819.

(13) Sobolewski, A. L.; Domcke, W. *Chem. Phys. Lett.* **1996**, *259*, 119-127.

(14) Sobolewski, A. L.; Sudholt, W.; Domcke, W. *J. Phys. Chem. A* **1998**, *102*, 2716-2722.

(15) Sluch, M. I.; Godt, A.; Bunz, U. H. F.; Berg, M. A. *J. Am. Chem. Soc.* **2001**, *123*, 6447-6448.

(16) Yang, J.-S.; Liau, K.-L.; Hwang, C.-Y.; Wang, C.-M. *J. Phys. Chem. A* **2006**, *110*, 8003-8010.

(17) Lippert, E.; Lüder, W.; Moll, F.; Nägele, W.; Boos, H.; Prigge, H.; Seybold-Blankenstein, I. *Angew. Chem. Int. Ed.* **1961**, *73*, 695-703.

(18) Techert, S.; Zachariasse, K. A. *J. Am. Chem. Soc.* **2004**, *126*, 5593-5600.

(19) Yoshihara, T.; Druzhinin, S. I.; Zachariasse, K. A. *J. Am. Chem. Soc.* **2004**, *126*, 8535-8539.

(20) Fuß, W.; Pushpa, K. K.; Rettig, W.; Schmid, W. E.; Trushin, S. A. *Photochem. Photobiol. Sci.* **2002**, *1*, 255-262.

(21) Zachariasse, K. A.; Druzhinin, S. I.; Bosch, W.; Machinek, R. *J. Am. Chem. Soc.* **2004**, *126*, 1705-1715.

(22) Serrano-Andres, L.; Merchan, M.; Roos, B. O.; Lindh, R. *J. Am. Chem. Soc.* **1995**, *117*, 3189-3204.

(23) Sobolewski, A. L.; Domcke, W. *Chemical Physics Letters* **1996**, *259*, 119-127.

(24) KiShler, G.; Rechthaler, K.; Rotkiewicz, K.; Rettig, W. *Chem. Phys.* **1996**, *207*, 85-101.

(25) Rappoport, D.; Furche, F. *J. Am. Chem. Soc.* **2004**, *126*, 1277-1284.

(26) Kohn, A.; Hattig, C. *J. Am. Chem. Soc.* **2004**, *126*, 7399-7410.

(27) Dreyer, J.; Kummrow, A. *J. Am. Chem. Soc.* **2000**, *122*, 2577-2585.

(28) Minezawa, N.; Kato, S. *J. Phys. Chem. A* **2005**, *109*, 5445-5453.

(29) Zachariasse, K. A.; Grobys, M.; von der Haar, T.; Hebecker, A.; Il'ichev, Y. V.; Jiang, Y.-B.; Morawski, O.; Kühnle, W. *J. Photochem. Photobiol. A: Chemistry* **1996**, *102*, 59-70.

(30) Zachariasse, K. A.; Grobys, M.; Haar, T. v. d.; Hebecker, A.; Illichev, Y. V.; Morawski, O.; Ruckert, I.; Kiihnle, W. *Journal of Photochemistry and Photobiology A: Chemistry* **1997**, *105*, 373-383.

(31) Zachariasse, K. A.; Druzhinin, S. I.; Bosch, W.; Machinek, R. *J. Am. Chem. Soc.* **2004**, *126*.

(32) Techert, S.; Zachariasse, K. A. *J. Am. Chem. Soc.* **2004**, *126*, 5593-5600.

(33) Zachariasse, K. A. *Chem. Phys. Lett.* **2000**, *320*, 8-13.

(34) Kwok, W. M.; Ma, C.; Matousek, P.; Parker, A. W.; Phillips, D.; Toner, W. T.; Towrie, M.; Umapathy, S. *The Journal of Physical Chemistry A* **2001**, *105*, 984-990.

(35) Okamoto, H.; Inishi, H.; Nakamura, Y.; Kohtani, S.; Nakagaki, R. *J. Phys. Chem. A* **2001**, *105*, 4182-4188.

(36) Okamoto, H. *J. Phys. Chem. A* **2000**, *104*, 4182-4187.

(37) Braun, M.; v. Korff-Schmising, C.; Kiel, M.; Zhavoronkov, N.; Dreyer, J.; Bargheer, M.; Elsaesser, T.; Root, C.; Schrader, T. E.; Gilch, P.; Zinth, W.; Woerner, M. *Phys. Rev. Lett.* **2007**, *98*, 248301-248305.

(38) Clark, J. L.; Miller, P. F.; Rumbles, G. A. *J. Phys. Chem.* **1998**, *102*, 4428.

(39) Druzhinin, S. I.; Kovalenko, S. A.; Senyushkina, T. A.; Demeter, A.; Machinek, R.; Noltemeyer, M.; Zachariasse, K. A. *J. Phys. Chem. A* **2008**, *112*, 8238-8253.

(40) Parusel, A. B. J.; Kohler, G.; Grimme, S. *J. Phys. Chem. A* **1998**, *102*, 6297-6306.

(41) LaFemina, J. P.; Schenter, G. K. *J. Phys. Chem.* **1991**, *94*, 7558-7559.

(42) Yang, J.-S.; Hwang, C.-Y.; Chen, M.-Y. *Tetrahedron Lett.* **2007**, *48*, 3097-3102.

(43) Aoki, S.; Kagata, D.; Shiro, M.; Takeda, K.; Kimura, E. *J. Am. Chem. Soc.* **2004**, *126*, 13377-13390.

(44) Nandi, P. K.; Mandal, K.; Kar, T. *Chem. Phys. Lett.* **2003**, *381*, 230-238.

(45) La Clair, J. J. *Angew. Chem., Int. Ed.* **1999**, *38*, 3045-3047.

(46) Brown, E. C.; Marks, T. J.; Ratner, M. A. *J. Phys. Chem. B* **2008**, *112*, 44–50.

(47) Kang, H.; Facchetti, A.; Jiang, H.; Cariati, E.; Righetto, S.; Ugo, R.; Zuccaccia, C.; Macchioni, A.; Stern, C. L.; Liu, Z.; Ho, S.-T.; Brown, E. C.; Ratner, M. A.; Marks, T. J. *J. Am. Chem. Soc.* **2007**, *129*, 3267–3286.

(48) Letard, J. F.; Lapouyade, R.; Rettig, W. *J. Am. Chem. Soc.* **1993**, *115*, 2441-2447.

(49) Lapouyade, R.; Czeschka, K.; Majenz, W.; Rettig, W.; Gilabert, E.; Rulliere, C. *J. Phys. Chem.* **1992**, *96*, 9643-9650.

(50) Pines, D.; Pines, E.; Rettig, W. *J. Phys. Chem. A* **2003**, *107*, 236-242.

(51) Il'ichev, Y. V.; Kühnle, W.; Zachariasse, K. A. *Chem. Phys.* **1996**, *211*, 441-453.

(52) Arzhantsev, S.; Zachariasse, K. A.; Maroncelli, M. *J. Phys. Chem. A* **2006**, *110*, 3454-3470.

(53) El-Gezawy, H.; Rettig, W. *Chem. Phys.* **2006**, *327*, 385-394.

(54) Yang, J.-S.; Liau, K.-L.; Wang, C.-M.; Hwang, C.-Y. *J. Am. Chem. Soc.* **2004**, *126*, 12325-12335.

(55) Yang, J.-S.; Liau, K.-L.; Tu, C.-W.; Hwang, C.-Y. *J. Phys. Chem. A* **2005**, *109*, 6450-6456.

(56) Yang, J.-S.; Yan, J.-L.; Hwang, C.-Y.; Chiou, S.-Y.; Liau, K.-L.; Gavin Tsai, H.-H.; Lee, G.-H.; Peng, S.-M. *J. Am. Chem. Soc.* **2006**, *128*, 14109-14119.

(57) Yang, J.-S.; Liau, K.-L.; Li, C.-Y.; Chen, M.-Y. *J. Am. Chem. Soc.* **2007**, *129*, 13183-13192.

(58) Yang, J.-S.; Lin, C.-K.; Lahoti, A. M.; Tseng, C.-K.; Liu, Y.-H.; Lee, G.-H.; Peng, S.-M. *J. Phys. Chem. A* **2009**, *113*, 4868-4877.

(59) Saltiel, J.; Marinari, A.; Chang, D. W.-L.; Mitchener, J. C.; Megarity, E. D. *J. Am. Chem. Soc.* **1979**, *101*, 2982-2996.

(60) Saltiel, J. *J. Am. Chem. Soc.* **1967**, *89*, 1036-1037.

(61) Meier, H.; Mühling, B.; Kolshorn, H. *Eur. J. Org. Chem.* **2004**, 1033-1042.

(62) Oelkrug, D.; Tompert, A.; Gierschner, J.; Egelhaaf, H.-J.; Hanack, M.; Hohloch, M.; Steinhuber, E. *J. Phys. Chem. B* **1998**, *102*, 1902-1907.

(63) Yang, J.-S.; Chiou, S.-Y.; Liau, K.-L. *J. Am. Chem. Soc.* **2002**, *124*, 2518-2527.

(64) Zucchero, A. J.; Wilson, J. N.; Bunz, U. H. F. *J. Am. Chem. Soc.* **2006**, *128*, 11872-11881.

(65) Woo, H. Y.; Liu, B.; Kohler, B.; Korystov, D.; Mikhailovsky, A.; Bazan, G. C. *J. Am. Chem. Soc.* **2005**, *127*, 14721-14729.

(66) Tolosa, J.; Zucchero, A. J.; Bunz, U. H. F. *J. Am. Chem. Soc.* **2008**, *130*, 6498-6506.

(67) Druzhinin, S. I.; Ernsting, N. P.; Kovalenko, S. A.; Lustres, L. P.; Senyushkina, T. A.; Zachariasse, K. A. *J. Phys. Chem. A* **2006**, *110*, 2955-2969.

(68) Candeias, L. P.; Wildeman, J.; Hadziioannou, G.Warman, J. M. *J. Phys. Chem. B* **2000**, *104*, 8366-8371.

(69) Ginocchietti, G.; Cecchetto, E.; Cola, L. D.; Mazzucato, U.; Spalletti, A. *Chem. Phys.* **2008**, *352*, 28-34.

(70) Sun, Y. P.; Wang, P.; Hamilton, N. B. *J. Am. Chem. Soc.* **1993**, *115*, 6378-6381.

(71) Druzhinin, S. I.; Dubbaka, S. R.; Knochel, P.; Kovalenko, S. A.; Mayer, P.; Senyushkina, T.; Zachariasse, K. A. *J. Phys. Chem. A* **2008**, *112*, 2749-2761.

(72) Arakia, Y.; Ito, O. *J. Photochem. Photobiol. C: Photochem. Rev.* **2008**, *9*, 93-110.

(73) Cogan, S.; Zilberg, S.; Haas, Y. *J. Am. Chem. Soc.* **2006**, *128*, 3335-3345.

(74) Eng, M. P.; Albinsson, B. *Chem. Phys.* **2009**, *357*, 132-139.

Chapter 6

H-Shaped OPV/OPE Oligomers: Two Dimensional Conjugated Fluorophore as Chemosensor

Overview

The goal of this chapter is to access the utility of H-shaped OPV/OPE chromophores as potential sensors for specific analytes. The properties that enhance molecular sensors are introduced and discussed. These principles will be used to access the performance of H-mers derivatized with electron donor and acceptors. The data will be discussed on the case-by-case bases.

Part A. Background

6.1 Introduction..284

6.1.1 Principles of Fluorescent Chemosensors..284

6.1.2 Different Design Principles for Fluorescent Sensors.........................291

6.1.3 Conjugated Polymer Based Fluorescent Sensors..............................294

Part B. Results and Discussions

6.2 Spectroscopic, Electronic Structure of D-OPE-D and Adducts.......................297

6.2.1 Spectroscopic Properties of 1,4-bis(phenylethynyl)benzene (BPEB)...297

6.2.2 Spectroscopic Properties of 4,4`-dimethylamino-1,4-bis(phenylethynyl)-benzene (D-OPE-D) 298

6.2.3 Spectroscopic Properties of D-OPE-D Adducts................................301

6.3 Spectroscopic, Electronic Structure of H-mers and H-mer Adducts..................308

6.3.1 Spectroscopic Properties of Donor and/or Acceptor Substituted H-mers...308

6.3.2 Spectroscopic Properties of SH-4D Adducts...................................320

6.3.3 Spectroscopic Properties of 2D-SH-2A Adducts...............................323

6.4 Substituent Affect on H-mers' Ground and Excited States Chemistry..............323

6.5 Conjugation Length Affect on H-mers' Ground and Excited States Chemistry...328

6.6 Conclusions...335

6.7 References...336

Part A. Background

6.1 Introduction

A chemosensor is a molecular device designed to detect a specific molecule or a class of molecules, which consists of two functional elements, a recognition site (receptor) and a signaling subunit. With regard to the recognition site, it is responsible for selectivity and the efficiency of binding, which depends on the receptor topology and the characteristics of the analytes. The signaling subunit acts as a signal transducer to translate chemical information taking place at the molecular level (the analyte binding process) into a signal expressed as color change,[1] temperature change,[2] changes in the photophysical characteristics of the fluorophore,[3-5] or changes in electrochemical properties such as the oxidation potential of redox active groups.[6] The detection sensitivity is determined by both the ability to measure the transduction event and the association constant of the receptor-analyte complex. Fluorescence is a highly sensitive optical transduction method. The use of fluorescence for sensing and switching offer distinct advantages in terms of sensitivity, selectivity, response time, and remote sensing by using optical fibers with a molecular sensor immobilized at the tip.[7-10]

6.1.1 Principles of Fluorescent Chemosensor

The essential structure of a fluorescent sensor is shown in Figure 6-1. A critical part of the chemosensor components is its binding selectivity towards specific analytes. The binding or interaction of the analytes changes or perturbs the properties of the sensor to indicate a detectable response such as enhancement or attenuation of photo-induced electron transfer (PET), photo-induced charge transfer (PCT), excimer/exciplex formation and extinction, or electronic energy transfer (EET).

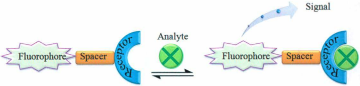
Fluorophore
Spacer
Receptor
Analyte
Signal
Fluorophore
Spacer
Receptor

Figure 6-1. The essential structure of a fluorescent sensor.

6.1.1.1 Photoinduced Electron Transfer (PET)

Photoinduced electron transfer sensors can be classified into two categories: fluorescence "turn-on" and fluorescence "turn-off" upon binding analytes. Fluorescence in a molecule is observed when an excited electron, *i.e.* in the lowest unoccupied molecular orbital (LUMO), undergoes a radiative transition to repopulate the ground state, releasing the excess of energy as light. For fluorescence "turn-off" sensors as shown in Figure 6-2, the receptors usually contain a non-bonding electron pair with relatively high

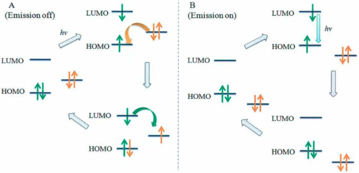
A
(Emission off)
LUMO
HOMO
hv
LUMO
HOMO
LUMO
HOMO
B
(Emission on)
LUMO
HOMO
hv
LUMO
HOMO
LUMO
HOMO

Figure 6-2. PET processes before interacting with analytes, A (off) and after interacting with analytes for fluorescence "turn-on" sensors, B (on).

energy between the HOMO and the LUMO of the fluorophore. In the absence of analytes, a PET from this fully filled orbital of the receptor to the HOMO of the fluorophore can take place. A further electron transfer from the LUMO of the fluorophore to the receptor orbital restores the ground state. Following this sequence, the transition from the excited state to the ground state takes place following a nonradiative path, leading to emission quench of the excited state luminescence. When this non-bonding electron pair interacts with analytes, rendering this electron pair less accessible, quenching will not occur and turn on the fluorescence of the chromophore.

In some cases in which there is an empty orbital from the analyte with energy between the HOMO and the LUMO of the fluorophore, a PET from the excited LUMO to the empty orbital of the analyte can occur, followed by a further electron transfer from this orbital to the HOMO of the fluorophore. Therefore, non-radiative deactivation occurs, resulting in a quenching and turning off the fluorescence of the chemosensor (Figure 6-3).

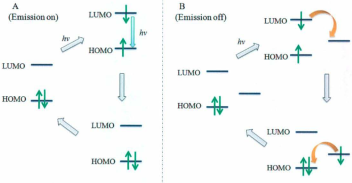

Figure 6-3. PET process with the participation of an empty orbital from the analyte for the fluorescence "turn-off" sensor.

The difference between the "turn-on" and "turn-off" mechanism is that the PET process takes place either before or after the analyte binding.

6.1.1.2 Electronic Energy Transfer (EET)

Electronic energy transfer (EET) is another mechanism that may be responsible for the fluorescence quenching upon analyte binding. In some organic fluorophore-analyte system, fluorescence quenching occurs by the Dexter energy transfer, as shown in Figure 6-4. The Dexter mechanism may be modeled as a simultaneous two-electron transfer, resulting in the fluorophore back to its ground state by non-radiative decay. In this case, fluorescence quenching requires a close contact and direct orbital overlap between the fluorophore and the analyte. Therefore, flexible spacers and appropriate relative energy levels of the fluorophore and the analyte maybe favor the occurrence of an intramolecular energy transfer process.

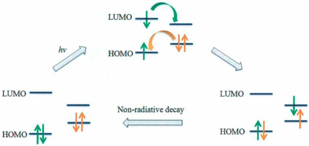

Figure 6-4. EET process for Dexter energy transfer between the excited fluorophore and the analyte bound to receptor followed by analyte return to the ground state by non-radiative decay.

As discussed in Chapter 1, the Förster energy transfer mechanism involves a long range dipole coupling, allowing for an excitation energy transfer through space in the absence of direct orbital overlap. For most conjugated polymer based chemosensory systems, usually the Dexter mechanism dominates because of the direct orbital overlap.

6.1.1.3 Photoinduced Intramolecular Charge Transfer

The fluorophore containing an electron-donating group conjugated to an electron-withdrawing group usually allows photoinduced intramolecular charge transfer (ICT) to occur upon excitation. ICT fluorophores optically express themselves with red shifted ICT absorption, emission spectra and large Stokes shift relative to the purely hydrocarbon systems of similar fluorophore size. Upon excitation into a charge transfer state, the electronic structure of the fluorophore is significantly changed, which typically gives rise to considerable structural changes such as the alteration of bond angles and distances, or the twisting of conformationally flexible bonds.[10-12] The degree of electron transfer and the molecular structural changes are two critical factors for the resulting ICT state. By integrating the ICT fluorophore structure into a ligand backbone, these factors could be controlled by molecular recognition.

When an electron-donating group within the fluorophore interacts with a cation, the cation reduces the electron-donating character of the donor group, which significantly alters the ground state π-bonding, as illustrated in Figure 6-5. Therefore, the absorption spectrum will be blue shifted with a concomitant decrease of the extinction coefficient. The fluorescence spectrum is also shifted in the same direction as the absorption spectrum due to the destabilization of the excited state. In addition to these shifts, changes in quantum yields and lifetimes may occur. These photophysical effects are dependent on the charge and the size of the cation[7,13]. On the contrary, if the cation interacts with the acceptor group, this will enhance the electron withdrawing character, giving rise to red shifted absorption and fluorescence spectra.

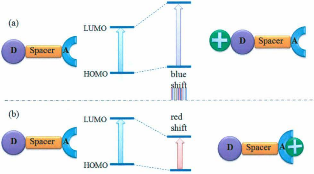

Figure 6-5. Photoinduced intramolecular charge transfer (ICT) by interacting with donor group (a) or acceptor group (b).

6.1.1.4 Excimer or Exciplex Formation

An excimer or electronically excited dimer can be defined as a complex formed by the interaction of an excited fluorophore with a ground state partner of the same structure.[7] Excimer formation requires two monomers to be in close proximity in order to give π stacking interactions in the excited state. In general, it is assumed that flat π-delocalized systems such as pyrene and anthracene show greater tendency to form excimers.[13,14]

An important aspect is that the emission spectrum of the excimer is red-shifted and the absence of vibronic features with respect to that of the monomer and in many cases, the dual emission of the monomer and the excimer is observed. Another is the long radiative lifetime, caused by the symmetry-forbidden nature of the transition. Typically, excimer formation occurs when the aromatic planes of the molecules are separated by 3-4 Å. Therefore, the excimer formation or excimer dissociation upon analyte binding results in fluorescent sensing by simple monitoring the emission band from excimer. The fluorescence "switch on" rather than "switch off" upon the recognition of analytes is usually preferred in order to observe a high signal output. For example, pyrene is a very useful fluorescent probe because of its well-defined monomer emission at 370-430 nm and a relatively efficient excimer formation with emission at around 480 nm. The intensity ratio of excimer to monomer emission (I_E/I_M) is sensitive to the conformational changes of the pyrene-appended receptors (Figure 6-6).[14] This calix[4]crown-5-bis-pyrenyl system was reported to display a strong excimer emission as a consequence of coordination with K^+. The excimer emission was extinguished by displacing K^+ with Pb^{2+}, leading to an ON-OFF switch based on the metal exchange.[15]

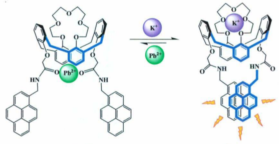

Switch off Switch on

Figure 6-6. On-off excimer formation process of calix[4]crown-5-bispyrenyl system.

6.1.2 Different Approaches for Fluorescent Sensors

Fluorescent sensors change their photophysical response to the surrounding medium or through specific molecular recognition events. A common approach to the development of chemosensors is to couple at least two units: the recognition site and the signaling subunit (see above Figure 6-1). These two parts can be covalently linked together or form a so-called "chemosensing ensemble", e.g. coordination complex. This general design principle is based on reversible reactions; this means that the interaction with the analyte and the change in color or fluorescence are essentially reversible. Other than this reversible approach, a different method is also employed to involve the selective chemical reactions (usually irreversible) between a particular analyte and chromogenic hosts, which is coupled to a color or emission variation.[16-21]

6.1.2.1 Recognition Site-Signaling Subunit Approach

The covalent attachment of signaling subunit and recognition site as shown in Figure 6-1 has been the most extensively used approach in the development of chemosensors. The principle for analyte recognition is based on a coordination reaction, forming a charge transfer complex, or inclusion complex, hydrogen bonding and electrostatic interactions. When making the choice of receptor for a certain analyte coordination, the shape or geometry of the analyte to coordinate, its charge, and its hydrophobicity should be taken into account. The receptors with Lewis base such as azacrown ethers,[22-25] benzocrown ethers,[10,26] polypyridyls[11] or polyamines,[1,27-29] and amino acids[30] have been coupled with fluorophore as metal ion sensors.

In order to tune the receptor properties for anion recognition, hydrogen-bonding groups have been widely used in binding sites for an anion receptor.[31-33] A hydrogen bond can be formed when a hydrogen covalently attached to a highly electronegative atom interacts with another electronegative atom (of the same or different molecule) with lone pairs. These receptors containing urea, thiourea, amine, amide, phenol, imidazolium and pyrrole groups are able to producing strong and unique $(X-H)^{+}\cdots Y^{-}$ hydrogen bonding, and have been used as anion chemosensors.[34-36]

Generally, sensing anions in aqueous solution requires a strong affinity for anions as well as the ability to convert anion recognition into a fluorescent or colorimetric signal. Due to the strong hydration effect of anions in an aqueous system, metal complexes have been used as an anion binding site by forming stronger bonds than those generally observed by using electrostatic or hydrogen-bonding interactions.[37-39]

The signaling subunit is to act as a signal transducer to translate chemical information at the molecular level into a signal. When the response to recognition events occurs, the receptor will definitely change its electronic properties. This, therefore, results in an observable changes in either absorption or fluorescence behavior. Usually, changes in absorption or fluorescence as the output signals are the most frequently used in the development of optical chemosensors because of the simplicity and low cost of the methods required.

6.1.2.2 Displacement Approach

An alternative method is a competition between the indicator and the analyte in the recognition unit. An indicator is displaced from the binding site upon addition of an analyte, reviving non-coordinated spectroscopic behavior of the indicator (Figure

6-7).[35,36] If the spectroscopic characteristics of the signaling subunit in the chemosensing ensemble are different from that in its non-coordinated state, the analyte binding process is coupled to a signaling event. The binding constant between the binding site and the signaling subunit must be lower than that between the binding site and the target analyte so that the displacement reaction can occur and the signaling event indicating the presence of the target analyte will be observed.

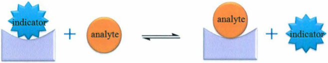

Figure 6-7. Fluorescent sensors based on the displacement approach.

6.1.2.3 Chemodosimeter: Concurrent Recognition and Reaction

A chemodosimeter approach involves the guest induced specific chemical reactions upon binding with the analyte, which is coupled to the suitable colorimetric variation. Such specific reactions are usually irreversible, and final compounds are chemically different from the original. Therefore, the spectroscopic characteristics of the solution should change, allowing determination of the analytes. This chemodosimeter approach and examples can be schematically shown in Figure 6-8. In the first example, the analyte reacts with the chemodosimeter remaining covalently bonded to the product[18] and the other in which the analyte catalyzes a chemical reaction.[16,40] Such specific reactions have advantages such as the high selectivity and its accumulative effect that is directly related to the analyte concentration.

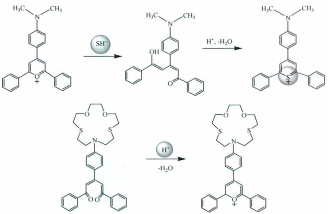

Figure 6-8. Chemodosimeter approach: in the first example, the anion reacts with the chemodosimeter and remains covalently attached, and in the second example, the cation catalyzes a chemical reaction.

6.1.3 Conjugated Polymer Based Fluorescent Sensors

Fluorescent sensors based on conjugated polymers are able to produce signal gain in response to interactions with analytes, and then transform a chemical signal into an easily measured electrical or optical event. Detection is facilitated by a change in the electronic structure of the sensor.[41,42] A key advantage of conjugated polymer based sensors over small molecules is that conjugated polymers have the potential to exhibit additive properties, which is sensitive to tiny perturbations from the environment. In analogy to microelectronic devices, the increased sensitivity is derived from the ability of a conjugated polymer to serve as a highly efficient transport medium. However, unlike a silicon circuit, which transports electrons or holes, conjugated polymers possesses electronic excited states where excitation leads the formation of a bound exciton $[e^-, h^+]$.[43]

Therefore, the geometric relaxation of molecular structure around an excited state has a significant effect on the sensitivity. This effect can be fine-tuned by the structure and topology of the conjugated polymers, thereby modifying the electronic properties.

Increases in the spatial dimensionality of the one-dimensional (1D) electronic conjugation expand the conjugation to a high degree, and consequently conjugated polymers possess multiple pathways for intramolecular electronic and photonic transfer.[44-48] In addition, the increase of the spatial dimensionality introduces an orientation factor dictating electronic interactions between segmented 1D subunits, and drive the structural folding and unfolding motions, which will fundamentally modify the photophysical properties associated with 2D conjugation.[43,49] An interesting architecture is the cross-shaped conjugated oligomers, sometimes referred to as cruciforms or X-mers, whose π-frameworks are usually composed of two spatially separated conjugated branches. These cruciform chromophores display two distinct molecular axes with either similar or dissimilar electronic properties. Attaching donor and/or acceptor substituents to cruciform at suitable positions can lead to independent electronic shifts of the HOMO and LUMO into opposite directions. As a consequence, the cruciform should be valuable functional scaffolds for differential metal sensor arrays.[50-52]

The OPEs, dehydrogenated congeners of the oligo(*p*-phenylenevinylene)s (OPV), are a class of conjugated oligomers with demonstrated sensory and device applications.[53-55] Their superb photophysical properties combined with their high stability and high electron affinity make them attractive and in many ways complementary to the OPVs. However, OPEs are at a disadvantage for applications in OLEDs compared to the OPVs.

The electron withdrawing nature of the alkyne groups inhibits the hole injection, and lowers the energy of the HOMO. Combining the stability, electron affinity, and high emissive quantum yield of the OPEs with the excellent hole injection capabilities of the OPVs will make cross conjugated OPV/OPE hybrids, in which styryl side chains decorate a OPE main chain, interesting. In this chapter, structural and electronic properties of 2D H-shaped OPV/OPE oligomers as well as their adducts were investigated by ab initio and density functional theory (DFT) calculations. These results were correlated with spectral data obtained from UV-Vis absorption, steady-state fluorescence experiments. In addition, substituent affect on H-mers ground and excited states, as well as equilibrium binding constants were also investigated.

Part B. Results and Discussions

6. 2 Spectroscopic, Electronic Structure of D-OPE-D and D-OPE-D Adducts

6.2.1 Spectroscopic Properties of 1,4-bis(phenylethynyl)benzene

Conjugated compounds such as 1,4-bis(phenylethynyl)benzene (BPEB) possesses interesting optical, optoelectronic and nonlinear transport properties (NLO), or charge carrier or charge transport properties, which are important in terms of molecular devices. As indicated in Chapter 3, the optical spectra of OPE show a strong asymmetry between absorption with λ_{max}= 328 nm (ε = 5.0×10^4 M^{-1}cm^{-1}, E_{op} = 30,500 cm^{-1}) and emission with λ_{em} = 348 nm (ϕ_f = 0.50, E_{em} = 28,730 cm^{-1}).[56] The absorption bands tend to be broad and structureless, while the corresponding emission spectra are narrower and structured. Moreover, the Stokes shift between both bands is very small. The computational study has been performed to elucidate the frontier orbitals of BPEP (Figure 6-9).[57,58] The absorption spectrum was calculated by using TD-B3LYP/6-311G(d, p) single point energy calculations with the optimized ground state geometries. The dominant absorption bands are found to be associated with electronic transition between the HOMO and LUMO levels, and all the other excited states are associated with smaller oscillator

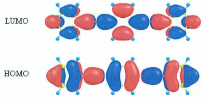

Figure 6-9. Calculated HOMO and LUMO orbitals (B3LYP/6-31+G(d, p)) of BPEP.

strengths (less than 0.1). The excited state geometry and emission calculated by using Configurational Interaction Singles (CIS) method with the 6-31G basis set agree with the available experimental values. Furthermore, the dipole moments of BPEB for both ground and excited states have been calculated and are negligible. The ground state rotational potential calculated with the AM1 method revealed a very shallow potential with a fully planar energy minimum that is only 0.5 kcal/mol lower than the perpendicular transition state. However, the excited-state rotational energies increase sharply at angles that are close to the perpendicular transition state and that they are relatively shallow near the energy minimum. Therefore, the ground and excited state potentials surface have very different curvature along the torsional coordinate.

6.2.2 Spectroscopic Properties of 4,4`-dimethylamino-1,4-bis(phenylethynyl)-benzene

The steady state absorption and fluorescence spectra of 4,4`-dimethylamino-1,4-bis(phenylethynyl)benzene (**D-O**PE-D) in $CHCl_3$ are shown in Figure 6-10. The absorption spectrum is characterized by an unstructured broad absorption band with λ_{max}= 368 nm (ε

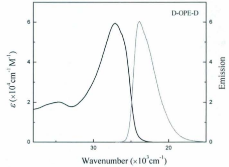

Figure 6-10. Absorption and emission of 4,4`-dimethyamino-1,4-bis(phenylethynyl)benzene.

= 6.0×10^4 $M^{-1}cm^{-1}$, E_{op} = 27,170 cm^{-1}) and discernable shoulder at 388 nm (ε =4.8×10^4 $M^{-1}cm^{-1}$, E_{op} = 25,770 cm^{-1}). Light excitation at 350 nm into the $S_0 \rightarrow S_1$ transition leads to an intense emission band at 418 nm (ϕ_f = 0.50, E_{em}= 23,920 cm^{-1}) reasonably assigned to a $S_1 \rightarrow S_0$ radiative transition. The dimethylamino group exerts a significant bathochromic (red shift) effect on the absorption and fluorescence spectra.

The introduction of electron donating and/or electron withdrawing groups not only influences the orbital energies, it also alters the electron correlation and consequently partially determines the electronic properties of molecules. In terms of a self-consistent field (SCF) theory, both the difference in the orbital energies ΔE_0 and the configuration interactions of one-electron function need to be taken into account for the excitation energy E ($S_0 \rightarrow S_1$). The influence of the donor and acceptor substitution in D-π-A systems on the energy of the electronic excitation is given by eq 6-1, illustrated in Figure 6-11.[59]

$$E = \Delta E_0 - (J - 2K) \qquad (6\text{-}1)$$

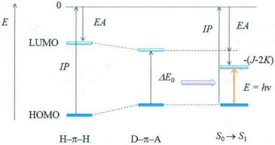

Figure 6-11. The influence of the donor and acceptor substitution in D-π-A systems on the energy of the electronic excitation.

where J is the Coulomb repulsion integral and K is the exchange integral. ΔE_0 is the difference of the ionization energy (*IP*) and electron affinity (*EA*) according to Koopmans theorem.[60] The excitation energy is always less than ΔE_0 because of $J > 2K \geq 0$. If there is a photoinduced charge transfer within the chromophore, the extent of charge transfer is longer than that found for a $\pi \to \pi^*$ transition. The net effect of charge transfer decreases the orbital overlap density, but the configuration interaction (J-$2K$) increases. From eq 6-1, the absorption energy will decrease and the absorption will shift to a longer wavelength. A decrease of the intramolecular charge transfer (ICT) effect accordingly blue shifts the band to shorter wavelength, the hypsochromic (blue shift) effect. There is less possibility for ICT in symmetric systems. The charge transfer band responds very differently upon the extension of the conjugation, because a hypsochromic effect resulting from the decrease in the ICT is opposite to the bathochromic effect caused by the extension of the conjugation. With increasing the conjugation length of D-π-A for OPEs, the overlap density of the HOMO and LUMO becomes smaller, and the transitions HOMO -1 → LUMO, HOMO → LUMO + 1, and HOMO -1 → LUMO + 1 become more important. The absorption band ($S_0 \to S_1$) is superimposed by the higher energy electronic transition $S_0 \to S_2$ as the conjugation length increases. Therefore, the HOMO → LUMO transition characterized by a strong ICT from the donor to the acceptor side plays a minor role among the other transitions.[59]

The energy $E_{DA}(n)$ of an electronic transition in D-π-A systems can be split into two terms $E_D(n)$ and $\Delta E_{DA}(n)$, expressed as:[61,62]

$$E_{DA}(n) = E_D(n) - \Delta E_{DA}(n) \qquad (6\text{-}2)$$

$E_D(n)$ refers to the stabilization energy imparted as n increases from the extension of conjugation and incorporates the substituent effect of the donor group as described by eq 6-3, which causes a pronounced bathochromic effect. The second term $\Delta E_{DA}(n)$ is a correction due to the polarization of electron density, which depends on the terminal donor/acceptor substitution, given by eq 6-4. The increase of n (the number of monomer units) attenuates $\Delta E_{DA}(n)$ as the inductive electronic effects of the substituents decrease as the molecular framework increases.

$$E_D(n) - E_\infty = [E_D(1) - E_\infty]e^{-a(n-1)} \qquad (6\text{-}3)$$

$$\Delta E_{DA}(n) = [E_D(1) - E_{DA}(1)]e^{-\Delta a(n-1)} \qquad (6\text{-}4)$$

where E_∞ is excitation energy. E(n) convergence with the extension of conjugation by increasing numbers of repeat units n, and a is less than 1 based on the coupled oscillator model suggested by Lewis and Calvin.[63] The above equations show that the conjugation effect and the ICT effect are offsetting energetic effects. Obviously, it depends on the acceptor strength and as to which of the two effects predominates. The system series having weak donors or weak acceptors, or both, always exhibit red shifts. For system series with a strong acceptor, depending on the strength of the acceptor, a rapidly decreasing term $[E_D(n) - E_\infty]$ with increasing numbers of n can also lead to the fact that $E_{DA}(n)$ goes through a minimum before it approaches to E_∞. Therefore, the ΔE_{DA} term will reverse the red shift effect to the blue shift in a series of conjugated oligomers.[59,62]

6.2.3 Spectroscopic Properties of D-OPE-D Adducts

Protonation of D-OPE-D. Protonation of the NMe_2 groups results in distinct changes in the absorption and emission spectra of D-OPE-D. Titration of D-OPE-D with concentrated trifluoroacetic acid (TFA) in $CHCl_3$ effectively diminished and red shifted the emission from 418 nm to 458 nm. However, the absorption was blue shifted from 368 nm to 324 nm and exhibited a similar profile as the absorption spectrum of BPEB, but with a pronounced absorption tail which extends to 450 nm (Figure 6-12). The source of this absorbance is due to non-protonated D-OPE-D, which under the conditions of this experiment is roughly 10% of the starting material.

The reaction of $\mathrm{Me_2\ddot{N}-OPE-\ddot{N}Me_2}$ with TFA appears to be consistent with eq 6-5,

$$\mathrm{Me_2\ddot{N}-OPE-\ddot{N}Me_2} + 2\mathrm{H}^+ \xrightleftharpoons{K_1} \mathrm{Me_2HN^+-OPE-{}^+NHMe_2} \qquad (6\text{-}5)$$

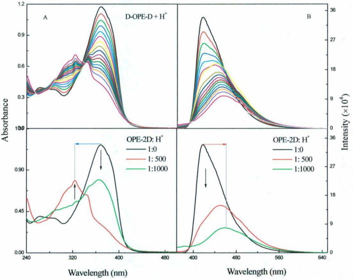

Figure 6-12. (A) Absorption and (B) emission spectral changes of D-OPE-D upon addition of TFA in $CHCl_3$.

which demands that two $\mathrm{Me_2\ddot{N}}$ groups in D-OPE-D are electronically independent. In comparison with the equilibrium constants for the reactions with Ag^+ and Cu^{2+} the constant for the TFA is abnormally small and not easily to rationalize given the known activity of the proton in non-aqueous media. If this is true, there will be only two species in the equilibrium system and the spectral changes upon addition of TFA will show one isosbestic point. However, this is not the case. In the other extreme, the reaction proceeds in two steps as eq 6-6:

$$\mathrm{Me_2\ddot{N}-OPE-\ddot{N}Me_2 + H^+ \xrightleftharpoons{K_1} Me_2\ddot{N}-OPE-N^+HMe_2} \quad (6\text{-}6a)$$

$$\mathrm{Me_2\ddot{N}-OPE-N^+HMe_2 + H^+ \xrightleftharpoons{K_2} Me_2HN^+-OPE-N^+HMe_2} \quad (6\text{-}6b)$$

Upon the first protonation of $\mathrm{Me_2N}$ by addition of TFA, $\mathrm{Me_2HN^+}$ becomes a strong acceptor. An attenuation of the chromophore D-OPE-A should result in a hypsochromic effect. However, an increase of the intramolecular charge transfer (ICT) character due to the decreased overlap density of the HOMO and LUMO also result in a bathochromic effect. These are offsetting effects which cancel each other and a red shift in the spectra were not observed when the donor group in combination with strong acceptors such as $\mathrm{NO_2}$ or $\mathrm{Me_2HN^+}$.[59] Further addition of TFA leads to the complete protonation of two $\mathrm{Me_2N}$ groups, and the original D-OPE-D system becomes an A-OPE-A system. The absorption spectrum of protonation shows an isosbestic point at 330 nm, which moves to 340 nm, consistent with two sequential steps where K_1 is much larger than K_2. On the contrary, the emission spectrum upon addition of TFA red shifted from 418 nm to 458 nm. The increasing Stokes shift as a function of $[H^+]$ is opposite to the trend that has been established for the blue-shifted absorption described above. The vertical electronic transition after optical absorption is followed by a relaxation to an excited state species which is thermally equilibrated with the surrounding solvent. Other than substitution effect, solvent also has an influence on the energetics of the excited state, *i.e.* a dipole moment change due to the different substitution in the ground and excited states will result in the solvent dependence of the emission and absorption spectra. Thus, further study is needed to understand the effect of solvent on optical properties of D-OPE-D.

For the further interpretation and identification of unknown intermediates and associated parameters upon protonation, the absorption and emission spectra are subjected to global analysis. The mathematical methods used to deal with and to analyze such data were described in Chapter 2 (experimental methodologies). The goal of the global analysis is to decompose the measured spectra data matrix Y into the product of two matrices C and A, which are the concentration profiles of the reacting species and the molar absorptivities. In all cases described in this chapter, the global analysis is used with known molar absorptivity spectra of initial species in order to constrain the fit and thereby the calculated parameters are not mathematically correlated, which is a significant problem in most equilibrium models. Furthermore, the analysis yields the spectra for those predicted species from the fit. If K_1 is comparable to K_2 in two-step consecutive protonation of eq 6-6, spectral changes upon addition of TFA will display the typical and familiar behavior for the consecutive reaction, in which the spectral intensity first reaches the maximum and then decreases with further addition of TFA. If this is the case, the concentration of D-OPE-A is comparable with the concentration of A-OPE-A, and the spectrum of D-OPE-A and A-OPE-A will be delivered by global analysis. Such spectra will allow structural assignment of unknown intermediates and can confirm the feasibility of a given mechanism.

However, the binding constant K_1 is much greater than K_2, and it is clearly revealed from the plot of spectral changes *vs*. addition of TFA at different wavelengths (Figure 6-13). There is no obvious spectral change, which features the typical and familiar behavior for the consecutive reaction in eq 6-6. As $K_1 \gg K_2$, the concentration of D-OPE-D in the equilibrium system is negligible when compared with the concentrations

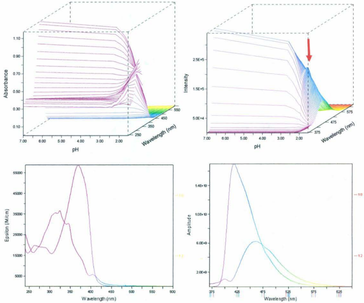

Figure 6-13. Spectral change of D-OPE-D upon addition of TFA plotted at different wavelengths (top), and the spectra for the extract colorful species (bottom).

of D-OPE-A and A-OPE-A. Actually, the recorded spectral changes correspond to the protonation of D-OPE-A to form A-OPE-A. As discussed above, the spectra of D-OPE-A is close to that of D-OPE-D, and the known spectrum of D-OPE-D with the molar absorptivity is used to constrain the fit. Therefore, one of the returned spectra for predicted species is the same as the known spectrum of D-OPE-D.

By using different binding models, the analysis results confirm that only two reacting species can be identified from the protonation reaction. The spectra of the extract colorful species are showed in Figure 6-13 (bottom), and the binding constants for protonation in the ground and excited states together with Ag$^+$ and Cu^{2+} coordination are listed in Table 6-1.

Table 6-1. Binding constants (log K_1) of D-OPE-D titration with TFA, AgOTf and Cu(OTf)$_2$ in CHCl$_3$.

Sample	**TFA**		**AgOTf**		**Cu (OTf)$_2$**	
	Ground State	Excited State	Ground State	Excited State	Ground State	Excited State
	log K_1	log K_1	log K_1	log K_1	log K_1	log K_1
OPE-2D	4.6 ± 0.086	4.6 ± 0.068	9.6 ± 0.13	9.7 ± 0.22	12.6 ± 0.84	13.0 ± 1.0

Coordination with Metal Cations. Titration of D-OPE-D with proton generates two reacting species in the reaction system. To further confirm the reaction scheme in which only two reacting species can be identified from the reaction system, titration of D-OPE-D with AgOTf and Cu(OTf)$_2$ were acquired in CHCl$_3$ for comparative purposes. Addition of AgOTf displays very similar reaction behavior to that of protonation. However, titration with Cu(OTf)$_2$ results in different absorption changes which effectively diminish but no red shift. Close to the saturation of titration, the absorption spectrum displays some fine structure (Figure 6-14). Global analysis of titration with AgOTf and $Cu(OTf)_2$ are consistent with a model in which two species with different absorption spectra are identified in the reaction scheme. The plot of spectral changes *vs*. the concentration of $Cu(OTf)_2$ addition at different wavelengths derived from the global

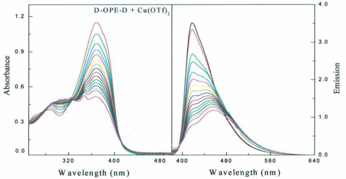

Figure 6-14. Absorption and emission change of D-OPE-D titration with $Cu(OTf)_2$.

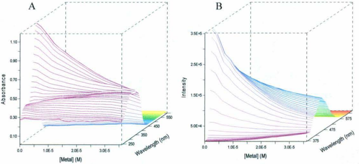

Figure 6-15. (A) Absorption and (B) emission changes of D-OPE-D *vs*. the concentration of $Cu(OTf)_2$ addition at different wavelengths.

analysis using the same model is shown in Figure 6-15, which is in agreement with the experimental data. The binding constants are summarized in Table 6-1.

6.3 Spectroscopic, Electronic Structure of Substituted H-mers and Their Adducts

6.3.1 Spectroscopic Properties of Donor and/or Acceptor Substituted H-mers

Grafting of suitable recognition units to the side chains of conjugated polymers (CP) provides bio- and chemosensory materials. It is obvious that the effective sensors must be highly sensitive, selective and possess a distinctive spectroscopic tag. In most sensor designs, the donor and acceptor units are spatially separated, allowing the HOMO and LUMO to be independently perturbed by Lewis acids or metal cations. The resulting chromophore system will display a two-stage response or differential binding to an electron deficient analyte. Substituted H-mers are valuable functional scaffolds for differential metal sensor arrays. Their photophysical properties and their spectroscopic responses to proton, metal cations will be investigated in this chapter, and the structure of 2D-SH-2A, SH-4D and SH-4A are shown in Scheme 6-1.

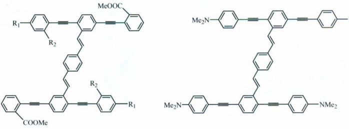

2D-SH-2A: R_1= NMe_2, R_2= H
SH- 4A: R_1= H, R_2= COOMe

SH-4D

Scheme 6-1. The structure of 2D-SH-2A, SH-4D and SH-4A.

Steady state absorption and emission spectral data, quantum yields and excited state lifetimes are summarized in Table 6-2. Comparative absorption and emission spectra for the 2D-SH-2A, SH-4D and SH-4A are respectively shown in Figure 6-16.

Table 6-2. Photophysical data for 2D-SH-2A, SH-4D and SH-4A in comparison with unfunctionalized SH, measured in $CHCl_3$ at 298±3K.

Entry	$\lambda_{abs}^{S_0\rightarrow S_1}$(nm) ε ($\times10^4$ $M^{-1}cm^{-1}$)	$E_{op}^{S_0\rightarrow S_1}$ (cm^{-1})	$\lambda_{em}^{S_1\rightarrow S_0}$ (nm)	$E_{em}^{S_1\rightarrow S_0}$ (cm^{-1})	E_{abs}-E_{em} (cm^{-1})	$\phi_F^{S_1\rightarrow S_0}$	τ_F, ns (k_d, s^{-1})
SH	328 (9.9)	30,580	425	23,530	2360	0.49	1.2 (8.3×10^8)
	386 (sh) (3.8)	25,910	450	22,220			1.2 (8.3×10^8)
			480(sh)	20,830			
2D-SH-2A	305(sh) (7.4)	32,790	510	19,600	8330	0.56	5.3 (1.9×10^8)
	358 (14)	27,930					
SH-4D	295 (0.48)	33,900	517	19,340	7910	0.43	6.4(1.6×10^8)
	368 (1.4)	27,250					
SH-4A	303(sh) (7.6)	33,000	443	22,620	6370	0.36	2.0 (5.0×10^8)
	345 (17)	28,990	462	21,650			2.0 (5.0×10^8)
	415(sh) (3.3)	24,100					

The absorption spectral envelopes for 2D-SH-2A and SH-4D are generally broad and unstructured. In comparison with the unfunctionalized SH, the absorption of 2D-SH-2A is red shifted with λ_{max} = 358 nm (ε=14×10^4 $M^{-1}cm^{-1}$, E_{op} = 27,900 cm^{-1}) and well-resolved shoulder at 305 nm (ε= 7.4×10^4 $M^{-1}cm^{-1}$, E_{op}= 32,800 cm^{-1}). The absorption of SH-4D assembly with four donors is further red shifted with λ_{max} = 368 nm (ε=1.4×10^4 $M^{-1}cm^{-1}$, E_{op} = 27,300 cm^{-1}). The emission spectra of 2D-SH-2A and SH-4D are broad and substantially red shifted with loss of vibronic fine structure relative to SH, which displays a distinct vibronic progression at λ_{em}= 425, 450 nm and some additional shoulders at 480

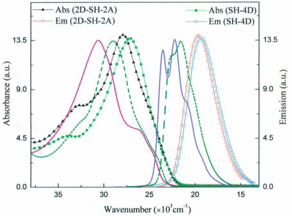

Figure 6-16. Absorption and emission spectra of 2D-SH-2A (▲), SH-4D (■) and SH-4A (dash line) in comparison with SH (solid line).

nm extending to the red. The vibronic spacing is measured 1310 cm^{-1}, which is associated with the C=C stretching mode in the central distyrylbenzene bridge. The electronic/steric origin for the variation of absorption and fluorescence of the substituted H-mers were ascertained from theoretical calculation. The molecular and electronic structures were optimized at HF/3-21G level of theory using the Spartan'06 package and calculated FMO plots are shown in Figure 6-17.[1] Computational studies reveal that the energetics of the HOMO and LUMO are very sensitive to the electronic nature of the substituents. For unfunctionalized SH, both HOMO and LUMO are located on the distyrylbenzene branch, which are spatially superimposable on each other. On the contrary, these donor and/or

---

[1] *ab initio* calculations (HF/3-21G) were performed by Dr. Yuming Zhao and is included here for completeness.

Entry	SH	SH-4A	2D-SH-2A	SH-4D
HOMO	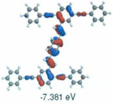	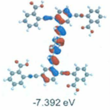	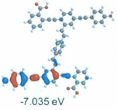	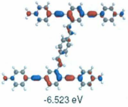
LUMO	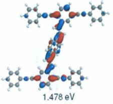	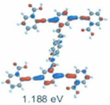	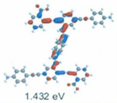	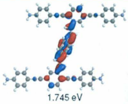

Figure 6-17. Optimized structures and FMOs of SH, SH-4A, 2D-SH-2A, and SH-4D.

acceptor substituted H-mers show a shifted FMO structure, spatially separated HOMO and LUMO, and do vary greatly with the strength and position of donor and acceptor groups. Consequently, the intramolecular charge transfer dramatically red shifts the absorption and emission spectra. The additional evidence to support the ICT assignment comes from the solvatochromic shifts in the UV-Vis as a function of solvent. With increasing the polarity of solvents, the absorption and emission spectra of the amino substituted H-mers are considerably red shifted, (The details on the solvent study will be discussed later in this chapter). The trend of red shift for the maximum absorption wavelengths (λ_{max}) is in good agreement with the order of decreasing HOMO-LUMO gaps from the theoretical calculations: SH (8.86 eV) > SH-4A (8.58 eV) > 2D-SH-2A (8.45 eV) > SH-4D (8.27 eV), which are associated to the electronic inductive and resonance effects with terminal donor-acceptor substitution. From the calculated FMO plots, it is apparent that the orbital overlap is relatively small by crossing distyrylbenzene bridge. The HOMO → LUMO transition is symmetry allowed in the one-electron approximation. The large Stokes shifts in these H-mers support the theoretical calculation of a significant electronic structure change between the ground and excited states. These shifted FMOs also explain the unusually long emission lifetime as a result of this weakly allowed Franck-Condon transition. The change of quantum yield upon red shift of the emission is not as expected, as nonradiative pathways (vibronic coupling) are more accessible with a smaller energy gap. There is no clean numerical correlation between excitation energy gap and emission quantum yields.

6.3.2 Spectroscopic Properties of SH-4D Adducts

The optical properties of amino derivatized chromophores undergo dramatic changes upon protonation or coordination of metal ions to the nitrogen lone pair. The protonation or coordination of the lone pairs on the amino substituent has three major effects. First, the protonation or coordination significantly attenuates the donor ability of the amino group and the resulting R_2N^+H or R_2N^+M becomes an electron acceptor, which inductively polarizes the electron density towards R_2N^+H or R_2N^+M group. Second, the protonation or coordination usually introduces net positive charge and the cationic substrate changes the solvation energy. Third, the protonation or coordination alters the nature of absorption transitions from ICT to $\pi\rightarrow\pi^*$. The response of the amino functionalized H-mers towards protonation and metal ion coordination are investigated in the following section.

Protonation with TFA. Protonation of the NMe_2 groups in SH-4D resulted in a blue shift in the absorption and emission spectra as shown in Figure 6-18. With addition of TFA, the absorption peak at 368 nm appreciably bleached, and a concomitant growth of new band at 328 nm. The isosbestic point was observed at 332 nm in the early part of titration, and shifted to 342 nm with approaching the saturation of titration. The emission intensity at 517 nm under the same acid titration considerably decreased, while three new bands at 428, 450, and 489 (sh) nm grew gradually. After complete protonation (saturated at around 12,000 molar equivalent of TFA), the absorption and emission profiles displayed great resemblance to those of the unfunctionalized SH (Figure 6-19). This indicates that the protonation of dimethylamino groups, where the HOMO resides,

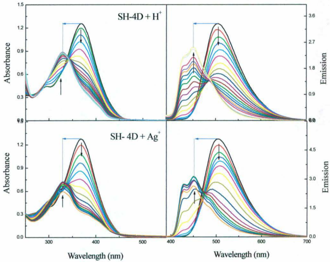

Figure 6-18. Absorption and emission spectral change of SH-4D upon protonation (top) and coordination (bottom) with AgOTf in $CHCl_3$.

will lead to a net stabilization of the HOMO, but will leave the LUMO unchanged. Therefore, this will lead to an increase of the HOMO-LUMO gap. In addition, the FMOs are not superimposable, and proton binding will polarize the electron density and rearrange the HOMO to distyrylbenzene bridge and LUMO to bisphenylethynylene branch (Figure 6-19). Therefore, the emission profile of the completely protonated species bears a strong resemblance to the emission spectrum of unsubstituted SH.

Coordination with AgOTf. Titration of SH-4D with AgOTf resulted in similar absorption and emission spectral changes to what observed in TFA titration (Figure 6-18). However, the equilibrium constants for Ag^+ coordination to SH-4D were significantly

Entry	SH-4D	SH-4D + 4H⁺	SH
HOMO	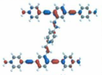 -6.523 eV	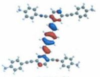 -9.986 eV	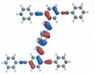 -7.381 eV
LUMO	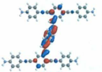 1.745 eV	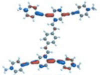 -2.101 eV	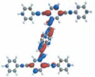 1.478 eV

Figure 6-19. Optimized structures and FMOs of SH-4D and SH-4D + 4H$^+$.

large when compared with the equilibrium constants for protonation of SH-4D in $CHCl_3$ described above.

Spectral changes upon protonation or Ag$^+$ coordination to SH-4D have isosbestic points that shift during the titration, suggesting a multiple-step process is involved in the reaction mechanism. Singular Value Decomposition of all spectral data for protonation and metal coordination offered some mechanistic insight and provided spectral evidence to identify the unknown intermediates. The plots of spectral intensity *vs.* the concentration of the metal ion addition at different wavelengths (Figure 6-20) were found to be consistent with a two-step process given by

$$\mathrm{SH-4D} + 2\mathrm{Ag}^+ \overset{K_1}{\rightleftharpoons} \mathrm{SH-4D}\cdot 2(\mathrm{Ag}^+) \qquad (6\text{-}7a)$$

$$\mathrm{SH-4D}\cdot 2(\mathrm{Ag}^+) + 2\mathrm{Ag}^+ \overset{K_2}{\rightleftharpoons} \mathrm{SH-4D}\cdot 4(\mathrm{Ag}^+) \qquad (6\text{-}7b)$$

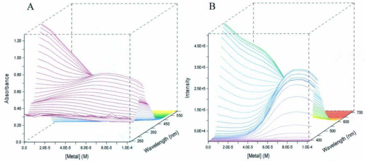

Figure 6-20. (A) Absorption and (B) emission changes of SH-4D *vs*. the concentration of AgOTf addition at different wavelengths.

The effects of the electron donating and accepting end groups on the electronic structure of the π-bridge in the ground state can be described as resonance between two limits with an electroneutral extreme and fully delocalized zwitterionic structure in eq 6-8.

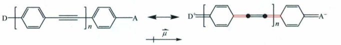

(6-8)

The influence of the donor/acceptor separation on the molecular electronic structure has been investigated by ^{13}C NMR and Stark spectroscopy.[62,64] For OPE systems, the values of δ (^{13}C-sp) between 86.9 and 94.8 ppm excluded any discernable contribution of a fully delocalized cumulene structure. Therefore, the donor and acceptor end groups show a very weak perturbation on the π bonding in the OPE bridge. On the other limit, for a very short bridge additional direct interaction of the donor and acceptor may be expected. Upon addition of proton, the resulting ammonium group becomes a very strong electron-withdrawing group, but the electronic perturbation through OPE bridge is still very weak. In the case investigated above, it is clear that protonation of the terminal amino groups polarizes the electron density in the σ bonded network, resulting in a decreased proton affinity of the second amino group. Therefore, this argument is consistent with K_1 much greater than K_2. This is an important point, as the separation of σ and π bonding effects is still controversial. This subject has been reviewed recently.[65]

For donor substituted H-mer, the electronic perturbation through OPE bridge is weak, but the electric field effect through intervening medium may be relatively significant even with solvent screening. After protonation of one OPE branch, the other OPE branch will be in the different electric field (Scheme 6-2). The dipole moment of a molecule in an electric field F is given by:[66]

$$\mu^F = \mu + \alpha \cdot F \qquad (6\text{-}9)$$

where μ^F and μ are the dipole moment vectors in the presence and absence of electric field, F, respectively, and α is the polarizability tensor. Because the dipole moment of a molecule changes in the presence of an electric field,[66,67] the interaction with other

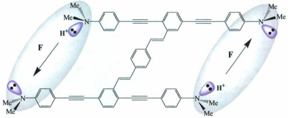

Scheme 6-2. Illustration of the electric field effect through intervening medium.

species carrying the opposite charge will be different from that in the absence of the electric field. Therefore, the binding constant K_2 will be different from K_1. This analysis is in agreement with the result from global analysis that only three colorful reacting species appear in the reaction system. The binding constants are summarized in Table 6-3. The observations outlined above are important because the H-mers can be compared to π-conjugated OPV/OPE films where the inter-chain interactions are important.

Table 6-3. Binding constants of SH-4D with proton and metal cations in the ground and excited states.

Titratant	Ground State		Excited State	
	$\log K_1$	$\log K_1K_2$	$\log K_1$	$\log K_1K_2$
TFA	3.5 ± 0.030	5.7 ± 0.015	3.6 ± 0.037	6.4 ± 0.045
AgOTf	9.6 ± 0.28	18.8 ± 0.28	10.6 ± 0.53	19.4 ± 0.50
Cu(OTf)$_2$	10.4 ± 0.30	22.2 ± 0.29	13.4 ± 0.74	22.8 ± 0.74

Coordination with M^{2+} Cations. The protonation and coordination of silver ions (+1 oxidation state) with D-OPE-D gave similar results. The study was extended to metal ions in their +2 oxidation state to ascertain how the nature of the metal cations affect the optical properties of the substituted H-mers. The dicationic metal ions Cu^{2+}, Zn^{2+}, Mg^{2+}, and Ba^{2+} as their triflate salts were employed to investigate the electrostatic effect and to assess the effect of charge to size ratios. Given the number of cations employed, in principle, the determined binding constants could be compared to the charge/size ratio, as well as determining if the radiative transitions change as the oxidation state changes.

Titration of SH-4D with $Cu(OTf)_2$ results in a different spectral response when compared to the titration with AgOTf and TFA respectively. Upon addition of $Cu(OTf)_2$, The intensity of ICT absorption band decreases, but there is no shift for λ_{max}. Over the course of the titration, the ICT band broadens resulting in a systematic increase in the UV-Vis baseline and becomes more prominent as the saturation limit is reached ([Cu^{2+}] reaches 1.6 mM). The changes in the emission spectrum are similar to that found in the absorption spectrum. The intensity of ICT band slowly diminished and λ_{max} did not shift. As the titration approaches the saturation point, other high-energy bands emerge, but the intensity is relatively low (Figure 6-21). The first isosbestic point appears at $\lambda = 438$ nm,

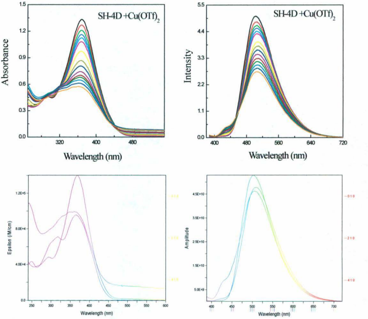

Figure 6-21. Spectral change of SH-4D by coordination with Cu(OTf)$_2$ (top), Spectra of the extracted colorful reacting species from global analysis (bottom).

and with continuous addition of $Cu(OTf)_2$ the isosbestic point moves to long wavelength at $\lambda = 460$ nm. Application of global analysis, the derived reaction mechanism is a consecutive first order reaction as eq 6-7, and the spectra for extracted colorful species is also shown in Figure 6-21. Possibly, due to the high positive charge of Cu^{2+}, the HOMO and LUMO from the final titration species are far separated, and the poor overlap will explain this weakly allowed Franck-Condon transition. Further evidence to support this proposition is required to measure the quantum yield and the excited state lifetime.

Titration with other M^{2+} cations, *i.e.* $Ba(OTf)_2$, $Mg(OTf)_2$, $Zn(OTf)_2$ were also acquired, but there is no visible changes upon addition with these metals ions. Relatively, the coordination of SH-4D with metal ions is selective.

6.3.3 Spectroscopic Properties of 2D-SH-2A Adducts

Protonation with TFA and Coordination with AgOTf. The spectral changes of 2D-SH-2A in response to titration of TFA or AgOTf (Figures 6-22) were similar to the titration behavior of SH-4D, but the absorption and emission profiles of the final protonated species and metal complex are similar to those of acceptor-substituted SH-4A. It is also clear that the fluorescence intensity of 2D-SH-2A increases with the increasing concentration of AgOTf. This is in agreement with calculated LUMO energy, which is lower than that of non-bound 2D-SH-2A. Usually, chemical systems whose excited states are stabilized can give strong emission.[15] During the titration process, the isosbestic point in emission spectrum shifted from $\lambda = 458$ nm to $\lambda = 485$ nm, but the absorption spectral changes were small.

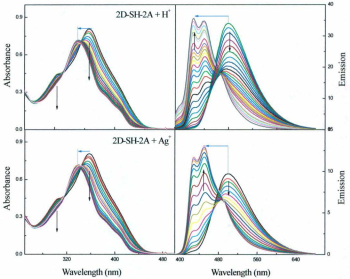

Figure 6-22. Absorption and emission change of 2D-SH-2A upon protonation (top) and complexion with AgOTf (bottom) in $CHCl_3$.

The interpretation of the spectral changes relies on the theoretical calculation of FMOs energetic for 2D-SH-2A and protonated 2D-SH-2A in comparison with SH-4A (Figure 6-23). It has been recognized that DFT calculations often overestimate the delocalization especially in π-conjugated systems. As such, the parameters should be interpreted with caution. The positions of HOMO and LUMO with protonation are dramatically influenced. The HOMO and LUMO switch their position, and the HOMO is located at the distyrylbenzene bridge as the HOMO of SH-4A. Given the inter-conversion of the HOMO and LUMO, the emission spectrum of the completely protonated species bears a great resemblance to the emission of SH-4A, where $\hbar\omega$ is 1250 cm^{-1}. In the

Entry	2D-SH-2A	2D-SH-2A + 4H⁺	SH-4A
HOMO	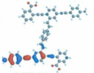 -7.035 eV	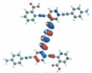 -12.679 eV	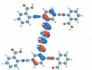 -7.392 eV
LUMO	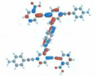 1.432 eV	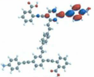 -4.757 eV	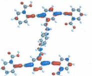 1.188 eV

Figure 6-23. Optimized structures and FMOs of 2D-SH-2A and 2D-SH-2A + 2H$^+$.

average mode approximation, vibronic structure characterized by the C=C stretching mode of the distyrylbenzene bridge is coupled to the electronic transitions.

The determination of the binding constants and the spectra of the intermediates was accomplished by global analysis. These titration spectra reveal that the protonation and coordination with Ag$^+$ is statistical. This means there is no long range through bond interactions. If there is a putative mono-binding species, there should be some build-up of an intermediate over the course of the titration given by eq 6-10.

$$\mathrm{2D-SH-2A + Ag^+ \xrightleftharpoons{K_1} Ag^+ \cdot 2D-SH-2A} \qquad (6\text{-}10a)$$

$$\mathrm{Ag^+ \cdot 2D-SH-2A + Ag^+ \xrightleftharpoons{K_2} 2Ag^+ \cdot 2D-SH-2A} \qquad (6\text{-}10b)$$

The plot of intensity *vs.* concentration at different wavelengths derived from global analysis (Figure 6-24) provides convincing evidence that the protonation or coordination is statistical. The binding constants are summarized in Table 6-4.

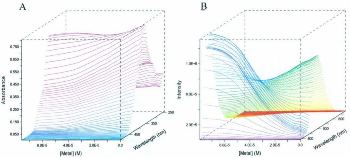

Figure 6-24. (A) Absorption and (B) emission changes of 2D-SH-2A *vs*. the concentration of AgOTf addition at different wavelengths.

Table 6-4. Binding constants (log K_1) of 2D-SH-2A with proton and metal cations in the ground and excited states.

TFA		Ag OTf		Cu (OTf)$_2$	
Ground State	Excited State	Ground State	Excited State	Ground State	Excited State
log K_1	log K_1	log K_1	log K_1	log K_1	log K_1
3.4±0.063	2.7±0.058	9.1±0.046	8. 8±0.088	9.4±0.11	8.9±0.80

6.4 Substituent Effect on H-mers' Ground and Excited States Chemistry

6.4.1 Substituent Effect on One-dimensional π systems

Substituent Effect on Optical Properties. Conjugated oligomers such as the oligo(*p*-phenylenevinylene)s (OPVs), oligo(*p*-phenyleneethynylene)s (OPEs) usually exhibit a monotonous and convergent bathochromic shift of both the absorption and fluorescence with the extension of π-bond by increasing the number of repeat units. However, some π systems with strong donor and strong acceptor groups in the terminal positions (D-π-A) display an opposite behavior: a hypsochromic shift, which is induced upon extending the length of the chromophores (Section 6.2.2). The conjugation effect and the ICT effect are offsetting and the net effect is determined by the electron acceptor properties and the polarizability of the π-bonding network between the donor and acceptor groups. OPE oligomers are somewhat more prone to overall hypsochromic effects than OPV oligomers. A monotonously decreasing $E_{DA}(n)$ value in a series having weak donors or weak acceptors, or both, always exhibit bathochromic shifts (Figure 6-25 A). The decrease of the ICT effect with increasing the number of monomers results in an overall hypsochromic shift (Figure 6-25 B). Alternatively, if the energy of the electronic transition is nearly independent on the conjugation length of the chromophore, the $E_{DA}(n)$ rapidly approaching to E_∞ will lead to the fact that $E_{DA}(n)$ goes through a minimum before it approaches to E_∞ (Figure 6-25 C).

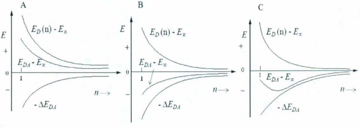

Figure 6-25. Illustration of the offsetting conjugation effect and ICT effect. (A) overall bathochromic effect, (B) overall hypsochromic behavior, (C) hypsochromic convergence after passing through a minimum of $E_{DA}(n)$. Reproduced from ref [59].

Electronic Structure of D-π-A. The D-π-A systems are often described by a valence bond (VB) model, which consists of resonance between an electroneutral and a zwitterionic structure. The "weight" of resonance structures depends on external factors such as the nature of the solvent, the external or internal electrical field, as well as the conjugated π system. Alternatively, the molecular orbital (MO) model contains two partial dipole moments at the terminus of oligomeric assembly. The partial dipole moments $\vec{\mu}_i$ ($i = 1, 2$) consists of an intrinsic and induced dipole. The polar group at the end of chain results in the intrinsic dipole moment, and the dipole moment on the opposite chain end causes the induced part, decreasing upon increasing the number of repeat units. The MO model, which accounts for partial dipole moments best describes D-OPE-A systems. The polarization of the chain depends on the electron density of the π-bond in the assembly is found to decrease from both chain ends to the center.[62]

A VB model was considered to explain D-OPV-A systems as a certain mixture of an electroneutral and a zwitterionic resonance structure for the ground state S_0 and the reversed mixture for the first singlet excited state S_1 (Scheme 6-3). However, ^{13}C NMR measurements are excellent probe for electron density at a carbon center in the ground

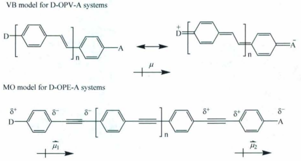

Scheme 6-3. VB model for D-OPV-A systems and MO model for D-OPE-A systems.

state S_0. The change of electron density following an ICT transition has demonstrated that the VB model is suitable for the stilbene (n =1);[62] and the MO model is much better for the longer OPVs (n = 2-4).[68] The energy of the dipolar resonance structure is determined by the charge separation as well as the change in the π system. The longer the chain, the higher the energy for the charge separation in the quinoid form.

6.4.2 Substituent Effect on Two-dimensional π systems

Substituent Effect on H-mers. Electronic conjugation in two-dimensional (2D) settings offers opportunities to fabricate molecules such that the electron density in the bonding and anti-bonding MOs that affects the ground and excited state electronic properties may be synthetically controlled. Therefore, the mixing of localized and delocalized components of the electronic wavefunctions associated with cross-linking can, in principle, be utilized as a probe to assess the conjugation in two-dimensional assemblies. For example, cruciform chromophores as discussed in Chapter 3 display two distinct molecular axes with either similar or dissimilar electronic properties. Attaching donor and/or acceptor substituents to the cruciform at suitable positions can lead to independent electronic shifts of the HOMO and LUMO into opposite directions or delocalized over the entire molecule.[3]

Substituents have a similar effect on H-mers as on the cruciform. HOMO and LUMO of unsubstituted H-mer with a center of symmetry are superimposable, located at the dominant chromophore of distyrylbenzene. Attaching donor groups in terminal phenylethynylenes reduces the symmetry of substituted H-mer, and will impact the energetics of the HOMO and LUMO, as well as the redistribution of the electron density after absorption of a photon. For example, with the HOMO situated on the branch with a donor group and the LUMO on the opposite part of molecule, away from the donor group (Figure 6-26). This molecule will be expected to have a large amount intramolecular charge transfer character upon $S_0 \rightarrow S_1$ excitation.

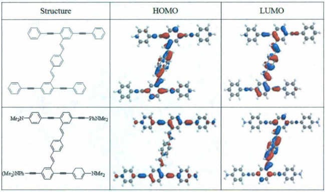

Figure 6-26. FMOs for H-mer and donor substituted H-mer calculated with HF/6-311G(d).

The study on solvent dependence of absorption and emission spectra has confirmed that the HOMO → LUMO transition has a large dipole change upon excitation. The ICT associated with the electronic excitation $S_0 \rightarrow S_1$ leads to a considerable increase in the dipole moments $\vec{\mu}$. With increasing the dielectric constant of the solvent, the emission spectra of donor and acceptor substituted H-mer show a significant red shift, providing evidence for the charge-transfer character of the $S_1 \rightarrow S_0$ radiative transition (Figure 6-27). Unlike the emission spectra, absorption maxima are less sensitive to solvent polarity, indicating a small difference between the dipole moments of the ground and Franck-Condon excited states as the nuclear and solvent coordinates do not change on

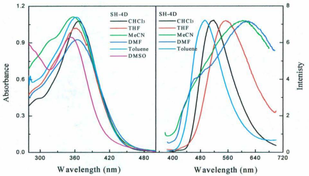

Figure 6-27. Solvent dependence of absorption and emission for donor substituted H-mer at 298±3K.

the time scale of the electronic transition. The Franck-Condon state has the electron configuration of the excited state, but the ground nuclear and solvent coordinates. This suggests that the ICT state originates from the relaxation of the initially formed Franck-Condon excited state.[69,70] In addition, relatively longer lifetime in comparison with unsubstituted H-mer reveals that there is a poor overlap between the HOMO and LUMO.

6.5 Conjugation Length Effect on H-mers' Ground and Excited States Chemistry

Introduction of donor and acceptor into the conjugated π systems usually results in a dramatic red shift of both the absorption and fluorescence due to the ICT. However, when the conjugation length increases (increasing the number of repeat units, n), donor and/or acceptor substituted long H-mers (LH) displays a blue shift in the fluorescence spectra in comparison with the fluorescence observed for the short H-mers. The structures of substituted long H-mers used to investigate the impact of conjugation length are shown in Scheme 6-4. The respective absorption and emission spectra are displayed in Figure

6-28, with detailed optical properties data summarized in Table 6-4.

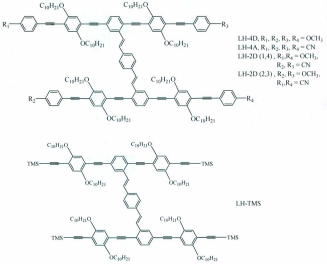
C10H21O
C10H21O
R1
R3
OC10H21
OC10H21
C10H21O
C10H21O
R2
R4
OC10H21
OC10H21
C10H21O
C10H21O
TMS
TMS
OC10H21
OC10H21
LH-TMS
C10H21O
C10H21O
TMS
TMS
OC10H21
OC10H21

LH-4D, R_1, R_2, R_3, R_4 = OCH_3
LH-4A, R_1, R_2, R_3, R_4 = CN
LH-2D (1,4) , R_1,R_4 = OCH_3,
R_2, R_3 = CN
LH-2D (2,3) , R_2, R_3 = OCH_3,
R_1,R_4 = CN

Scheme 6-4. Structure of donor and/or acceptor substituted long H-mers.

Table 6-4. Photophysical data for donor and/or acceptor substituted LH measured in $CHCl_3$ at 298±3K.

Entry	$\lambda_{abs}^{S_0\rightarrow S_1}$(nm) ε ($\times10^4$ $M^{-1}cm^{-1}$)	$E_{op}^{S_0\rightarrow S_1}$ (cm^{-1})	$\lambda_{em}^{S_1\rightarrow S_0}$ (nm)	$E_{em}^{S_1\rightarrow S_0}$ (cm^{-1})	$\lambda_{t,}$ cm^{-1}	$\phi_F^{S_1\rightarrow S_0}$	τ_F, ns (k_d, s^{-1})
LH-TMS	324 (0.28) 376 (0.46)	30,860 26,595	439 465	22,780 21,560	1908	0.54	2.0 (5.0×10^8) 2.0 (5.0×10^8)
LH-4D	325 (6.5) 386 (11)	30,700 25,910	450 480(sh)	22,220 20,830	1845	0.52	1.6 (6.0×10^8) 1.8 (5.5×10^8)
LH-4A	322(6.7) 397 (11)	31,060 25,190	450 480(sh)	22,220 20,830	1490	0.72	1.3(7.7×10^8) 1.3(7.7×10^8)
LH-2D(2,3)	326 (1.9) 395 (3.2)	30,670 25,580	450 480(sh)	22,220 20,830	1580	0.70	1.3(7.7×10^8) 1.3(7.7×10^8)
LH-2D(1,4)	323 (1.0) 391(1.6)	30,960 25,280	450 488 (sh)	22,220 20,490	1530	0.62	1.5 (7.0×10^8) 1.5 (7.0×10^8)

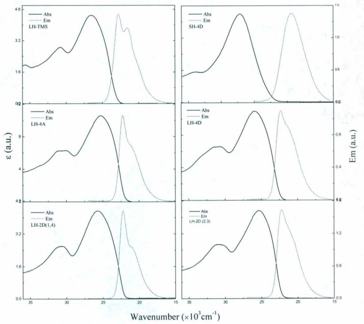

Figure 6-28. Absorption and emission spectra of substituted LH in comparison with substituted SH, measured in $CHCl_3$ at 298±3K.

It is apparent that the effect of the ICT on the transition energies of H-mers is significantly reduced with the extension of the conjugation length of the OPE branch. The Stokes shifts of all substituted LH are much smaller than those of substituted SH, which indicates that the distortion between the first excited state and the ground state is relatively constant in comparison with SH. All substituted LH have the same profile for both absorption and emission, which is similar to those observed for analogous substituted stilbenes and dialkoxy-substituted oligo (*p*-phenyleneethynylene).[71-73]

Conjugation Length Effect on One-Dimensional D-OPE-A Systems. As discussed in Chapter 3, conjugation effect and ICT effect are offsetting effects with increasing the repeating unit n. These donor and acceptor effects are best described by MO model having partial dipole moments located at the terminal groups at each end of the oligomer. The electronic polarization of a π-conjugated oligomer containing polarizable C≡C triple bonds decreases from the termini to the central point of the oligomer. The polarization of OPE (n = 2) approaches to maximum at the chain ends. A further increase in the distance between D and A will result in fairly constant charge distributions in both terminal double bonds and very small effects for the inner double bonds.[68] Moreover, with increasing the conjugation length, other π orbitals approach the π (HOMO) and other π* orbitals approach π* (LUMO). The HOMO → LUMO transition is combined with a large ICT, but the participation of the HOMO → LUMO transition decreases in the electronic excitation. "For example, in $Me_2N-(PE)_n-NO_2$ series, the $S_0 \rightarrow S_1$ transition consists 67% of an electron excitation from the HOMO to the LUMO with n =1. This transition is connected with a strong ICT from the donor side to the acceptor side. On proceeding to longer chromophores, the participation of the HOMO→ LUMO transition for $S_0 \rightarrow S_1$ decreases and approaches 7% for n = 4. The other fractions, HOMO -1 → LUMO, HOMO → LUMO -1, and HOMO -1 → LUMO -1, have either a small ICT or no ICT at all.[62]

Conjugation Length Effect on Two-dimensional H-mer Systems. From electronic spectral data, it is obvious that donor and acceptor groups do not have any influence on the emission spectra of substituted LH, all of which have the same emission energy, and similar lifetime, quantum yield. Emission spectral analyses (as described in Chapter 2) indicate that solvent reorganization energies in LH system are much smaller than those of substituted SH systems. The spectral fitting parameters E_0, S and $\Delta\bar{\nu}_{1/2}$ with $\hbar\omega$ = 1350cm^{-1} are listed in Table 6-5. S and $\hbar\omega$ are the average values for contributions from a series of stretching modes mainly C=C and C≡C in character. The studies of photophysical properties of substituted LH series together with SH series reveal that the long-range interaction decrease significantly with increasing the distance between donor and acceptor. Therefore, the ICT effect is significantly attenuated with going from

Table 6-5. Emission spectral fitting data for donor and/or acceptor substituted LH.[2]

Entry	LH-TMS	LH-4D	LH-4A	LH-2D(2,3)	LH-2D(1,4)
E_{em}, cm^{-1}	22,780 21,510	22,220 20,880	22,220 20,830	22,220 20,830	22,220 20,490
E_0, cm^{-1}	23,100	22,135	22,154	22,090	22,160
S_m	1.40	1.30	0.90	1.29	1.25
S_l	1.20				1.00
$\Delta\nu_{1/2}$, cm^{-1}	1165	1573	1224	1470	1198
$\hbar\omega$, cm^{-1}	1550	1620	1350	1550	1400
E_{abs} -E_{em} , cm^{-1}	3815	3690	2980	3160	3060
λ_t , cm^{-1}	1908	1855	1445	1640	1690
λ_{vib} , cm^{-1}	2170	2106	1215	2000	1750
λ_o , cm^{-1}	266	1078	653	941	625
ln[(Fcalc)]	-30.73	-27.97	-40.07	-29.44	-35.29
γ	1.38	1.35	1.90	1.40	1.68

---

[2] Calculated by using eqs 3-8, 3-9, 3-10, 3-11, 3-14.

the repeating unit n = 2 to n = 4. Further evidence to support the decreased ICT effect is the studies on the solvent dependence of emission spectra and metal cation titration.

Solvent effect studies of substituted LH, as shown in Figure 6-29, indicate that optical spectra show no response with varying the dielectric constant of the solvent. This is in agreement with the conclusion that the participation of the ICT approaches zero with increasing the conjugation length.

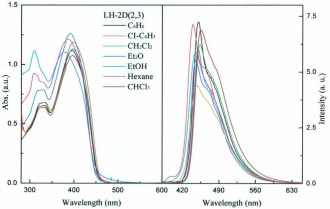

Figure 6-29. Solvent effect on optical properties of LH-2D (2, 3).

Upon titration with AgOTf, only LH-TMS interacts with a silver cation (Figure 6-30). With addition of AgOTf, the intensity of emission diminishes with a loss of vibronic fine structure. The absorption intensity decreases relatively slow associated with a red shift. The absorption spectrum of AgOTf titration displays one isosbestic point, but the reaction mechanism is not clear.

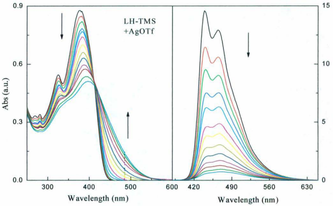

Figure 6-30. Absorption and emission spectral changes with AgOTf titration in $CHCl_3$ at 298±3K.

6.6 Conclusions.

1. For LH systems, E_0 is independent on the donor/acceptor substituents.
2. The H-mers containing NR_2 groups possess ICT bands from amino group to phenyl group and π-π* bands localized on the distyrylbenzene bridge.
3. The H-mers which contain NR_2 groups react with TFA, AgOTf, $Cu(OTf)_2$. The equilibrium constants for the ground and excited states have been measured, with the binding constants K_1 and K_2 following the order: $H^+ < Ag^+ < Cu^{2+}$. The binding constants for H^+ are enormously small when compared with the binding constants for Ag^+ and Cu^{2+}.
4. The substituents on the H-mers do not dramatically change the absorption and emission energetics. This behavior would be expected where the chromophore is localized on the distyrylbenzene bridge.
5. The distyrylbenzene bridge does not provide an electronic pathway for OPE end units.

6.5 References

(1) Ranyuk, E.; Douaihy, C. M.; Bessmertnykh, A.; Denat, F.; Averin, A.; Beletskaya, I.; Guilard, R. *Org. Lett.* **2009**, *11*, 987-990.

(2) Ryu, S.; Yoo, I.; Song, S.; Yoon, B.; Kim, J.-M. *J. Am. Chem. Soc.* **2009**, *131*, 3800-3801.

(3) Zucchero, A. J.; Wilson, J. N.; Bunz, U. H. F. *J. Am. Chem. Soc.* **2006**, *128*, 11872-11881.

(4) Wang, J.; Qian, X. *Org. Lett.* **2006**, *8*, 3721-3724.

(5) Li, J.; Kendig, C. E.; Nesterov, E. E. *J. Am. Chem. Soc.* **2007**, *129*, 15911-15918.

(6) Beer, P. D.; Cadman, J. *Coord. Chem. Rev.* **2000**, *205*, 131-155.

(7) de Silva, A. P.; Gunaratne, H. Q. N.; Gunnlaugsson, T.; Huxley, A. J. M.; McCoy, C. P.; Rademacher, J. T.; Rice, T. E. *Chem. Rev.* **1997**, *97*, 1515-1566.

(8) Huang, H.; Wang, K.; W.Tan; An, D.; Yang, X.; Huang, S.; Zhai, Q.; Zhou, L.; Jin, Y. *Angew. Chem. Int. Ed.* **2004**, *43*, 5635-5638.

(9) Liu, Z.-Q.; Shi, M.; Li, F.-Y.; Fang, Q.; Chen, Z.-H.; Yi, T.; Huang, C.-H. *Org. Lett.* **2005**, *7*, 5481-5484.

(10) Liu, Y.; Han, M.; Zhang, H.-Y.; Yang, L.-X.; Jiang, W. *Org. Lett.* **2008**, *10*, 2873-2876.

(11) Miao, Q.; Huang, X. B.; Cheng, Y. Q.; Liu, Y.; Zong, L. L.; Cheng, Y. X. *J. Appl. Poly. Sci.* **2009**, *111*, 3137-3143.

(12) Yang, J.-S.; Lin, C.-K.; Lahoti, A. M.; Tseng, C.-K.; Liu, Y.-H.; Lee, G.-H.; Peng, S.-M. *J. Phys. Chem. A* **2009**, *113*, 4868-4877.

(13) Valeur, B.; Leray, I. *Coord. Chem. Rev.* **2000**, *205*, 3-40.

(14) Yang, J.-S.; Lin, C.-S.; Hwang, C.-Y. *Org. Lett.* **2001**, *3*, 889-892.

(15) Kim, S. K.; Lee, S. H.; Lee, J. Y.; Lee, J. Y.; Bartsch, R. A.; Kim, J. S. *J. Am. Chem. Soc.* **2004**, *126*, 16499-16506.

(16) Sancenón, F.; Descalzo, A. B.; Martínez-Máñez, R.; Miranda, M. A.; Soto, J. *Angew. Chem. Int. Ed.* **2001**, *40*, 2640-2643.

(17) Sancenón, F.; Martínez-Máñez, R.; Miranda, M. A.; Seguí, M.-J.; Soto, J. *Angew. Chem. Int. Ed.* **2003**, *42*, 647-650.

(18) Jimenez, D.; Martinez-Manez, R.; Sancenon, F.; Ros-Lis, J. V.; Benito, A.; Soto, J. *J. Am. Chem.*

Soc. **2003**, *125*, 9000-9001.

(19) Lee, K.-S.; Kim, H.-J.; Kim, G.-H.; Shin, I.; Hong, J.-I. *Org. Lett.* **2008**, *10*, 49-51.

(20) Kim, S. Y.; Hong, J.-I. *Org. Lett.* **2007**, *9*, 3109-3112.

(21) Wu, J.-S.; Hwang, I.-C.; Kim, K. S.; Kim, J. S. *Org. Lett.* **2007**, *9*, 907-910.

(22) Pond, S. J. K.; Tsutsumi, O.; Rumi, M.; Kwon, O.; Zojer, E.; Brédas, J. L.; Marder, S. R.; Perry, J. W. *J. Am. Chem. Soc.* **2004**, *126*, 9291-9306.

(23) Kim, J. S.; Shon, O. J.; Lee, J. K.; Lee, S. H.; Kim, J. Y.; Park, K.-M.; Lee, S. S. *J. Org. Chem.* **2002**, *67*, 1372-1375.

(24) Kim, J. S.; Shon, O. J.; Rim, J. A.; Kim, S. K.; Yoon, J. *J. Org. Chem.* **2002**, *67*, 2348-2351.

(25) Kim, J. S.; Shon, O. J.; Yang, S. H.; Kim, J. Y.; Kim, M. J. *J. Org. Chem.* **2002**, *67*, 6514-6518.

(26) Li, C.-K.; Lu, X.-X.; Wong, K. M.-C.; Chan, C.-L.; Zhu, N.; Yam, V. W.-W. *Inorg. Chem.* **2004**, *43*, 7421-7430.

(27) Lodeiro, C.; Pina, F. *Coord. Chem. Rev.* **2009**, *253*, 1353-1383.

(28) Aoki, S.; Kagata, D.; Shiro, M.; Takeda, K.; Kimura, E. *J. Am. Chem. Soc.* **2004**, *126*, 13377-13390.

(29) Wu, Z.; Zhang, Y.; Ma, J. S.; Yang, G. *Inorg. Chem.* **2006**, *45*, 3140-3142.

(30) Ryu, D.; Park, E.; Kim, D.-S.; Yan, S.; Lee, J. Y.; Chang, B.-Y.; Ahn, K. H. *J. Am. Chem. Soc.* **2008**, *130*, 2394-2395.

(31) Lee, C.-H.; Na, H.-K.; Yoon, D.-W.; Won, D.-H.; Cho, W.-S.; Lynch, V. M.; Shevchuk, S. V.; Sessler, J. L. *J. Am. Chem. Soc.* **2003**, *125*, 7301-7306.

(32) Kim, S. K.; Singh, N. J.; Kim, S. J.; Kim, H. G.; Kim, J. K.; Lee, J. W.; Kim, K. S.; Yoon, J. *Org. Lett.* **2003**, *5*, 2083-2086.

(33) Gale, P. A. *Acc. Chem. Res.* **2006**, *39*, 465-475.

(34) Kwon, J. Y.; Singh, N. J.; Kim, H. N.; Kim, S. K.; Kim, K. S.; Yoon, J. *J. Am. Chem. Soc.* **2004**, *126*, 8892-8893.

(35) Kim, S. K.; Lee, D. H.; Hong, J.-I.; Yoon, J. *Acc. Chem. Res.* **2009**, *42*, 23-31.

(36) Suksai, C.; Tuntulani, T. *Chem. Soc. Rev.* **2005**, *32*, 192-202.

(37) Amendola, V.; Fabbrizzi, L.; Mangano, C.; Pallavicini, P.; Poggi, A.; Taglietti, A. *Coord. Chem.*

Rev. **2001**, *219-221*, 821-837.

(38) Fabbrizzi, L.; Licchelli, M.; Rabaioli, G.; Taglietti, A. *Coord. Chem. Rev.* **2000**, *205*, 85-108.

(39) Lee, D. H.; Lee, K. H.; Hong, J.-I. *Org. Lett.* **2001**, *3*, 5-8.

(40) Ko, S.-K.; Yang, Y.-K.; Tae, J.; Shin, I. *J. Am. Chem. Soc.* **2006**, *128*, 14150-14155.

(41) Zhou, Q.; Swager, T. M. *J. Am. Chem. Soc.* **1995**, *117*, 7017-7018.

(42) Zhou, Q.; Swager, T. M. *J. Am. Chem. Soc.* **1995**, *117*, 12593-12602.

(43) Thomas, S. W.; Joly, G. D.; Swager, T. M. *Chem. Rev.* **2007**, *107*, 1339-1386.

(44) Li, H.; Valiyaveettil, S. *Macromolecules* **2007**, *40*, 6057-6066.

(45) Opsitnick, E.; Lee, D. *Chem. Eur. J.* **2007**, *13*, 7040-7049.

(46) Yang, J.-S.; Huang, H.-H.; Ho, J.-H. *J. Phys. Chem. B* **2008**, *112*, 8871-8878.

(47) Jiang, X.; Bollinger, J. C.; Lee, D. *J. Am. Chem. Soc.* **2006**, *128*, 11732-11733.

(48) McGrier, P. L.; Solntsev, K. M.; Miao, S.; Tolbert, L. M.; Miranda, O. R.; Rotello, V. M.; Bunz, U. H. F. *Chem. Eur. J.* **2008**, *14*, 4503- 4510.

(49) Swager, T. M. *Acc. Chem. Res.* **2008**, *41*, 1181-1189.

(50) Bangcuyo, C. G.; Rampey-Vaughn, M. E.; Quan, L. T.; Angel, S. M.; Smith, M. D.; Bunz, U. H. F. *Macromolecules* **2002**, *35*, 1563-1568.

(51) Tolosa, J.; Zucchero, A. J.; Bunz, U. H. F. *J. Am. Chem. Soc.* **2008**, *130*, 6498-6506.

(52) Wilson, J. N.; Bunz, U. H. F. *J. Am. Chem. Soc.* **2005**, *127*, 4124-4125.

(53) Yang, J.-S.; Swager, T. M. *J. Am. Chem. Soc.* **1998**, *120*, 11864-11873.

(54) Marshall, A. R.; Bunz, U. H. F. *Macromolecules* **2001**, *34*, 4688-4690.

(55) Weder, C.; Sarwa, C.; Montali, A.; Bastiaansen, C.; Smith, P. *Science* **1998**, *279*, 835-837.

(56) Yamaguchi, Y.; Tanaka, T.; Kobayashi, S.; Wakamiya, T.; Matsubara, Y.; Yoshida, Z. *J. Am. Chem. Soc.* **2005**, *127*, 9332-9333.

(57) Santhanamoorthi, N.; Senthilkumar, K.; Kolandaivel, P. *Molecular Phys.* **2009**, *107*, 1629 -1639.

(58) Levitus, M.; Schmieder, K.; Ricks, H.; Shimizu, K. D.; Bunz, U. H. F.; Garcia-Garibay, M. A. *J. Am. Chem. Soc.* **2001**, *123*, 4259-4265.

(59) Meier, H. *Angew. Chem. Int. Ed.* **2005**, *44*, 2482-2506.

(60) Koopmans, T. *Physica* **1933**, *1*, 104-113.

(61) Meier, H.; Gerold, J.; Kolshorn, H.; Baumann, W.; M. Bletz *Angew. Chem. Int. Ed.* **2002**, *41*, 292-295.

(62) Meier, H.; Mühling, B.; Kolshorn, H. *Eur. J. Org. Chem.* **2004**, 1033-1042.

(63) Lewis, G. N.; Calvin, M. *Chem. Rev.* **1939**, *39*, 273 – 328.

(64) Bubiltz, G. U.; Oritz, R.; Marder, S. R.; Boxer, S. G. *J. Am. Chem. Soc.* **1997**, *119*, 3365-3376.

(65) Krygowski, T. M.; Stepien, B. T. *Chem. Rev.* **2005**, *105*, 3482-3512.

(66) Gosztola, D.; Yamada, H.; Wasielewski, M. R. *J. Am. Chem. Soc.* **1995**, *117*, 2041-2048.

(67) Nakayama, H.; Morita, T.; Kimura, S. *Phys. Chem. Chem. Phys.* **2009**, *11*, 3967-3976.

(68) Meier, H.; Gerold, J.; Kolshorn, H.; Muhling, B. *Chem. Eur. J.* **2004**, *10*, 360-370.

(69) Woo, H. Y.; Liu, B.; Kohler, B.; Korystov, D.; Mikhailovsky, A.; Bazan, G. C. *J. Am. Chem. Soc.* **2005**, *127*, 14721-14729.

(70) Huang, F.; Tian, Y.; Chen, C.-Y.; Cheng, Y.-J.; Young, A. C.; Jen, A. K.-Y. *J. Phys. Chem. C* **2007**, *111*, 10673-10681.

(71) Stalmach, U.; Detert, H.; Meier, H.; Gebhardt, V.; Haarer, D.; Bather, A.; Schmidt, H. W. *Optical Materials* **1998**, *9*, 77-81.

(72) Stalrnach, U.; Kolshorn, H.; Brehm, I.; Meier, H. *Liebigs Ann* **1996**, 1449-1456.

(73) Meier, H.; Ickenroth, D.; Stalmach, U.; Koynov, K.; Bahtiar, A.; Bubeck, C. *Eur. J. Org. Chem.* **2001**, 4431-4443.

Chapter 7

Summary and Important Issues to be Addressed

7.1 Executive Summaries

Three main structural geometries for π-conjugated OPV/OPE oligomers investigated in this work are shown in Scheme 3-1. These structures are designed such that the OPV serves both as the primary chromophore and as the structural backbone. The structures studied included: a linear π-framework, *i.e.* **SL**, which is symmetrically substituted at the 4, 4` positions of the styrene substituents; and the isomeric cruciform, *i.e.* **SC**, where the molecular array may be synthetically elaborated in two directions or "dimensions" by introducing substituents into the 2 and 5 positions of the central phenyl ring of the OPV; and H-mers which have the substituents at 2, 5 positions of the terminal phenyl rings. The modular synthetic methodologies employed here allow the systematic variation of the structural component in the {R-(π-B$_L$)$_n$-[OPV]$_{C/L}$-(π-B$_L$)$_n$ -R} assembly. The synthetic control in these systems allowed the creation of a family of closely related assemblies from which correlations between the structure and electronic properties were derived. Described below are the conclusions from the steady-state and time-resolved absorption, emission experiments as well as the analysis of the data from absorption and emission spectral fitting, DFT and TD-DFT calculation. Taken together the vibronic, electronic structure and topological parameters that govern the energetics and intensities of absorption and emission bands and reaction dynamics in the π-conjugated OPV/OPE systems, the major conclusions described in each chapter are outlined in point form below.

7.1.1 Ground and Excited State Properties of π Systems

Detailed analysis of the absorption and emission spectra for the cruciform (**SC**), linear (**SL**), and H-mer (**SH**) has been performed and the data show the following trends.

1. The absorption spectral manifolds arise due to a superposition of underlying $\pi \rightarrow \pi^*$ transitions that are best described as composite multi-electronic donor and acceptor states.
2. Spectral deconvolution of **SL** and **SC** coupled with TD-DFT calculations revealed that the pattern of transitions and the orbital contribution for each transition observed for **SC**, **SL** and **SH** were similar in energy, but the intensities of the underlying absorption bands were dependent on the placement and the nature of the OPE "substituent".
3. The absorption bands are broadened due to a distribution of rotamers in the ground state characterized by small kinetic barriers for rotation estimated at 10 KJ/mol based on similar systems described by Berg.[1,2] The asymmetry between the absorption and the emission spectra are consistent with the quadratic coupling model of Berg, where the electronic coupling depended on the torsion angle as illustrated in Chapter 3.
4. The results of the Franck-Condon line shape analysis of the emission spectra (emission spectral fitting) :
   - S_m (Huang Rhys Factor), a dimensionless parameter reflecting λ_i, systematically

decreases as more OPE monomers are introduced to lengthen the bridge. Extension of the bridge allows a mechanism where Δq and electron repulsion are minimized.

- With OPE incorporated $\hbar\omega$ increases due to the participation of C≡C vibrational modes in the excited state decay. This is an important observation because in the one mode limit the excited state is extended over several nuclear coordinates.
- The electron redistribution in the excited state does not dramatically change the dipole moments $\Delta\vec{\mu}$. Therefore, the solvent reorganization energetics is roughly constant in each structurally related family. At present, there is not enough data to assess the validity of dielectric continuum theory.
- **SL** and **LL** appear to be weakly coupled in the ground state based on the similar shape and energetics of the spectral band envelopes of the assemblies. The spectra of **SC** and **LC** are distinct from the components' spectra; therefore, the cruciform systems are strongly coupled systems. However, the C_{60} and the π-bridge in the C_{60} adducts are weakly coupled.

7.1.2 Photoinduced ET and EnT in π-Bridged C_{60} Assemblies

The mechanism for the charge separation occurs in two-steps. The first step is the energy transfer from the $^1(\pi\text{-B})^*$ to $^1C_{60}^*$, followed by the electron transfer to quench $^1C_{60}^*$ and form the redox split state.

1. The charge separation ($\Delta G^o/\lambda \sim 1$ - 2) and charge recombination ($\Delta G^o/\lambda \sim 8$ - 10) for short bridged systems SC-$(C_{60})_2$ and SL-$(C_{60})_2$ lie in the inverted region, but the

charge recombination is more deeply down to the inverted region. Therefore, the rate constant for charge recombination is much smaller than the forward charge separation. The sensitivity of ET to bridge length is consistent with the superexchange mechanism being the dominant mode for the D-A electronic coupling.

2. The long bridged systems LC-$(C_{60})_2$ and LL-$(C_{60})_2$ do not yield a charge separation state after photon capture, which is due to an attenuation of $\hat{H}_{DA}$ with increasing the donor-acceptor separation distance.
3. Due to the orientation effect, the charge separation in SL-$(C_{60})_2$ is less efficient than in SC-$(C_{60})_2$.
4. The introduction of *N, N*-diphenylamino groups to distyrylbenzene significantly increases the energy gap between the donor and the bridge, and then attenuates the electronic coupling term V_{DA}. The efficiency of charge separation is reduced with the attenuated electronic coupling. In addition, the kinetic competition between the charge separation and intersystem crossing is favorable for the formation of $^3C_{60}^*$.
5. The reorganization energy of DSC/DLC-$(C_{60})_2$ is much larger than that of SC/LC-$(C_{60})_2$ due to the primary excitation having a large degree of charge transfer character. Therefore, the rate constants for charge separation and charge recombination are very close to each other.

7.2 Future Directions and Questions:

1. Understanding how the physical and spectroscopic properties of π-conjugated oligomers depend on the length and medium. Detailed solvent studies coupled to ultrafast spectroscopic measurements will be important to assess the solvent dynamics.

2. For multi-dimensional polymers, what governs the efficiency of intra *vs.* inter charge carrier dynamics? How does the nature of the matrix impact charge transfer properties. Extended spectroscopic studies on the effect of concentration in the fluid solution, inert non-conducting rigid films and finally conductive films of the OPV/OPE need to be considered.

3. Vibronic /rotational dynamics:

   - Stark experiments will provide the information of the charge transfer distance. If the systems are truly electronically delocalized, the excited state transition dipole should be larger in magnitude. Similar studies in the nano-scale dye-sensitized TiO_2 systems[3,4] have definitely shown that the electron injection site is localized on one metal center. These studies should be extended to π-conjugated assemblies as a function of length and dimensionality to assess the nature of the optically induced absorption transition and characterize the response of the bound exciton to external applied electric field.

   - Raman and resonance Raman studies need to be done to identify the vibrational modes coupled to the LUMO-HOMO transition. These studies need to be extended to systems where the length is systematically increased. The resonance Raman data provide spectroscopic information that can be subjected to the time dependent intensity analysis as described by Woodruff and Myers-Kelley.[5] The analysis allows the direct determination of the absolute bond distortions whose vibrational modes are coupled directly to the optical excitation between the ground and excited states. If the systems are delocalized, Δq will decrease with the increasing polymer chain length. Using the model of Meier[6,7] where the main transition energy asymptotically approaches a limiting value after 10 repeating units calls to the validity of the question of delocalization *vs*. the charge transfer degree in the polymers. The distortion of the bonds will respond differently to the mechanisms described above where the delocalization will give rise to the systematic decrease in Δq.

7.3 Reference:

(1) Liu, L. T.; Yaron, D.; Sluch, M. I.; Berg, M. A. *J. Phys. Chem. B* **2006**, *110*, 18844-18852.

(2) Liu, L. T.; Yaron, D.; Berg, M. A. *J. Phys. Chem. C* **2007**, *111*, 5770-5782.

(3) Khoudiakov, M.; Parise, A. R.; Brunschwig, B. S. *J. Am. Chem. Soc.* **2003**, *125*, 4637-4642.

(4) Harris, J. A.; Trotter, K.; Brunschwig, B. S. *J. Phys. Chem. B* **2007**, *111*, 6695-6702.

(5) Barbara, P. F.; Meyer, T. J.; Ratner, M. A. *J. Phys. Chem.* **1996**, *100*, 13148-13168.

(6) Meier, H.; Mühling, B.; Kolshorn, H. *Eur. J. Org. Chem.* **2004**, 1033-1042.

(7) Meier, H.; Gerold, J.; Kolshorn, H.; Muhling, B. *Chem. Eur. J.* **2004**, *10*, 360-370.

Contents

I. **Emission Spectral Fitting Data**

II. **Gaussian Deconvolution**

III. **Global Analyses**

IV. **Time-resolved Fluorescence**

I. Emission Spectral Fitting

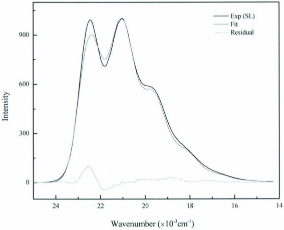

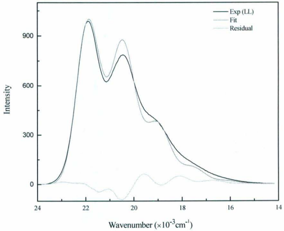

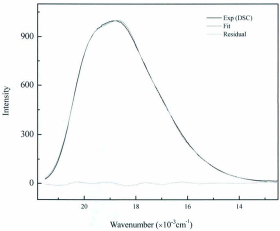
Exp (DSC)
Fit
Residual
Intensity
900
600
300
0
20
18
16
14
Wavenumber ($\times 10^{-3}$cm^{-1})

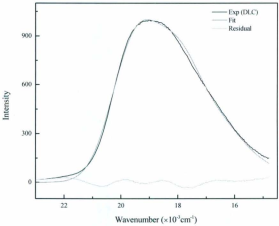
Exp (DLC)
Fit
Residual
Intensity
900
600
300
0
22
20
18
16
Wavenumber ($\times 10^{-3}$cm^{-1})

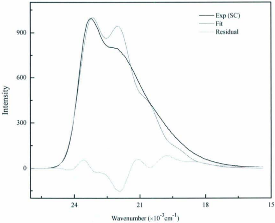
Exp (SC)
Fit
Residual
Intensity
900
600
300
0
24
21
18
15
Wavenumber ($\times10^{-3}$cm^{-1})

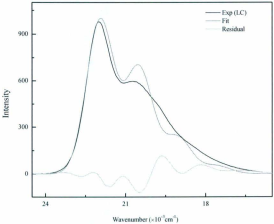
Exp (LC)
Fit
Residual
Intensity
900
600
300
0
24
21
18
Wavenumber ($\times10^{-3}$cm^{-1})

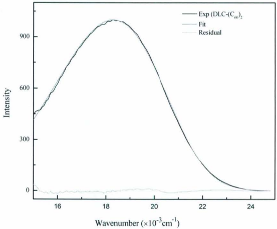
Exp (DLC-(C_{60})$_2$
Fit
Residual
Intensity
900
600
300
0
16
18
20
22
24
Wavenumber ($\times10^{-3}$cm^{-1})

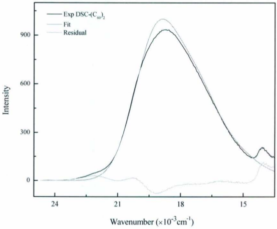
Exp DSC-(C_{60})$_2$
Fit
Residual
Intensity
900
600
300
0
24
21
18
15
Wavenumber ($\times10^{-3}$cm^{-1})

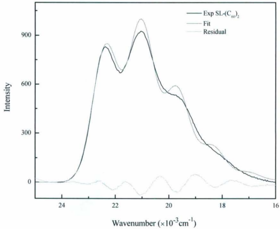
Exp SL-$(C_{60})_2$
Fit
Residual
Intensity
900
600
300
0
24
22
20
18
16
Wavenumber ($\times 10^{-3}$cm^{-1})

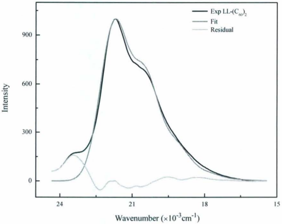
Exp LL-$(C_{60})_2$
Fit
Residual
Intensity
900
600
300
0
24
21
18
15
Wavenumber ($\times 10^{-3}$cm^{-1})

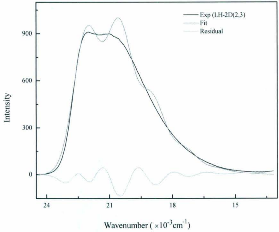
Exp (LH-2D(2,3)
Fit
Residual
Intensity
900
600
300
0
24
21
18
15
Wavenumber ($\times 10^{-3}$cm^{-1})

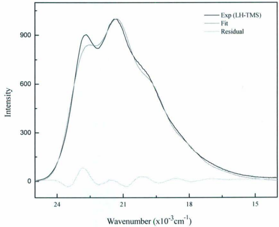
Exp (LH-TMS)
Fit
Residual
Intensity
900
600
300
0
24
21
18
15
Wavenumber (x10^{-3}cm^{-1})

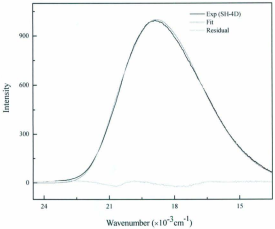
Exp (SH-4D)
Fit
Residual
Intensity
900
600
300
0
24
21
18
15
Wavenumber ($\times 10^{-3}$cm^{-1})

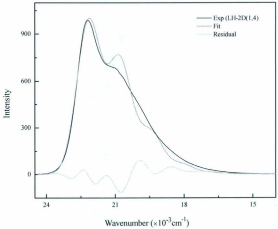
Exp (LH-2D(1,4)
Fit
Residual
Intensity
900
600
300
0
24
21
18
15
Wavenumber ($\times 10^{-3}$cm^{-1})

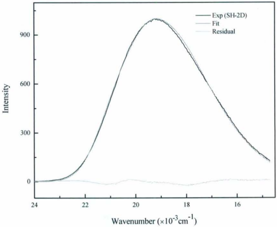
Exp (SH-2D)
Fit
Residual
Intensity
900
600
300
0
24
22
20
18
16
Wavenumber ($\times10^{-3}$cm^{-1})

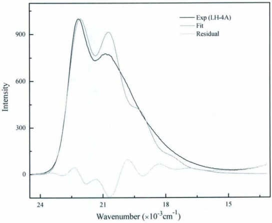
Exp (LH-4A)
Fit
Residual
Intensity
900
600
300
0
24
21
18
15
Wavenumber ($\times10^{-3}$cm^{-1})

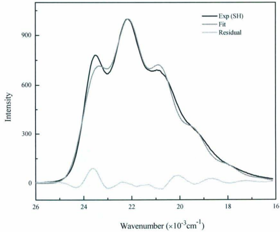
Exp (SH)
Fit
Residual
Intensity
900
600
300
0
26
24
22
20
18
16
Wavenumber ($\times 10^{-3}$cm^{-1})

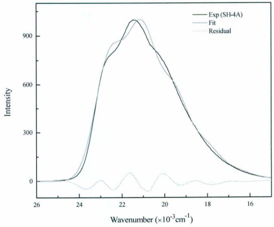
Exp (SH-4A)
Fit
Residual
Intensity
900
600
300
0
26
24
22
20
18
16
Wavenumber ($\times 10^{-3}$cm^{-1})

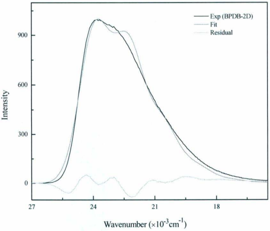
Exp (BPDB-2D)
Fit
Residual
Intensity
0
300
600
900
27
24
21
18
Wavenumber ($\times10^{-3}$cm^{-1})

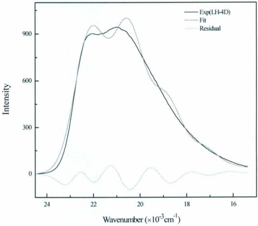
Exp(LH-4D)
Fit
Residual
Intensity
0
300
600
900
24
22
20
18
16
Wavenumber ($\times10^{-3}$cm^{-1})

Gaussian Deconvolution

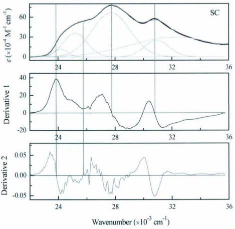

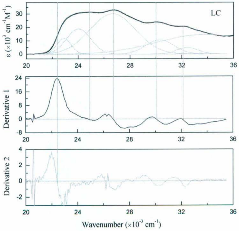

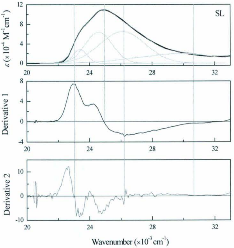
SL
ε (×10⁻⁴ M⁻¹cm⁻¹)
Derivative 1
Derivative 2
12
8
4
0
-4
10
-10
20
24
28
32
Wavenumber (×10⁻³ cm⁻¹)

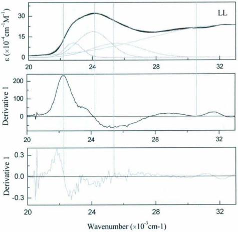
LL
ε (×10⁻⁴cm⁻¹M⁻¹)
Derivative 1
Derivative 1
30
15
0
200
100
0.3
0.0
-0.3
20
24
28
32
Wavenumber (×10⁻³cm-1)

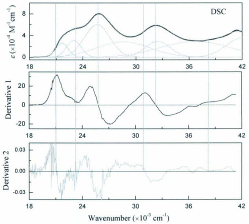
DSC
ε ($\times 10^{-4}$ M^{-1}cm^{-1})
8
4
0
18
24
30
36
42
Derivative 1
20
0
-20
Derivative 2
0.03
0.00
-0.03
Wavenumber ($\times 10^{-3}$ cm^{-1})

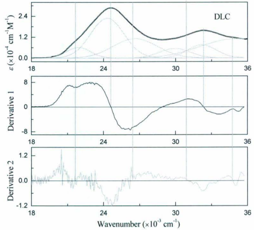
DLC
ε ($\times 10^{-4}$ cm^{-1}M^{-1})
2.4
1.2
0.0
18
24
30
36
Derivative 1
8
0
-8
Derivative 2
1.2
0.0
-1.2
Wavenumber ($\times 10^{-3}$ cm^{-1})

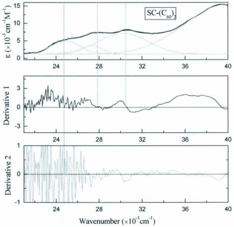
SC-$(C_{60})_2$
ε (×10^{-3}cm^{-1}M^{-1})
15
10
5
0
24
28
32
36
40
Derivative 1
3
0
-3
24
28
32
36
40
Derivative 2
1
0
-1
24
28
32
36
40
Wavenumber (×10^{-3}cm^{-1})

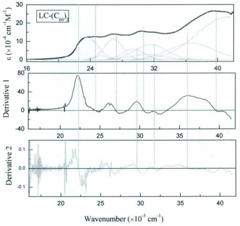
LC-$(C_{60})_2$
ε (×10^{-4} cm^{-1}M^{-1})
30
20
10
0
16
24
32
40
Derivative 1
80
40
0
-40
20
25
30
35
40
Derivative 2
0.1
0.0
-0.1
20
25
30
35
40
Wavenumber (×10^{-3} cm^{-1})

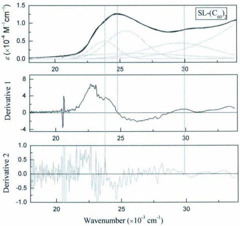
SL-$(C_{60})_2$
ε ($\times10^{-4}$ $M^{-1}cm^{-1}$)
1.5
1.0
0.5
0.0
Derivative 1
8
4
0
-4
Derivative 2
1.0
0.5
0.0
-0.5
-1.0
20
25
30
Wavenumber ($\times10^{-3}$ cm^{-1})

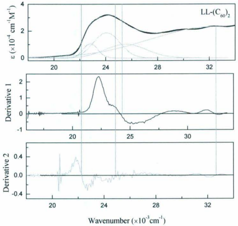
LL-$(C_{60})_2$
ε ($\times10^{-4}$ $cm^{-1}M^{-1}$)
4
2
0
20
24
28
32
Derivative 1
2
1
0
-1
20
25
30
Derivative 2
0.4
0.0
-0.4
20
24
28
32
Wavenumber ($\times10^{-3}cm^{-1}$)

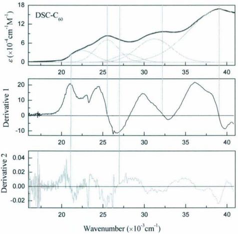
DSC-C_{60}
$\varepsilon (\times 10^{-4} cm^{-1}M^{-1})$
18
12
6
0
20
25
30
35
40
Derivative 1
20
10
0
-10
Derivative 2
0.04
0.02
0.00
-0.02
Wavenumber ($\times 10^{-3}cm^{-1}$)

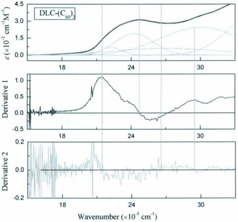
DLC-$(C_{60})_2$
$\varepsilon (\times 10^{-3} cm^{-1}M^{-1})$
4.5
3.0
1.5
0.0
18
24
30
Derivative 1
1.0
0.5
0.0
-0.5
Derivative 2
0.2
0.0
-0.2
Wavenumber ($\times 10^{-3} cm^{-1}$)

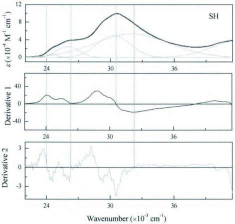
SH
$\varepsilon (\times 10^{-4}\ M^{-1}\ cm^{-1})$
12
8
4
0
Derivative 1
40
0
-40
Derivative 2
3
0
-3
24
30
36
Wavenumber ($\times 10^{-3}$ cm^{-1})

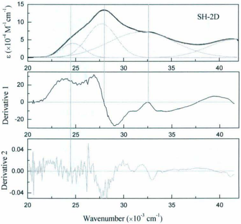
SH-2D
$\varepsilon (\times 10^{-4}\ M^{-1} cm^{-1})$
15
10
5
0
Derivative 1
20
0
-20
Derivative 2
0.04
0.00
-0.04
20
25
30
35
40
Wavenumber ($\times 10^{-3}$ cm^{-1})

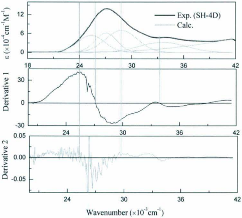
ε (×10⁻⁴cm⁻¹M⁻¹)
12
6
0
Exp. (SH-4D)
Calc.
18
24
30
36
42
Derivative 1
30
0
-30
24
30
36
42
Derivative 2
0.05
0.00
-0.05
24
30
36
42
Wavenumber (×10⁻³cm⁻¹)

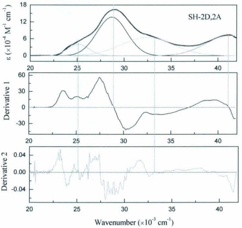
ε (×10⁻⁴ M⁻¹ cm⁻¹)
18
12
6
0
SH-2D,2A
20
25
30
35
40
Derivative 1
60
30
0
-30
20
25
30
35
40
Derivative 2
0.04
0.00
-0.04
20
25
30
35
40
Wavenumber (×10⁻³ cm⁻¹)

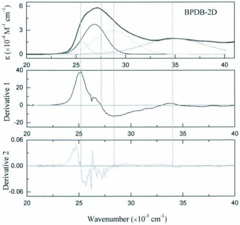
BPDB-2D
ε (×10^{-4} M^{-1} cm^{-1})
0
3
6
Derivative 1
-20
0
20
40
Derivative 2
-0.06
0.00
0.06
20
25
30
35
40
Wavenumber (×10^{-3} cm^{-1})

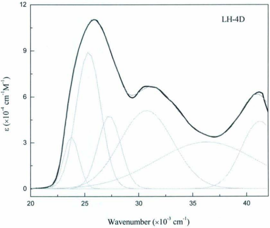
LH-4D
ε (×10^{-4} cm^{-1}M^{-1})
0
3
6
9
12
20
25
30
35
40
Wavenumber (×10^{-3} cm^{-1})

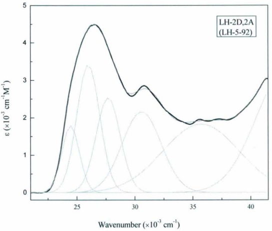
LH-2D,2A
(LH-5-92)
ε (×10-3 cm-1 M-1)
0
1
2
3
4
5
25
30
35
40
Wavenumber (×10-3 cm-1)

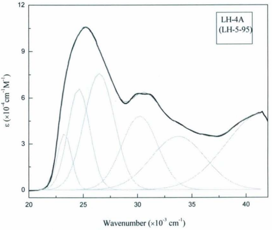
LH-4A
(LH-5-95)
ε (×10-4 cm-1 M-1)
0
3
6
9
12
20
25
30
35
40
Wavenumber (×10-3 cm-1)

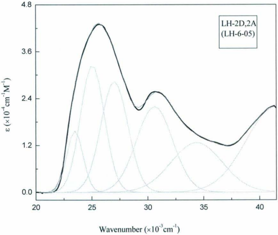
4.8
3.6
2.4
1.2
0.0
20
25
30
35
40
ε (×10⁻⁴ cm⁻¹M⁻¹)
Wavenumber (×10⁻³cm⁻¹)
LH-2D,2A
(LH-6-05)

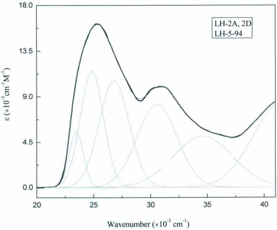
18.0
13.5
9.0
4.5
0.0
20
25
30
35
40
ε (×10⁻³cm⁻¹M⁻¹)
Wavenumber (×10⁻³ cm⁻¹)
LH-2A, 2D
LH-5-94

Table S-1. Gaussian deconvolution of absorption spectra of OPV/OPE oligomers and bisfullerene terminated derivatives.

Entry	Peak 1				Peak 2				Peak 3				Peak 4			
	Center	Area	Width	Height	Center	Area	Width	Height	Center	Area	Width	Height	Center	Area	Width	Height
SL	23405	3.1488E6	879.07	2858.0	24596	1.3985E7	1736.1	6427.1	26124	2.3729E7	2906.0	6515.2	29776	1.3577E7	5447.5	1988.6
SC	24197	1.3367E7	869.57	12265	25202	7.4934E7	1665.9	35589	27734	2.2020E8	2637.1	66624	30934	5.4646E7	1747.3	24954
LL	22940	1.5666E8	1032.3	1.211E5	24194	7.7814E8	2167.9	2.864E5	26088	8.1232E8	3412.7	1.899E5	32602	1.0673E9	7081.8	1.203E5
LC	22900	1.6408E7	1097.7	11927	24035	4.4225E7	1870.2	18867	26666	1.3263E8	3511.9	30134	30301	2.8566E7	2155.6	10574
SL-$(C_{60})_2$	23802	1.2210E7	1943.8	5011.8	25452	2.8317E7	2872.8	7864.8	25923	1.4837E7	8054.3	1469.8	29557	2.7853E7	5021.5	4425.7
SC-$(C_{60})_2$	24867	1.2913E7	2710.4	3801.3	27359	5.8772E6	1884.9	2487.8	30222	3.4903E7	4614.3	6035.2	39888	1.3941E8	7789.4	14280
LL-$(C_{60})_2$	22817	1.4917E8	1106.1	1.076E5	24066	4.8050E8	2035.9	1.023E5	25531	4.0554E8	3162.6	1.023E5	32350	2.8097E9	9659.0	2.321E5
LC-$(C_{60})_2$	23588	3.8749E8	2675.4	1.156E5	26512	2.8512E8	2602.3	87420	30220	7.5127E8	4728.6	1.268E5	39920	2.9570E9	8854.6	2.664E5
DSC	21661	4.4924E7	1342.7	26695	22996	6.4503E7	1606.4	32039	25629	2.1856E8	2864.4	60882	32455	1.0444E8	2813.7	29617
DLC	21917	1.5202E7	1964.7	6173.6	24132	7.9888E7	2775.4	22967	26631	5.1297E7	3642.9	11235	29939	1.7552E7	2539.8	5514.1
DSC-$(C_{60})_2$	22581	1.3441E8	2893.5	37063	25528	2.4424E8	2755.2	70732	27924	8.8143E7	2762.1	25462	31239	3.8796E8	4199.2	73714
DLC-$(C_{60})_2$	22259	1.5328E6	1780.6	686.83	24273	7.9358E6	3313.6	1910.9	26981	6.7118E6	9196.8	582.29	29991	2.1038E7	6835.1	2455.8

Table S-1. Gaussian deconvolution of absorption spectra of OPV/OPE oligomers and bisfullerene terminated derivatives.

Entry	Peak 1				Peak 2				Peak 3				Peak 4			
	Center	Area	Width	Height	Center	Area	Width	Height	Center	Area	Width	Height	Center	Area	Width	Height
DEB (NZ-6-89)	25600	2.1918E7	1104.0	15840	26863	1.0693E8	2268.1	37616	28772	1.3847E8	3694.7	29904	34927	1.4682E8	6187.4	18933
SH-4D (NZ-6-42)	25330	2.1075E8	3098.6	54266	27028	1.9651E8	2544.1	61631	28819	3.2229E8	3670.8	70052	33548	2.1804E8	5364.5	32430
SH-2D (NZ-7-22)	24693	1.2053E8	2364.3	40676	27713	3.6636E8	3032.3	96402	31910	6.2429E8	6863.7	72573	41687	3.6159E8	5687.8	50723
SH (NZ-6-51)	24532	9.4115E6	987.07	7607.6	25999	5.9157E7	2008.9	23496	30336	1.9770E8	3159.1	49934	32007	4.9016E8	7361.9	53123
SH-4A (NZ-6-55)	25107	1.1373E8	2228.8	40713	28694	5.4766E8	3175.6	1.3760E5	32445	4.4353E8	5480.3	64574	41169	4.4019E8	4916.9	71431
LH-TMS (NZ-5-92)	24461	3.3857E6	1506.3	1793.4	25990	8.5036E6	1984.8	3418.4	27698	6.6362E6	2087.7	2536.31	30586	9.1319E6	3369.9	2162.1
LH-4A (NZ-5-95)	23283	5.9869E7	1295.4	36876	24605	1.6650E8	2010.4	66081	26484	2.6508E8	2787.5	75876	30207	2.0043E8	3324.9	48098
LH-4D (NZ-5-79)	23766	5.9735E7	1399.6	34054	25364	2.5426E8	2271.7	89304	27283	1.2688E8	2122.7	47690	30730	3.1420E8	4915.2	51004
LH-2AD (NZ-5-94)	23489	8.6827E6	1237.8	5597.0	24854	2.9648E7	2038.1	11607	26808	3.5386E7	2666.2	10589	30581	3.6662E7	3546.1	8249.2
LH-2AD (NZ-6-05)	23487	2.8594E7	1452.9	15703	25065	8.7282E7	2143.4	32491	27023	8.6054E7	2424.1	28324	30613	8.9380E7	3253.3	21921

II. Global Analyses

```
[PROGRAM]
Name = SPECFIT
Version = 3.0

[FILE]
Name = SH-4D (NZ-6-42) TITRATION WITH AG(OTF) (FL).EXP
Path = C:\PROGRAM FILES\SPECFIT\DATA\H-MER JULY2009\
Date = 20-Jul-09
Time = 4:30:42 PM
Ncomp = 2
Nmeas = 15
Nwave = 333

[MODEL]
Date = 20-Jul-09
Time = 4:30:42 PM
Model = 0
Index = 0
Function = 1
Species = 4
Params = 4

[SPECIES]     [COLORED]     [FIXED]       [SPECTRUM]
1 0 0                       False         False
0 1 0                       True          True          NZ642AGFL.FIX
2 1 0                       True          False
4 1 0                       True          False

[SPECIES]     [FIXED]       [PARAMETER]        [ERROR]
1 0 0                       True          0.00000E+00   +/-      0.00000E+00
0 1 0                       True          0.00000E+00   +/-      0.00000E+00
2 1 0                       False         1.05870E+01   +/-      5.26383E-01
4 1 0                       False         1.92572E+01   +/-      5.05829E-01

[CONVERGENCE]
Iters = 11
Convergence = 1.000E-03
MarqConv = 5.537E-04
MarqPar = 0.0
SqSumY = 6.440E+11
SigmaY = 1.136E+04

[COVARIANCE]
5.571E+00     5.173E+00
5.173E+00     4.862E+00

[CORRELATION]
1.000E+00     9.940E-01
9.940E-01     1.000E+00

[END FILE]
```

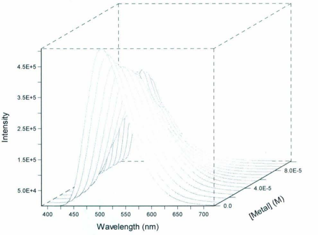
Intensity
4.5E+5
3.5E+5
2.5E+5
1.5E+5
5.0E+4
400
450
500
550
600
650
700
Wavelength (nm)
0.0
4.0E-5
8.0E-5
[Metal] (M)

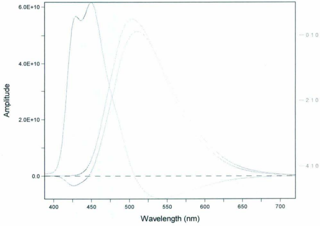
Amplitude
6.0E+10
4.0E+10
2.0E+10
0.0
400
450
500
550
600
650
700
Wavelength (nm)
0 1 0
2 1 0
4 1 0

```
[PROGRAM]
Name = SPECFIT
Version = 3.0

[FILE]
Name = SH-4D (NZ-6-42) TITRATION WITH TFA (UV).EXP
Path = C:\PROGRAM FILES\SPECFIT\DATA\H-MER OCT 2008\
Date = 14-Nov-08
Time = 5:21:07 PM
Ncomp = 1
Nmeas = 21
Nwave = 361

[MODEL]
Date = 14-Nov-08
Time = 5:21:07 PM
Model = 0
Index = 0
Function = 3
Species = 3
Params = 3

[SPECIES]         [COLORED]        [FIXED]            [SPECTRUM]
1 0                       True             True               NZ642HUV.FIX
1 2                       True             False
1 4                       True             False

[SPECIES]         [FIXED]          [PARAMETER]            [ERROR]
1 0                       True             0.00000E+00   +/-       0.00000E+00
1 2                       False            3.49640E+00   +/-       2.97661E-02
1 4                       False            5.73230E+00   +/-       1.47326E-01

[CONVERGENCE]
Iters = 13
Convergence = 1.000E-03
MarqConv = 3.568E-04
MarqPar = 0.0
SqSumY = 5.802E-01
SigmaY = 8.749E-03

[COVARIANCE]
5.033E-03         1.430E-02
1.430E-02         1.631E-01

[CORRELATION]
1.000E+00         4.990E-01
4.990E-01         1.000E+00

[END FILE]
```

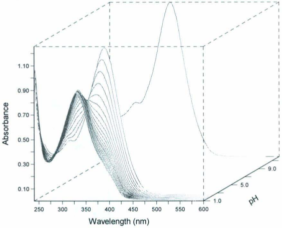
1.10
0.90
0.70
0.50
0.30
0.10
Absorbance
250
300
350
400
450
500
550
600
Wavelength (nm)
1.0
5.0
9.0
pH

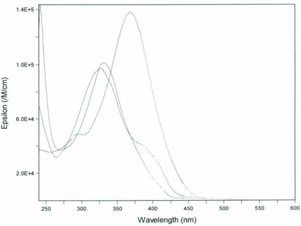
1.4E+5
1.0E+5
6.0E+4
2.0E+4
Epsilon (/M/cm)
250
300
350
400
450
500
550
600
Wavelength (nm)

```
[PROGRAM]
Name = SPECFIT
Version = 3.0

[FILE]
Name = SH-4D (NZ-6-42) TITRATION WITH CU(OTF)2 FL.FAC
Path = C:\PROGRAM FILES\SPECFIT\DATA\LI JULY 2009\
Date = 21-Jul-09
Time = 8:26:14 AM
Ncomp = 2
Nmeas = 15
Nwave = 333

[MODEL]
Date = 21-Jul-09
Time = 8:27:52 AM
Model = 0
Index = 0
Function = 1
Species = 4
Params = 4

[SPECIES]     [COLORED]     [FIXED]       [SPECTRUM]
1 0 0                       False         False
0 1 0                       True          True          NZ642CUFL.FIX
2 1 0                       True          False
4 1 0                       True          False

[SPECIES]     [FIXED]       [PARAMETER]          [ERROR]
1 0 0                       True          0.00000E+00   +/-      0.00000E+00
0 1 0                       True          0.00000E+00   +/-      0.00000E+00
2 1 0                       False         1.34056E+01   +/-      7.47516E-01
4 1 0                       False         2.28743E+01   +/-      7.40076E-01

[CONVERGENCE]
Iters = 14
Convergence = 1.000E-03
MarqConv = -2.781E-04
MarqPar = 0.0
SqSumY = 2.603E+10
SigmaY = 2.283E+03

[COVARIANCE]
2.108E+01     2.042E+01
2.042E+01     2.022E+01

[CORRELATION]
1.000E+00     9.892E-01
9.892E-01     1.000E+00

[END FILE]
```

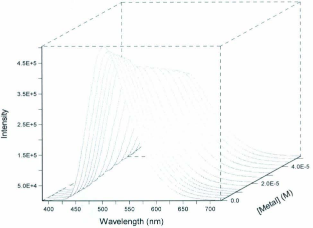
4.5E+5
3.5E+5
2.5E+5
1.5E+5
5.0E+4
Intensity
400
450
500
550
600
650
700
Wavelength (nm)
0.0
2.0E-5
4.0E-5
[Metal] (M)

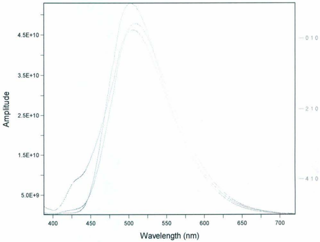
4.5E+10
3.5E+10
2.5E+10
1.5E+10
5.0E+9
Amplitude
400
450
500
550
600
650
700
Wavelength (nm)
0 1 0
2 1 0
4 1 0

```
[PROGRAM]
Name = SPECFIT
Version = 3.0

[FILE]
Name = SH-4D (NZ-6-42) TITRATION WITH CU(OTF)2 UV.EXP
Path = C:\PROGRAM FILES\SPECFIT\DATA\H-MER OCT 2008\
Date = 14-Nov-08
Time = 4:59:19 PM
Ncomp = 2
Nmeas = 15
Nwave = 361

[MODEL]
Date = 14-Nov-08
Time = 4:59:19 PM
Model = 0
Index = 3
Function = 1
Species = 4
Params = 4

[SPECIES]      [COLORED]     [FIXED]         [SPECTRUM]
1 0 0              False         False
0 1 0              True          True               NZ642CUUV.FIX
2 1 0              True          False
4 1 0              True          False

[SPECIES]      [FIXED]       [PARAMETER]          [ERROR]
1 0 0              True          0.00000E+00    +/-          0.00000E+00
0 1 0              True          0.00000E+00    +/-          0.00000E+00
2 1 0              False         1.03743E+01    +/-          2.96282E-01
4 1 0              False         2.02482E+01    +/-          2.87464E-01

[CONVERGENCE]
Iters = 3
Convergence = 1.000E-03
MarqConv = 5.671E-08
MarqPar = 0.0
SqSumY = 3.015E-01
SigmaY = 7.462E-03

[COVARIANCE]
9.570E-01      8.175E-01
8.175E-01      8.808E-01

[CORRELATION]
1.000E+00      8.904E-01
8.904E-01      1.000E+00

[END FILE]
```

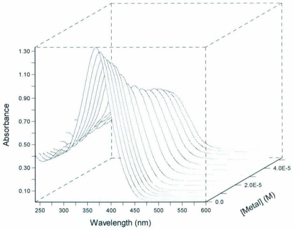
1.30
1.10
0.90
0.70
0.50
0.30
0.10
Absorbance
250
300
350
400
450
500
550
600
Wavelength (nm)
0.0
2.0E-5
4.0E-5
[Metal] (M)

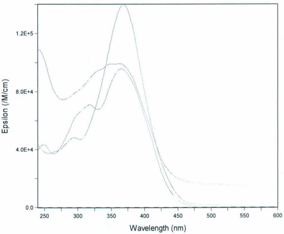
1.2E+5
8.0E+4
4.0E+4
0.0
Epsilon (/M/cm)
250
300
350
400
450
500
550
600
Wavelength (nm)

```
[PROGRAM]
Name = SPECFIT
Version = 3.0

[FILE]
Name = SH-4D (NZ-6-42) TITRATION WITH TFA FL.FAC
Path = C:\Program Files\SPECFIT\DATA\
Date = 20-Jul-09
Time = 2:50:27 PM
Ncomp = 1
Nmeas = 21
Nwave = 333

[MODEL]
Date = 20-Jul-09
Time = 2:55:10 PM
Model = 0
Index = 0
Function = 3
Species = 3
Params = 3

[SPECIES]       [COLORED]       [FIXED]         [SPECTRUM]
1 0                  True            True          NZ642HFL.FIX
1 2                  True            False
1 4                  True            False

[SPECIES]       [FIXED]         [PARAMETER]         [ERROR]
1 0                  True       0.00000E+00   +/-      0.00000E+00
1 2                  False      3.62979E+00   +/-      3.73655E-02
1 4                  False      6.35581E+00   +/-      4.46075E-02

[CONVERGENCE]
Iters = 5
Convergence = 1.000E-03
MarqConv = 4.957E-05
MarqPar = 0.0
SqSumY = 4.186E+10
SigmaY = 2.447E+03

[COVARIANCE]
8.072E-03       7.575E-03
7.575E-03       1.170E-02

[CORRELATION]
1.000E+00       7.794E-01
7.794E-01       1.000E+00

[END FILE]
```

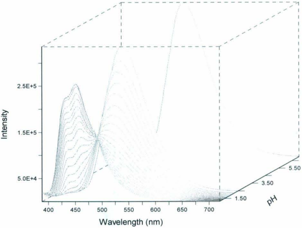
Intensity
2.5E+5
1.5E+5
5.0E+4
400
450
500
550
600
650
700
Wavelength (nm)
1.50
3.50
5.50
pH

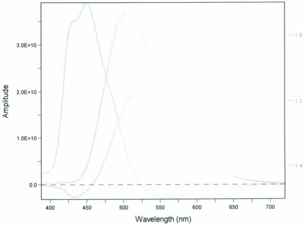
Amplitude
3.0E+10
2.0E+10
1.0E+10
0.0
1.0
1.2
1.4
400
450
500
550
600
650
700
Wavelength (nm)

```
[PROGRAM]
Name = SPECFIT
Version = 3.0

[FILE]
Name = SH-2D (NZ-7-22) TITRATION WITH AG(OTF) (FL.EXP
Path = C:\Program Files\SPECFIT\DATA\
Date = 20-Jul-09
Time = 3:51:30 PM
Ncomp = 2
Nmeas = 18
Nwave = 291

[MODEL]
Date = 20-Jul-09
Time = 3:51:32 PM
Model = 0
Index = 3
Function = 1
Species = 3
Params = 3

[SPECIES]      [COLORED]     [FIXED]       [SPECTRUM]
1 0 0                        False         False
0 1 0                        True          True           NZ722AGFL.FIX
2 1 0                        True          False

[SPECIES]      [FIXED]       [PARAMETER]          [ERROR]
1 0 0                        True          0.00000E+00   +/-     0.00000E+00
0 1 0                        True          0.00000E+00   +/-     0.00000E+00
2 1 0                        False         8.77795E+00   +/-     8.87809E-02

[CONVERGENCE]
Iters = 12
Convergence = 1.000E-03
MarqConv = -1.813E-01
MarqPar = 1.000E+02
SqSumY = 1.091E+13
SigmaY = 4.563E+04

[COVARIANCE]
5.145E-02

[CORRELATION]
1.000E+00
[END FILE]
```

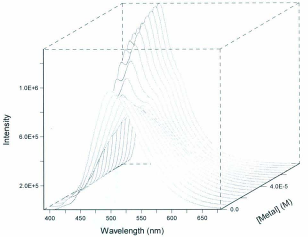
Intensity
1.0E+6
6.0E+5
2.0E+5
400
450
500
550
600
650
Wavelength (nm)
0.0
4.0E-5
[Metal] (M)

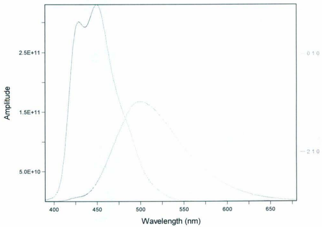
Amplitude
2.5E+11
1.5E+11
5.0E+10
400
450
500
550
600
650
Wavelength (nm)
0 1 0
2 1 0

```
[PROGRAM]
Name = SPECFIT
Version = 3.0

[FILE]
Name = SH-2D (NZ-7-22) TITRATION WITH AG(OTF) (UV).FAC
Path = C:\PROGRAM FILES\SPECFIT\DATA\LI WANG\H-MER TITRATION(FIT)\
Date = 26-Oct-08
Time = 1:17:42 PM
Ncomp = 2
Nmeas = 18
Nwave = 261

[MODEL]
Date = 26-Oct-08
Time = 1:18:09 PM
Model = 0
Index = 3
Function = 1
Species = 3
Params = 3

[SPECIES]         [COLORED]        [FIXED]          [SPECTRUM]
1 0 0                  False              False
0 1 0                  True               False
2 1 0                  True               False

[SPECIES]         [FIXED]          [PARAMETER]             [ERROR]
1 0 0                  True         0.00000E+00    +/-         0.00000E+00
0 1 0                  True         0.00000E+00    +/-         0.00000E+00
2 1 0                  False        9.09334E+00    +/-         4.59026E-02

[CONVERGENCE]
Iters = 5
Convergence = 1.000E-03
MarqConv = 2.088E-05
MarqPar = 0.0
SqSumY = 8.993E-02
SigmaY = 4.376E-03

[COVARIANCE]
1.243E-02

[CORRELATION]
1.000E+00

[END FILE]
```

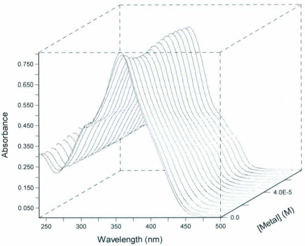
Absorbance
0.750
0.650
0.550
0.450
0.350
0.250
0.150
0.050
250
300
350
400
450
500
Wavelength (nm)
0.0
4.0E-5
[Metal] (M)

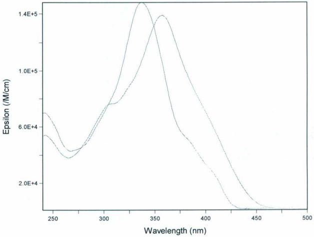
Epsilon (/M/cm)
1.4E+5
1.0E+5
6.0E+4
2.0E+4
250
300
350
400
450
500
Wavelength (nm)

```
[PROGRAM]
Name = SPECFIT
Version = 3.0

[FILE]
Name = SH-2D (NZ-7-22) TITRATION WITH TFA (FL).DAT
Path = C:\Program Files\SPECFIT\DATA\
Date = 20-Jul-09
Time = 4:07:41 PM
Ncomp = 1
Nmeas = 27
Nwave = 291

[MODEL]
Date = 20-Jul-09
Time = 4:09:38 PM
Model = 0
Index = 2
Function = 3
Species = 2
Params = 2

[SPECIES]     [COLORED]     [FIXED]         [SPECTRUM]
1 0                True          True             NZ722HFL.FIX
1 2                True          False

[SPECIES]     [FIXED]       [PARAMETER]         [ERROR]
1 0                True          0.00000E+00   +/-      0.00000E+00
1 2                False         2.70122E+00   +/-      5.82216E-02

[CONVERGENCE]
Iters = 6
Convergence = 1.000E-03
MarqConv = 4.032E-06
MarqPar = 0.0
SqSumY = 1.120E+12
SigmaY = 1.194E+04

[COVARIANCE]
2.058E-02

[CORRELATION]
1.000E+00

[END FILE]
```

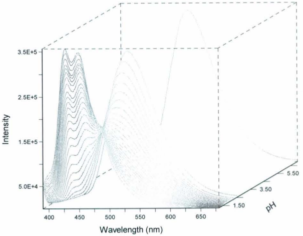
3.5E+5
2.5E+5
1.5E+5
5.0E+4
Intensity
400
450
500
550
600
650
Wavelength (nm)
1.50
3.50
5.50
pH

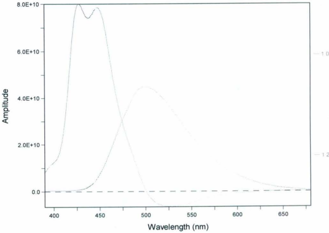
8.0E+10
6.0E+10
4.0E+10
2.0E+10
0.0
Amplitude
400
450
500
550
600
650
Wavelength (nm)
1 0
1 2

```
[PROGRAM]
Name = SPECFIT
Version = 3.0

[FILE]
Name = SH-2D (NZ-7-22) TITRATION WITH TFA (UV).EXP
Path = C:\PROGRAM FILES\SPECFIT\DATA\H-MER OCT 2008\
Date = 27-Oct-08
Time = 3:05:57 PM
Ncomp = 1
Nmeas = 27
Nwave = 261

[MODEL]
Date = 27-Oct-08
Time = 3:05:57 PM
Model = 0
Index = 2
Function = 3
Species = 2
Params = 2

[SPECIES]       [COLORED]       [FIXED]         [SPECTRUM]
1 0                  True            True            NZ722HUV.FIX
1 2                  True            False

[SPECIES]       [FIXED]         [PARAMETER]          [ERROR]
1 0                  True            0.00000E+00   +/-        0.00000E+00
1 2                  False           3.41277E+00   +/-        6.31895E-02

[CONVERGENCE]
Iters = 9
Convergence = 1.000E-03
MarqConv = 7.604E-04
MarqPar = 0.0
SqSumY = 2.890E+00
SigmaY = 2.025E-02

[COVARIANCE]
2.453E-02

[CORRELATION]
1.000E+00

[END FILE]
```

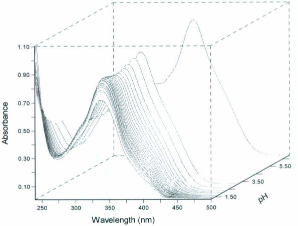
1.10
0.90
0.70
0.50
0.30
0.10
Absorbance
250
300
350
400
450
500
Wavelength (nm)
1.50
3.50
5.50
pH

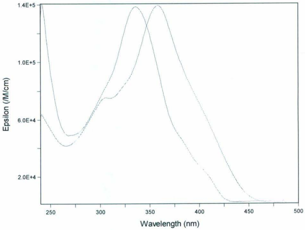
1.4E+5
1.0E+5
6.0E+4
2.0E+4
Epsilon (/M/cm)
250
300
350
400
450
500
Wavelength (nm)

```
[PROGRAM]
Name = SPECFIT
Version = 3.0

[FILE]
Name = SH-2D (NZ-7-22) TITRATION WITH CU(OTF)2 FL.DAT
Path = C:\Program Files\SPECFIT\DATA\
Date = 20-Jul-09
Time = 4:02:44 PM
Ncomp = 2
Nmeas = 19
Nwave = 301

[MODEL]
Date = 20-Jul-09
Time = 4:03:17 PM
Model = 0
Index = 3
Function = 1
Species = 3
Params = 3

[SPECIES]      [COLORED]      [FIXED]        [SPECTRUM]
1 0 0                         False          False
0 1 0                         True           True           NZ722CUFL.FIX
2 1 0                         True           False

[SPECIES]      [FIXED]        [PARAMETER]          [ERROR]
1 0 0                         True           0.00000E+00   +/-     0.00000E+00
0 1 0                         True           0.00000E+00   +/-     0.00000E+00
2 1 0                         False          8.85560E+00   +/-     7.98357E-02

[CONVERGENCE]
Iters = 7
Convergence = 1.000E-03
MarqConv = 3.159E-04
MarqPar = 0.0
SqSumY = 1.845E+11
SigmaY = 5.680E+03

[COVARIANCE]
4.073E-02

[CORRELATION]
1.000E+00

[END FILE]
```

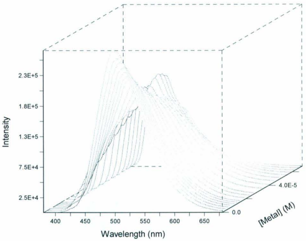
Intensity
2.3E+5
1.8E+5
1.3E+5
7.5E+4
2.5E+4
400
450
500
550
600
650
Wavelength (nm)
0.0
4.0E-5
[Metal] (M)

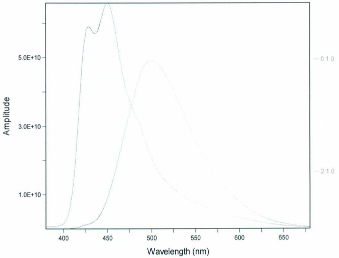
Amplitude
5.0E+10
3.0E+10
1.0E+10
400
450
500
550
600
650
Wavelength (nm)
0 1 0
2 1 0

```
[PROGRAM]
Name = SPECFIT
Version = 3.0

[FILE]
Name = NZ-7-22 TITRATION WITH CU(OTF)2 (UV).EXP
Path = C:\PROGRAM FILES\SPECFIT\DATA\H-MER JULY2009\
Date = 21-Jul-09
Time = 8:46:55 AM
Ncomp = 2
Nmeas = 19
Nwave = 261

[MODEL]
Date = 21-Jul-09
Time = 8:46:55 AM
Model = 0
Index = 3
Function = 1
Species = 3
Params = 3

[SPECIES]      [COLORED]      [FIXED]       [SPECTRUM]
1 0 0                         False         False
0 1 0                         True          True          NZ722CUUV.FIX
2 1 0                         True          False

[SPECIES]      [FIXED]        [PARAMETER]         [ERROR]
1 0 0                         True          0.00000E+00   +/-     0.00000E+00
0 1 0                         True          0.00000E+00   +/-     0.00000E+00
2 1 0                         False         9.36805E+00   +/-     1.09833E-01

[CONVERGENCE]
Iters = 3
Convergence = 1.000E-03
MarqConv = 1.397E-08
MarqPar = 0.0
SqSumY = 7.153E-01
SigmaY = 1.201E-02

[COVARIANCE]
8.280E-02

[CORRELATION]
1.000E+00

[END FILE]
```

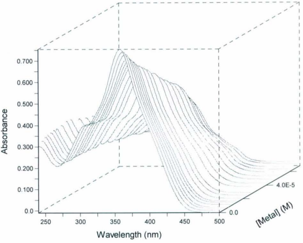
Absorbance
0.700
0.600
0.500
0.400
0.300
0.200
0.100
0.0
250
300
350
400
450
500
Wavelength (nm)
4.0E-5
0.0
[Metal] (M)

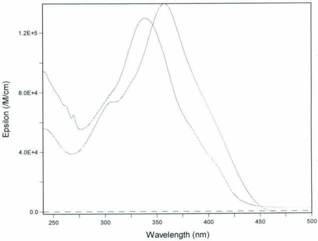
Epsilon (/M/cm)
1.2E+5
8.0E+4
4.0E+4
0.0
250
300
350
400
450
500
Wavelength (nm)

```
[PROGRAM]
Name = SPECFIT
Version = 3.0

[FILE]
Name = OPE-2D (NZ-6-89)  TITRATION WITH AG(OTF) FL.EXP
Path = C:\Program Files\SPECFIT\DATA\
Date = 20-Jul-09
Time = 3:13:03 PM
Ncomp = 2
Nmeas = 15
Nwave = 281

[MODEL]
Date = 20-Jul-09
Time = 3:13:03 PM
Model = 0
Index = 3
Function = 1
Species = 3
Params = 3

[SPECIES]       [COLORED]       [FIXED]         [SPECTRUM]
1 0 0                           False           False
0 1 0                           True            True            NZ689AGFL.FIX
2 1 0                           True            False

[SPECIES]       [FIXED]         [PARAMETER]             [ERROR]
1 0 0                           True            0.00000E+00    +/-      0.00000E+00
0 1 0                           True            0.00000E+00    +/-      0.00000E+00
2 1 0                           False           9.68861E+00    +/-      2.19421E-01

[CONVERGENCE]
Iters = 3
Convergence = 1.000E-03
MarqConv = 3.617E-08
MarqPar = 0.0
SqSumY = 7.109E+11
SigmaY = 1.299E+04

[COVARIANCE]
4.321E-01

[CORRELATION]
1.000E+00

[END FILE]
```

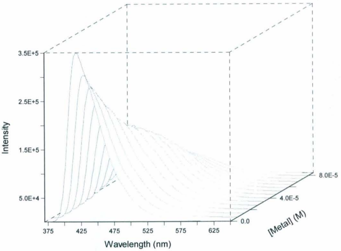
Intensity
3.5E+5
2.5E+5
1.5E+5
5.0E+4
375
425
475
525
575
625
Wavelength (nm)
0.0
4.0E-5
8.0E-5
[Metal] (M)

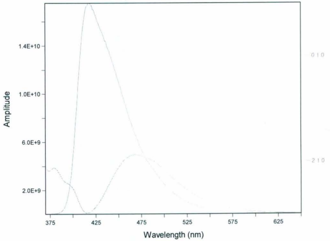
Amplitude
1.4E+10
1.0E+10
6.0E+9
2.0E+9
375
425
475
525
575
625
Wavelength (nm)
0 1 0
2 1 0

```
[PROGRAM]
Name = SPECFIT
Version = 3.0

[FILE]
Name = OPE-2D (NZ-6-89 )TITRATION WITH AG(OTF) UV.EXP
Path = C:\PROGRAM FILES\SPECFIT\DATA\H-MER JULY2009\
Date = 21-Jul-09
Time = 8:40:34 AM
Ncomp = 2
Nmeas = 14
Nwave = 361

[MODEL]
Date = 21-Jul-09
Time = 8:40:35 AM
Model = 0
Index = 3
Function = 1
Species = 3
Params = 3

[SPECIES]      [COLORED]     [FIXED]        [SPECTRUM]
1 0 0                        False          False
0 1 0                        True           True          NZ689AGUV.FIX
2 1 0                        True           False

[SPECIES]      [FIXED]       [PARAMETER]           [ERROR]
1 0 0                        True           0.00000E+00  +/-     0.00000E+00
0 1 0                        True           0.00000E+00  +/-     0.00000E+00
2 1 0                        False          9.08622E+00  +/-     1.34427E-01

[CONVERGENCE]
Iters = 15
Convergence = 1.000E-03
MarqConv = -2.818E-01
MarqPar = 1.000E-01
SqSumY = 2.098E+00
SigmaY = 2.038E-02

[COVARIANCE]
1.316E-01

[CORRELATION]
1.000E+00

[END FILE]
```

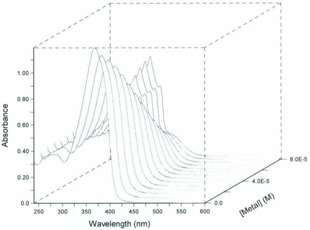
Absorbance
1.00
0.80
0.60
0.40
0.20
0.0
250
300
350
400
450
500
550
600
Wavelength (nm)
0.0
4.0E-5
8.0E-5
[Metal] (M)

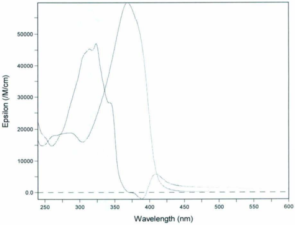
Epsilon (/M/cm)
50000
40000
30000
20000
10000
0.0
250
300
350
400
450
500
550
600
Wavelength (nm)

```
[PROGRAM]
Name = SPECFIT
Version = 3.0

[FILE]
Name = OPE-2D (NZ-6-89) TITRATION WITH CU2+ FL.EXP
Path = C:\Program Files\SPECFIT\DATA\
Date = 20-Jul-09
Time = 3:27:49 PM
Ncomp = 2
Nmeas = 18
Nwave = 281

[MODEL]
Date = 20-Jul-09
Time = 3:27:49 PM
Model = 0
Index = 0
Function = 1
Species = 3
Params = 3

[SPECIES]      [COLORED]      [FIXED]        [SPECTRUM]
1 0 0                         False          False
0 1 0                         True           True              NZ689CUFL.FIX
2 1 0                         True           False

[SPECIES]      [FIXED]        [PARAMETER]          [ERROR]
1 0 0                         True           0.00000E+00    +/-        0.00000E+00
0 1 0                         True           0.00000E+00    +/-        0.00000E+00
2 1 0                         False          1.29805E+01    +/-        1.02711E+00

[CONVERGENCE]
Iters = 8
Convergence = 1.000E-03
MarqConv = 1.777E-04
MarqPar = 0.0
SqSumY = 5.235E+11
SigmaY = 1.017E+04

[COVARIANCE]
9.301E+01

[CORRELATION]
1.000E+00

[END FILE]
```

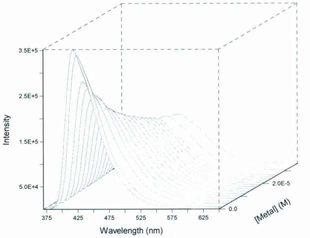
3.5E+5
2.5E+5
1.5E+5
5.0E+4
Intensity
375
425
475
525
575
625
Wavelength (nm)
0.0
2.0E-5
[Metal] (M)

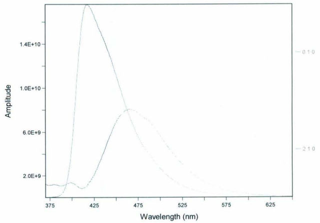
1.4E+10
1.0E+10
6.0E+9
2.0E+9
Amplitude
375
425
475
525
575
625
Wavelength (nm)
0 1 0
2 1 0

```
[PROGRAM]
Name = SPECFIT
Version = 3.0

[FILE]
Name = OPE-2D (NZ-6-89 ) TITRATION WITH CU2+ UV.EXP
Path = C:\PROGRAM FILES\SPECFIT\DATA\H-MER JULY2009\
Date = 21-Jul-09
Time = 8:51:48 AM
Ncomp = 2
Nmeas = 18
Nwave = 361

[MODEL]
Date = 21-Jul-09
Time = 8:51:48 AM
Model = 0
Index = 3
Function = 1
Species = 3
Params = 3

[SPECIES]       [COLORED]       [FIXED]         [SPECTRUM]
1 0 0                           False           False
0 1 0                           True            True            NZ689CUUV.FIX
2 1 0                           True            False

[SPECIES]       [FIXED]         [PARAMETER]             [ERROR]
1 0 0                           True            0.00000E+00  +/-        0.00000E+00
0 1 0                           True            0.00000E+00  +/-        0.00000E+00
2 1 0                           False           1.26299E+01  +/-        8.41745E-01

[CONVERGENCE]
Iters = 7
Convergence = 1.000E-03
MarqConv = -1.562E-04
MarqPar = 0.0
SqSumY = 1.788E+00
SigmaY = 1.659E-02

[COVARIANCE]
3.536E+01

[CORRELATION]
1.000E+00

[END FILE]
```

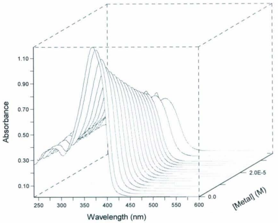
Absorbance
1.10
0.90
0.70
0.50
0.30
0.10
250
300
350
400
450
500
550
600
Wavelength (nm)
0.0
2.0E-5
[Metal] (M)

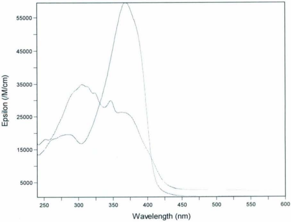
Epsilon (/M/cm)
55000
45000
35000
25000
15000
5000
250
300
350
400
450
500
550
600
Wavelength (nm)

```
[PROGRAM]
Name = SPECFIT
Version = 3.0

[FILE]
Name = OPE-2D (NZ-6-89) TITRATION WITH TFA FL.FAC
Path = C:\Program Files\SPECFIT\DATA\
Date = 20-Jul-09
Time = 3:33:56 PM
Ncomp = 1
Nmeas = 18
Nwave = 281

[MODEL]
Date = 20-Jul-09
Time = 3:36:02 PM
Model = 0
Index = 2
Function = 3
Species = 2
Params = 2

[SPECIES]        [COLORED]        [FIXED]            [SPECTRUM]
1 0                   True              True              NZ689HFL.FIX
1 2                   True              False

[SPECIES]        [FIXED]            [PARAMETER]           [ERROR]
1 0                   True              0.00000E+00    +/-      0.00000E+00
1 2                   False             4.56650E+00    +/-      6.86389E-02

[CONVERGENCE]
Iters = 7
Convergence = 1.000E-03
MarqConv = 5.553E-04
MarqPar = 0.0
SqSumY = 4.574E+11
SigmaY = 9.510E+03

[COVARIANCE]
2.932E-02

[CORRELATION]
1.000E+00

[END FILE]
```

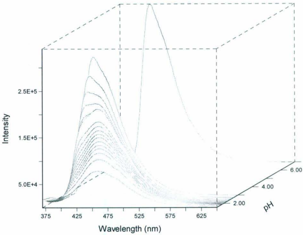
Intensity
2.5E+5
1.5E+5
5.0E+4
375
425
475
525
575
625
Wavelength (nm)
6.00
4.00
2.00
pH

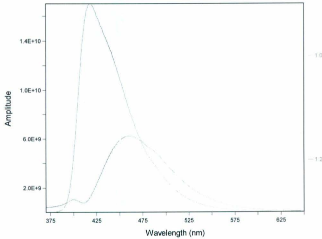
Amplitude
1.4E+10
1.0E+10
6.0E+9
2.0E+9
375
425
475
525
575
625
Wavelength (nm)
1.0
1.2

```
[PROGRAM]
Name = SPECFIT
Version = 3.0

[FILE]
Name = OPE-2D ( NZ-6-89) TITRATION WITH TFA UV.EXP
Path = C:\PROGRAM FILES\SPECFIT\DATA\
Date = 14-Nov-08
Time = 6:02:00 PM
Ncomp = 1
Nmeas = 18
Nwave = 361

[MODEL]
Date = 14-Nov-08
Time = 6:02:00 PM
Model = 0
Index = 2
Function = 3
Species = 2
Params = 2

[SPECIES]      [COLORED]      [FIXED]        [SPECTRUM]
1 0                 True          True              NZ689HUV.FIX
1 2                 True          False

[SPECIES]      [FIXED]        [PARAMETER]        [ERROR]
1 0                 True      0.00000E+00    +/-       0.00000E+00
1 2                 False     4.22754E+00    +/-       6.23277E-02

[CONVERGENCE]
Iters = 3
Convergence = 1.000E-03
MarqConv = 3.073E-05
MarqPar = 0.0
SqSumY = 2.658E+00
SigmaY = 2.022E-02

[COVARIANCE]
2.382E-02

[CORRELATION]
1.000E+00

[END FILE]
```

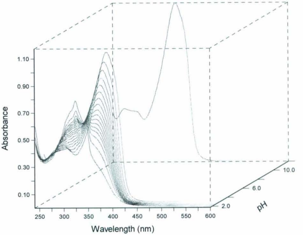
Absorbance
1.10
0.90
0.70
0.50
0.30
0.10
250
300
350
400
450
500
550
600
Wavelength (nm)
2.0
6.0
10.0
pH

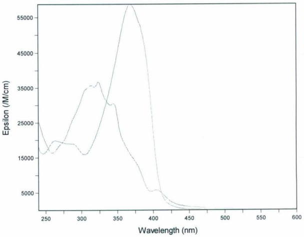
Epsilon (/M/cm)
55000
45000
35000
25000
15000
5000
250
300
350
400
450
500
550
600
Wavelength (nm)

```
[PROGRAM]
Name = SPECFIT
Version = 3.0

[FILE]
Name = SL (NZ-2-23), SLB-FIT.DAT
Path = C:\PROGRAM FILES\SPECFIT\DATA\LI WANG\FULLERENE\
Date = 17-Jan-09
Time = 1:37:58 PM
Ncomp = 3
Nmeas = 60
Nwave = 42

[MODEL]
Date = 17-Jan-09
Time = 1:37:58 PM
Model = 2
Index = 0
Function = 0
Species = 3
Params = 3

[SPECIES]        [INIT.CONC]       [BUFFERED]       [COLORED]       [FIXED]
        [SPECTRUM]
A               1.000E+00          False            True            False
B               0.000E+00          False            False           False
C               1.000E+00          False            True            False

[NAME]  [REACTION]
k1      A --> B
k2      A --> C
k3      C --> B

[NAME]  [TYPE]  [LINK]  [PARAMETER]     [ERROR]           [RATIO]
k1      VAR     0       5.92773E+07     +/-        7.92368E+06
k2      VAR     0       1.86028E+08     +/-        7.92368E+06
k3      VAR     0       9.06075E+03     +/-        6.20449E+02

[PARAMETER COEFFICIENTS]
 1  0  0
 1  0  0
 0  0  1

[SPECIES COEFFICIENTS]
-1  1  0
-1  0  1
 0  1 -1

[REACTANT STOICHIOMETRIES]
 1  0  0
 1  0  0
 0  0  1

[PRODUCT STOICHIOMETRIES]
 0  1  0
 0  0  1
 0  1  0

[TIME ZERO]
Tzero = 4.981E-07

[CONVERGENCE]
Iters = 4
Convergence = 1.000E-03
MarqConv = -1.751E-04
MarqPar = 0.0
SqSumY = 7.867E-04
SigmaY = 5.588E-04

[COVARIANCE]
```

```
6.278E+13       -6.278E+13      -1.651E+08
-6.278E+13      6.278E+13       1.651E+08
-1.651E+08      1.651E+08       3.850E+05

[CORRELATION]
1.000E+00       -1.000E+00      -3.358E-02
-1.000E+00      1.000E+00       3.358E-02
-3.358E-02      3.358E-02       1.000E+00
[END FILE]
```

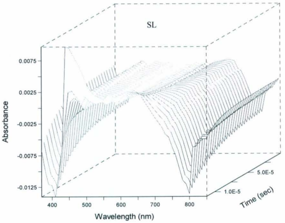

```
[PROGRAM]
Name = SPECFIT
Version = 3.0

[FILE]
Name = SL-C60 (NZ-2-24), SLB.DAT
Path = C:\PROGRAM FILES\SPECFIT\DATA\LI WANG\FULLERENE\
Date = 06-Jun-07
Time = 1:59:39 PM
Ncomp = 3
Nmeas = 62
Nwave = 65
[MODEL]
Date = 20-Jan-09
Time = 3:39:57 PM
Model = 2
Index = 0
Function = 0
Species = 3
Params = 2

[SPECIES]         [INIT.CONC]      [BUFFERED]      [COLORED]      [FIXED]
          [SPECTRUM]
A                 1.000E+00        False           True           False
B                 0.000E+00        False           False          False
C                 5.000E-01        False           True           False

[NAME]   [REACTION]
```

```
k1       A --> B
k2       C --> B

[NAME]  [TYPE]  [LINK]   [PARAMETER]      [ERROR]           [RATIO]
k1       VAR     0       1.15600E+09    +/-         1.64692E+02
k2       VAR     0       3.38772E+05    +/-         2.98912E+04

[PARAMETER COEFFICIENTS]
 1    0    0
 0    0    1

[SPECIES COEFFICIENTS]
-1    1    0
 0    1   -1

[REACTANT STOICHIOMETRIES]
 1    0    0
 0    0    1

[PRODUCT STOICHIOMETRIES]
 0    1    0
 0    1    0

[TIME ZERO]
Tzero = 5.991E-08

[CONVERGENCE]
Iters = 3
Convergence = 1.000E-03
MarqConv = 2.862E-04
MarqPar = 0.0
SqSumY = 9.639E-04
SigmaY = 4.891E-04

[COVARIANCE]
2.712E+04           1.256E+05
1.256E+05           8.935E+08

[CORRELATION]
1.000E+00           2.552E-02
2.552E-02           1.000E+00
[END FILE]
```

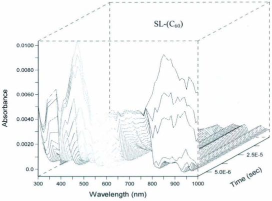

```
[PROGRAM]
Name = SPECFIT
Version = 3.0
[FILE]
Name = LL (NZ-3-68), LLB.DAT
Path = C:\PROGRAM FILES\SPECFIT\DATA\LI WANG\FULLERENE\
Date = 21-Jun-07
Time = 5:13:32 PM
Ncomp = 3
Nmeas = 60
Nwave = 45

[MODEL]
Date = 18-Jan-09
Time = 2:22:03 PM
Model = 2
Index = 0
Function = 0
Species = 3
Params = 3

[SPECIES]         [INIT.CONC]         [BUFFERED]        [COLORED]         [FIXED]
          [SPECTRUM]
A                 1.000E+00           False             True              False
B                 0.000E+00           False             False             False
C                 1.000E+00           False             True              False

[NAME]  [REACTION]
k1      A --> B
k2      A --> C
k3      C --> B

[NAME]  [TYPE]  [LINK]  [PARAMETER]     [ERROR]          [RATIO]
k1      VAR     0       1.97124E+09    +/-        6.29148E+03
k2      VAR     0       9.33083E+08    +/-        6.29242E+03
k3      VAR     0       5.05274E+03    +/-        1.84273E+02

[PARAMETER COEFFICIENTS]
 1   0   0
 1   0   0
 0   0   1

[SPECIES COEFFICIENTS]
-1   1   0
-1   0   1
 0   1  -1

[REACTANT STOICHIOMETRIES]
 1   0   0
 1   0   0
 0   0   1

[PRODUCT STOICHIOMETRIES]
 0   1   0
 0   0   1
 0   1   0

[TIME ZERO]
Tzero = 2.981E-07

[CONVERGENCE]
Iters = 11
Convergence = 1.000E-03
MarqConv = 7.103E-05
MarqPar = 0.0
SqSumY = 4.239E-04
SigmaY = 3.963E-04

[COVARIANCE]
3.958E+07          -3.959E+07          -6.782E+04
```

```
-3.959E+07      3.959E+07       6.783E+04
-6.782E+04      6.783E+04       3.396E+04

[CORRELATION]
1.000E+00       -1.000E+00      -5.850E-02
-1.000E+00      1.000E+00       5.850E-02
-5.850E-02      5.850E-02       1.000E+00
[END FILE]
```

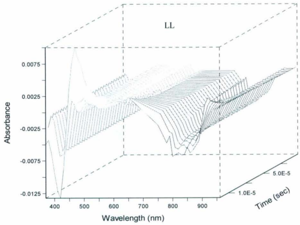

```
[PROGRAM]
Name = SPECFIT
Version = 3.0
[FILE]
Name = DSC (NZ-1-64), DSC.FAC
Path = C:\PROGRAM FILES\SPECFIT\DATA\LI WANG\FULLERENE\
Date = 21-Jan-09
Time = 3:16:46 PM
Ncomp = 3
Nmeas = 60
Nwave = 56

[MODEL]
Date = 23-Jan-09
Time = 1:24:32 PM
Model = 2
Index = 0
Function = 0
Species = 3
Params = 2

[SPECIES]       [INIT.CONC]     [BUFFERED]      [COLORED]       [FIXED]
        [SPECTRUM]
A               1.000E+00       False           True            False
B               0.000E+00       False           False           False
C               1.000E+00       False           True            False

[NAME]  [REACTION]
k1      A--> B
```

```
k2      C --> B

[NAME]  [TYPE]  [LINK]  [PARAMETER]     [ERROR]         [RATIO]
k1      VAR     0       5.05850E+05     +/-         1.23366E+04
k2      VAR     0       6.69367E+03     +/-         1.02871E+03

[PARAMETER COEFFICIENTS]
 1   0   0
 0   0   1

[SPECIES COEFFICIENTS]
-1   1   0
 0   1  -1

[REACTANT STOICHIOMETRIES]
 1   0   0
 0   0   1

[PRODUCT STOICHIOMETRIES]
 0   1   0
 0   1   0

[TIME ZERO]
Tzero = 1.308E-07

[CONVERGENCE]
Iters = 3
Convergence = 1.000E-03
MarqConv = 1.971E-07
MarqPar = 0.0
SqSumY = 1.257E-04
SigmaY = 1.935E-04

[COVARIANCE]
1.522E+08        2.918E+06
2.918E+06        1.058E+06

[CORRELATION]
1.000E+00        2.299E-01
2.299E-01        1.000E+00
[END FILE]
```

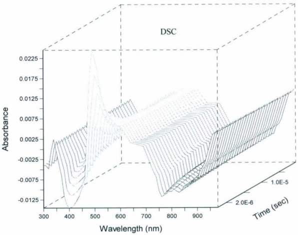

```
[PROGRAM]
Name = SPECFIT
Version = 3.0
[FILE]
Name = DLC (NZ-2-57), DLC.FAC
Path = C:\PROGRAM FILES\SPECFIT\DATA\LI WANG\FULLERENE\
Date = 21-Jan-09
Time = 3:22:25 PM
Ncomp = 3
Nmeas = 60
Nwave = 61

[MODEL]
Date = 23-Jan-09
Time = 1:36:26 PM
Model = 2
Index = 0
Function = 0
Species = 3
Params = 2

[SPECIES]          [INIT.CONC]        [BUFFERED]        [COLORED]        [FIXED]
        [SPECTRUM]
A                  1.000E+00          False             True             False
B                  0.000E+00          False             False            False
C                  5.000E-01          False             True             False

[NAME]  [REACTION]
k1      A --> B
k2      C --> B

[NAME]  [TYPE]   [LINK]   [PARAMETER]    [ERROR]           [RATIO]
k1      VAR      0        6.05855E+05    +/-          2.15746E+04
k2      VAR      0        7.19096E+04    +/-          5.99156E+03

[PARAMETER COEFFICIENTS]
```

```
 1  0  0
 0  0  1

[SPECIES COEFFICIENTS]
-1  1  0
 0  1 -1

[REACTANT STOICHIOMETRIES]
 1  0  0
 0  0  1

[PRODUCT STOICHIOMETRIES]
 0  1  0
 0  1  0

[TIME ZERO]
Tzero = 9.082E-08

[CONVERGENCE]
Iters = 5
Convergence = 1.000E-03
MarqConv = 7.485E-04
MarqPar = 0.0
SqSumY = 1.258E-03
SigmaY = 5.863E-04

[COVARIANCE]
4.655E+08        -5.857E+07
-5.857E+07       3.590E+07

[CORRELATION]
1.000E+00        -4.531E-01
-4.531E-01       1.000E+00
[END FILE]
```

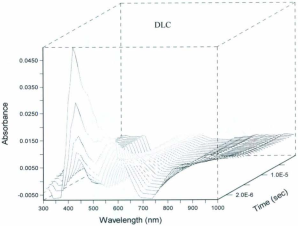

```
[PROGRAM]
Name = SPECFIT
Version = 3.0

[FILE]
Name = OPE (NZ-3-61), R-FIT.FAC
Path = C:\PROGRAM FILES\SPECFIT\DATA\LI WANG\FULLERENE\
Date = 17-Jan-09
Time = 1:40:44 PM
Ncomp = 3
Nmeas = 59
Nwave = 38

[MODEL]
Date = 17-Jan-09
Time = 1:40:44 PM
Model = 2
Index = 0
Function = 0
Species = 3
Params = 3

[SPECIES]          [INIT.CONC]        [BUFFERED]         [COLORED]          [FIXED]
          [SPECTRUM]
A                  1.000E+00          False              True               False
B                  0.000E+00          False              False              False
C                  1.000E+00          False              True               False

[NAME]    [REACTION]
k1        A --> B
k2        A --> C
k3        C --> B

[NAME]    [TYPE]    [LINK]    [PARAMETER]      [ERROR]            [RATIO]
k1        VAR       0         5.92598E+07     +/-      3.70986E+04
k2        VAR       0         2.77540E+08     +/-      3.70986E+04
k3        VAR       0         2.77698E+04     +/-      9.44271E+00

[PARAMETER COEFFICIENTS]
 1   0   0
 1   0   0
 0   0   1

[SPECIES COEFFICIENTS]
-1   1   0
-1   0   1
 0   1  -1

[REACTANT STOICHIOMETRIES]
 1   0   0
 1   0   0
 0   0   1

[PRODUCT STOICHIOMETRIES]
 0   1   0
 0   0   1
 0   1   0

[TIME ZERO]
Tzero = 4.981E-07

[CONVERGENCE]
Iters = 3
Convergence = 1.000E-03
MarqConv = -6.166E-05
MarqPar = 0.0
SqSumY = 1.152E-02
SigmaY = 2.267E-03
```

```
[COVARIANCE]
1.376E+09        -1.376E+09        -2.993E+05
-1.376E+09       1.376E+09         2.993E+05
-2.993E+05       2.993E+05         8.916E+01

[CORRELATION]
1.000E+00        -1.000E+00        -8.544E-01
-1.000E+00       1.000E+00         8.544E-01
-8.544E-01       8.544E-01         1.000E+00

[END FILE]
```

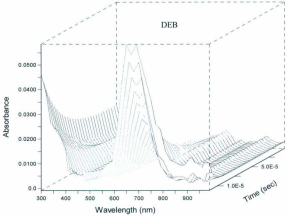

```
[PROGRAM]
Name = SPECFIT
Version = 3.0
[FILE]
Name = OPE-C60 (NZ-3-63), C60-R.FAC
Path = C:\PROGRAM FILES\SPECFIT\DATA\LI WANG\FULLERENE\
Date = 21-Jan-09
Time = 3:04:28 PM
Ncomp = 3
Nmeas = 60
Nwave = 69

[MODEL]
Date = 21-Jan-09
Time = 3:07:32 PM
Model = 2
Index = 0
Function = 0
Species = 3
Params = 2

[SPECIES]       [INIT.CONC]        [BUFFERED]      [COLORED]      [FIXED]
          [SPECTRUM]
A               1.000E+00          False           True           False
C               0.000E+00          False           False          False
B               1.000E+00          False           True           False
```

```
[NAME]  [REACTION]
k3      A --> C
k4      B --> C

[NAME]  [TYPE]  [LINK]  [PARAMETER]    [ERROR]         [RATIO]
k3      VAR     0       4.10131E+05    +/-         5.64677E+04
k4      VAR     0       5.97934E+04    +/-         3.19444E+03

[PARAMETER COEFFICIENTS]
 1   0   0
 0   0   1

[SPECIES COEFFICIENTS]
-1   1   0
 0   1  -1

[REACTANT STOICHIOMETRIES]
 1   0   0
 0   0   1

[PRODUCT STOICHIOMETRIES]
 0   1   0
 0   1   0

[TIME ZERO]
Tzero = 2.981E-07

[CONVERGENCE]
Iters = 3
Convergence = 1.000E-03
MarqConv = 3.444E-05
MarqPar = 0.0
SqSumY = 8.051E-04
SigmaY = 4.410E-04

[COVARIANCE]
3.189E+09          -1.264E+07
-1.264E+07         1.020E+07

[CORRELATION]
1.000E+00          -7.009E-02
-7.009E-02         1.000E+00
[END FILE]
```

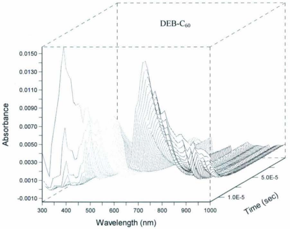

III. Time-resolved Fluorescence

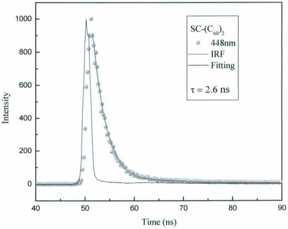

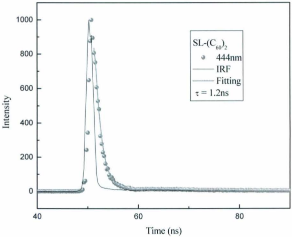
SL-$(C_{60})_2$
444nm
IRF
Fitting
τ = 1.2ns
Intensity
0
200
400
600
800
1000
40
60
80
Time (ns)

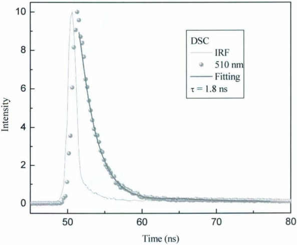
DSC
IRF
510 nm
Fitting
τ = 1.8 ns
Intensity
0
2
4
6
8
10
50
60
70
80
Time (ns)

Appendix II: Synthetic Schemes

I. Synthetic Scheme for cruciform OPV/OPE co-oligomer

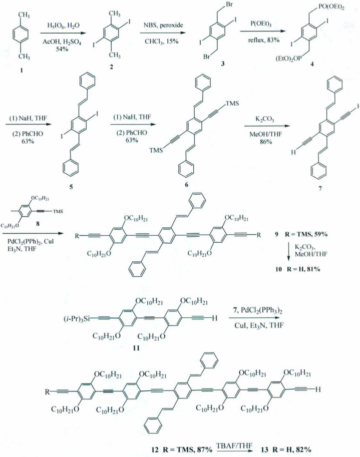
CH3
CH3
1
H5IO6, H2O
AcOH, H2SO4
54%
CH3
I
I
CH3
2
NBS, peroxide
CHCl3, 15%
Br
I
I
Br
3
P(OEt)3
reflux, 83%
PO(OEt)2
I
I
(EtO)2OP
4
(1) NaH, THF
(2) PhCHO
63%
I
I
5
(1) NaH, THF
(2) PhCHO
63%
TMS
TMS
6
K2CO3
MeOH/THF
86%
H
H
7
OC10H21
TMS
C10H21O
8
PdCl2(PPh)2, CuI
Et3N, THF
R
OC10H21
C10H21O
OC10H21
C10H21O
R
9 R = TMS, 59%
K2CO3,
MeOH/THF
10 R = H, 81%
OC10H21
OC10H21
(i-Pr)3Si
H
C10H21O
C10H21O
11
7, PdCl2(PPh3)2
CuI, Et3N, THF
OC10H21
OC10H21
OC10H21
OC10H21
R
H
C10H21O
C10H21O
C10H21O
C10H21O
12 R = TMS, 87%
TBAF/THF
13 R = H, 82%

II. Synthetic scheme for donor-substituted cruciform OPV/OPE co-oligomers.

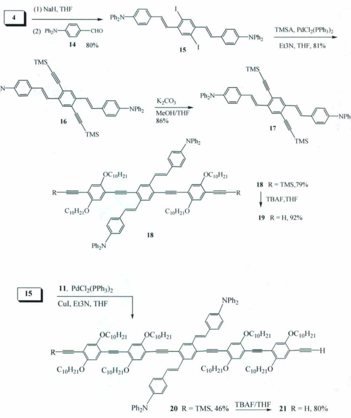
4
(1) NaH, THF
(2) Ph2N–C6H4–CHO
14 80%
15
TMSA, PdCl2(PPh3)2
Et3N, THF, 81%
16
K2CO3
MeOH/THF
86%
17
18
18 R = TMS, 79%
TBAF, THF
19 R = H, 92%
15
11, PdCl2(PPh3)2
CuI, Et3N, THF
20 R = TMS, 46%
TBAF/THF
21 R = H, 80%
Ph2N
NPh2
TMS
OC10H21
C10H21O
R
H
I

III. Synthetic scheme for linear OPV/OPE co-oligomers.

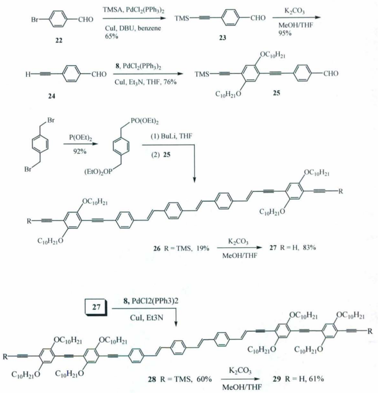
Br
CHO
22
TMSA, PdCl2(PPh3)2
CuI, DBU, benzene
65%
TMS
CHO
23
K2CO3
MeOH/THF
95%
H
CHO
24
8, PdCl2(PPh3)2
CuI, Et3N, THF, 76%
TMS
OC10H21
C10H21O
CHO
25
Br
Br
P(OEt)3
92%
PO(OEt)2
(EtO)2OP
(1) BuLi, THF
(2) 25
R
OC10H21
C10H21O
OC10H21
C10H21O
R
26 R = TMS, 19%
K2CO3
MeOH/THF
27 R = H, 83%
27
8, PdCl2(PPh3)2
CuI, Et3N
R
OC10H21
OC10H21
C10H21O
C10H21O
OC10H21
OC10H21
C10H21O
C10H21O
R
28 R = TMS, 60%
K2CO3
MeOH/THF
29 R = H, 61%

IV. Synthetic scheme of bis(fullero)-OPV/OPE hybrids via in situ alkynylation.

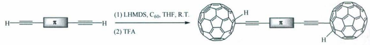
H
π
H
(1) LHMDS, C_{60}, THF, R.T.
(2) TFA
H
π
H

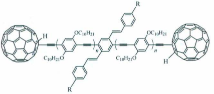
R
H
$OC_{10}H_{21}$
$OC_{10}H_{21}$
$C_{10}H_{21}O$
n
$C_{10}H_{21}O$
n
H
R

30 R = H, n = 1, 41%
31 R = H, n = 2, 21%
32 R = NPh_2, n = 1, 17%
33 R = NPh_2, n = 2, 17%

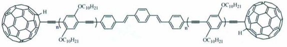
H
$OC_{10}H_{21}$
n
$OC_{10}H_{21}$
$OC_{10}H_{21}$
n
$OC_{10}H_{21}$
H

34 n = 1, 39%
35 n = 2, 40%

V. Synthetic scheme of short H-shaped OPV/OPE co-ologomers.

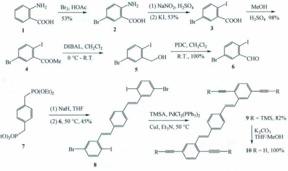
NH_2
COOH
1
Br_2, HOAc
53%
Br
NH_2
COOH
2
(1) $NaNO_2$, H_2SO_4
(2) KI, 53%
Br
I
COOH
3
MeOH
H_2SO_4, 98%
Br
I
COOMe
4
DIBAL, CH_2Cl_2
0 °C - R.T.
Br
I
OH
5
PDC, CH_2Cl_2
R.T., 100%
Br
I
CHO
6
$PO(OEt)_2$
$(EtO)_2OP$
7
(1) NaH, THF
(2) 6, 50 °C, 45%
I
Br
Br
I
8
TMSA, $PdCl_2(PPh_3)_2$
CuI, Et_3N, 50 °C
R
R
R
R
9 R = TMS, 82%
K_2CO_3
THF/MeOH
10 R = H, 100%

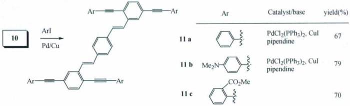
10
ArI
Pd/Cu
Ar
Ar
Ar
Ar
Ar
Catalyst/base
yield(%)
11 a
PdCl$_2$(PPh$_3$)$_2$, CuI
pipendine
67
11 b
Me$_2$N
PdCl$_2$(PPh$_3$)$_2$, CuI
pipendine
79
11 c
CO$_2$Me
70

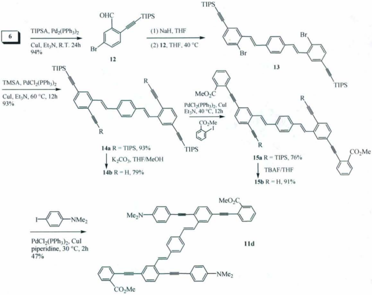
6
TIPSA, Pd$_2$(PPh$_3$)$_2$
CuI, Et$_3$N, R.T. 24h
94%
OHC
TIPS
Br
12
(1) NaH, THF
(2) 12, THF, 40 °C
TIPS
Br
Br
TIPS
13
TMSA, PdCl$_2$(PPh$_3$)$_2$
CuI, Et$_3$N, 60 °C, 12h
93%
TIPS
R
R
TIPS
14a R = TIPS, 93%
K$_2$CO$_3$, THF/MeOH
14b R = H, 79%
MeO$_2$C
PdCl$_2$(PPh$_3$)$_2$, CuI
Et$_3$N, 40 °C, 12h
CO$_2$Me
I
R
R
CO$_2$Me
15a R = TIPS, 76%
TBAF/THF
15b R = H, 91%
I
NMe$_2$
PdCl$_2$(PPh$_3$)$_2$, CuI
piperidine, 30 °C, 2h
47%
MeO$_2$C
Me$_2$N
11d
NMe$_2$
CO$_2$Me

CENTRE FOR NFLD. STUDIES
JUL 18 1978
MEMORIAL UNIVERSITY
OF NEWFOUNDLAND